

REPORT NUMBER 146

MARCH 1964

AD 639236

ESTIMATED STATIC STABILITY & DYNAMICS

CLEARINGHOUSE FOR FEDERAL SCIENTIFIC AND TECHNICAL INFORMATION			
Hardcopy	Microfiche		
\$ 6.00	\$ 1.25	230 pp.	78
1 ARCHIVE COPY			

REPORT NUMBER 146

MARCH 1964

AD 639236

ESTIMATED STATIC STABILITY & CONTROL CHARACTERISTICS

1964 AIRCRAFT RESEARCH AIRCRAFT PROGRAM



DDC AVAILABILITY NOTICES

1. Distribution of this document is unlimited.
2. This document is subject to special report controls and each transmittal to foreign governments or foreign nationals may be made only with prior approval of US Army Aviation Materiel Laboratories, Fort Eustis, Virginia 23604.
3. In addition to security requirements which must be met, this document is subject to special export controls and each transmittal to foreign governments or foreign nationals may be made only with prior approval of USAAVLABS, Fort Eustis, Virginia 23604.
4. Each transmittal of this document outside the agencies of the US Government must have prior approval of US Army Aviation Materiel Laboratories, Fort Eustis, Virginia 23604.
5. In addition to security requirements which apply to this document and must be met, each transmittal outside the agencies of the US Government must have prior approval of US Army Aviation Materiel Laboratories, Fort Eustis, Virginia.
6. Each transmittal of this document outside the Department of Defense must have prior approval of US Army Aviation Materiel Laboratories, Fort Eustis, Va.
7. In addition to security requirements which apply to this document and must be met, each transmittal outside the Department of Defense must have prior approval of US Army Aviation Materiel Laboratories, Fort Eustis, Virginia 23604.
8. This document may be further distributed by any holder only with specific prior approval of US Army Aviation Materiel Laboratories, Fort Eustis, Va. 23604.
9. In addition to security requirements which apply to this document and must be met, it may be further distributed by the holder only with specific prior approval of US Army Aviation Materiel Laboratories, Fort Eustis, Virginia 23604.

DISCLAIMER

10. The findings in this report are not to be construed as an official Department of the Army position unless so designated by other authorized documents.
11. When Government drawings, specifications, or other data are used for any purpose other than in connection with a definitely related Government procurement operation, the United States Government thereby incurs no responsibility nor any obligation whatsoever; and the fact that the Government may have formulated, furnished, or in any way supplied the said drawings, specifications, or other data is not to be regarded by implication or otherwise as in any manner licensing the holder or any other person or corporation, or conveying any rights or permission, to manufacture, use, or sell any patented invention that may in any way be related thereto.
12. Trade names cited in this report do not constitute an official endorsement or approval of the use of such commercial hardware or software.

DISPOSITION INSTRUCTIONS

13. Destroy this report when no longer needed. Do not return it to originator.

14. When this report is no longer needed, Department of the Army organizations will destroy it in accordance with the procedures given in AR 380-5. Navy and Air Force elements will destroy it in accordance with applicable directions. Department of Defense contractors will destroy the report according to the requirement of Section 14 of the Industrial Security Manual for Safeguarding Classified Information. All others will return the report to US Army Aviation Materiel Laboratories, Fort Eustis, Virginia 23604.

REPORT NUMBER 146
March, 1964

ACCESSION NO.		
CFSTI	WHITE SECTION	<input checked="" type="checkbox"/>
DOC	BUFF SECTION	<input checked="" type="checkbox"/>
ANNOUNCED		
IFICATION		
SECTION/AVAILABILITY CODES		
DIS.	AVAIL.	and/or SPECIAL

ESTIMATED STATIC STABILITY AND
CONTROL CHARACTERISTICS

XV-5A LIFT FAN

FLIGHT RESEARCH AIRCRAFT PROGRAM

DDC
RECEIVED
SEP 28 1966
RECEIVED
B

ADVANCED ENGINE AND TECHNOLOGY DEPARTMENT

GENERAL ELECTRIC COMPANY

CINCINNATI, OHIO 45215

31 MAY 1966

MF

CONTENTS

SECTION		PAGE
1.0	SUMMARY	1
2.0	INTRODUCTION	2
3.0	CONVENTIONAL FLIGHT CHARACTERISTICS	3
3.1	Conventional Flight, Low Speed, Longitudinal	4
3.2	Conventional Flight, Low Speed, Lateral-Directional	7
3.3	Conventional Flight, High Speed, Longitudinal	8
3.4	Conventional Flight, High Speed, Lateral-Directional	10
3.5	Conventional Flight, Low Speed, Control Effectiveness	11
3.6	Conventional Flight, High Speed, Control Effectiveness	13
3.7	Conventional Flight, Low Speed, Control Surface Hinge Moments	15
3.8	Conventional Flight, High Speed, Control Surface Hinge Moments	16
4.0	LIFT FAN MODE CHARACTERISTICS	115
4.1	Fan Mode, Transition, Longitudinal	115
4.2	Conversion, Longitudinal	127
4.3	Fan Thrust and Power Characteristics	127
4.4	Fan Mode, Lateral-Directional	129
4.5	Fan Mode, Lateral-Directional Control Effectiveness	131
4.6	Fan Mode, Hovering Stability	132
5.0	CONCLUSIONS	169
6.0	APPENDIX	171

BLANK PAGE

LIST OF FIGURES

FIGURE		PAGE
3.1	Low Speed $C_{L_{M-T}}$ Vs α , Landing Gear Up	17
3.2	Low Speed $C_{m_{C.G.}}$ Vs α , Tail-Off, Landing Gear Up, c.g. @ F.S. 240	18
3.3	Low Speed $C_{m_{C.G.}}$ Vs α , Tail-Off, Landing Gear Up, c.g. @ F.S. 246	19
3.4	Low Speed Downwash	20
3.5	Estimated $C_{L_{M-T}}$ Vs α in Ground Effect	21
3.6	Estimated $C_{m_{C.G. M-T}}$ Vs α in Ground Effect c.g. @ F.S. 240	22
3.7	Estimated $C_{m_{C.G. M-T}}$ Vs α in Ground Effect c.g. @ F.S. 246	23
3.8	Estimated Downwash in Ground Effect	24
3.9	Low Speed $C_{L_{CM}}$ Vs α Untrimmed, Landing Gear Up	25
3.10	Low Speed $C_{m_{C.G.}}$ Vs α , Landing Gear Up c.g. @ F.S. 240	26
3.11	Low Speed $C_{m_{C.G.}}$ Vs α , Landing Gear Up c.g. @ F.S. 246	27
3.12	Low Speed $C_{L_{CM}}$ Vs $C_{m_{C.G.}}$, Landing Gear Up	28
3.13	Low Speed $C_{L_{CM}}$ Vs $C_{m_{C.G.}}$, Landing Gear Up	29
3.14	Estimated Low Speed q_t/q_0 Vs α	30
3.15	Low Speed C_{L_t} Vs α_t	31

LIST OF FIGURES (Continued)

FIGURE		PAGE
3.16	Low Speed C_{L_t} Vs C_{D_t}	32
3.17	Low Speed $C_{L_{CM}}$ Vs α , Trimmed, Landing Gear Up	33
3.18	Low Speed $C_{L_{CM}}$ Vs α , Trimmed, Landing Gear Up	34
3.19	Trimmed Drag Polar, Low Speed	35
3.20	Pitching Moment Coefficient Due to Sideslip, Model Minus Tail	36
3.21	Pitching Moment Coefficient Due to Sideslip, Low Speed	37
3.22	Estimated Change in Lift and Pitching Moment Due to Lowering of Landing Gear	38
3.23	Side Force Coefficient Due to Sideslip Angle, Low Speed	39
3.24	Yawing Moment Coefficient Due to Sideslip Angle, Low Speed	40
3.25	Yawing Moment Coefficient Due to Sideslip Angle, Low Speed	41
3.26	Rolling Moment Coefficient Due to Sideslip Angle, Low Speed	42
3.27	$C_{L_{\alpha_{M-T}}}$ Vs Mach Number	43
3.28	$C_{m_{\alpha_{M-T}}}$ Vs Mach Number	44
3.29	$C_{m_{\alpha_{M-T}}}$ Vs Mach Number	45
3.30	A. C. $M-T$ Location Vs Mach Number	46
3.31	$\alpha_{oL_{M-T}}$ and $C_{m_{oM-T}}$ Vs Mach Number	47
3.32	ϵ_{oL} and $\partial \epsilon / \partial \alpha$ Vs Mach Number	48

LIST OF FIGURES (Continued)

FIGURE		PAGE
3.33	$C_L \alpha_{CM}$ Vs Mach Number	49
3.34	$C_m \alpha_{CM}$ Vs Mach Number	50
3.35	$C_m \alpha_{CM}$ Vs Mach Number	51
3.36	$C_{L_{Limit}}$ Vs Mach Number	52
3.37	$C_m C_{L_{CM}}$ Vs Mach Number	53
3.38	$C_m C_{L_{CM}}$ Vs Mach Number	54
3.39	$C_L \alpha_{CM_{Trimmed}}$ Vs Mach Number	55
3.40	$C_L \alpha_{CM_{Trimmed}}$ Vs Mach Number	56
3.41	$C_L \delta_i$ Vs Mach Number	57
3.42	$C_m \delta_i$ Vs Mach Number	58
3.43	$C_m \delta_i$ Vs Mach Number	59
3.44	Trimmed Drag Polar, High Speed	60
3.45	Pitching Moment Coefficient Due to Sideslip, High Speed	61
3.46	$C_Y \beta_{M-T}$ Vs Mach Number	62
3.47	$C_Y \beta_{CM}$ Vs Mach Number	63
3.48	$C_n \beta_{M-T}$ Vs Mach Number	64

LIST OF FIGURES (Continued)

FIGURE		PAGE
3.49	$C_{n\beta}$ CM Vs Mach Number	65
3.50	$C_{n\beta}$ CM Vs Mach Number	66
3.51	C M-T Vs Mach Number	67
3.52	$C_{l\beta}$ CM Vs Mach Number	68
3.53	Aileron Deflection Schedule	69
3.54	Aileron Deflection Schedule	70
3.55	Side Force Coefficient Due to Aileron Deflection, Low Speed	71
3.56	Yawing Moment Coefficient Due to Aileron Deflection, Low Speed	72
3.57	Yawing Moment Coefficient Due to Aileron Deflection, Low Speed	73
3.58	Yawing Moment Coefficient Due to Aileron Deflection, Low Speed	74
3.59	Rolling Moment Coefficient Due to Aileron Deflection, Low Speed	75
3.60	Rolling Moment Coefficient Due to Aileron Deflection, Low Speed	76
3.61	Elevator Effectiveness Parameter, Low Speed	77
3.62	$C_{L\delta_e}$ Vs Mach Number	78
3.63	$C_{m\delta_e}$ Vs Mach Number	79
3.64	$C_{m\delta_e}$ Vs Mach Number	80

LIST OF FIGURES (Continued)

FIGURE		PAGE
3.65	Side Force Coefficient Due to Rudder Deflection, High Speed	81
3.66	Yawing Moment Coefficient Due to Rudder Deflection, High Speed	82
3.67	Rolling Moment Coefficient Due to Rudder Deflection, High Speed	83
3.68	Side Force Coefficient Due to Aileron Deflection, High Speed	84
3.69	Yawing Moment Coefficient Due to Aileron Deflection, High Speed	85
3.70	Rolling Moment Coefficient Due to Aileron Deflection, High Speed	86
3.71	Low Speed C_{h_e} Vs δ_e (Balanced)	87
3.72	Low Speed C_{h_e} Vs α_t (Balanced)	88
3.73	Low Speed C_{h_e} Vs α_t or δ_e (Unbalanced)	89
3.74	Low Speed C_{h_r} Vs δ_r (Balanced)	90
3.75	Low Speed C_{h_r} Vs β (Balanced)	91
3.76	Low Speed C_{h_r} Vs β or δ_r (Unbalanced)	92
3.77	C_{h_a} Vs δ_a , Low Speed	93
3.78	Low Speed C_{h_a} Vs α_w (Balanced)	94
3.79	Low Speed C_{h_a} Vs α_w or δ_a (Unbalanced)	95
3.80	C_{h_e} Vs Mach Number (Balanced) δ_e	96
3.81	C_{h_e} Vs Mach Number (Balanced) α_t	97

LIST OF FIGURES (Continued)

FIGURE		PAGE
3.82	$C_{h_e \delta_e}$ and $C_{h_e \alpha_t}$ Vs Mach Number (Unbalanced)	98
3.83	$C_{h_r \delta_r}$ Vs Mach Number (Balanced)	99
3.84	$C_{h_r \beta}$ Vs Mach Number (Balanced)	100
3.85	$C_{h_r \delta_r}$ and $C_{h_r \beta}$ Vs Mach Number (Unbalanced)	101
3.86	$C_{h_a \delta_a}$ and $C_{h_a \alpha}$ Vs Mach Number	102
3.87	$C_{h_t \delta_t}$, $C_{h_t \delta_a}$, and $C_{h_a \delta_t}$ Vs Mach Number	103
3.88	$C_{h_a \delta_a}$ and $C_{h_a \alpha_w}$ Vs Mach Number (Unbalanced)	104
3.89	Elastic Lift Curve Slope Parameter Vs Mach Number, Model Minus Tail	105
3.90	Elastic Pitching Moment Curve Slope Parameter Vs Mach Number, Model Minus Tail	106
3.91	Elastic Angle of Zero Lift and Pitching Moment Coefficient at Zero Lift Parameters Vs Mach Number, Model Minus Tail	107
3.92	Elastic Rolling Moment Coefficient with Aileron Deflection Parameter Vs Mach Number	108
3.93	Elastic Roll Damping Parameter Vs Mach Number	109
3.94	Elastic Roll Coefficient Vs Mach Number	110
3.95	Elastic Tail Coefficient Vs Mach Number	111
3.96	Elastic Tail Coefficient Vs Mach Number	112
3.97	Horizontal Tail Effective Lift Curve Slope Vs Horizontal Tail Aspect Ratio	113

LIST OF FIGURES (Continued)

FIGURE		PAGE
3.98	Incremental Change in Rolling Moment with Sideslip Angle Coefficient Vs Dihedral Angle	114
4.1	Estimated Lift Characteristics in Fan Mode	134
4.2	Estimated Drag Characteristics in Fan Mode	135
4.3	Estimated Pitching Moment Characteristics in Fan Mode	136
4.4	Variation of Lift Curve Slope with Thrust Coefficient and Vector Angle	137
4.5	Estimated ΔC_D^S Due to Angle of Attack, $\beta_v = 0^\circ$	138
4.6	Estimated ΔC_D^S Due to Angle of Attack, $\beta_v = 50^\circ$	139
4.7	Estimated ΔC_D^S Due to Angle of Attack, $\beta_v = 50^\circ$	140
4.8	Variation of Pitching Moment Curve Slope with Thrust Coefficient	141
4.9	Incremental Lift and Drag Coefficients Due to Exit Louver Vector Angle, Tail-Off	142
4.10	Incremental Pitching Moment Coefficient Due to Exit Louver Vector Angle	143
4.11	Effect of Exit Louver Stagger on Longitudinal Characteristics	144
4.12	Longitudinal Coefficients in Transition Speed Range	145
4.13	Horizontal Tail Effectiveness in Fan Powered Flight Mode	146
4.14	Downwash at Horizontal Tail Vs Aircraft Angle of Attack	147
4.15	Estimated Longitudinal Static Stability in Transition Speed Range	148
4.16	Nose Fan Static Lift Variation with Thrust Reverser Door Position	149
4.17	Estimated Nose Fan Lift and Drag Coefficients	150

LIST OF FIGURES (Continued)

FIGURE		PAGE
4. 18	Estimated Tail-Off Longitudinal Characteristics for Conversion	151
4. 19	Estimated Tail-On Pitching Moment Curve Slope for Conversion	152
4. 20	Wing Fan Static Lift and Power	153
4. 21	Nose Fan Static Lift and Power	154
4. 22	Variation of Power Coefficient with Exit Louver Angle	155
4. 23	Variation of Nose Fan Power Coefficient Ratio in Transition	156
4. 24	Estimated Side Force Derivative with Sideslip in Fan Powered Flight	157
4. 25	Estimated Yawing Moment Derivative with Sideslip in Fan Powered Flight	158
4. 26	Estimated Rolling Moment with Sideslip in Fan Powered Flight	159
4. 27	Cross-Coupling of Pitching Moment with Sideslip in Fan Flight	160
4. 28	Cross-Coupling Derivative of Pitching Moment with Sideslip in Fan Powered Flight	161
4. 29	Yawing Moment Derivative with Aileron Deflection in Fan Powered Flight	162
4. 30	Rudder Control Effectiveness Derivative in Fan Powered Flight	163
4. 31	Effect of Vertical Velocity on Lift and Pitching Moment Coefficient	164
4. 32	Damping in Vertical Flight with the Nose Fan at Various Thrust Levels	165
4. 33	Longitudinal and Lateral Characteristics in Lateral Translation	166
4. 34	Longitudinal Characteristics in Rearward Flight	167

LIST OF FIGURES (Continued)

FIGURE		PAGE
4.35	Effect of Negative Vectoring and Pitch Angle in Rearward Flight	168
6.1	Lift and Moment Increments Due to Flap Deflection	180
6.2	Effect of Aileron Droop on Longitudinal Characteristics	181
6.3	Typical Variation of Lift Curve Slope with Vector Angle	182
6.4	Variation of Incremental Drag Coefficient Due to Angle of Attack with Vector Angle	183
6.5	Increase in the Incremental Drag Coefficient Due to Angle of Attack with 15° Aileron Droop	184
6.6	Comparison of Full-Scale and 1/6-Scale Static Stability with the Tail-Off	185
6.7	Incremental Lift and Drag Coefficients Due to Vector Angle	186
6.8	Incremental Pitching Moment Coefficient Due to Vector Angle	187
6.9	Compilation of Exit Louver Stagger Effectiveness Data	188
6.10	Effect of Nose Fan on Longitudinal Static Stability	189
6.11	Incremental Lift and Moment Coefficients Due to Nose Fan Operation	190
6.12	Incremental Drag Coefficient Due to Nose Fan Operation	191
6.13	Fan Speed Variation with Forward Speed and Vector Angle	192
6.14	Side Force Derivative with Sideslip in Fan Flight	193
6.15	Yawing Moment Derivative with Sideslip in Fan Flight	194
6.16	Rolling Moment Derivative with Sideslip in Fan Flight	195

LIST OF FIGURES (Continued)

FIGURE		PAGE
6.17	Incremental Effect of Nose Fan on Side Force Derivative with Sideslip	196
6.18	Incremental Effect of Nose Fan on Yawing Moment Derivative with Sideslip	197
6.19	Incremental Effect of Nose Fan on Rolling Moment Derivative with Sideslip	198
6.20	Comparison of Full-Scale and 1/6-Scale Lateral- Directional Data	199
6.21	Variation of Rolling Moment Coefficient with Differential Aileron	200
6.22	Estimated Yawing Moment Coefficient Due to Differential Aileron Deflection Schedule	201

1.0 SUMMARY

The XV-5A is a two-engine, two-place V/STOL research aircraft with a design gross weight of 9200 pounds and an aspect ratio 3.42 wing of 260 square feet. In conventional flight mode the aircraft has a power-off flaps-down stall speed of 89 knots and a design maximum speed of 450 knots. In fan flight mode the aircraft can sustain flight at any speed from hovering to speeds in excess of conventional stall speed.

This report represents an estimate of the Ryan Aeronautical Company of the XV-5A Aerodynamic Characteristics, based on theoretical and empirical considerations, including the results of 420 hours of wind tunnel tests of 1/8 and 1/6 scale models. In developing the fan-powered flight aerodynamic characteristics, extensive use has also been made of unpublished data obtained from tests of a full-scale model similar to the XV-5A aircraft, conducted at the NASA-Ames Research Center's 40 x 80 wind tunnel.

In the fan flight mode, the aircraft is estimated to be statically unstable in pitch with the most aft cg at low speeds below approximately 70 knots but with an increasing stability with speed to the conversion speed where the stability level corresponds to that for conventional flight.

The aircraft possesses positive lateral and directional static stability with sideslip at all forward speeds in fan-powered flight and the effectiveness of the conventional flight control system is shown to be unaffected by fan operation.

The exit louver control system is capable of providing the required propulsive force for acceleration of the airplane from a minimum of 10 knots rearward to conversion speed and provides a thrust attenuation of up to 22% for hovering lift control.

Estimated XV-5A conventional flight static stability is satisfactory throughout the flight envelope. Low speed static longitudinal stability flaps down, near stall angles becomes marginal, but due to high damping, this is considered acceptable. Increased horizontal tail area has been added to account for losses in longitudinal stability at high speed due to aeroelastic effects. Satisfactory lateral directional characteristics have been insured by increasing the wing outboard panel dihedral to +4 degrees. Control effectiveness and hinge moment data have been evaluated throughout the speed range.

2.0 INTRODUCTION

This report contains the aerodynamic stability and control characteristics of the U. S. Army XV-5A Lift Fan Research Aircraft. The XV-5A was designed and built by the Ryan Aeronautical Company for the flight evaluation testing of the General Electric X-353-5 lift fan propulsion system, and is a V/STOL aircraft capable of conventional operations at high subsonic speed

The XV-5A incorporates two separate flight control systems. A conventional aerodynamic control system is actuated during all modes of flight; a fan flight control system provides both attitude and altitude control in hovering and low-speed operation and is phased out with wing fan exit louver vector angle as flight speed increases and the conventional control system gains effectiveness. The conventional system consists of elevator, ailerons and rudder. The fan system consists of the nose fan with thrust reverser doors for longitudinal trim and control, and the wing fan exit louvers for roll, yaw, hovering lift, and forward flight propulsion control.

The aerodynamic data presented in this report are the result of extensive analysis of small-scale and full-scale wind tunnel test data conducted to obtain initial definition of the static aerodynamic characteristics of the XV-5A aircraft in the conventional flight and lift fan flight modes. The conventional flight data are separated into three major classifications according to flight mode, speed range, and type of data. The fan-flight data are non-dimensionalized in slipstream notation in terms of the static installed fan thrust. Where it is believed helpful to show supporting data to aid the understanding of the data analysis methods used, the supporting data is presented in the Appendix. This is particularly true of the fan flight characteristics for which much of the referenced data is unpublished.

The aerodynamic characteristics of this report provided the basis for analysis of the stability and control characteristics of the aircraft and typify the input data for the Ryan Flight Simulator. Additional information covering dynamic stability and flying qualities characteristics will be submitted in subsequent aircraft reports.

3.0 CONVENTIONAL FLIGHT CHARACTERISTICS

The static aerodynamic characteristics of the XV-5A presented in this section were derived primarily from a series of low and high speed wind tunnel tests of a 1/8 scale conventional flight model, and a 1/6 scale lift fan powered model (Ref. 1, 2, and 3). The data obtained from these tests dictated several modifications to the original airplane design which were subsequently evaluated in additional wind tunnel tests or by theoretical and/or empirical means. The design changes which were incorporated are summarized below and discussed individually in the appropriate section of this report.

- Aileron droop - Both ailerons deflected trailing edge down in conjunction with wing flap deflection at the rate of one degree aileron per three degrees flap.
- Wing dihedral - Outboard wing panel dihedral increased from -6° to $+4^{\circ}$.
- Horizontal Tail span - Increased ten inches full-scale.
- Rudder span - Increased eight inches full-scale parallel to the hinge line.
- Aileron horn balance removed.

Only a limited amount of data applicable to the low speed conventional flight mode was obtained from the 1/6 scale, lift-fan powered model. Correlation of test data from the two models (1/6 scale model, lift-fans off) was generally acceptable; however, irregularities in the 1/6 scale model conventional flight mode data attributed to test conditions and model support system led to virtually exclusive use of the 1/8 scale model test data for definition of the conventional flight aerodynamic characteristics. This does not necessarily reflect on the validity of the 1/6 scale model fan powered data which are discussed in another section of this report. The 1/6 scale model test data which were used out of necessity to define the conventional flight characteristics were taken as incremental effects (e.g., effect of aileron droop) and applied to the basic data from the 1/8 scale model.

No scale effect corrections were applied to the model test data to obtain full scale airplane characteristics with the exception of the drag.

3.1 CONVENTIONAL FLIGHT, LOW SPEED, LONGITUDINAL

The basic longitudinal characteristics (C_L , C_m , ϵ) of the model minus tail (M-T), flaps up and down in free air were taken directly from the 1/8 scale model wind tunnel test data (Ref. 1). The aileron droop feature which was incorporated specifically to improve transition characteristics in the lift-fan mode was evaluated only on the 1/6 scale fan powered model. Therefore, an incremental C_L , C_m , and ϵ due to aileron droop were determined from that data (Ref. 2) and applied to the corresponding 1/8 scale conventional flight model configuration without aileron droop to arrive at the final M-T characteristics presented in Figures 3.1 through 3.8.

The data of Figure 3.1 indicates a $C_{L_{max}}$ of 1.56 for the wing body configuration at full flap deflection and a gentle stall is indicated by the gradual reduction and reversal in lift curve slope for all flap deflections as the angle of attack for maximum lift (at 16 degrees) is approached and exceeded. The pitching moment data of Figures 3.2 and 3.3 show a very stable break in the wing-body moment at stall due to a rapidly retreating wing center of pressure when $C_{L_{max}}$ is reached. This is indicative of an occurrence of initial wing stall on the inboard wing panels and is a desirable characteristic because of the retention of lateral control effectiveness and the lack of large lateral-directional upsetting moments in the region of the stall normally associated with such characteristics. The effect has been achieved by using increased airfoil section camber and twist (washout) in the outboard wing panels.

The M-T longitudinal characteristics in ground effect shown in Figures 3.5 to 3.8 were estimated by the empirical method of Ref. 4 which is based on the known characteristics in free air or out of ground effect. A comparison of the empirical method and a small amount of ground effect data obtained from the 1/6 scale wind tunnel model showed at least qualitative agreement. The following equations from Ref. 4 were used to calculate the M-T longitudinal characteristics in ground effect for the case where the 25% wing MAC is 0.374 semi-spans above the ground at $\alpha = 0^\circ$.

$$C_{LG} = C_L \left[1 + \frac{57.3 C_L \alpha}{\pi A} \left(1 - \frac{A}{A_G} \right) \right]$$

$$C_{m_G} = C_m + \frac{X_{c.g.} - X_{a.c.}}{\bar{c}} \left[C_{L_G} - C_L \right]$$

$$\epsilon_G = \epsilon \left[1 - \frac{b_{eff}^2 + (H_H - H_W)^2}{b_{eff}^2 + (H_H + H_W)^2} \right]$$

The terms A_G and b_{eff} were obtained from Section 4.4.1 of Ref. 4 and H_H and H_W are respectively the height of the horizontal tail and wing 25% MAC above the ground plane. An additional increment of 0.5° was added to ϵ_G in order to reflect the general trend of the limited amount of wind tunnel data. Since the above equations are strictly applicable within the linear range of C_L versus α , the maximum lift coefficient of the M-T in ground effect was estimated from experimental data presented in Ref. 5 to be:

$$C_{L_{max_G}} = 1.01 C_{L_{max}} \quad \delta_f = 0^\circ$$

$$C_{L_{max_G}} = 0.975 C_{L_{max}} \quad \delta_f = 30^\circ + \delta_d = 10^\circ$$

$$C_{L_{max_G}} = 0.95 C_{L_{max}} \quad \delta_f = 45^\circ + \delta_d = 15^\circ$$

Because of the high location of the tee-type horizontal tail, the tail is always out of ground effect except for the influence of the altered wing downwash field.

Application of estimated aeroelastic effects to the high speed wind tunnel, rigid model test data led to an increase in the horizontal tail span so as to provide improved longitudinal stability of the elastic airframe at high speed. Low speed wind tunnel data was subsequently obtained for an 8-inch extension of the horizontal tail semi-span and a 5-inch extension was ultimately selected for the final aircraft configuration. Inasmuch as actual test data did not exist for the final horizontal tail size, its effectiveness was obtained by interpolating between the known characteristics of the two tails which were tested in the wind tunnel. The only significant parameters involved which affect the stabilizer effectiveness in this case are the change in aspect ratio and planform area. A linear

interpolation with aspect ratio to obtain $C_{L\alpha_H} \eta$ as shown in Figure 3.97 was considered sufficiently accurate in view of the small range of aspect ratios involved. Thus, the low speed linear effectiveness of the final tail configuration was calculated from the following definitive equations:

$$C_{L_{iH}} = C_{L\alpha_H} \frac{S_H}{S} \eta$$

$$C_{m_{iH}} = C_{L_{iH}} \frac{l_H}{\bar{c}}$$

In order to determine more accurately the variation of complete model static stability (C_m vs C_L) with the final tail configuration through wing stall, where $\eta = q_H/q$ is not a constant, a direct interpolation at constant wing angle of attack between the two respective wind tunnel curves for the basic tail and the 8-inch semi-span extension was made. Since the interpolation was made at constant wing angle of attack, the only variables involved were the tail lift curve slope and area. The resultant complete model lift and pitching moment curves are presented in Figures 3.9 through 3.13 for a stabilizer setting of zero.

The dynamic pressure ratio (η) at the horizontal tail shown in Figure 3.14 was estimated from wind tunnel and theoretical data by the following equation.

$$\eta = \frac{C_{m_{M-T}} - C_{m_{CM}}}{\left[\left(C_{L_H} \cos \epsilon - C_{D_H} \sin \epsilon \right) \frac{l_H}{t} + \left(C_{L_H} \sin \epsilon + C_{D_H} \cos \epsilon \right) \frac{z_H}{\bar{c}} \right] \frac{S_H}{S}}$$

While the wing body configuration displays a very stabilizing stall behavior, the pitching moment data for the complete model at high flap deflections (Figures 3.10, 3.11) show a mild instability as stall is approached. This effect is due to the contribution of the horizontal tail to pitching moment and at angles of attack below stall can be attributed (as shown in Figures 3.4 and 3.14) to an increasing rate of change of downwash angle and increasing negative rate of change of local horizontal stabilizer dynamic pressure as angle of attack is increased. (Figures 3.14 and 3.15.) Highly non-linear downwash and dynamic pressure effects are indicated

for angles of attack at, and above, $C_{L_{\max}}$ by the complete model pitching moment data.

Flight simulation investigations have been conducted to determine pitching moment characteristics in performing flight near stall. It has indicated that no difficulty is associated with the low level of static stability at these conditions due in part to the high pitch damping associated with the use of the large horizontal stabilizer. Wind tunnel tests of the 1/6 scale model have shown that the instability indicated for operation out-of-ground effect vanishes when in proximity to the ground. (See Figure 3.11.)

The tail lift coefficient C_{L_H} shown in Figure 3.15 for the isolated horizontal tail was estimated theoretically from Ref. 6 and the tail drag term C_{D_H} shown in Figure 3.16 was obtained from wind tunnel data.

The trimmed lift and drag characteristics ($C_m = 0$) are presented in Figures 3.17 through 3.19. A rather extensive analysis of the wind tunnel drag data and corrections thereto is presented in Ref. 13. Therefore, only the final trimmed drag curves are contained in this report. The data indicate a trimmed $C_{L_{\max}}$ of 1.0 without flaps and 1.52 with full flaps at an intermediate cg location. A maximum L/D of approximately 10 is shown.

Low and high speed wind tunnel data revealed a significant variation of pitching moment with sideslip angle. As indicated by Figures 3.20 and 3.21 the predominant contribution is from the horizontal tail and the complete model incremental pitching moment due to sideslip is insensitive to angle of attack. Longitudinal trim change due to landing gear is small and is presented in Figure 3.22.

3.2 CONVENTIONAL FLIGHT, LOW SPEED, LATERAL-DIRECTIONAL

The low speed lateral-directional characteristics presented in Figures 3.23 to 3.26 were derived from a combination of the low and high speed wind tunnel test results because of an unaccountable disagreement between the derivatives C_{Y_β} and C_{n_β} for flaps 0° at $M = 0.285$ (low speed test) and $M = 0.40$ (high speed test). The high speed test data yielded values for the complete model C_{Y_β} and C_{n_β} that were

respectively 40% and 125% greater than those from the low speed test at $\alpha = 0^\circ$. In either case positive static directional stability was indicated over the full angle of attack range. In the case of the lateral stability derivative C_{l_β} , agreement between the two tests was considered satisfactory.

The results of a low speed wind tunnel study of the effect of outboard wing panel dihedral angle on C_{l_β} are presented in Figure 3.98. An increase in dihedral from -6° to $+4^\circ$ was considered necessary because of an unexpectedly large effect of wing-body interference on C_{l_β} and a positive complete model C_{l_β} at Mach numbers greater than about 0.6.

The only final configuration change pertinent to lateral-directional stability which was not tested on the 1/8 scale model was aileron droop; however, 1/6 scale model test data indicated no discernible effect of aileron droop on any of the lateral-directional derivatives.

3.3 CONVENTIONAL FLIGHT, HIGH SPEED, LONGITUDINAL

The high speed, longitudinal characteristics are presented in Figures 3.27 to 3.43. Generally acceptable agreement between the low and high speed wind tunnel tests was obtained for the longitudinal characteristics of the model. The most notable exception was the slope of the pitching moment curve of the M-T, $C_{m_\alpha} \alpha_{M-T}$. The low speed test data indicated

the tail-off configuration to be approximately 15% more destabilizing than did the high speed data which also showed no noticeable variation in longitudinal stability for the Mach number range of 0.4 to 0.7. The disagreement in $C_{m_\alpha} \alpha_{M-T}$ was not considered especially significant inasmuch as the complete model data agreed quite well.

Subsequent to the high speed wind tunnel test, two significant modifications were made to the final aircraft configuration. Namely, a 5-inch extension of the horizontal tail semi-span and an increase in outboard wing panel dihedral from -6° to $+4^\circ$. It was assumed throughout the Mach number range and confirmed by wind tunnel data at low speed that the change in dihedral had no effect on the static longitudinal stability characteristics. The stabilizer effectiveness for the final tail configuration was determined at low speed as stated in Section 3.1. The high speed test data was corrected by using the following relationship to determine the stabilizer effectiveness throughout the Mach number range.

$$C_{L_{iH}} = \left[\frac{(C_{L_{iH}})_{\text{calc}}}{(C_{L_{iH}})_{\text{test}}} \right]_{\text{low speed}} \times \left[(C_{L_{iH}})_{\text{test}} \right]_{\text{high speed}}$$

$$C_{m_{iH}} = C_{L_{iH}} \frac{\ell_H}{\bar{c}}$$

The stabilizer effectiveness thus calculated was used to correct the complete model characteristics to the proper horizontal tail configuration by the following equations:

$$C_{L_{\alpha_{CM}}} = C_{L_{\alpha_{M-T}}} + C_{L_{iH}} \left(1 - \frac{\partial \epsilon}{\partial \alpha} \right)$$

$$C_{m_{\alpha_{CM}}} = C_{m_{\alpha_{M-T}}} + C_{m_{iH}} \left(1 - \frac{\partial \epsilon}{\partial \alpha} \right)$$

High speed wind tunnel data have shown, at the higher Mach numbers, a decrease in static longitudinal stability with increase in angle of attack. Figure 3.36 shows the definable boundary for zero static longitudinal stability as a function of Mach number and lift coefficient for the complete model. Although the available data shows a gradual deterioration of static stability with angle of attack, extreme caution should be exercised during initial flight test investigations when the boundaries of Figure 3.36 are approached.

The wing body neutral point from Figure 3.30 is shown to lie between 13 and 16 percent mean aerodynamic chord up to approximately 0.80 Mach number. The complete model data of Figure 3.35 shows the aircraft to be statically stable with an aft center of gravity up to Mach 0.84. The horizontal stabilizer control effectiveness, $C_{m_{it}}$, shows a deterioration below the low speed value above $M = 0.81$ and at $M = 0.9$, has an effectiveness equal to 1/3 of that shown for low speeds.

The high speed trimmed lift and drag coefficients are presented in Figures 3.39 to 3.44. As mentioned previously, a complete drag analysis is presented in Ref. 13; therefore, only the final trimmed drag is presented herein.

The variation with Mach number of the complete model pitching moment coefficient due to sideslip angle is presented in Figure 3.45. Note that C_m varies hyperbolically with β at constant Mach number and the parameter K_{CM} represents a family of hyperbolas.

The effect of aeroelasticity on the longitudinal stability derivatives is presented in Figures 3.89 to 3.96 in terms of the ratio of the elastic airframe value to the rigid airframe value. These data are derived and discussed extensively in Ref. 11; therefore, only the final results are presented in this report.

3.4 CONVENTIONAL FLIGHT, HIGH SPEED, LATERAL-DIRECTIONAL

The high speed lateral-directional characteristics are presented in Figures 3.46 to 3.52. The excessively large disagreement between the high speed and low speed test values for the derivatives $C_{Y\beta}$ and $C_{n\beta}$ discussed in Section 3.2 could not be physically explained as the difference in Mach number (0.285 to 0.40) was too small to justify the difference in test values on the basis of compressibility effects. Therefore, as reasonable a fairing as possible was made of the derivatives versus Mach number. In any event the magnitude of $C_{Y\beta}$, and the more important directional stability derivative $C_{n\beta}$, are satisfactory from the stability standpoint throughout the full range of Mach numbers investigated.

The only lateral-directional derivative from the high speed test data which had to be corrected because of subsequent aircraft configuration changes was $C_{l\beta}$. This was due to the increase in outboard wing panel dihedral from -6° to $+4^\circ$. As mentioned previously in Section 3.2, low speed wind tunnel test data was obtained on the effect of varying the dihedral angle and this data is shown in Figure 3.98. Since the theoretical effect of compressibility presented in Section 5.1.2 of Ref. 4 indicates less than a 10% total variation in the incremental $C_{l\beta}$ due to dihedral from $M = 0$ to 0.8 and in the absence of high speed experimental data the low speed wind tunnel test values of $\Delta C_{l\beta}$ due to dihedral were applied throughout the Mach range. Positive dihedral effect is shown for the complete model at the critical zero angle of attack condition up to $M = .82$ (Figure 3.52).

3.5 CONVENTIONAL FLIGHT, LOW SPEED, CONTROL EFFECTIVENESS

The XV-5A conventional flight mode control system consists of typical elevator, ailerons and rudder to provide pitch, roll and yaw control respectively. The rudder and left aileron are equipped with conventional trim tabs for trimming the control stick force to zero whereas longitudinal stick force trim is accomplished by the all movable horizontal stabilizer. The elevator and rudder are purely manual control systems wherein the cockpit controls are connected directly to the control surface through a tension regulated cable system. The lateral control is a full power system with pilot force feel provided by a servo tab on each aileron. The servo tabs also assist in reducing the aileron hinge moment. The lateral system is powered by two independent hydraulic systems, each of which is supplied by the hydraulic pump from one engine. Under normal conditions each system provides one-half of the total hydraulic power so that in the event of failure of one system, one-half of the normal power available remains.

The incorporation of aileron droop in conjunction with flap deflection required the use of a differential deflection rate between the up-going and down-going aileron in order to provide sufficient maximum roll power since the aileron rolling effectiveness deteriorates rather rapidly beyond 20° trailing edge down. In addition, the differential rate reduces the maximum adverse yawing moment. The rigid system deflection schedules are shown in Figures 3.52 and 3.53. Mechanical limitations of the system result in a small differential rate existing also at flaps 0° .

The low speed aileron effectiveness is presented in Figures 3.55 to 3.60, while the low speed elevator and rudder effectiveness are taken at the low speed end of the Mach number curves. A low speed correction factor for large elevator deflections is presented in Figure 3.61. These data were derived from wind tunnel test data and corrected as necessary for subsequent modification of the control surface or aircraft geometry.

The 5-inch extension to the horizontal tail semi-span required the elevator effectiveness as obtained from wind tunnel data be corrected for the increase in tail reference area and lift curve slope. The effectiveness of the extended span tail was calculated as shown in Section 3.1 of this report and the corrected elevator effectiveness was calculated from the following equation:

$$C_{m_{\delta_e}} = \left(C_{m_{\delta_e}} \right)_{\text{test}} \times \frac{\left(C_{m_{iH}} \right)_{\text{calc}}}{\left(C_{m_{iH}} \right)_{\text{test}}}$$

The low speed test data indicated a significant reduction in elevator pitching moment effectiveness, $C_{m_{\delta_e}}$, at deflections greater than 5° , although it was not possible to determine this reduction in the lift effectiveness because $C_{L_{\delta_e}}$ is rather small in magnitude. An empirical correction factor shown in Figure 3.61 was determined from test data to account for the nonlinear nature of pitching moment coefficient due to elevator deflection. This empirical factor is defined as follows:

$$K_e = \frac{\Delta C_{m_{\text{elev}}}}{\left(C_{m_{\delta_e}} \right)_{\delta_e = 0} \times \delta_e}$$

In view of the relative unimportance of lift due to elevator deflection, no correction factor was determined for $C_{L_{\delta_e}}$.

The span of the rudder parallel to the hinge line was increased 8 inches full scale over that which was tested on the wind tunnel model. The effectiveness of the extended span rudder was determined from Ref. 6 by calculating a theoretical increment in effectiveness due to the span extension and adding this to the test based value of the smaller span rudder so that:

$$C_{Y_{\delta_r}} = C_{Y_{\delta_r}}_{\text{test}} + \left(\Delta C_{Y_{\delta_r}} \right)_{\text{calc}}$$

The low speed aileron effectiveness derivatives for flaps 0° were all taken directly from the 1/8 scale model low speed test data for equal and opposite aileron deflections. The differential aileron deflection rate employed in the flaps 45° case with 15° aileron drop required obtaining the individual contributions of the up-going and down-going ailerons. The individual rolling and yawing moment coefficients were estimated from the 1/6 scale model test data for one aileron deflected. The yawing moment data obtained from the 1/6 scale model was quite

erratic in the conventional flight mode and, therefore, the data presented in Figure 3.56 represents a best estimate for the yawing moment coefficient due to one deflected aileron. Nevertheless, a summation of the yawing moment coefficient from Figure 3.57 for the two ailerons deflected equally and oppositely will yield values in agreement with the 1/8 scale model test data. A summation of the yawing moment from Figure 3.59 according to the deflection schedule of Figure 3.54 for flaps 45° and 15° aileron droop is shown in Figure 3.58. The discontinuity in C_n versus $(\delta_{aL} - \delta_{aR})$ occurs where the up-going aileron passes through zero deflection.

The 1/6 scale model sideforce coefficient due to one deflected aileron was, if anything, more erratic than the yawing moment coefficient and as a result it was not possible to separate the individual effects of each aileron. In view of the small magnitude and relative unimportance of the sideforce coefficient due to aileron deflection, $C_Y \delta_a$, it was not considered worthy of extensive analysis. $C_Y \delta_a$ based on equal and opposite deflection of the two ailerons from 1/8 scale model test data is shown in Figure 3.55 for flaps 0° and 45°.

3.6 CONVENTIONAL FLIGHT, HIGH SPEED, CONTROL EFFECTIVENESS

A brief description of the basic control system and the necessary corrections to the low speed wind tunnel test values of control effectiveness were discussed in Section 3.5 of this report.

High speed control effectiveness as a function of Mach number are presented in Figures 3.62 through 3.70.

The high speed elevator effectiveness test data was corrected for the 5-inch extension of the horizontal tail semi-span by the following equation which is the same as that used for the low speed case.

$$C_{m\delta_e} = \left(C_{m\delta_e} \right)_{\text{test}} \times \frac{\left(C_{m_{iH}} \right)_{\text{calc}}}{\left(C_{m_{iH}} \right)_{\text{test}}}$$

The agreement between the high speed and low speed test values of elevator effectiveness was considered very good. The elevator control

effectiveness, $C_{m_{\delta_e}}$, data of Figures 3.63 and 3.64 show a rather rapid deterioration of elevator effectiveness above Mach 0.75 reaching a level at 0.9 Mach number of approximately 10 percent of the low speed value.

The high speed effectiveness of the extended span rudder was calculated from the following equation:

$$C_{Y_{\delta_r}} = \left\{ \frac{C_{Y_{\delta_r}}}{\left(C_{Y_{\delta_r}} \right)_{\text{test}}} \right\}_{\text{low speed}} \times \left\{ \left(C_{Y_{\delta_r}} \right)_{\text{test}} \right\}_{\text{high speed}}$$

Directional control effectiveness, $C_{n_{\delta_r}}$, given in Figure 3.66, indicates a gradual decrease in rudder effectiveness from approximately 0.6 Mach number reaching a level of 25 percent of its low speed value at 0.9 Mach number.

The aileron as tested in the high speed wind tunnel had a shorter span than that tested in the low speed wind tunnel because the horn balance was removed by cutting the aileron chordwise inboard of the horn. The horn balance was removed because of hinge moment characteristics which are discussed in Section 3.7. Since the aileron on the full scale airplane extends to the wing tip it was necessary to correct the high speed test data for this span increment. This correction was made by calculating a theoretical increment to $C_{l_{\delta_a}}$ from Ref. 4 to account for the change in span and adding it to the high speed test value as indicated by the following equation:

$$C_{l_{\delta_a}} = \left(C_{l_{\delta_a}} \right)_{\text{test}} + \left(\Delta C_{l_{\delta_a}} \right)_{\text{calc}}$$

The corrected value thus obtained at $M = 0.4$ was in excellent agreement with the low speed test value. The aileron derivatives $C_{Y_{\delta_a}}$ and $C_{n_{\delta_a}}$ were not considered significant enough to warrant corrections.

The reduction in aileron rolling effectiveness $C_{l_{\delta_a}}$ due to the servo tab was estimated from Ref. 4 to be approximately 8 percent. This loss was taken to be constant throughout the Mach number range since the calculated variation with Mach number was negligibly small.

Aileron control effectiveness, $C_{l_{\delta_a}}$, is shown in Figure 3.70. The data indicates rather large variations with angle of attack change and full loss of control effectiveness at 0.9 Mach number.

3.7 CONVENTIONAL FLIGHT, LOW SPEED, CONTROL SURFACE HINGE MOMENTS

The rudder, elevator and ailerons are all equipped with a sealed, internal pressure balance to reduce the aerodynamic hinge moment and in addition, the ailerons are equipped with a servo tab. Aerodynamic hinge moment and balance cavity static pressure data were obtained from low speed wind tunnel tests of the 1/8 scale conventional flight model. The model elevator and rudder were not equipped with a sealed pressure balance as was the aileron, and the aileron had no servo tab installed.

The aileron as tested at low speed had a horn balance which was subsequently removed because the test data indicated the aileron to be undesirably overbalanced at small deflections ($\pm 5^\circ$). Although hinge moment data were obtained on the aileron without a horn balance at $M = 0.4$ (high speed test) these data were limited to $\pm 5^\circ$ deflection and were generally too erratic to inspire much confidence. Consequently, the low speed aileron hinge moment derivatives presented in Figures 3.77 to 3.79 were estimated primarily by theoretical and empirical methods.

The unbalanced aileron hinge moment derivatives $C_{h_a \alpha}$ and $C_{h_a \delta_a}$ were estimated from the lifting line theory of Ref. 10 with lifting surface theory corrections from Ref. 7 and 8. The contribution of the internal pressure balance was estimated from the empirical data of Ref. 3. The non-linear variation of the hinge moment coefficient with aileron deflection was estimated from the general trend of the available wind tunnel test data.

The hinge moment derivatives of the aileron servo tab were necessarily estimated by theoretical and empirical methods since no test data existed for the tab. The tab derivatives $C_{h_t \delta_t}$ and $C_{h_t \delta_a}$ were estimated from Ref. 7, 8 and 10 and the derivative $C_{h_a \delta_t}$ was estimated from Ref. 9.

The tab hinge moment coefficients were assumed linear with tab deflection because the tab deflection never exceeds $+10^\circ$ or -12° .

3.8 CONVENTIONAL FLIGHT, HIGH SPEED, CONTROL SURFACE HINGE MOMENTS

The conventional flight control surface aerodynamic balances and the derivation of the low speed hinge moment parameters were discussed in the previous section. High speed hinge moment and balance cavity pressure data were obtained in addition to the low speed wind tunnel data, but only for $\pm 5^\circ$ control surface deflection on all three controls.

The high speed aileron data were viewed with considerable skepticism because of inconsistencies in the test data. The test data were also limited to $M = 0.7$ because the hinge moment fluctuations due to the model aileron dynamics exceeded the capabilities of the data measuring system. The low speed values of Section 3.7 were considered valid over most of the subcritical Mach number range at least to a Mach number of about 0.7. High speed control hinge moments are presented as a function of Mach number in Figures 3.80 through 3.88.

XV-5A
LOW SPEED $C_{L_{M-T}}$ Vs α
LANDING GEAR UP

NOTES:

1- RIGID DATA

2- FREE AIR

3- STABILITY AXES

4- $\delta_f = 0^\circ$

5- $\delta_f = 30^\circ + \delta_a = 10^\circ$

6- $\delta_f = 45^\circ + \delta_a = 15^\circ$

7- REFERENCE: 1 & 2

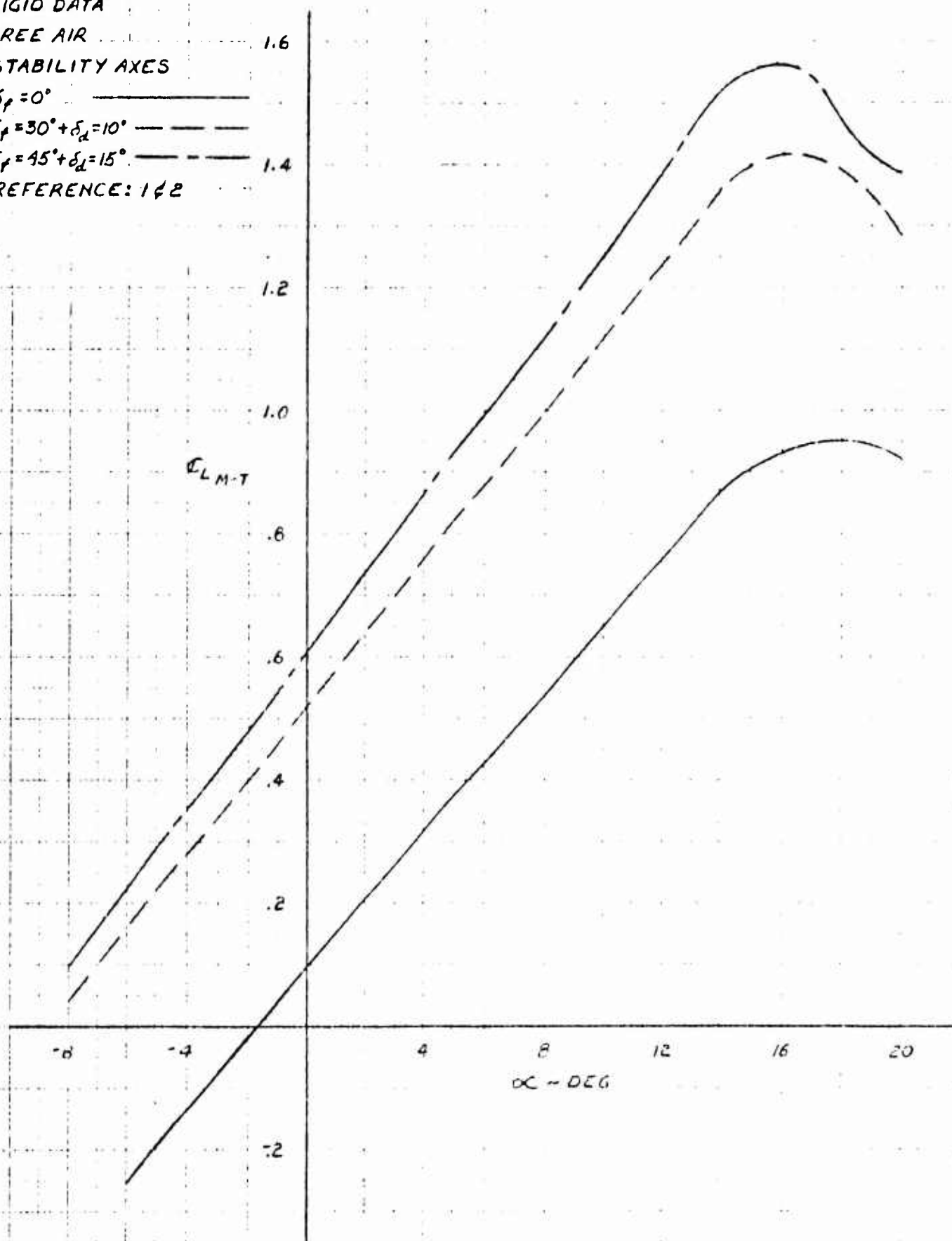


Figure 3.1

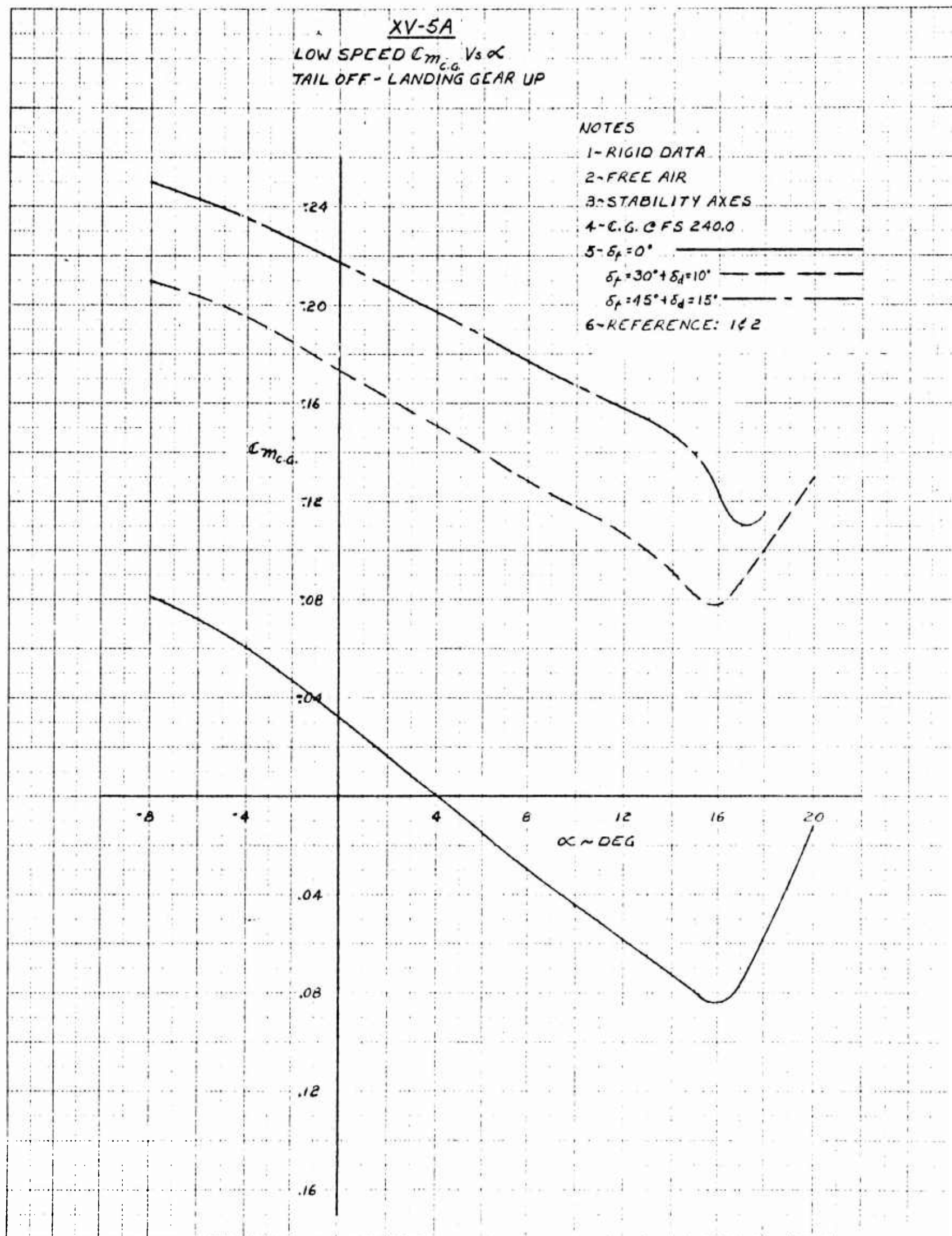


Figure 3.2

XV-5A

LOW SPEED $C_{m_{c.g.}}$ Vs α
TAIL OFF - LANDING GEAR UP

NOTES

1-RIGID DATA

2-FREE AIR

3-STABILITY AXES

4-C.G. @ FS 246.0

5- $\delta_f = 0^\circ$

$\delta_f = 30^\circ + \delta_d = 10^\circ$

$\delta_f = 45^\circ + \delta_d = 15^\circ$

6-REFERENCE: 1/2

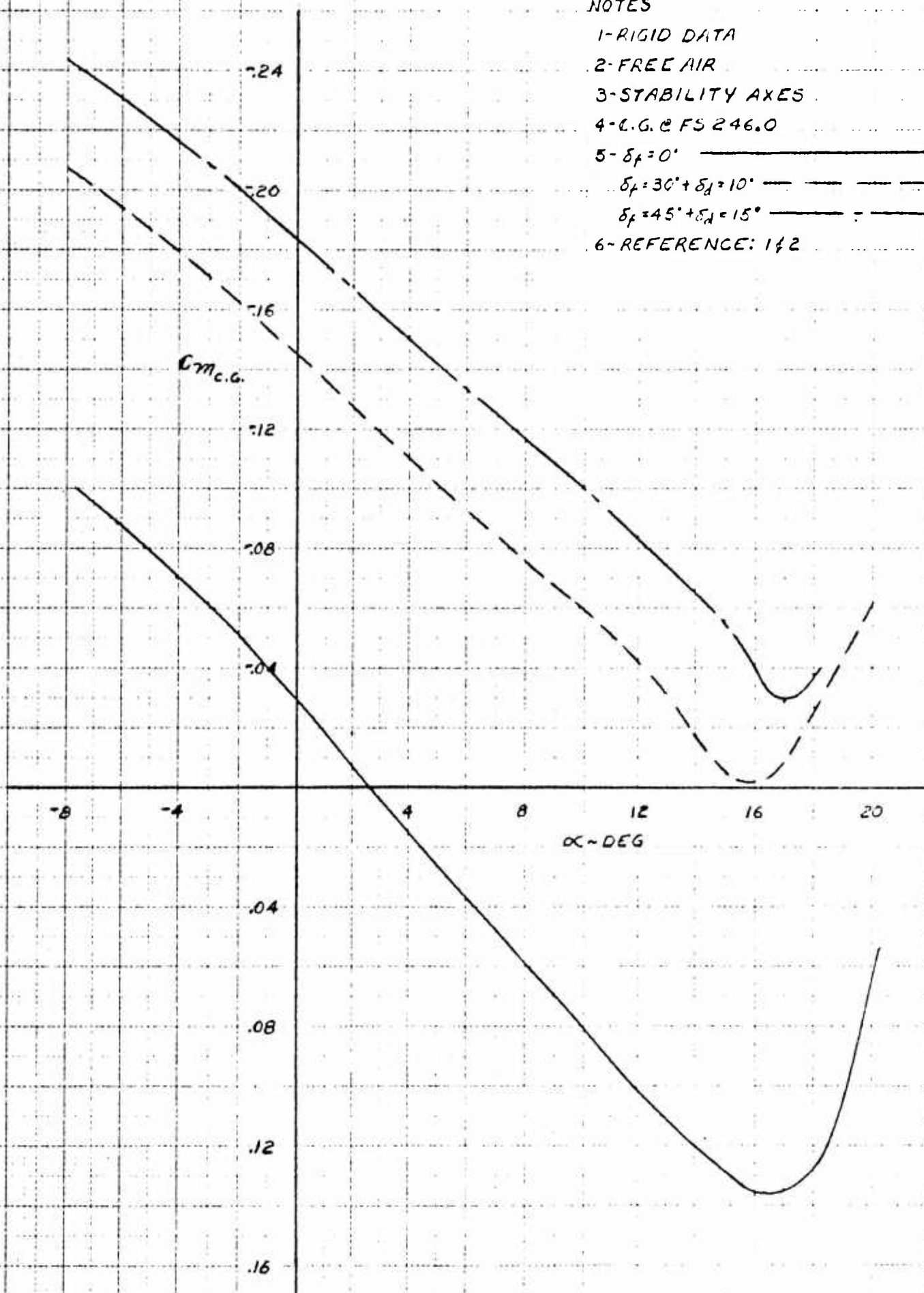


Figure 3.3

XV-5A
LOW SPEED DOWNWASH

NOTES:

- 1- RIGID DATA
- 2- FREE AIR
- 3- STABILITY AXES
- 4- $\delta_f = 0^\circ$
- 5- $\delta_f = 30^\circ + \delta_d = 10^\circ$
- 6- $\delta_f = 45^\circ + \delta_d = 15^\circ$
- 7- REFERENCE: 1 & 2

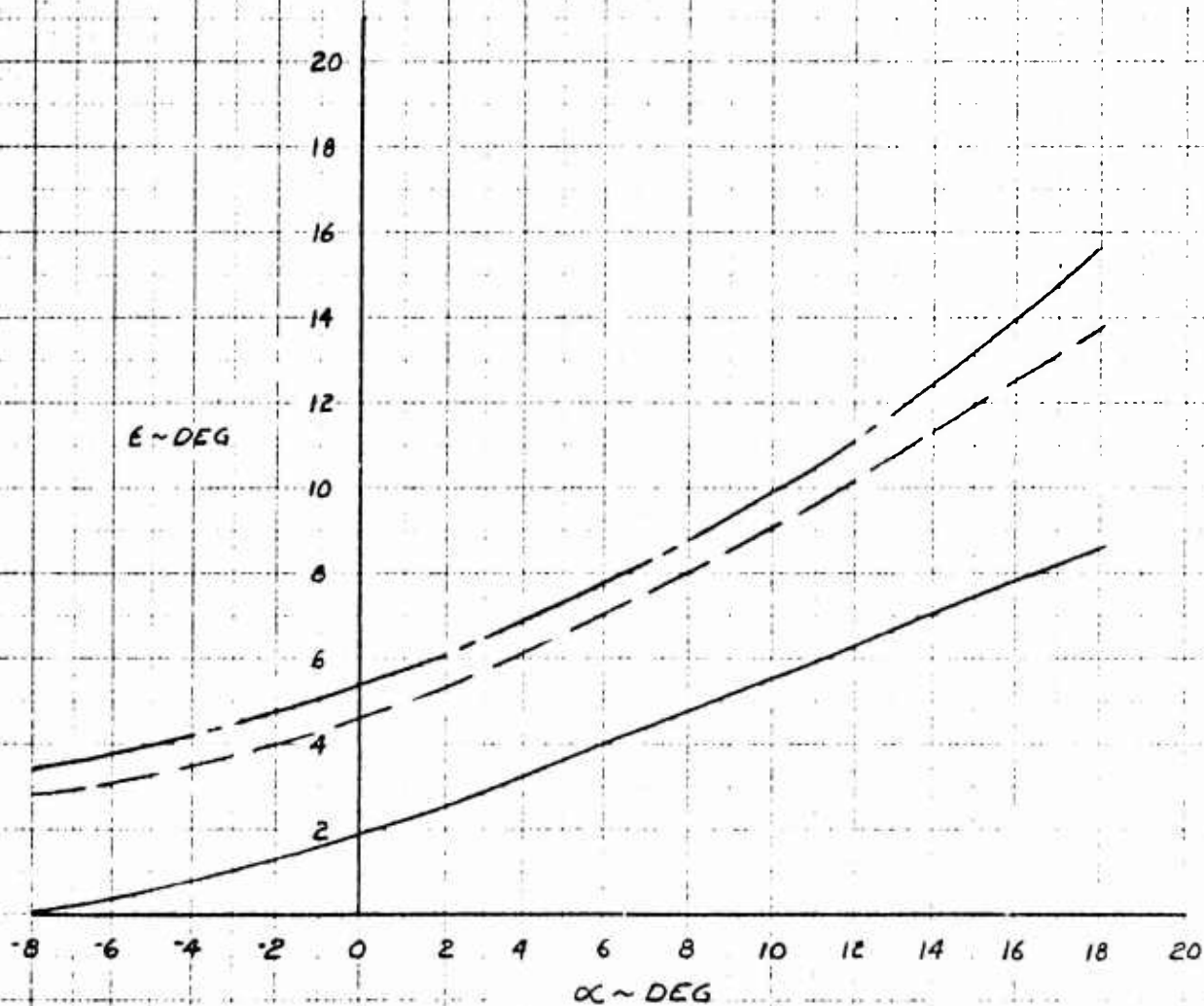
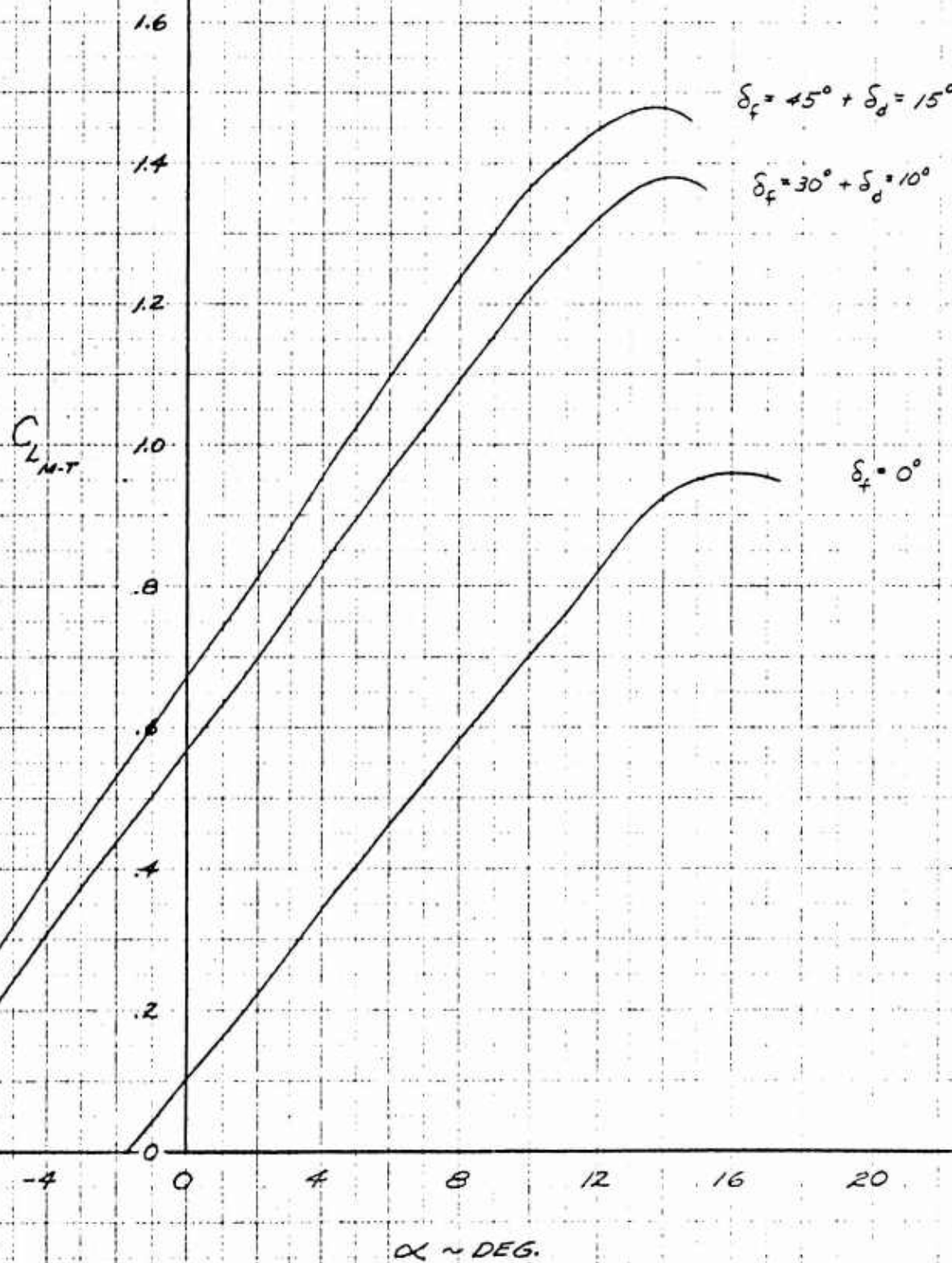


Figure 3.4

XV-5A
ESTIMATED $C_{L_{M-T}}$ VS. α
IN GROUND EFFECT

NOTE:

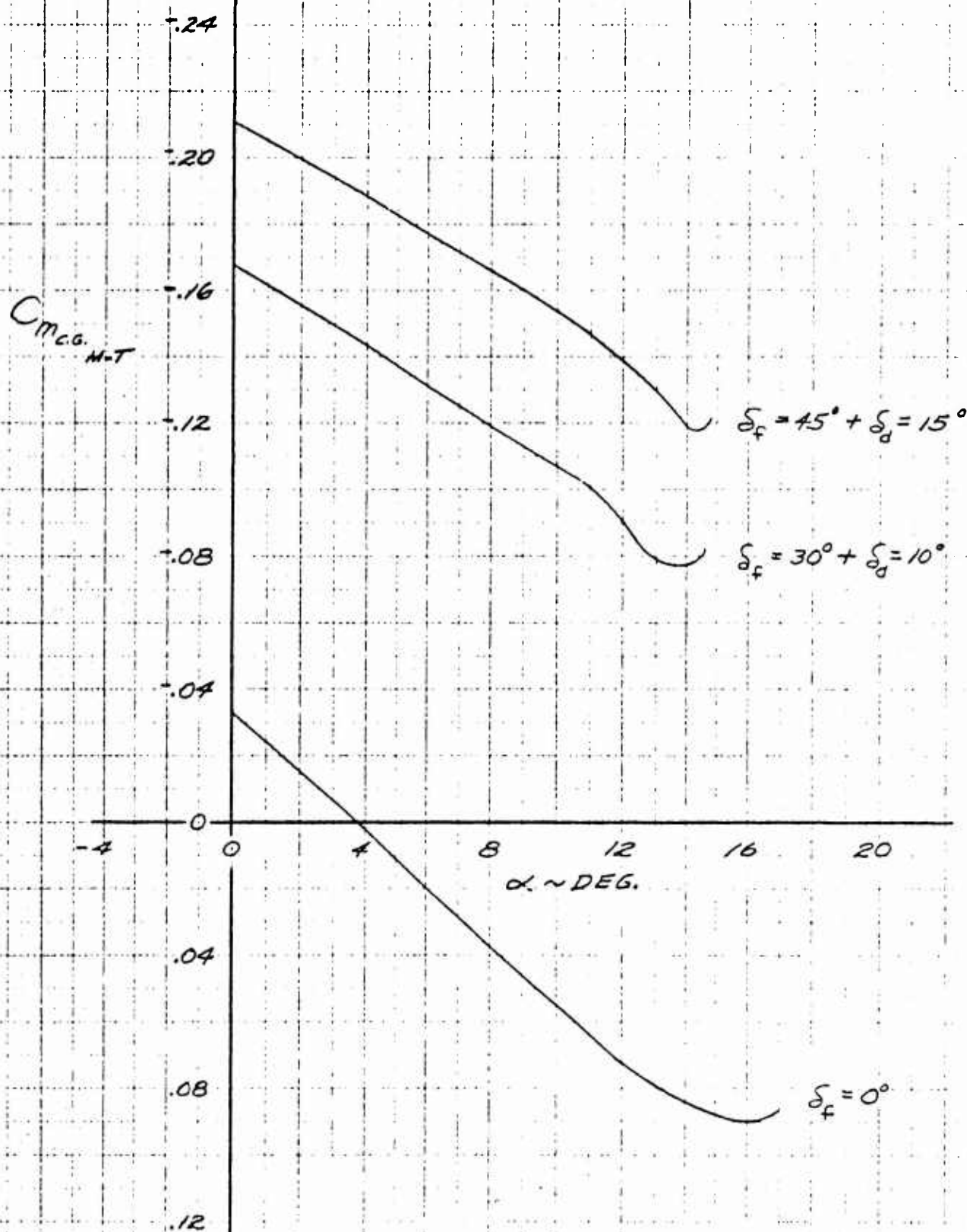
1. RIGID DATA
2. STABILITY AXES



XV-5A
ESTIMATED $C_{m_{CG, M-T}}$ VS. α
IN GROUND EFFECT

NOTE:

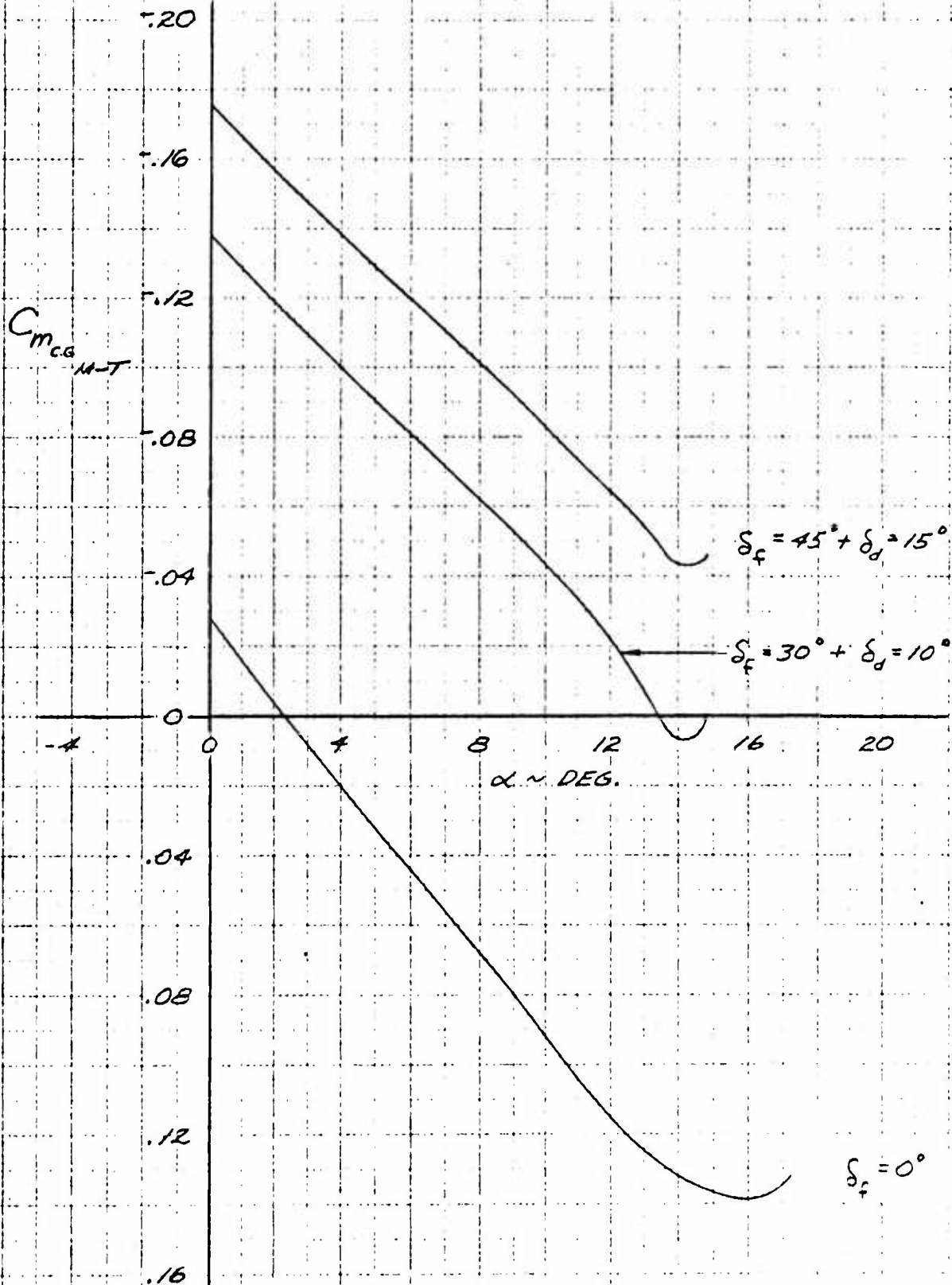
1. RIGID DATA
2. STABILITY AXES
3. C.G. @ F.S. 240.0



XV-5A
ESTIMATED $C_{m_{c.g. M-T}}$ VS. α
IN GROUND EFFECT

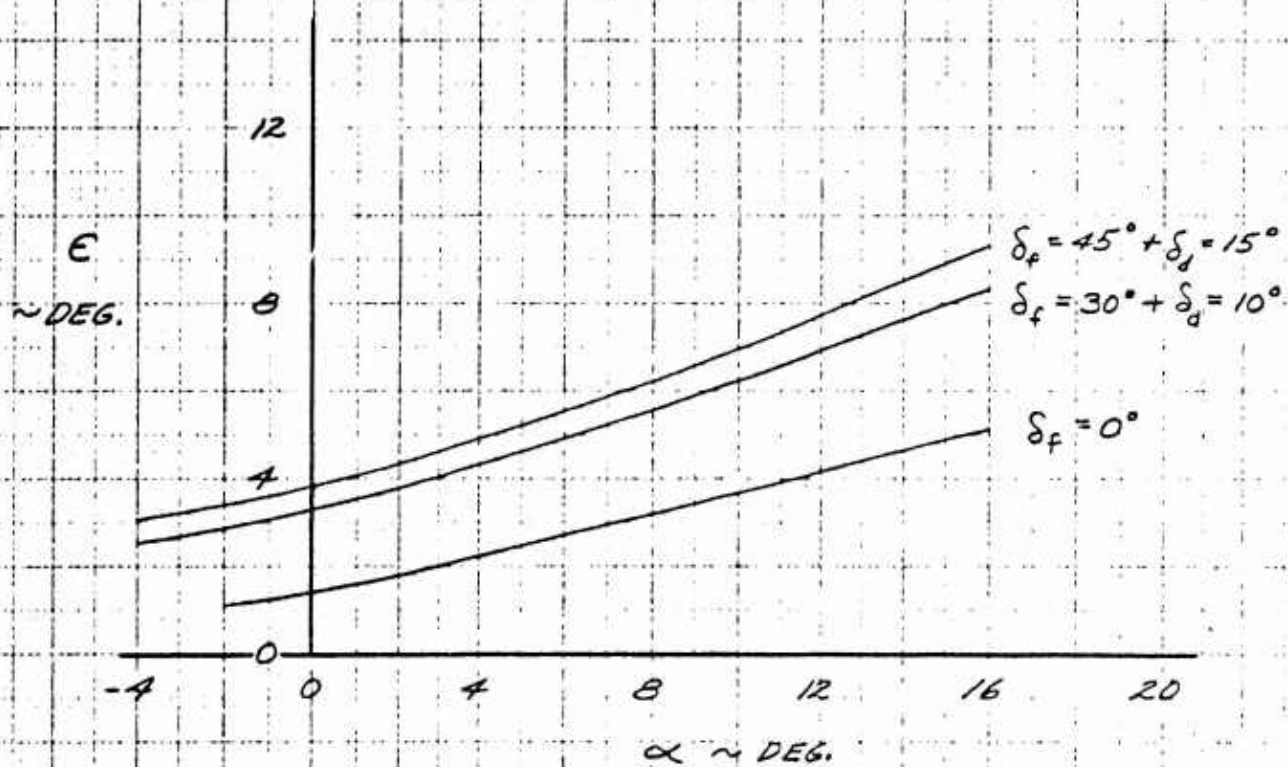
NOTE:

1. RIGID DATA
2. STABILITY AXES
3. C.G. @ F.S. 246.0



XV-5A
ESTIMATED DOWNWASH
IN GROUND EFFECT

NOTE:
1. RIGID DATA



XV-5A
LOW SPEED $C_{L_{CM}}$ Vs α
UNTRIMMED-LANDING GEAR UP

NOTES:

1-RIGID DATA

2-FREE AIR

3-STABILITY AXES

4- $S_c/S_w = .203$

5- $\delta_f = 0^\circ$

$\delta_f = 30^\circ + \delta_d = 10^\circ$

$\delta_f = 45^\circ + \delta_d = 15^\circ$

6- REFERENCE: 14.2

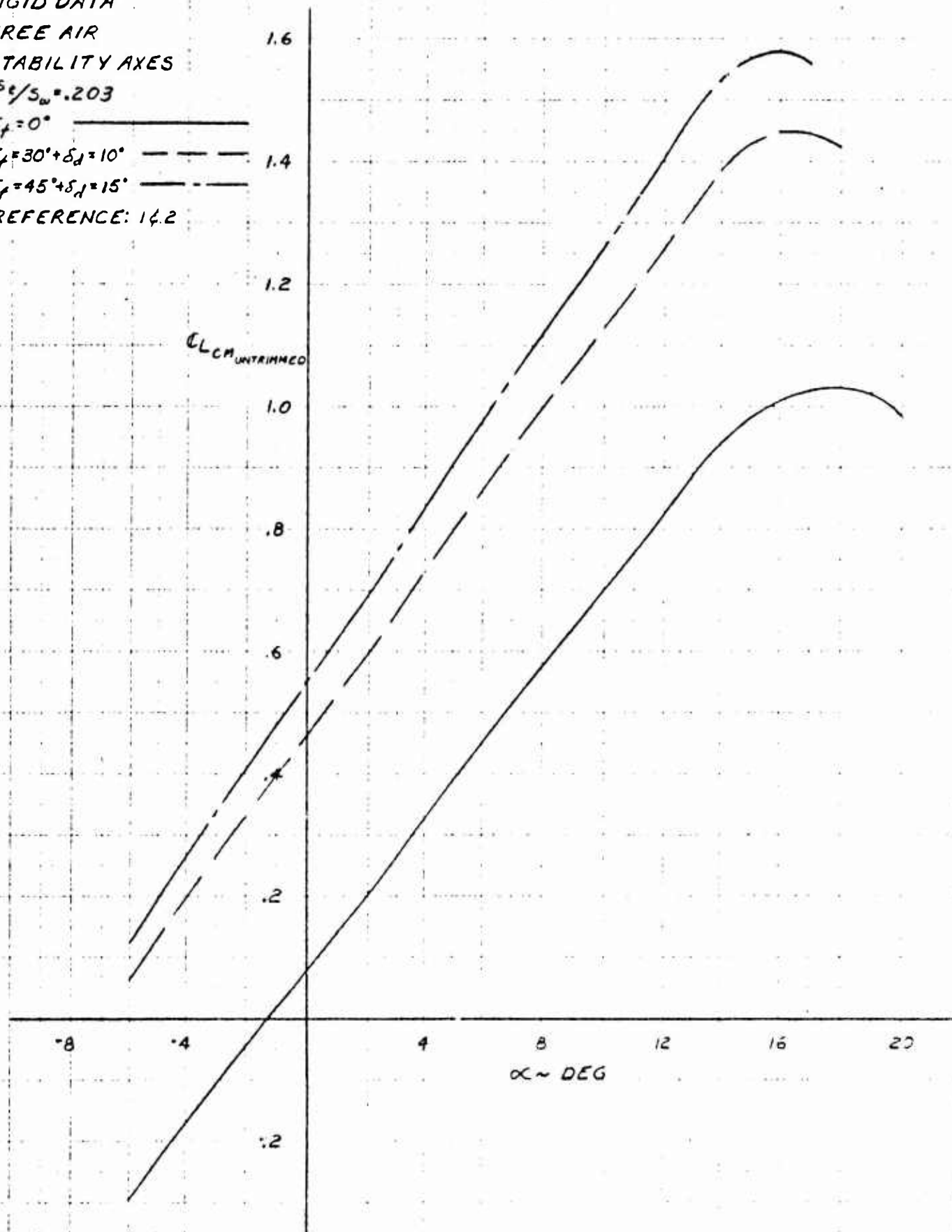


Figure 3.9

XV-5A
LOW SPEED $C_{m_{c.g.}}$ Vs α
LANDING GEAR UP

NOTES

1-RIGID DATA

2-FREE AIR

3-STABILITY AXES

4-C.G. @ FS240.0

5- $\delta_f = 0^\circ$

$\delta_f = 30^\circ + \delta_d = 10^\circ$

$\delta_f = 45^\circ + \delta_d = 15^\circ$

6- $s_{y_s} = .203$, $l_{y_s} = 2.241 (\alpha = 0^\circ)$, $l_{y_s} = 0^\circ$

7-REFERENCE: 1 & 2

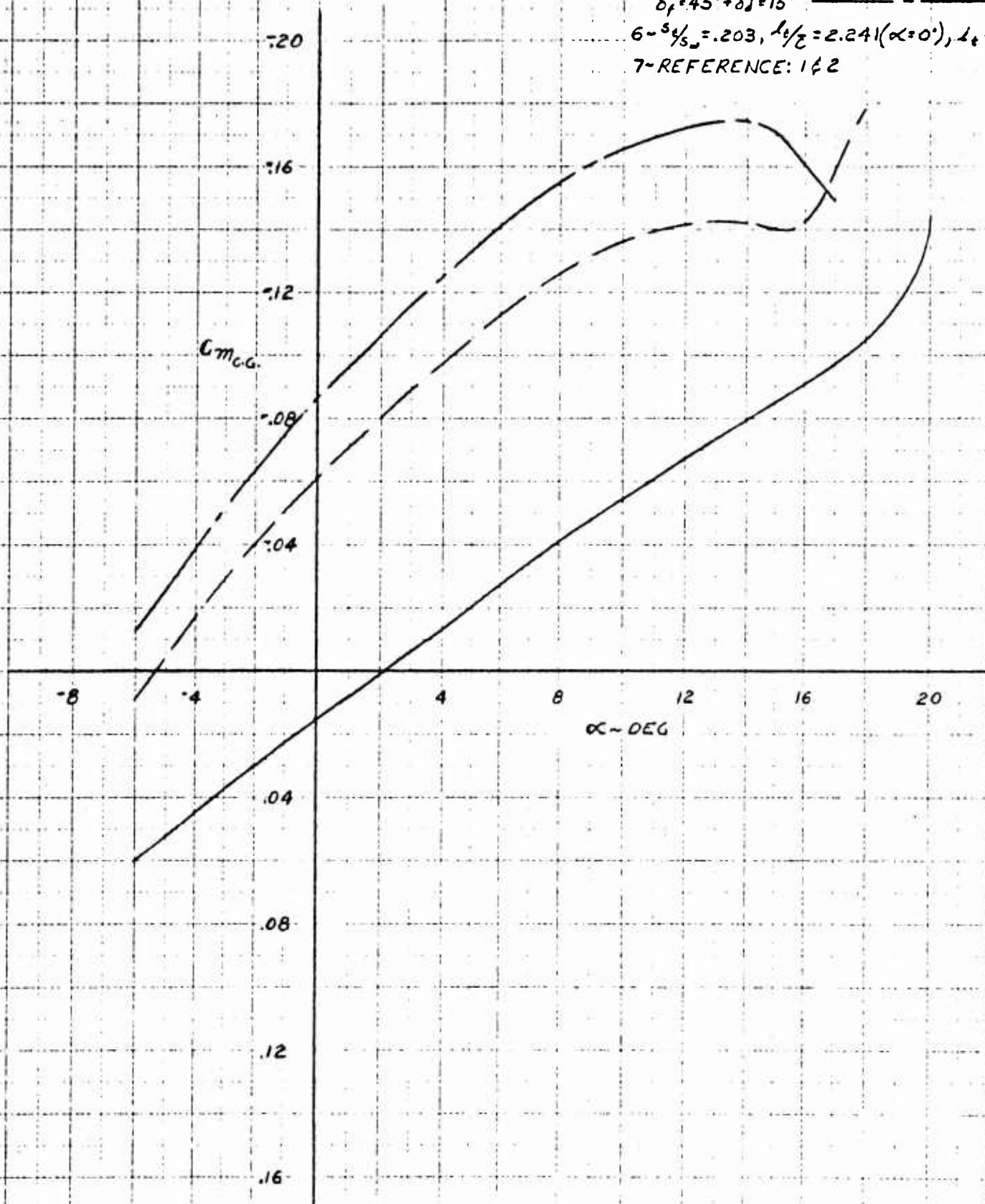


Figure 3.10

XV-5A
LOW SPEED $C_{m,c.g.}$ Vs α
LANDING GEAR UP

NOTES

1-RIGID DATA

2-FREE AIR

3-STABILITY AXES

4-C.G. CFS 246.0

5- $\delta_f = 0^\circ$

$\delta_f = 30^\circ + \delta_d = 10^\circ$

$\delta_f = 45^\circ + \delta_d = 15^\circ$

6- $S_{c,w} = .203$, $l_{c/c} = 2.128 (\alpha = 0^\circ)$, $i_c = 0^\circ$

7-REFERENCE: 142

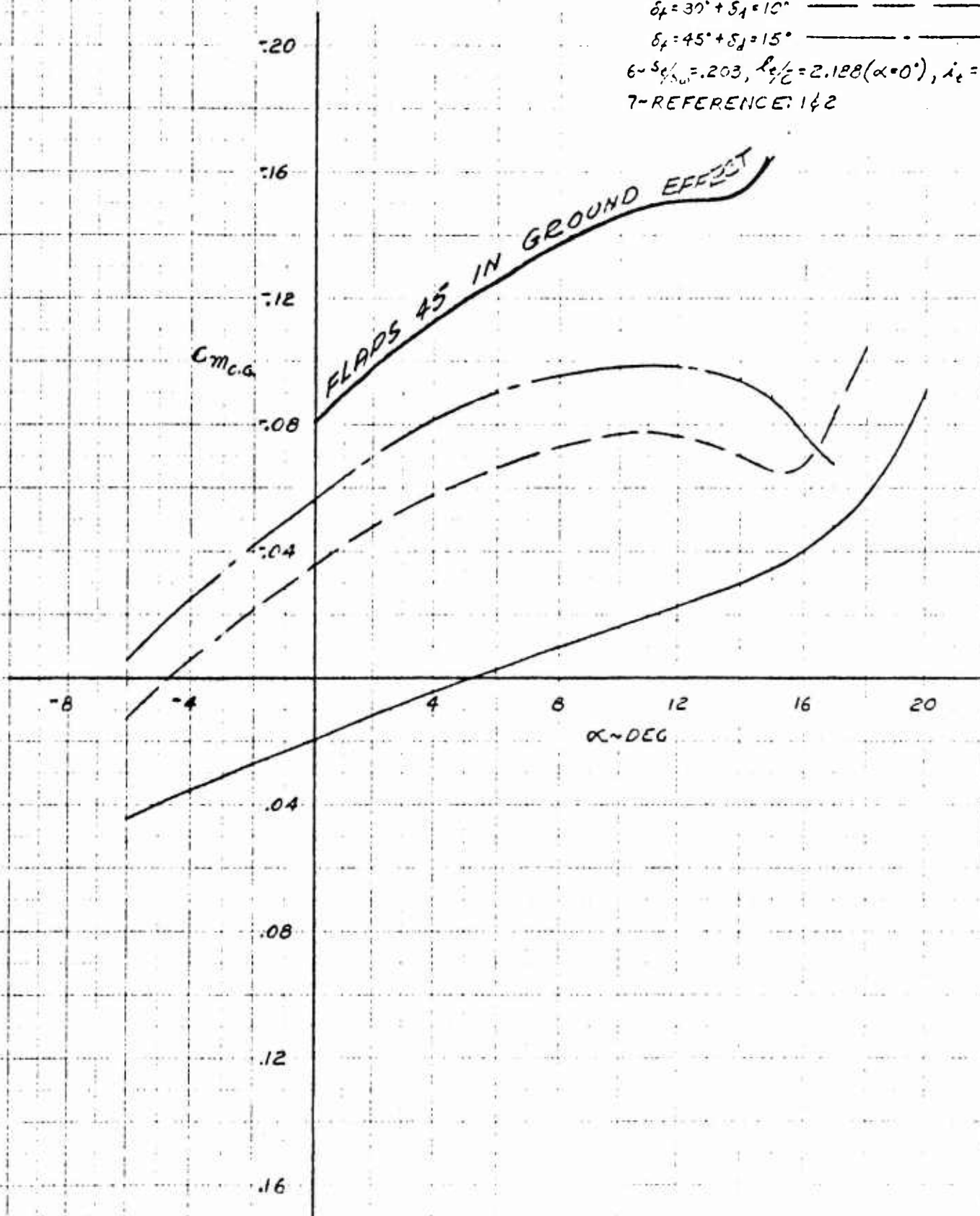


Figure 3.11

XV-5A
LOW SPEED $C_{L_{CM}}$ Vs $C_{m_{C.G.}}$
LANDING GEAR UP

NOTES:

- 1- RIGID DATA
- 2- FREE AIR
- 3- STABILITY AXES
- 4- C.G. @ FS 240.0

5- $\delta_f = 0^\circ$

$\delta_f = 30^\circ + \delta_j = 10^\circ$

$\delta_f = 45^\circ + \delta_j = 15^\circ$

6- $S_i/S_w = .203$, $L_i/C = 2.241 (\alpha = 0^\circ)$, $i_e = 0^\circ$

7- REFERENCE: 1 & 2

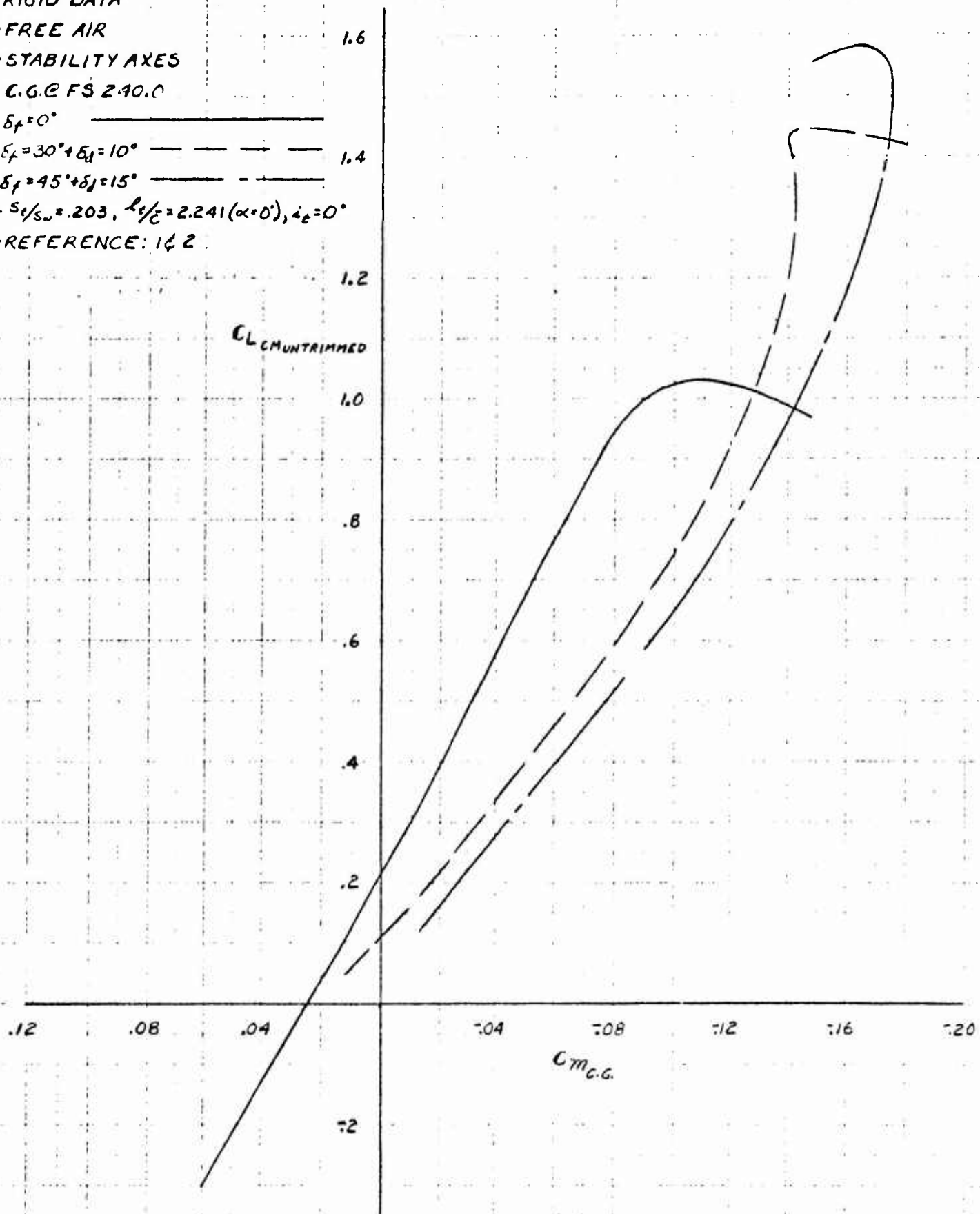


Figure 3.12

XV-5A
LOW SPEED $C_{L_{CM}}$ Vs $C_{m_{c.g.}}$
LANDING GEAR UP

NOTES

1- RIGID DATA

2- FREE AIR

3- STABILITY AXES

4- C.G. CFS 246.0

5- $\delta_f = 0^\circ$

$\delta_f = 30^\circ + \delta_d = 10^\circ$

$\delta_f = 45^\circ + \delta_d = 15^\circ$

6- $S_c/S_w = .203$, $l_{cg}/\bar{c} = 2.188$ ($\alpha = 0^\circ$), $i_c = 0^\circ$

7- REFERENCE: 142

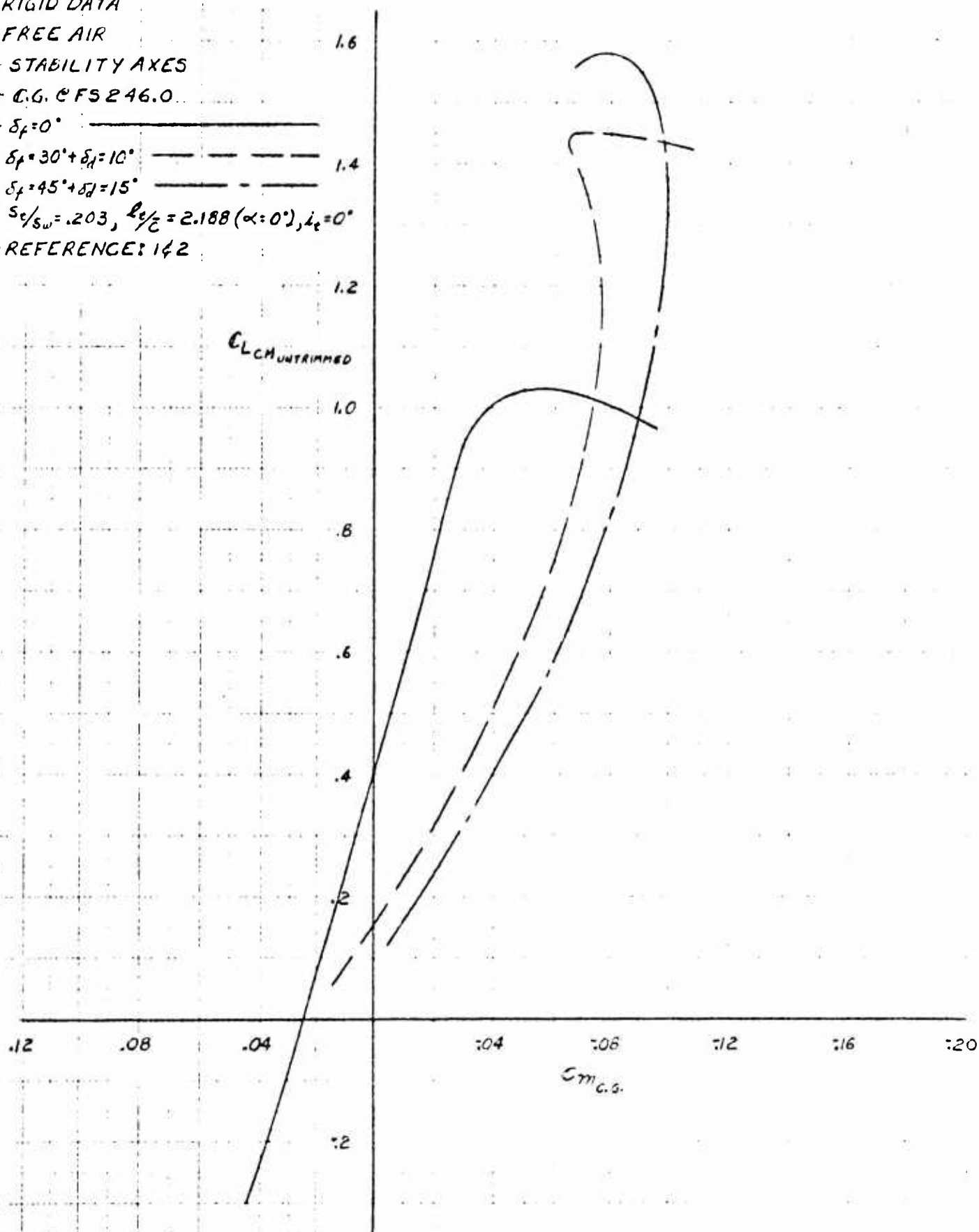


Figure 3.13

XV-5A
ESTIMATED LOWSPEED $\frac{q_c}{q_0} V_0 \propto$

NOTES:

1- RIGID DATA

2- FREE AIR

3- STABILITY AXES

4- $\delta_f = 0^\circ$

$\delta_f = 30^\circ + \delta_d = 10^\circ$

$\delta_f = 45^\circ + \delta_d = 15^\circ$

5- REFERENCE: 1

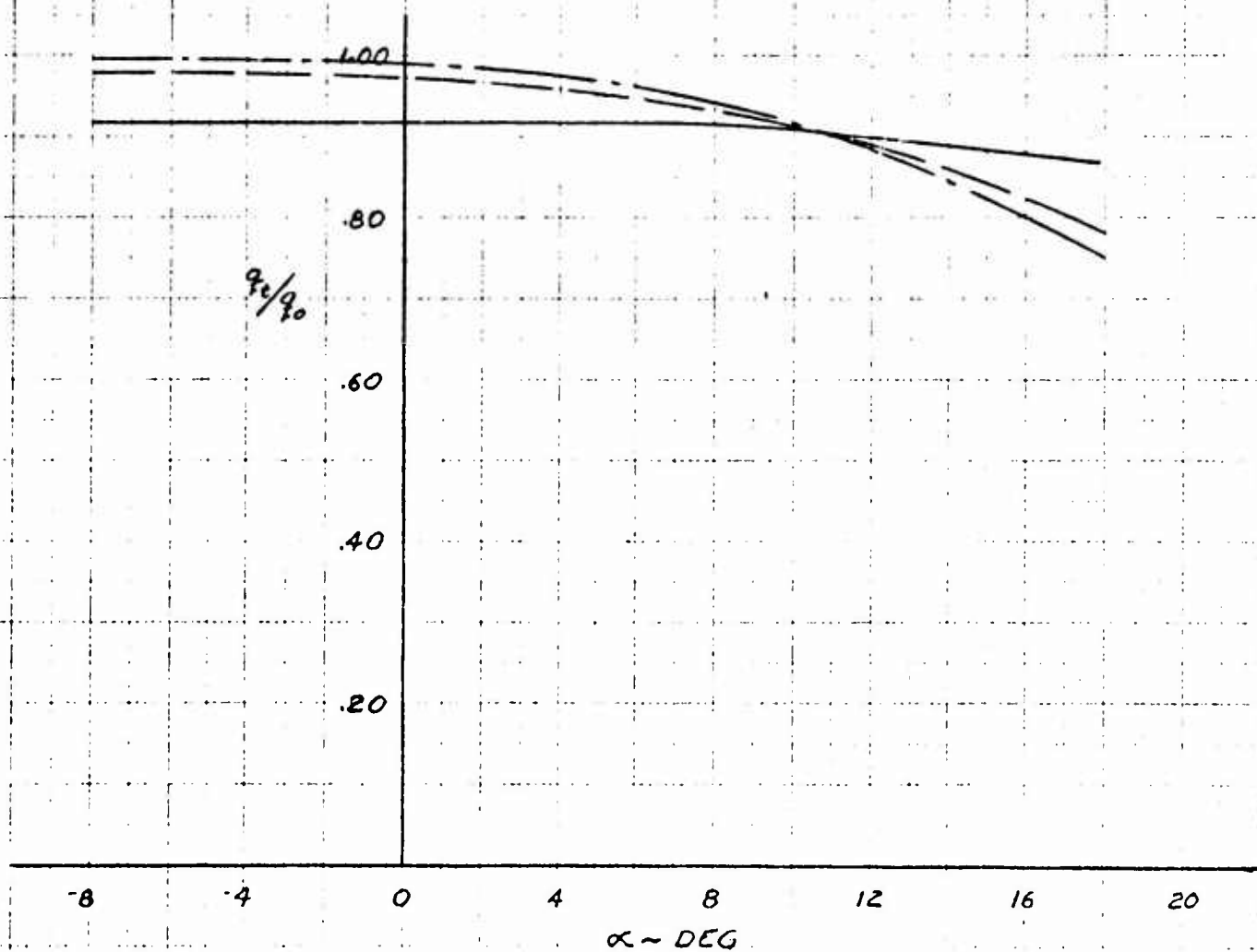


Figure 3.14

XV-5A
LOW SPEED C_{L_e} Vs α_e

NOTES:

- 1- RIGID DATA
- 2- FREE AIR
- 3- STABILITY AXES
- 4- REF. AREA, $S_e = 52.865 \text{ FT.}^2$
- 5- REFERENCE: 1

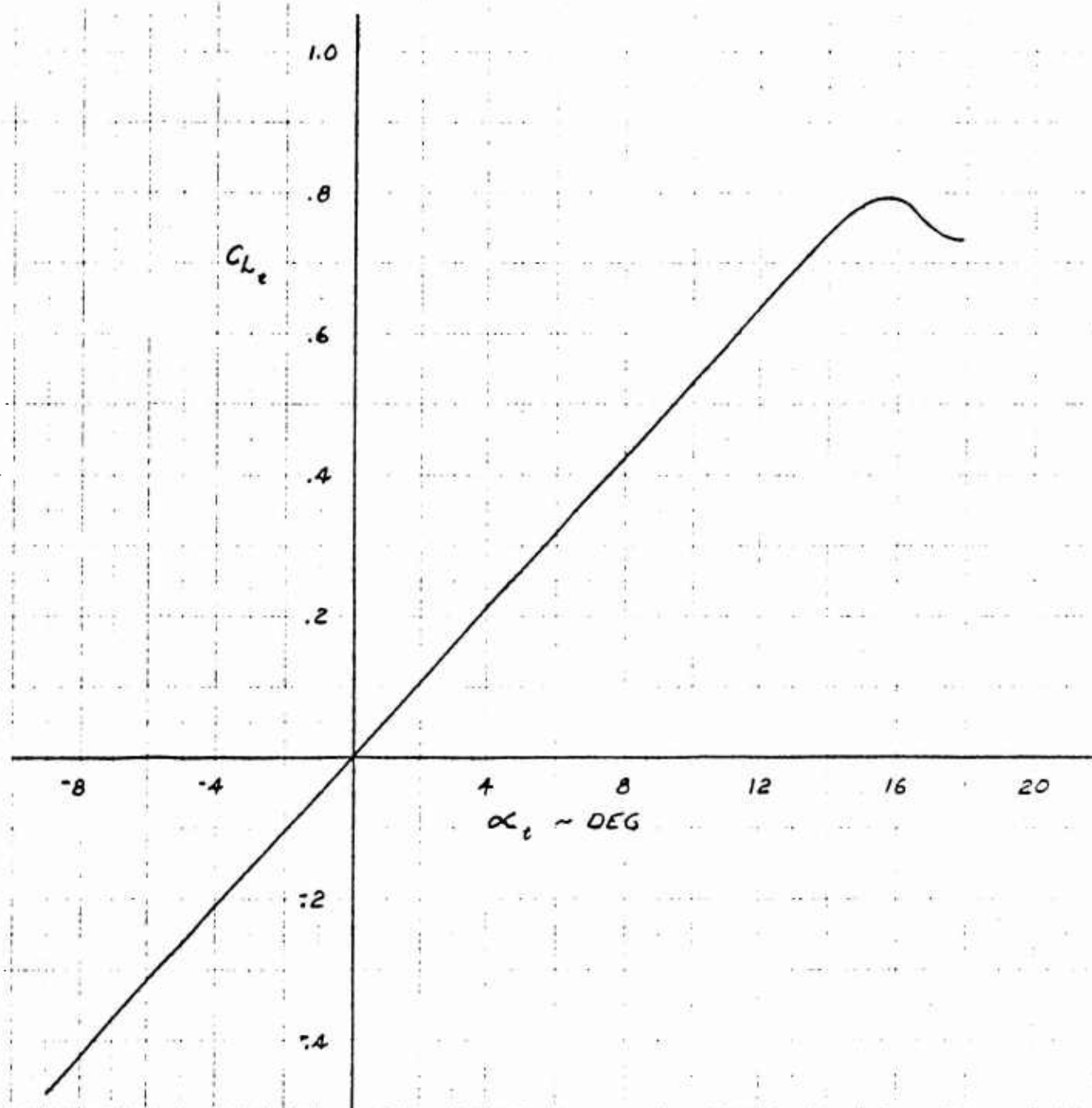


Figure 3.15

XV-5A
LOW SPEED C_{L_t} vs C_{D_t}

NOTES:

1~RIGID DATA

2~FREE AIR

3~STABILITY AXES

4~REF. AREA, $S_t = 52.865 \text{ FT.}^2$

5~REFERENCE: 1

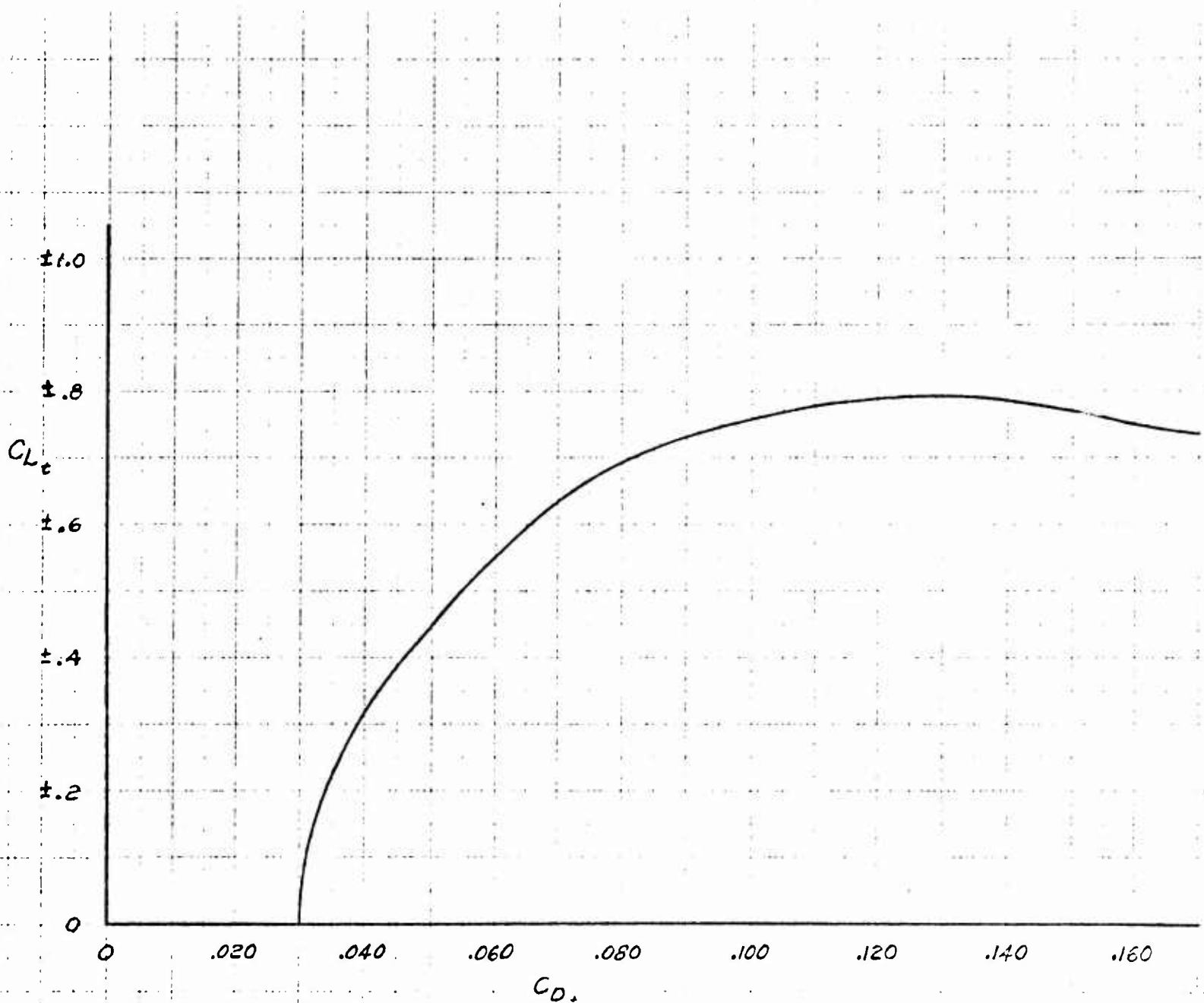


Figure 3.16

XV-5A
LOW SPEED $C_{L_{cr}}$ Vs α
TRIMMED-LANDING GEAR UP

NOTES

1-RIGID DATA

2-FREE AIR

3-STABILITY AXES

4-C.G. @ F.S. 240.0

5- $\delta_f = 0^\circ$

$\delta_f = 30^\circ + \delta_A = 10^\circ$

$\delta_f = 45^\circ + \delta_A = 15^\circ$

6- $S_{c/s} = .203$, $l_{c/c} = 2.241$ ($\alpha = 0^\circ$)

7-REFERENCE: 1 & 2

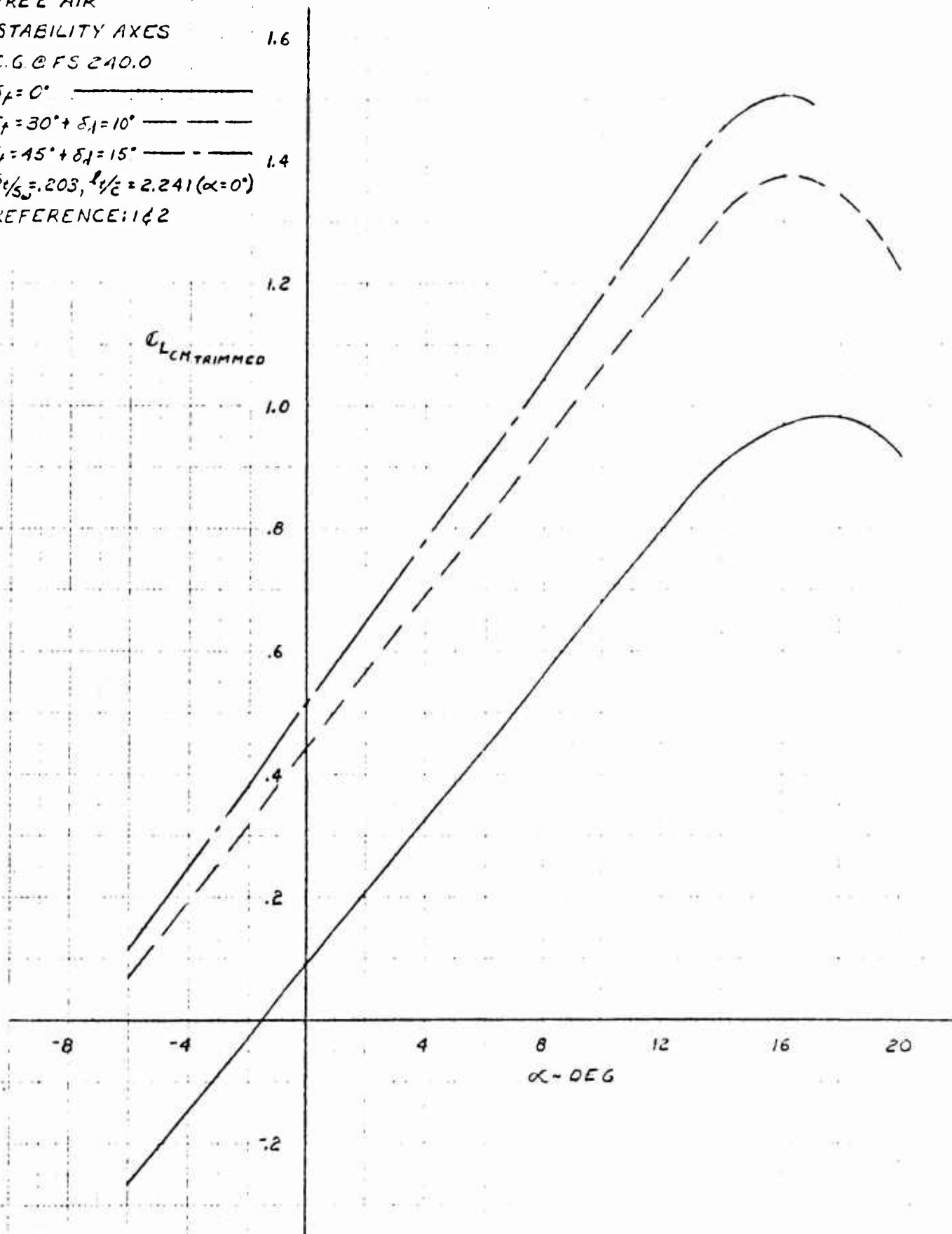


Figure 3.17

XV-5A

LOW SPEED $C_{L_{CM}}$ Vs α
TRIMMED - LANDING GEAR UP

NOTES:

1-RIGID DATA

2-FREE AIR

3-STABILITY AXES

4-C.G. @ F.S. 246.0

5- $\delta_f = 0^\circ$

$\delta_f = 30^\circ + \delta_d = 10^\circ$

$\delta_f = 45^\circ + \delta_d = 15^\circ$

6- $S_4/S_w = .203$, $L_4/L_2 = 2.188 (\alpha = 0^\circ)$

7-REFERENCE: 142

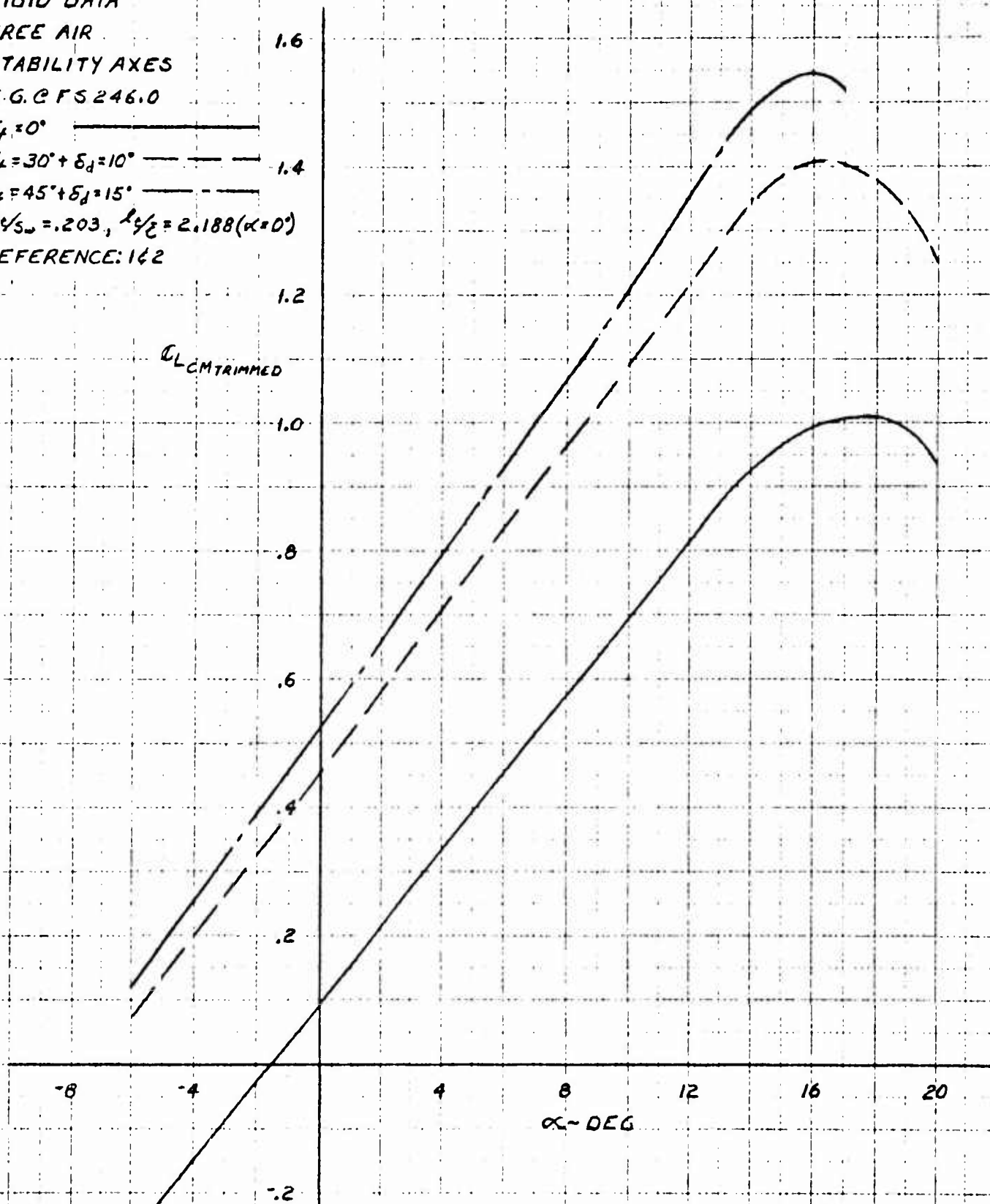


Figure 3.18

XV-5A TRIMMED DRAG POLAR - LOW SPEED

NOTE:

1. BASED ON WIND TUNNEL TEST DATA
2. REYNOLD'S NUMBER CORRECTION TO ANA #421, 2500 FT, HOT DAY
3. ENGINE DUCT MASS FLOW RATIO = 1.0
4. FULLY TURBULENT BOUNDARY LAYER
5. INCLUDES ESTIMATED DRAG DUE TO GAPS AND COOLING AIR.
6. C.G. @ F.S. 246.0

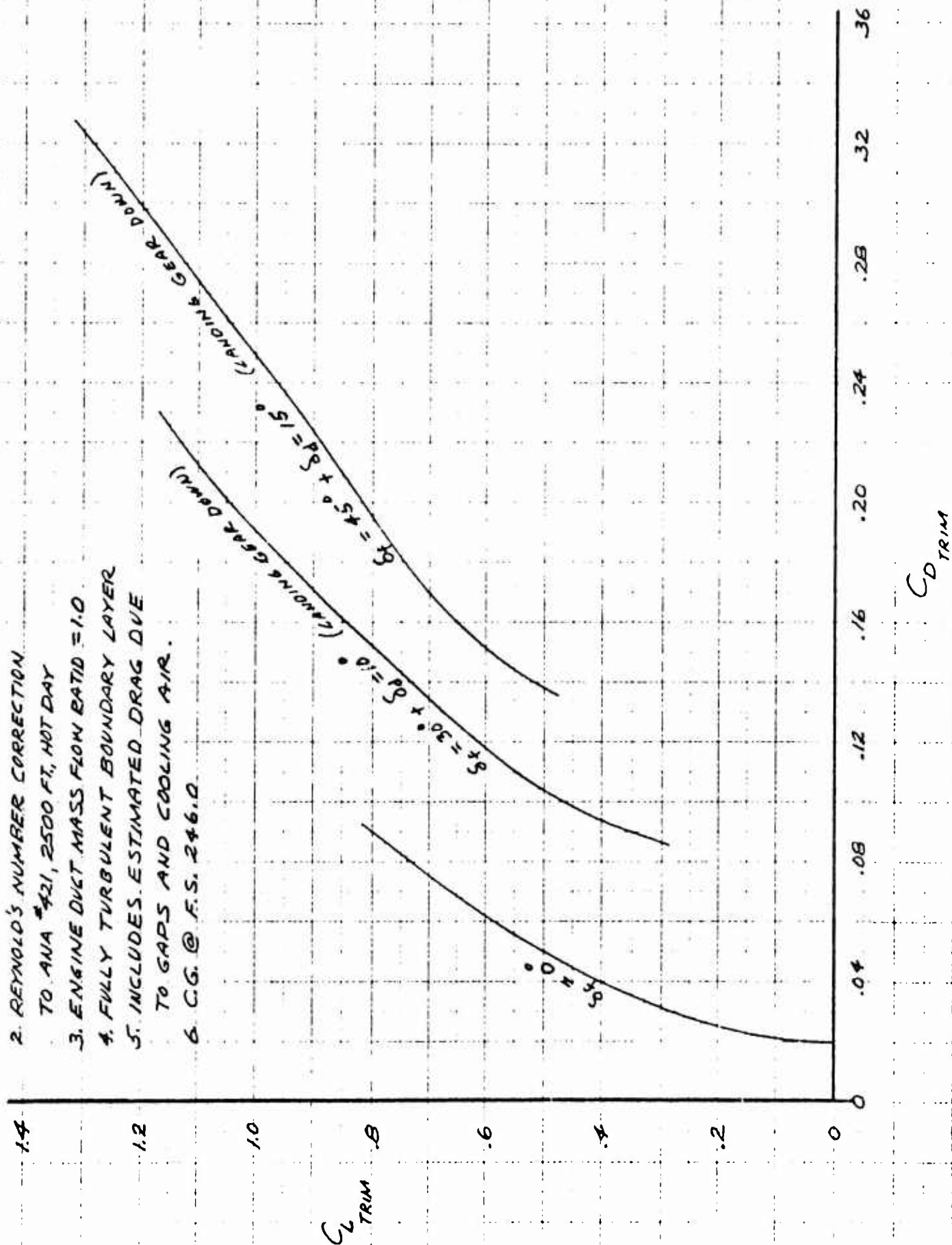


Figure 3.19

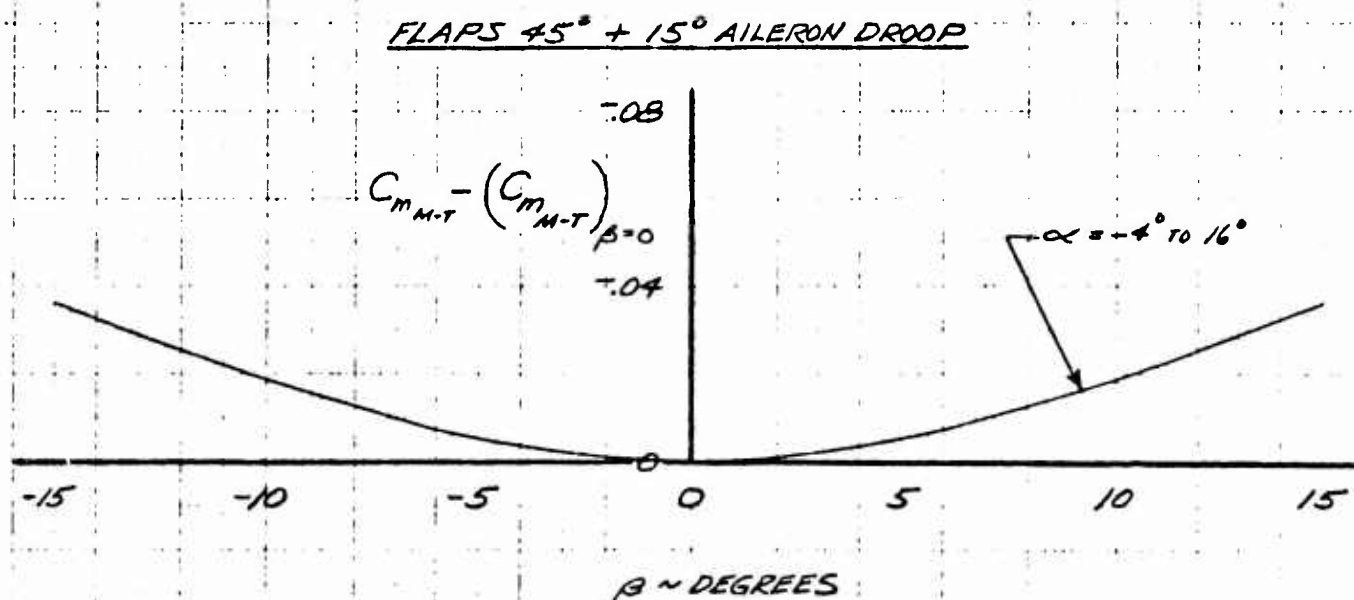
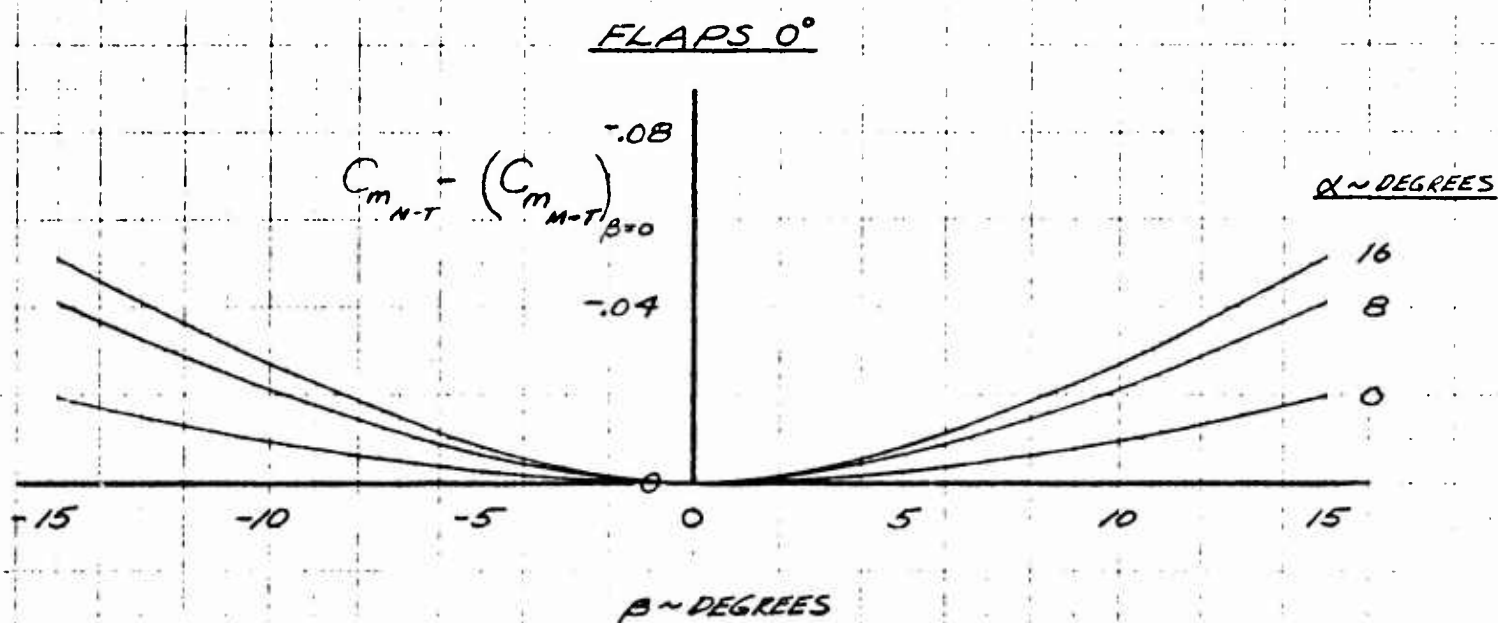
XV-5A
PITCHING MOMENT COEFFICIENT
DUE TO SIDESLIP

MODEL-TAIL

LOW SPEED

NOTE:

1. C.G. @ F.S. 246.0
2. STABILITY AXES



XV-5A
PITCHING MOMENT COEFFICIENT
DUE TO SIDESLIP

LOW SPEED

NOTE:

1. C.G. @ F.S. 2+0.0-246.0
2. STABILITY AXES
3. $\alpha = -4^\circ$ TO 16°

(FLAPS 0°) $C_{m_{cm}} = (C_{m_{cm}})_{\beta=0} + .05(1 - \sqrt{1 + .025\beta^2})$

(FLAPS $45^\circ + 15^\circ$ AIL. DROOP) $C_{m_{cm}} = (C_{m_{cm}})_{\beta=0} + .05(1 - \sqrt{1 + .0385\beta^2})$

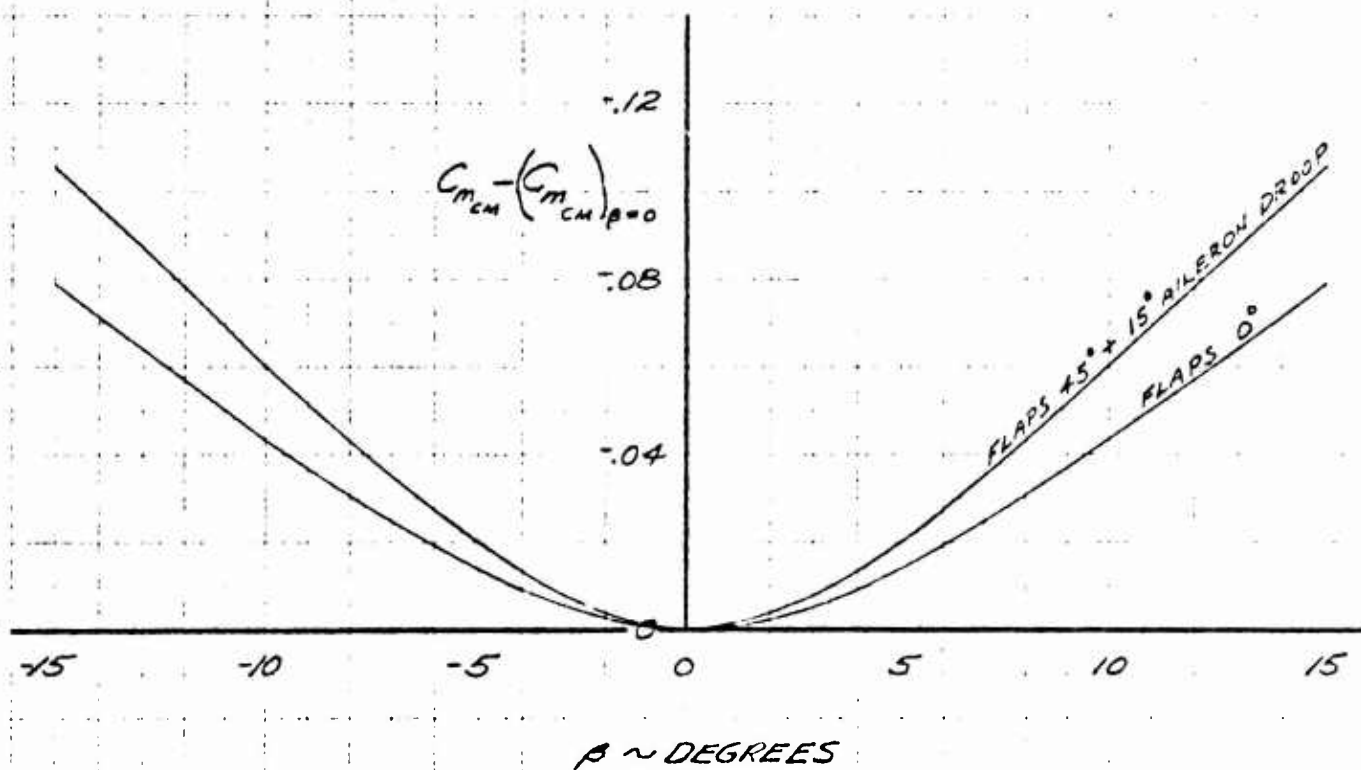


Figure 3.21

XV-5A
ESTIMATED CHANGE IN LIFT & PITCHING
DUE TO LOWERING OF LANDINGGEAR
C.G. @ F.S. 246.

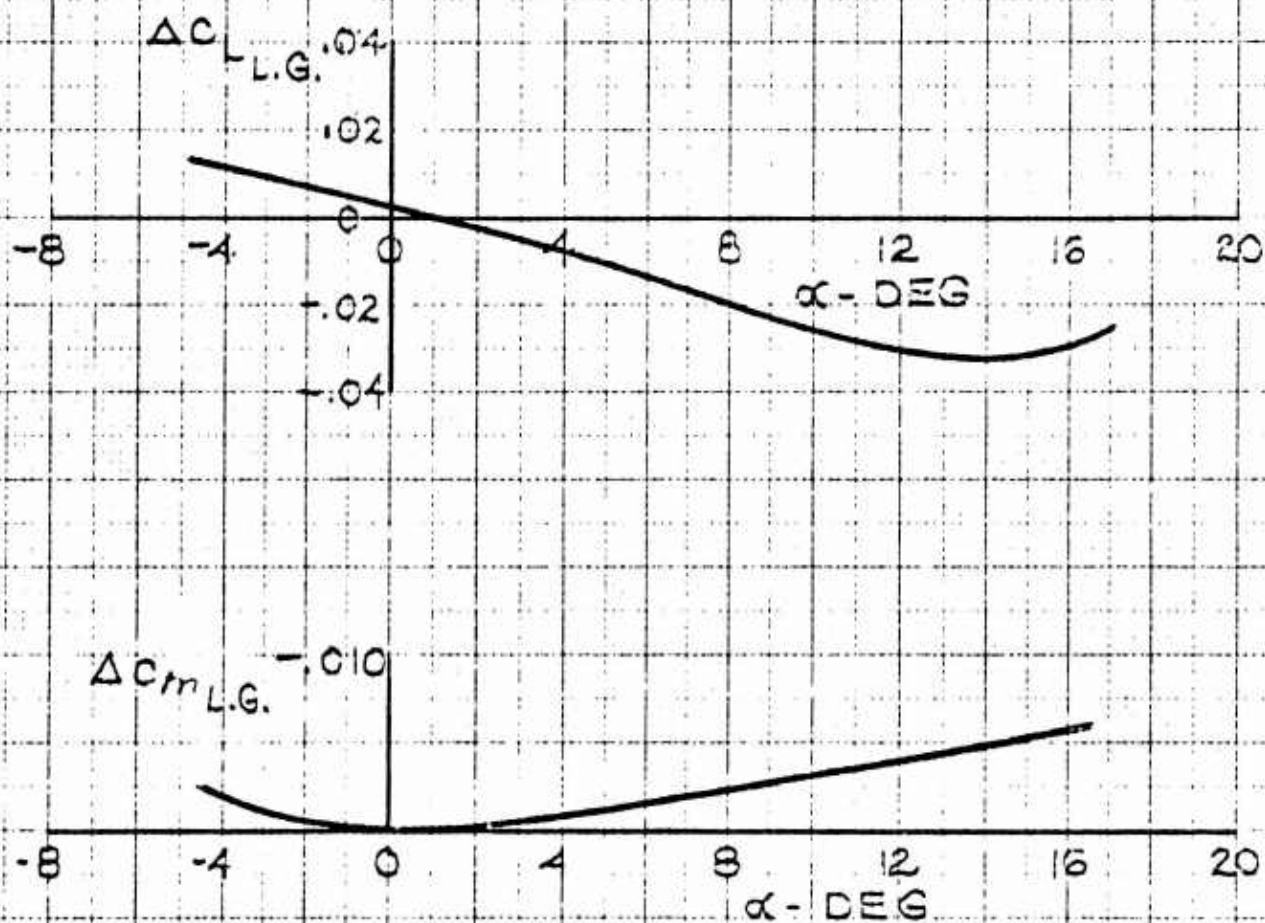


Figure 3.22

XV-5A
SIDEFORCE COEFFICIENT
DUE TO SIDESLIP ANGLE

LOW SPEED

NOTE:

1. STABILITY AXES
2. VALID TO $\beta = \pm 6^\circ$
3. LEGEND:

—— COMPLETE MODEL
 ---- MODEL-TAIL

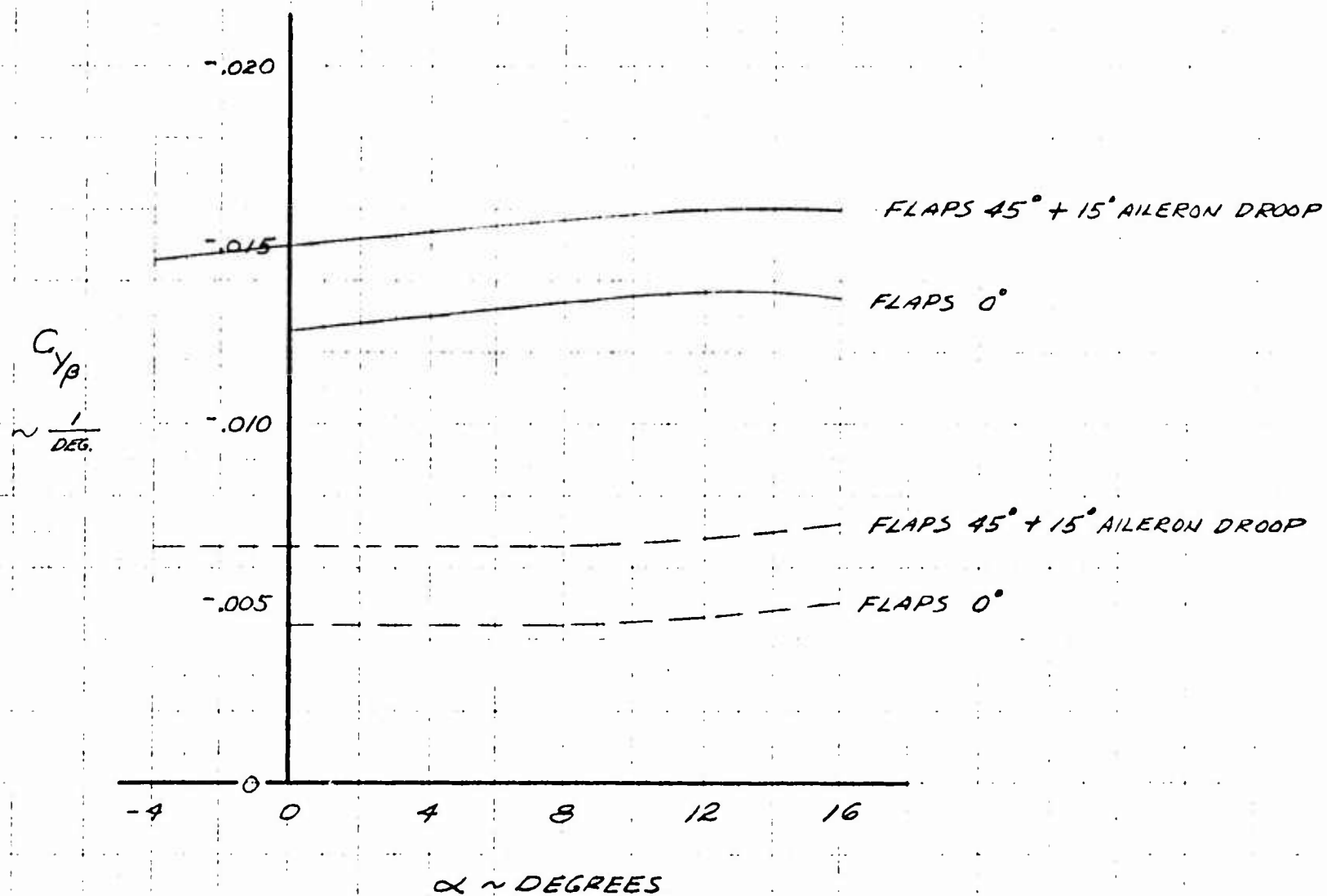


Figure 3.23

XV-5A
YAWING MOMENT COEFFICIENT
DUE TO SIDESLIP ANGLE

LOW SPEED

NOTE:

1. STABILITY AXES
2. C.G. @ F.S. 240.0
3. VALID TO $\beta = \pm 6^\circ$
4. LEGEND:

—— COMPLETE MODEL
 ---- MODEL - TAIL

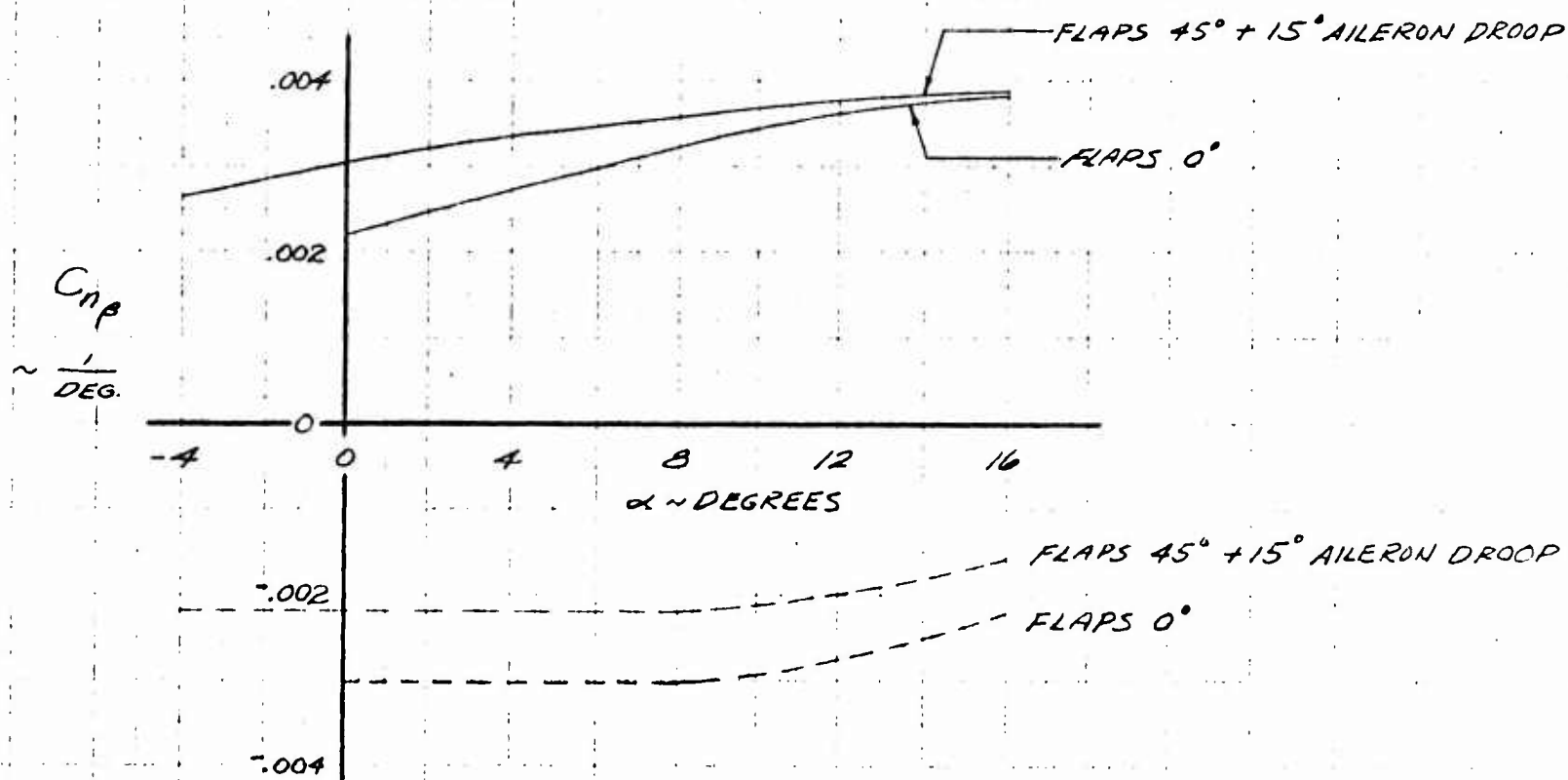


Figure 3.24

XV-5A
YAWING MOMENT COEFFICIENT
DUE TO SIDESLIP ANGLE

LOW SPEED

NOTE:

1. STABILITY AXES
2. C.G. @ F.S. 246.0
3. VALID TO $\beta = \pm 6^\circ$
4. LEGEND:

— COMPLETE MODEL
 --- MODEL-TAIL

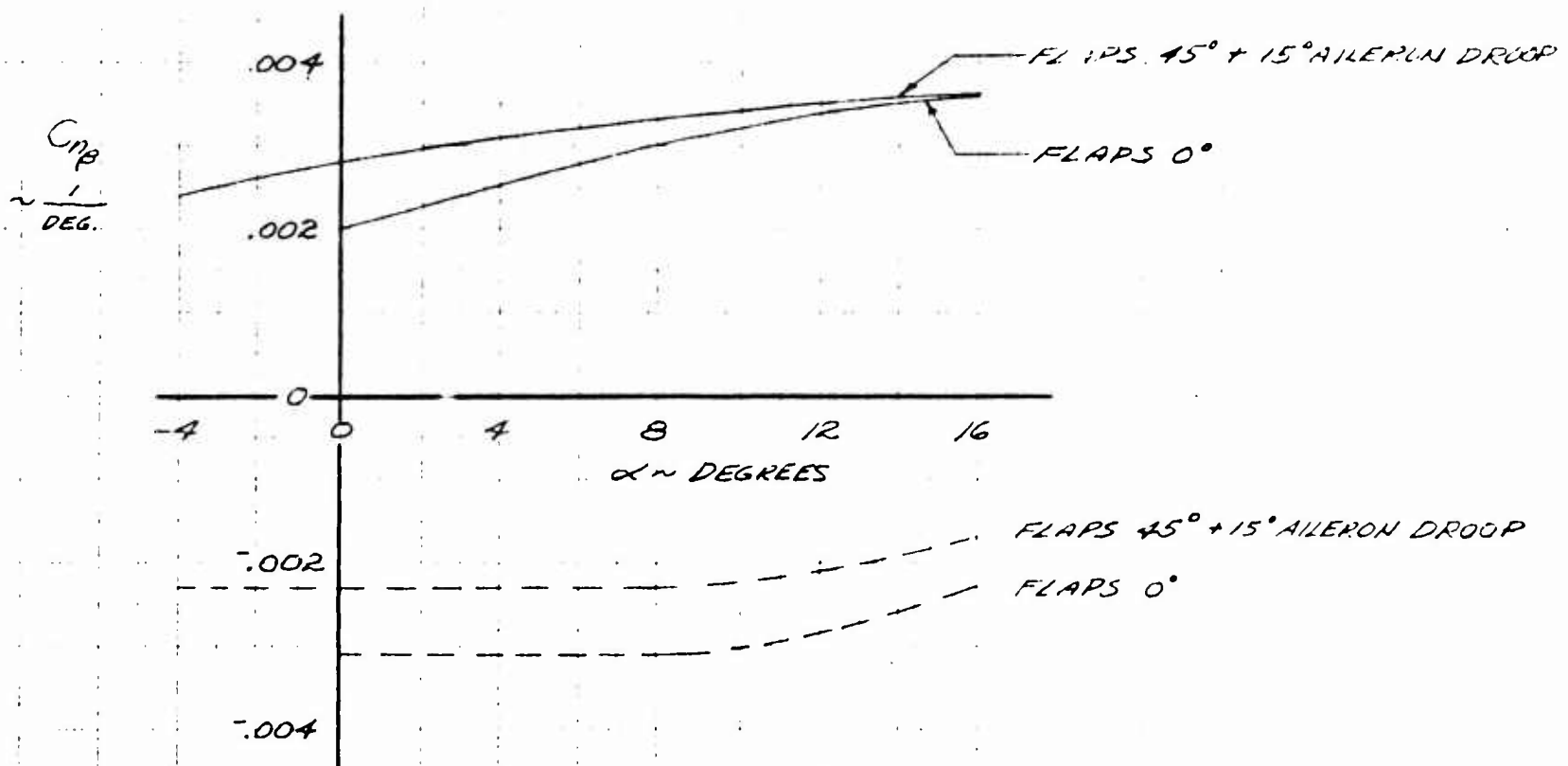


Figure 3.25

XV-5A
ROLLING MOMENT COEFFICIENT
DUE TO SIDESLIP ANGLE

LOW SPEED

NOTE:

1. STABILITY AXES
2. C.G. @ W.L. 112.0
3. VALID TO $\beta = \pm 6^\circ$
4. LEGEND:

——— COMPLETE MODEL
----- MODEL - TAIL

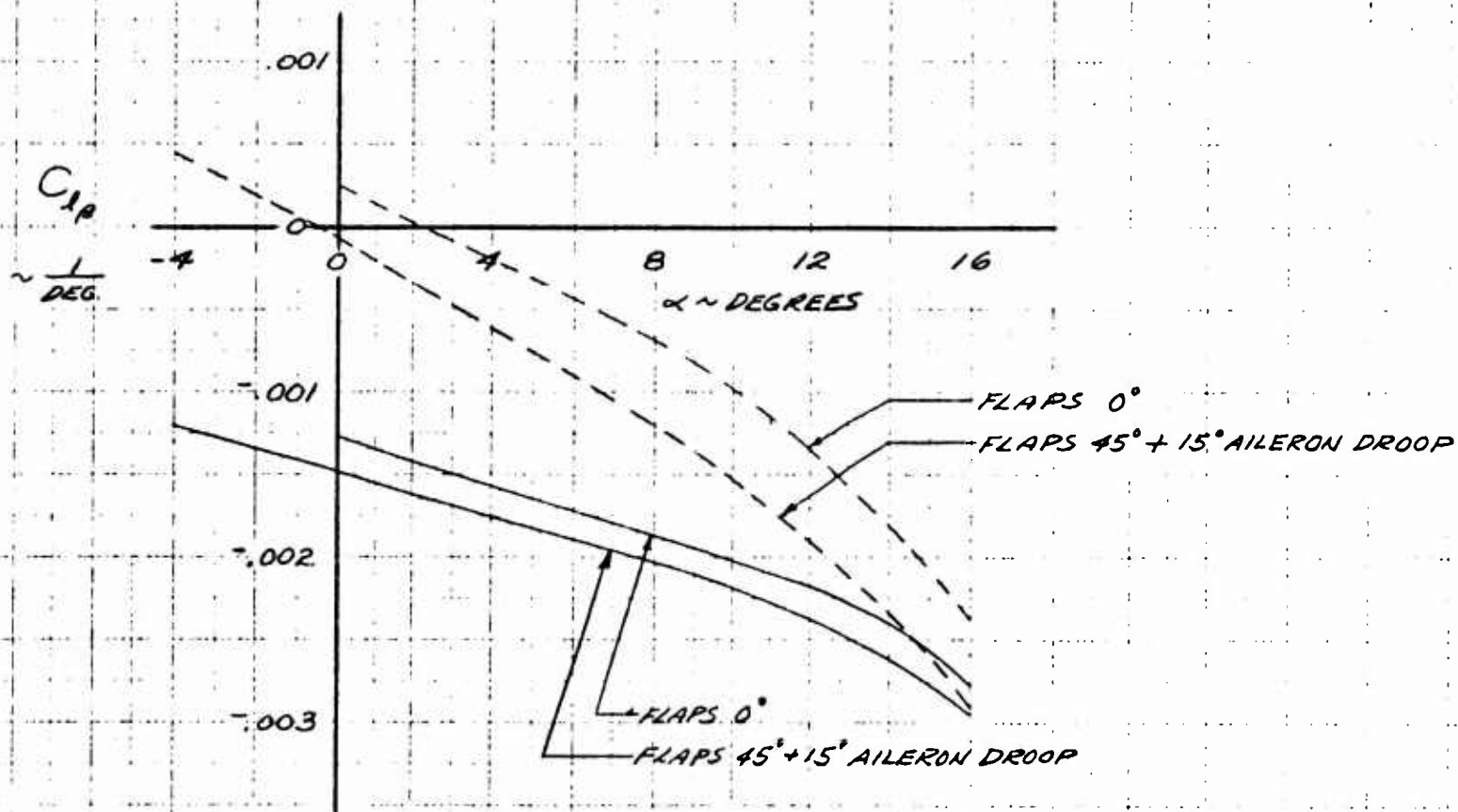


Figure 3.26

NOTES:

1- RIGID DATA

2- FREE AIR

3- STABILITY AXES

4- $\delta_f = 0^\circ$

5- REFERENCE: 143

XV-5A
 $C_{L\alpha_{M-T}}$ VS MACH NUMBER

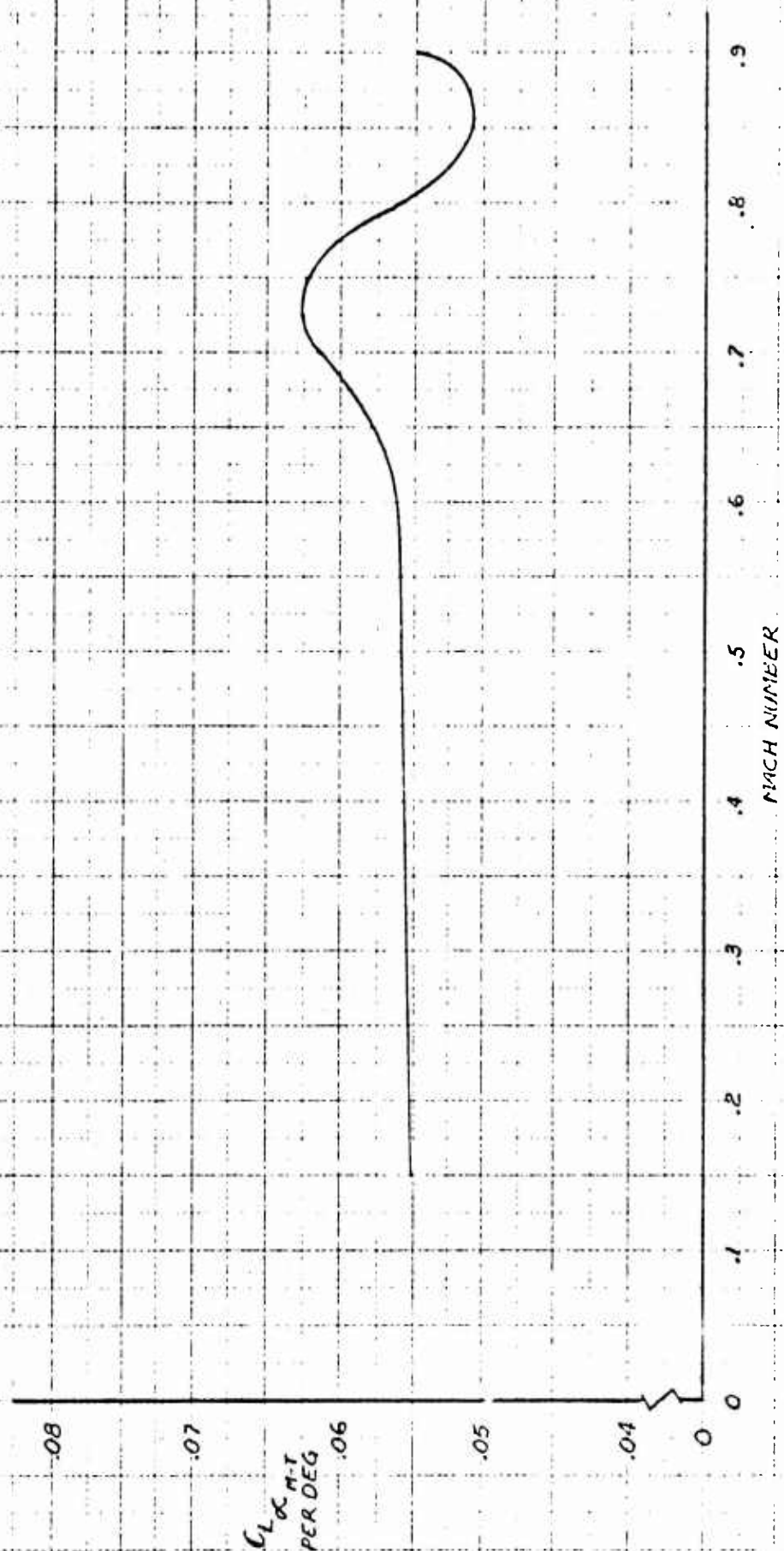


Figure 3.27

NOTES:

1- RIGID DATA

2- FREE AIR

3- STABILITY AXES

4- C.G. @ FS 240.0

5- $\delta_f = 0^\circ$

6- REFERENCE: 143

XV-5A
 $C_{m\alpha M-T}$ VS MACH NUMBER

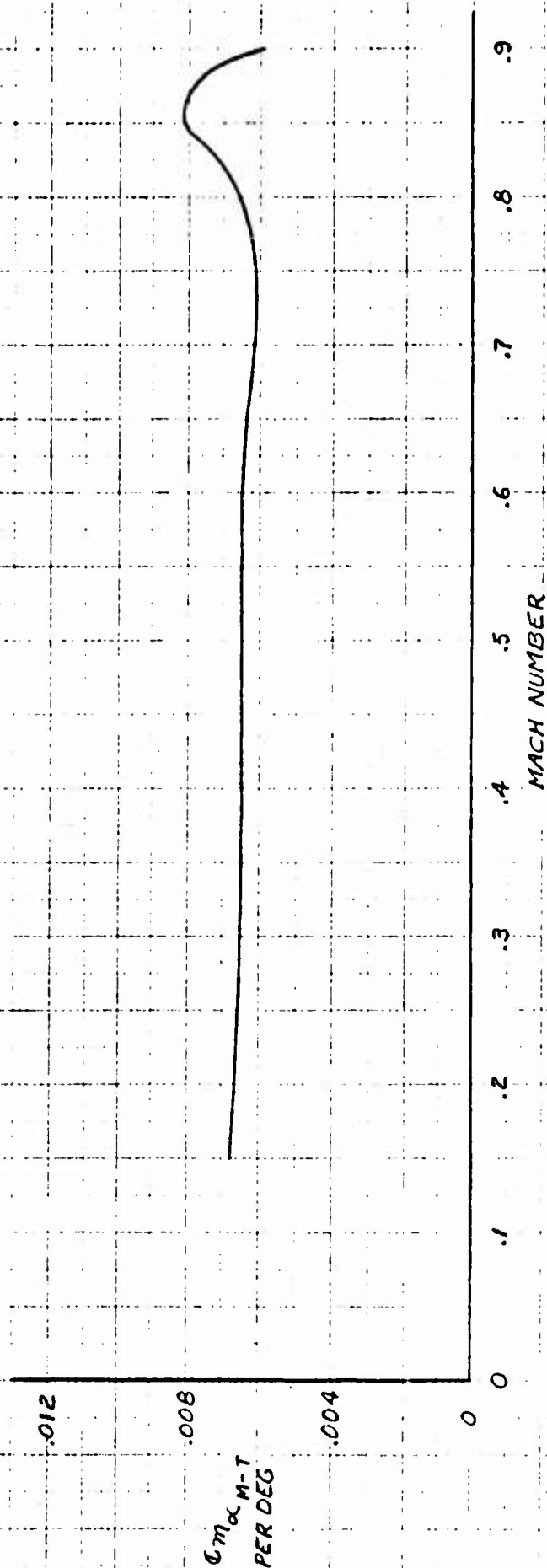


Figure 3.28

NOTES:

1- RIGID DATA

2- FREE AIR

3- STABILITY AXES

4- C.G. C.F.S. 246.0

5- $\delta_f = 0^\circ$

6- REFERENCE: 143

XV-5A
 $C_{m\alpha M-T}$ VS MACH NUMBER

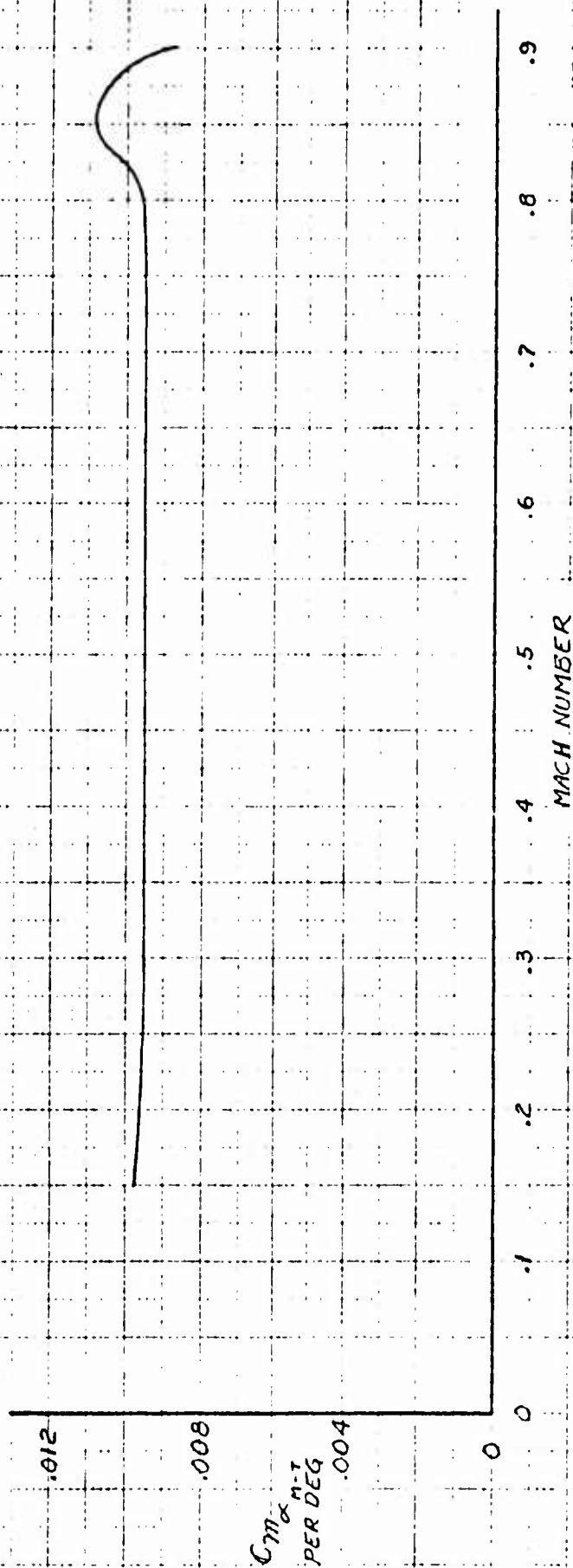


Figure 3.29

NOTES:

- 1- RIGID DATA
- 2- FREE AIR
- 3- STABILITY AXES
- 4- $\delta_F = 0^\circ$
- 5- $\bar{C} = 112.92$ INCHES
- 6- L.E. OF \bar{C} OF S. 211.14
- 7- REFERENCE: 143

XV-5A
Q.C. _{M-T} LOCATION VS MACH NUMBER

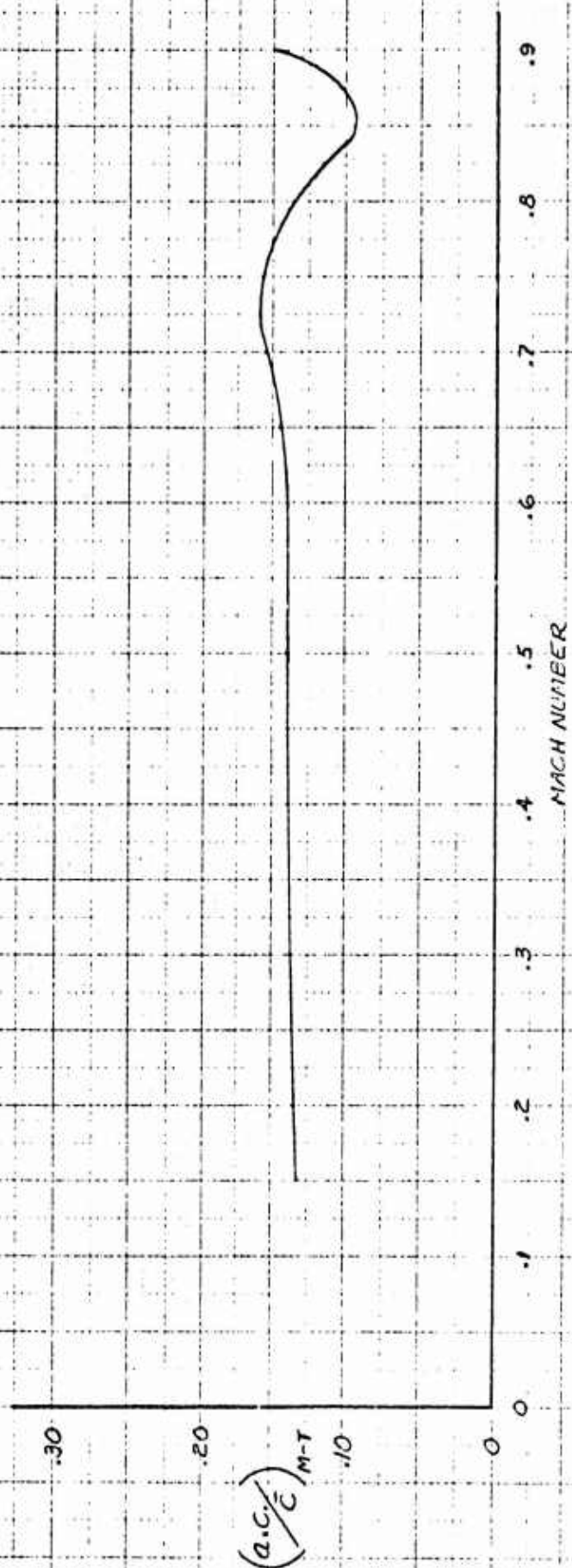


Figure 3.30

NOTES:

1-RIGID DATA

2-FREE AIR

3-STABILITY AXES

4- $\delta_f = 0^\circ$

5-REFERENCE: 143

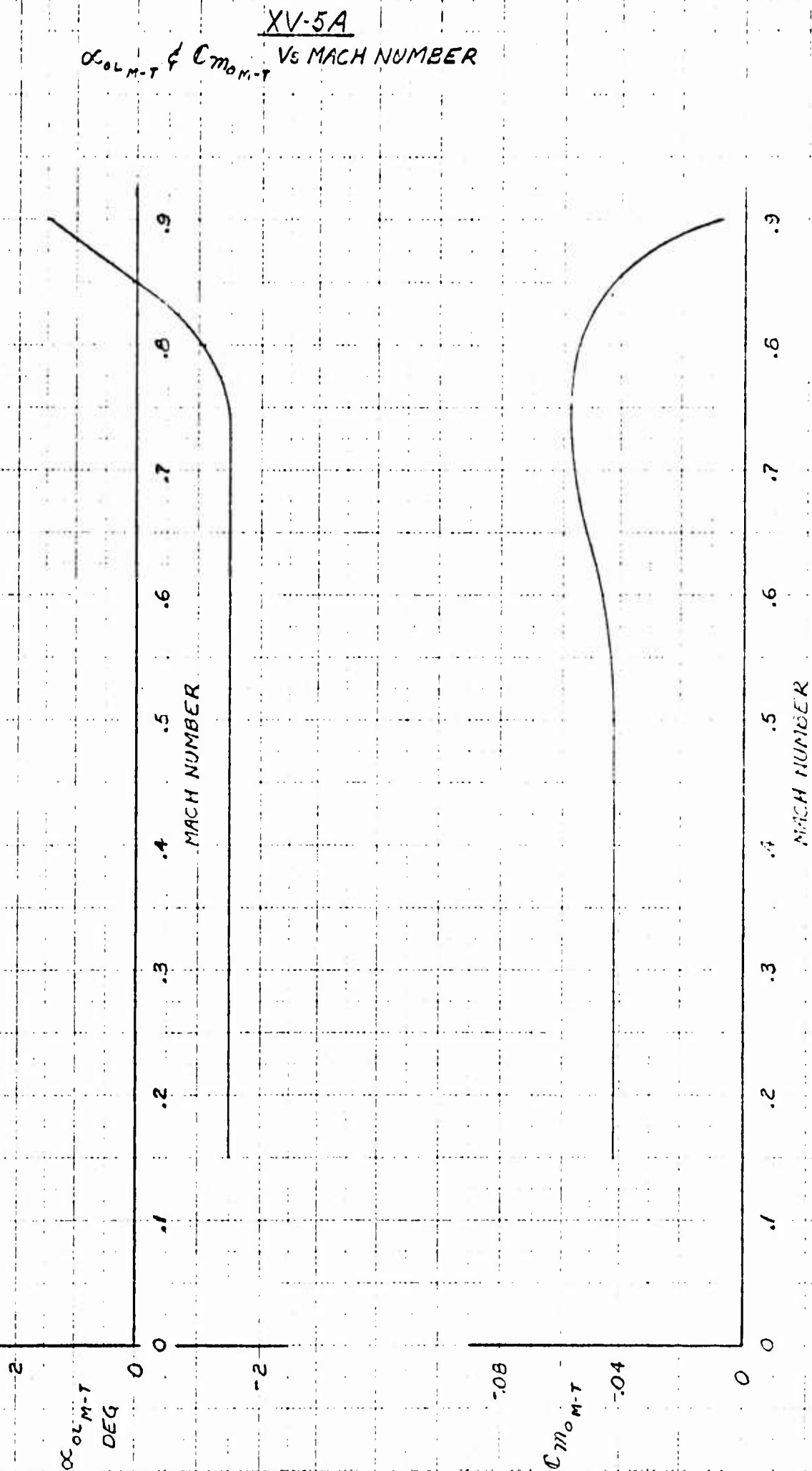


Figure 3.31

XV-5A ϵ_{OL} & $\partial \epsilon / \partial \alpha$ VS. MACH NUMBER

NOTES:

1- RIGID DATA

2- FREE AIR

3- STABILITY AXES

4- $\delta_f = 0^\circ$

5- ϵ VS α IS NON-LINEAR

6- REFERENCE: 143

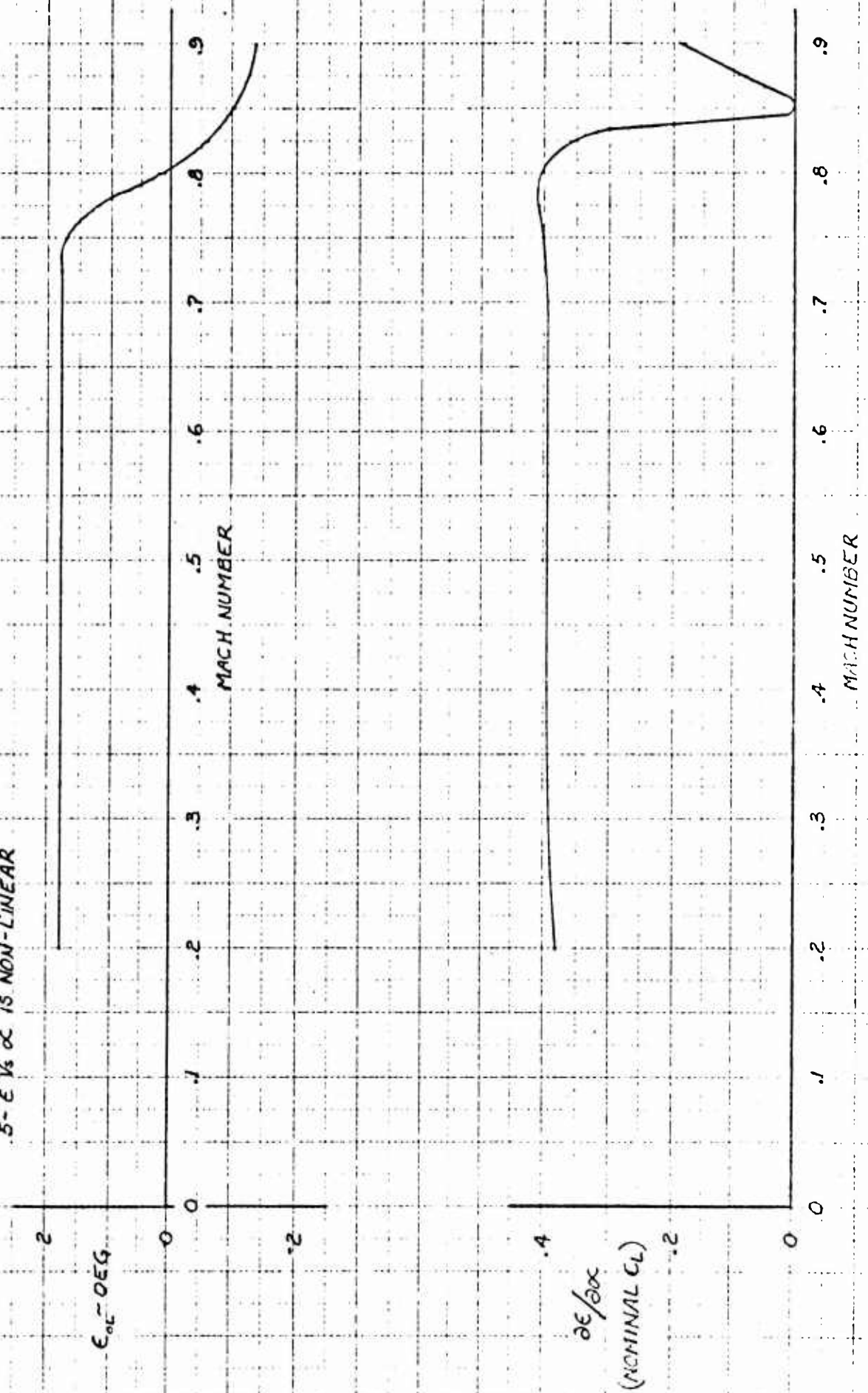


Figure 3.32

NOTES:

1- RIGID DATA

2- FREE AIR

3- STABILITY AXES

4- $\delta_f = 0^\circ$

5- REFERENCE: 143

XV-5A
VS MACH NUMBER
 $CL_{\alpha_{cm}}$

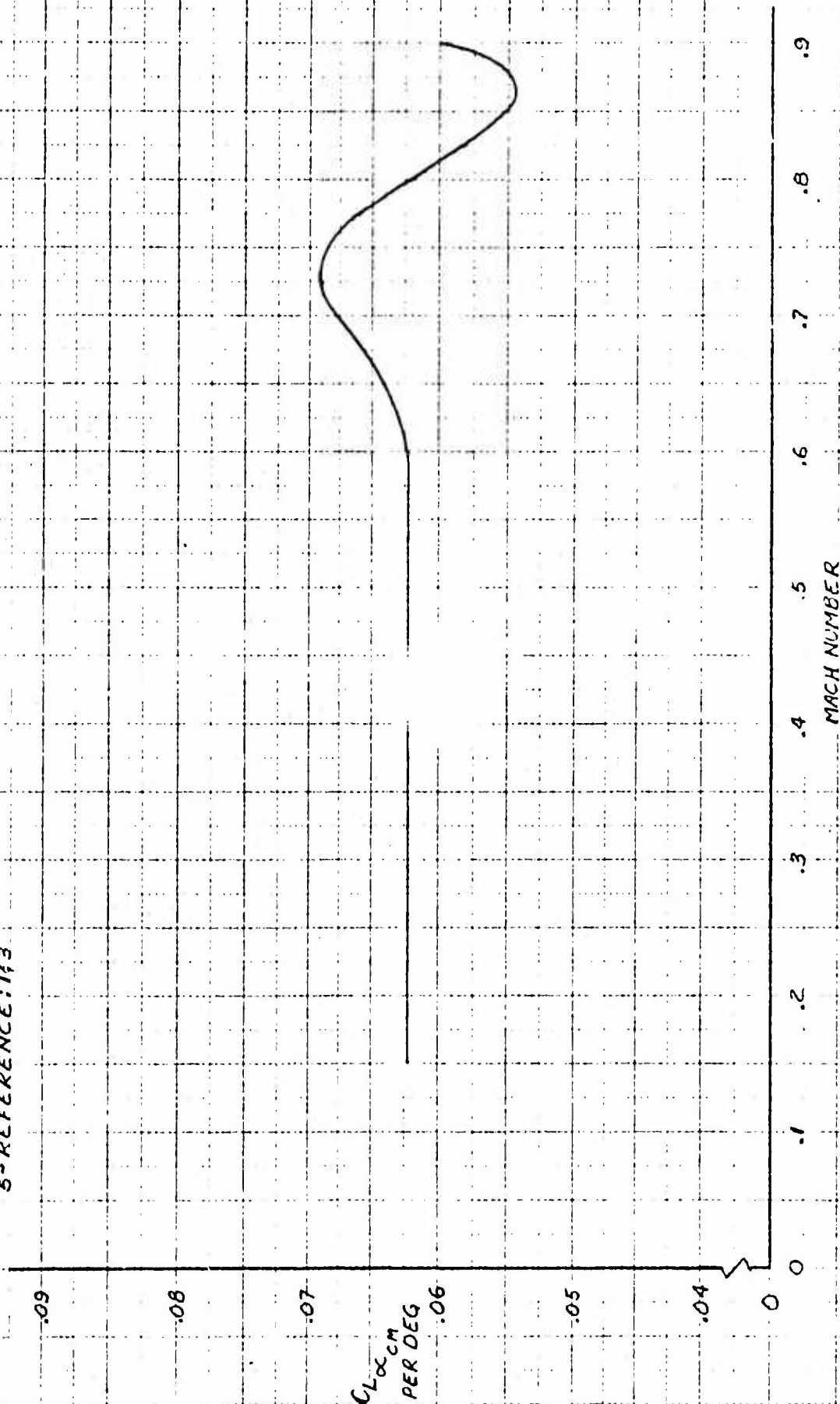


Figure 3.33

- NOTES:
- 1- RIGID DATA
 - 2- FREE AIR
 - 3- STABILITY AXES
 - 4- C.G. @ F.S. 240.0.
 - 5- $\delta_f = 0^\circ$
 - 6- $\frac{1}{C} = 2.241$
 - 7- REFERENCE: 143

$C_{m\alpha}$ vs MACH NUMBER

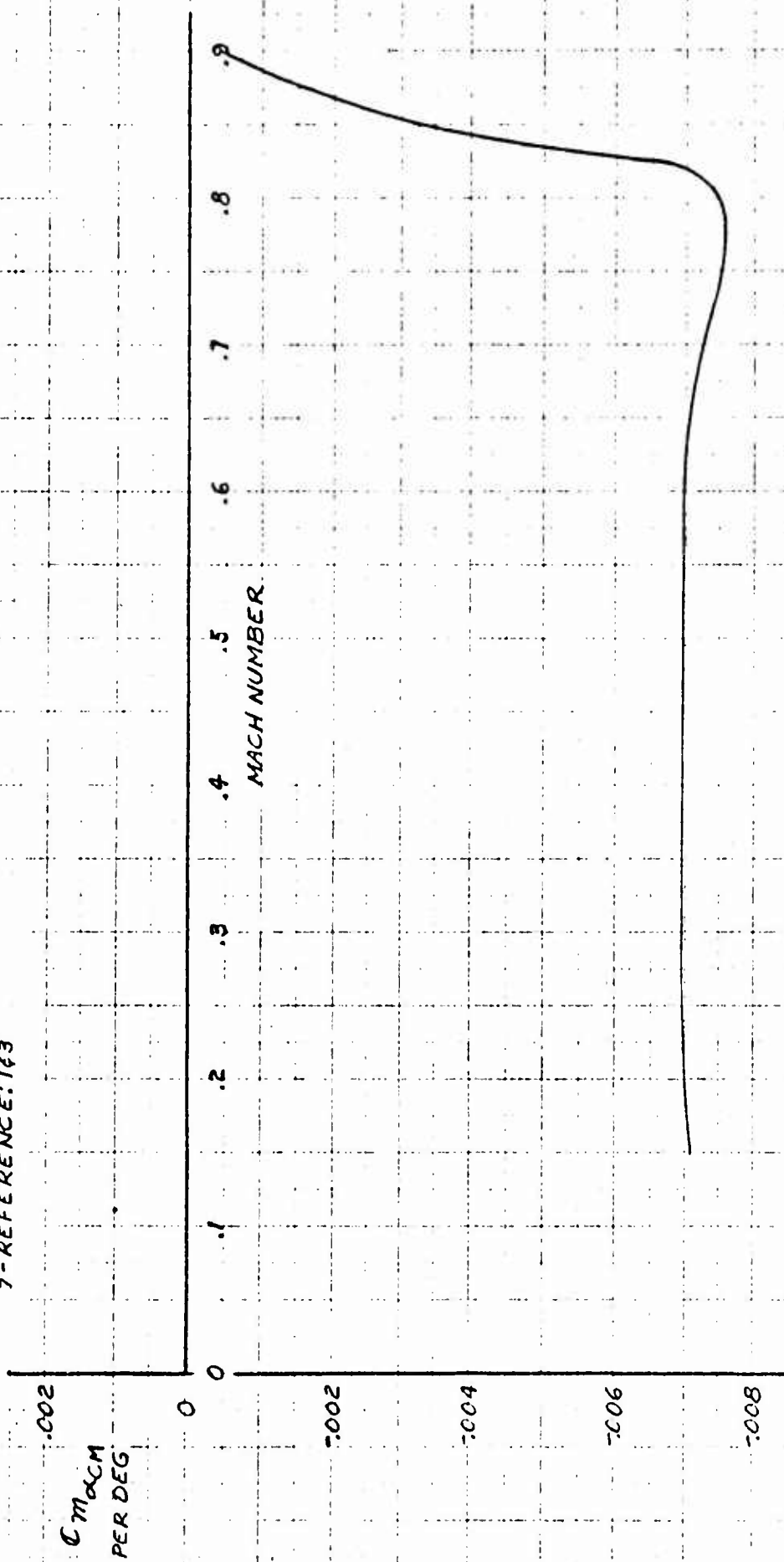


Figure 3.34

NOTES:

- 1- RIGID DATA
- 2- FREE AIR
- 3- STABILITY AXES
- 4- C.G. C.F.S. 216.0
- 5- $\delta_f = 0^\circ$
- 6- $\frac{d\delta_f}{d\alpha} = 2.188$
- 7- REFERENCE: 143

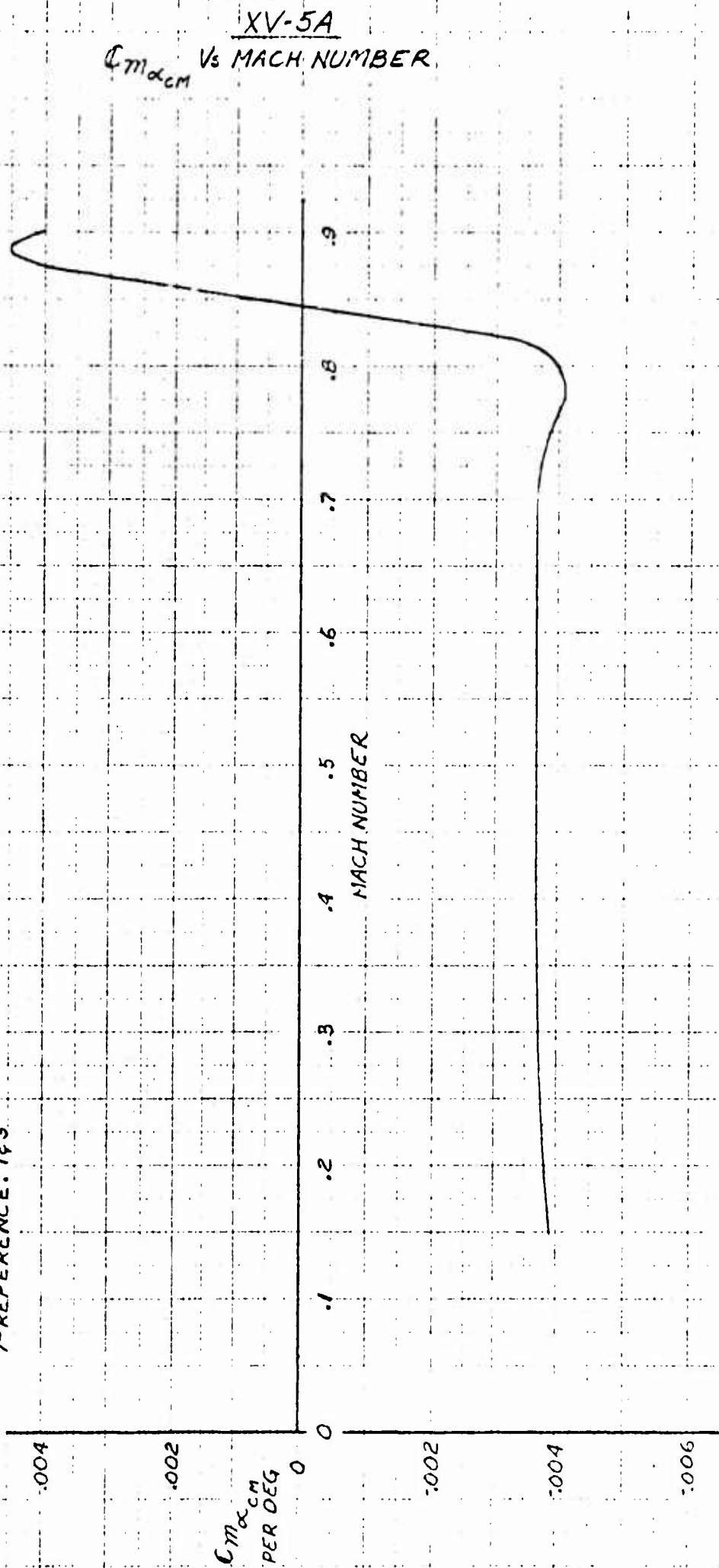
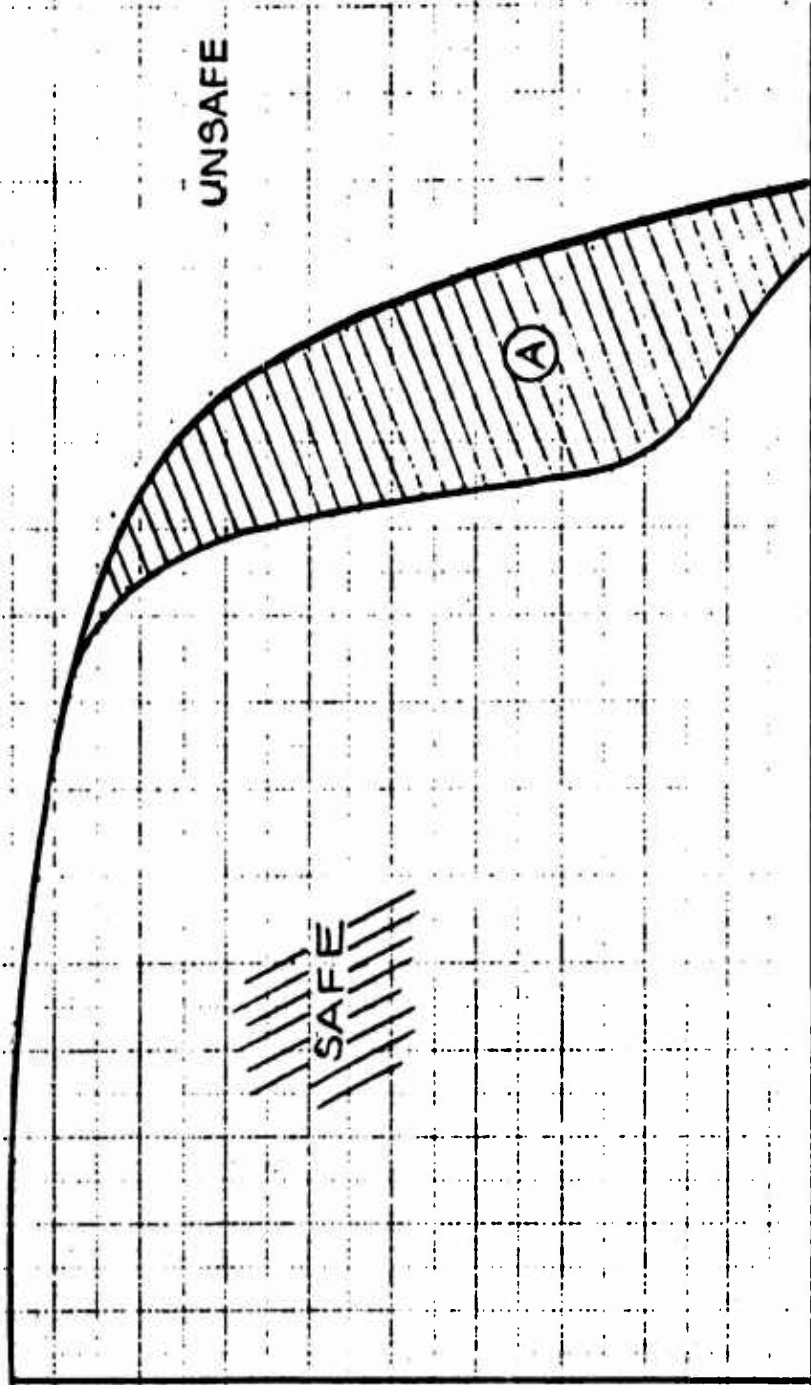


Figure 3.35

XV-5A ESTIMATED STABILITY LIMITS

FLAPS UP STALL G.W. 9200 LBS. S.L. 9.0

LIMIT LIFT COEFFICIENT - C_L



MACH NO.

(A) QUESTIONABLE AREA

Figure 3.36

NOTES:

1- RIGID DATA

2- FREE AIR

3- STABILITY AXES

4- C.G. C.F.S. 240.0

5- $\delta_f = 0^\circ$

6- $\frac{L}{V} = 2.241$

7- REFERENCE: 143

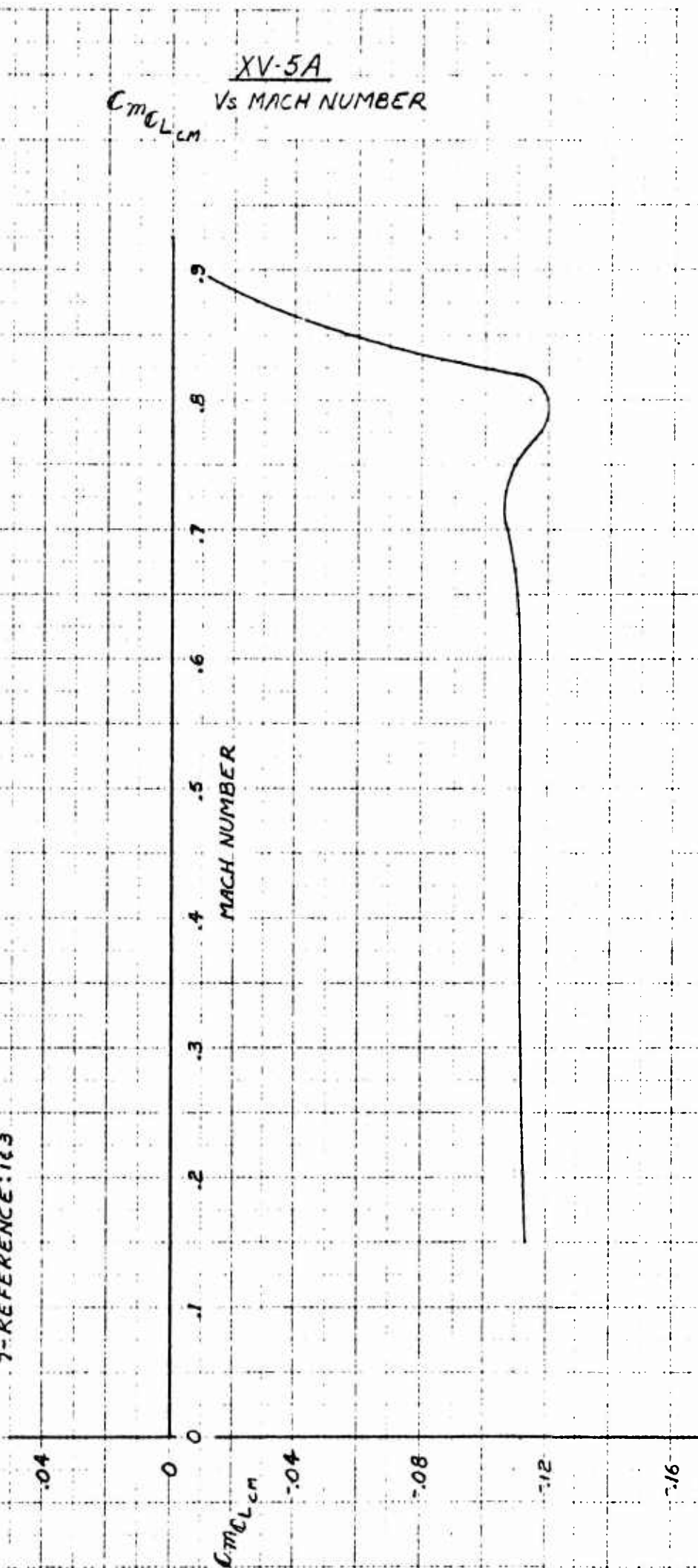


Figure 3.37

NOTES:

1- RIGID DATA

2- FREE AIR

3- STABILITY AXES

4- C.G.C.F.S. 246.0

5- $\delta_f = 0^\circ$

6- $\frac{1}{2} \sqrt{2} = 2.168$

7- REFERENCE: 143

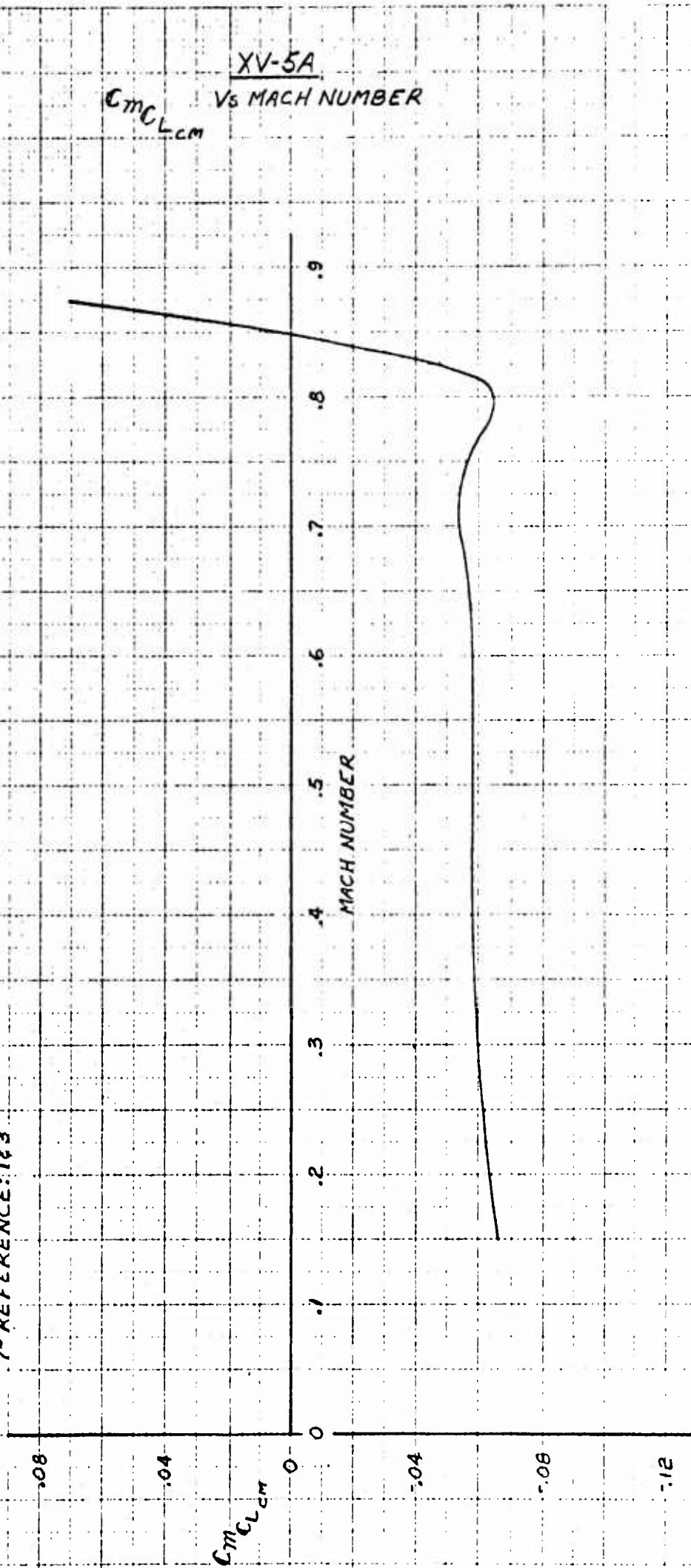


Figure 3.38

NOTES:

- 1- RIGID DATA
- 2- FREE AIR
- 3- STABILITY AXES
- 4- C.G @ FS 240.0
- 5- $\delta_f = 0^\circ$
- 6- REFERENCE: 143

XV-54
CL α_{CMTRIM} VS MACH NUMBER

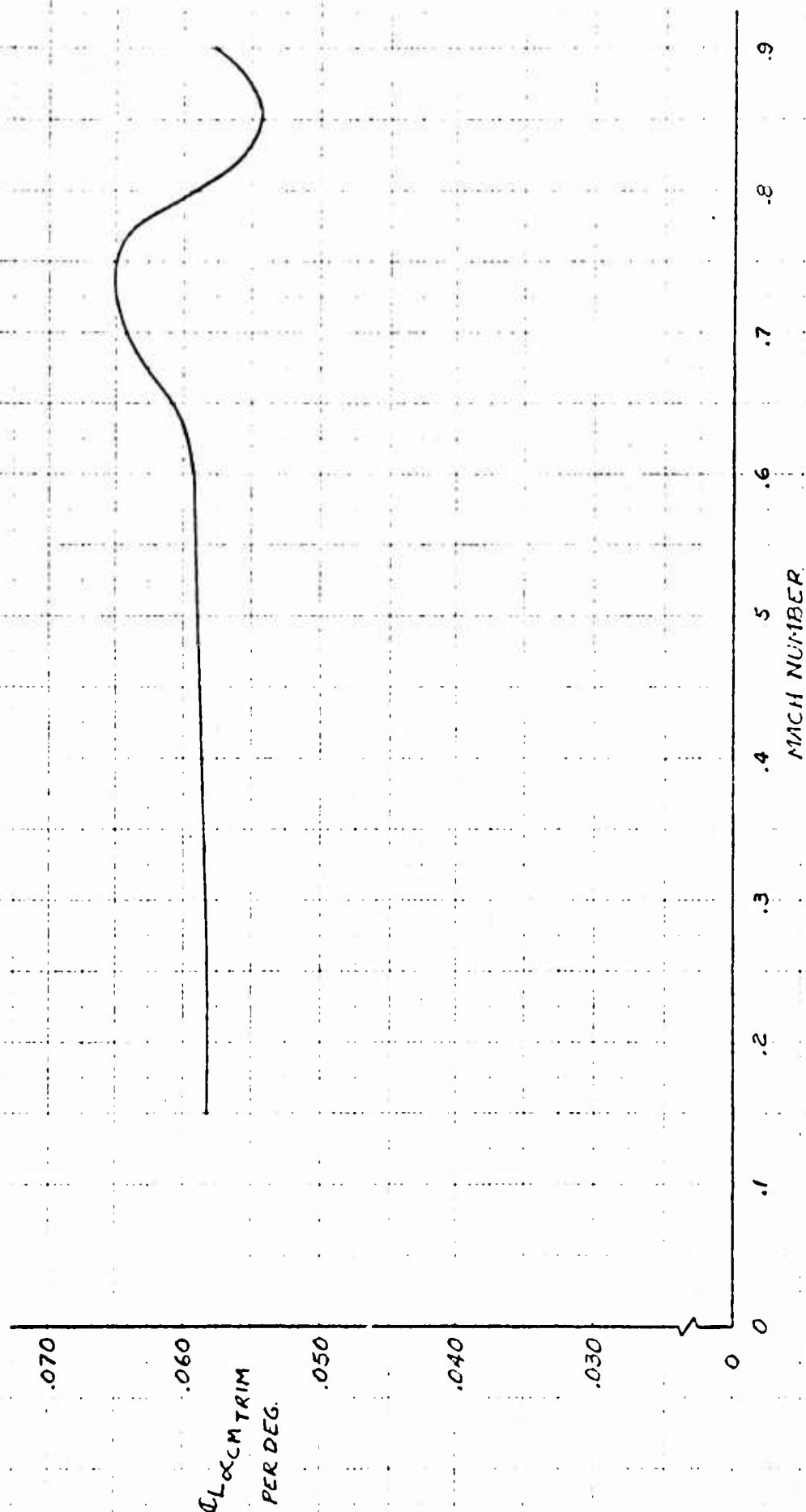


Figure 3.39

NOTES:

- 1- RIGID DATA
- 2- FREE AIR
- 3- STABILITY AXES
- 4- C.G.C.F.S. 245.0
- 5- $\delta_f = 0^\circ$
- 6- REFERENCE: 143

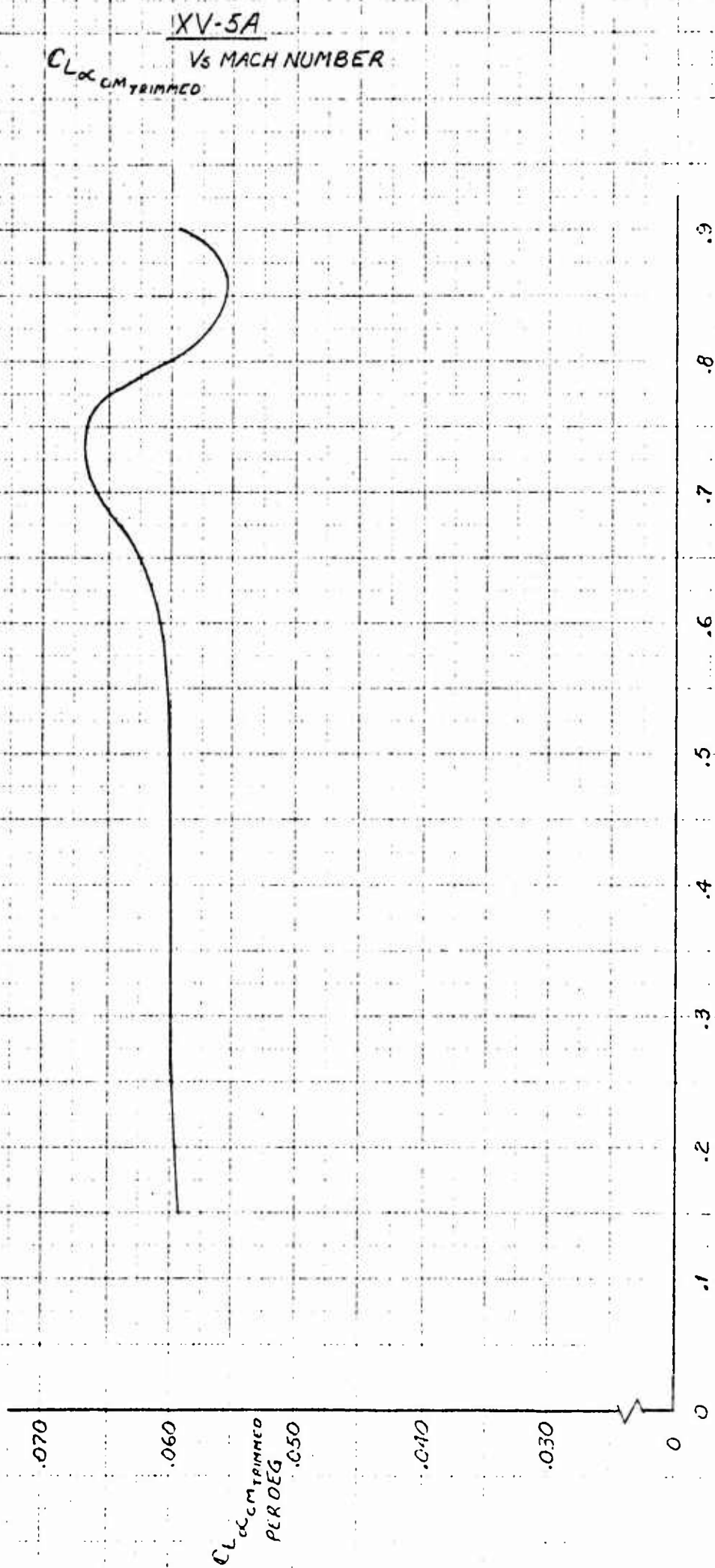


Figure 3.40

NOTES:

1- RIGID DATA

2- FORCE AIR

3- STABILITY AXES

4- $\delta_T = 0^\circ$

5- $S_1/S_2 = .203$

6- REFERENCE: 143

XV-5A
CL_{8L} VS MACH NUMBER

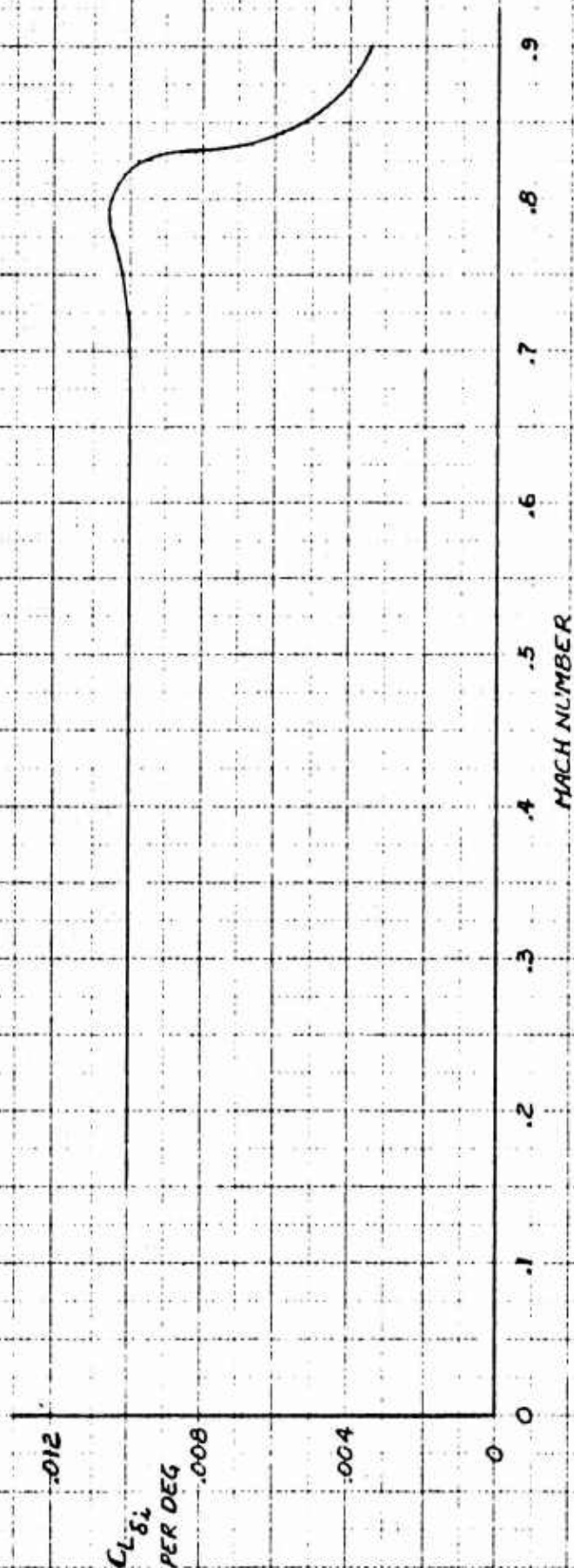


Figure 3.41

NOTES:

- 1- RIGID DATA
- 2- FREE AIR
- 3- STABILITY AXES
- 4- C.G. C.F.S. 240.0
- 5- $\delta_f = 0^\circ$
- 6- $S_e/S_w = .203, l_e/c = 2.241$
- 7- REFERENCE: 143

XV-5A
 $C_{m\delta_e}$ Vs MACH NUMBER

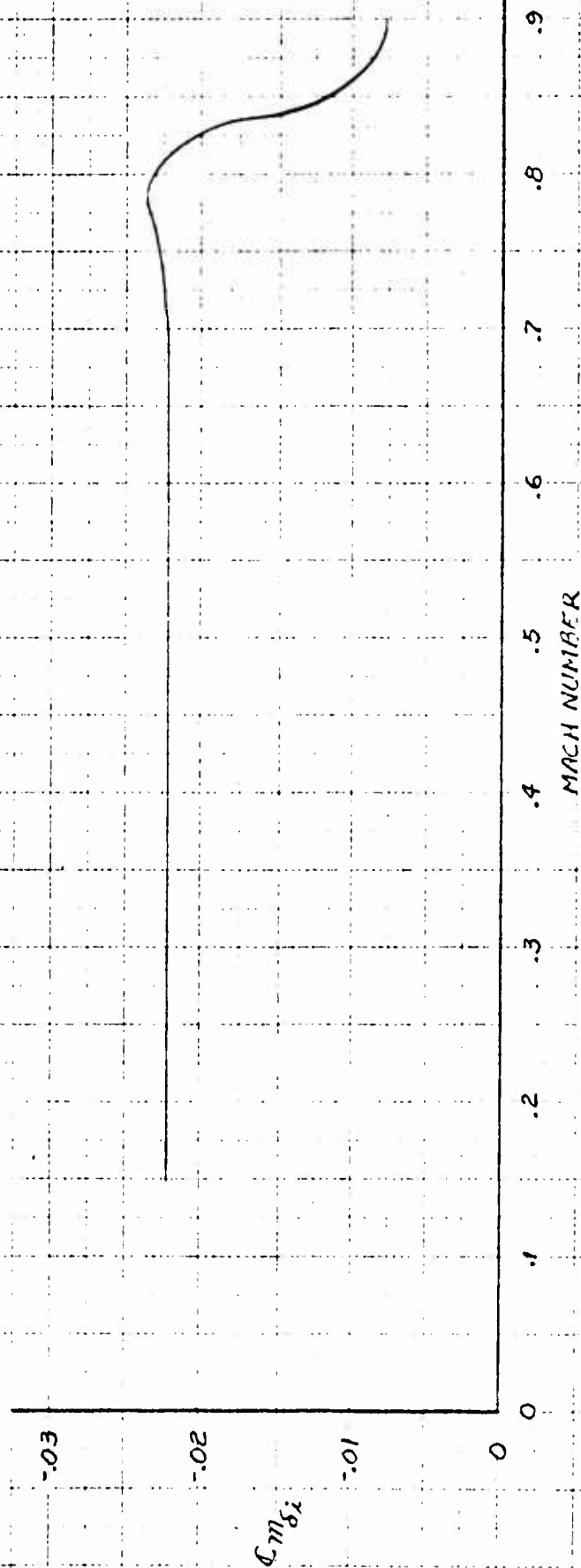


Figure 3.42

XV-5A
 $C_{m\delta_x}$ VS MACH NUMBER

NOTES:

- 1- RIGID DATA
- 2- FREE AIR
- 3- STABILITY AXES
- 4- C.G. C.F.S. 246.0
- 5- $\delta_x = 0^\circ$
- 6- $S_{\delta_x}/S_w = .203$, $l_{\delta_x}/\bar{c} = 2.188$
- 7- REFERENCE: 143

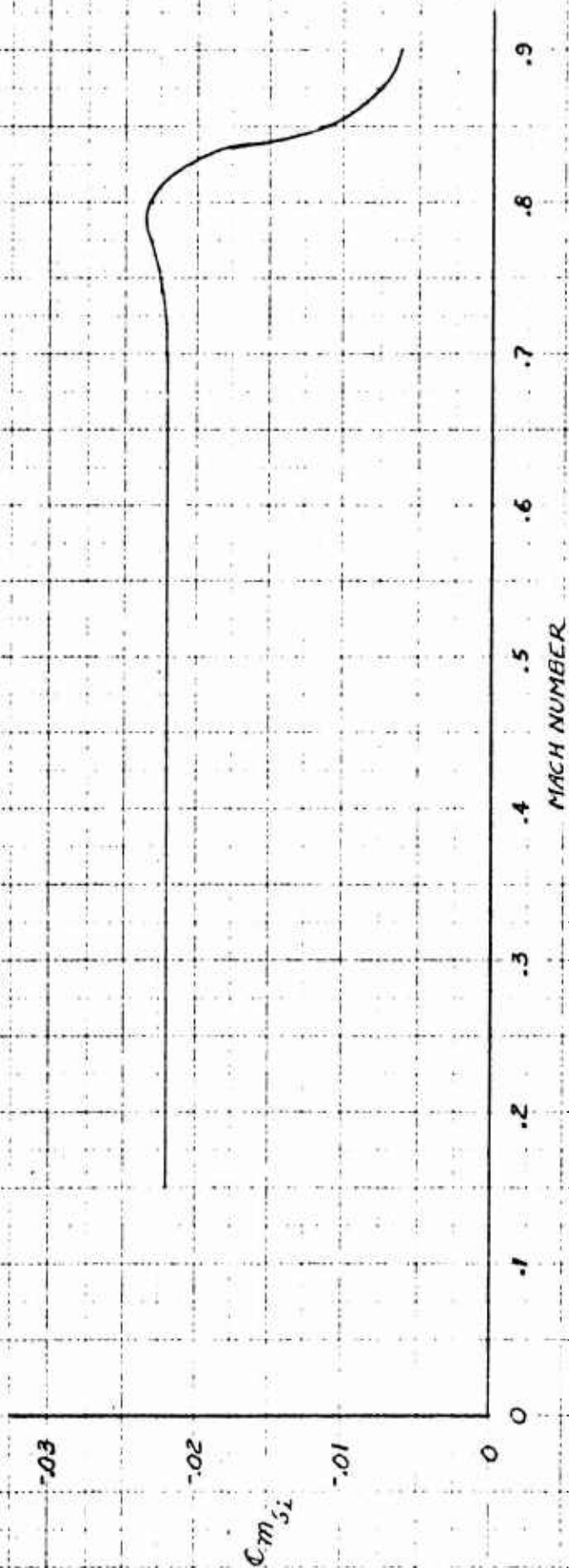


Figure 3.43

XY-5A
TRIMMED DRAG POLAR, HIGH SPEED

NOTE:

1. BASED ON WIND TUNNEL TEST DATA
2. REYNOLD'S NUMBER CORRECTION
TO ANA #421, 2500 FT., HOT DAY
3. ENGINE DUCT MASS FLOW RATIO = 1.0
4. FULLY TURBULENT BOUNDARY LAYER
5. INCLUDES ESTIMATED DRAG FOR
GAPS AND COOLING AIR.
6. C.G. @ F.S. 246.0

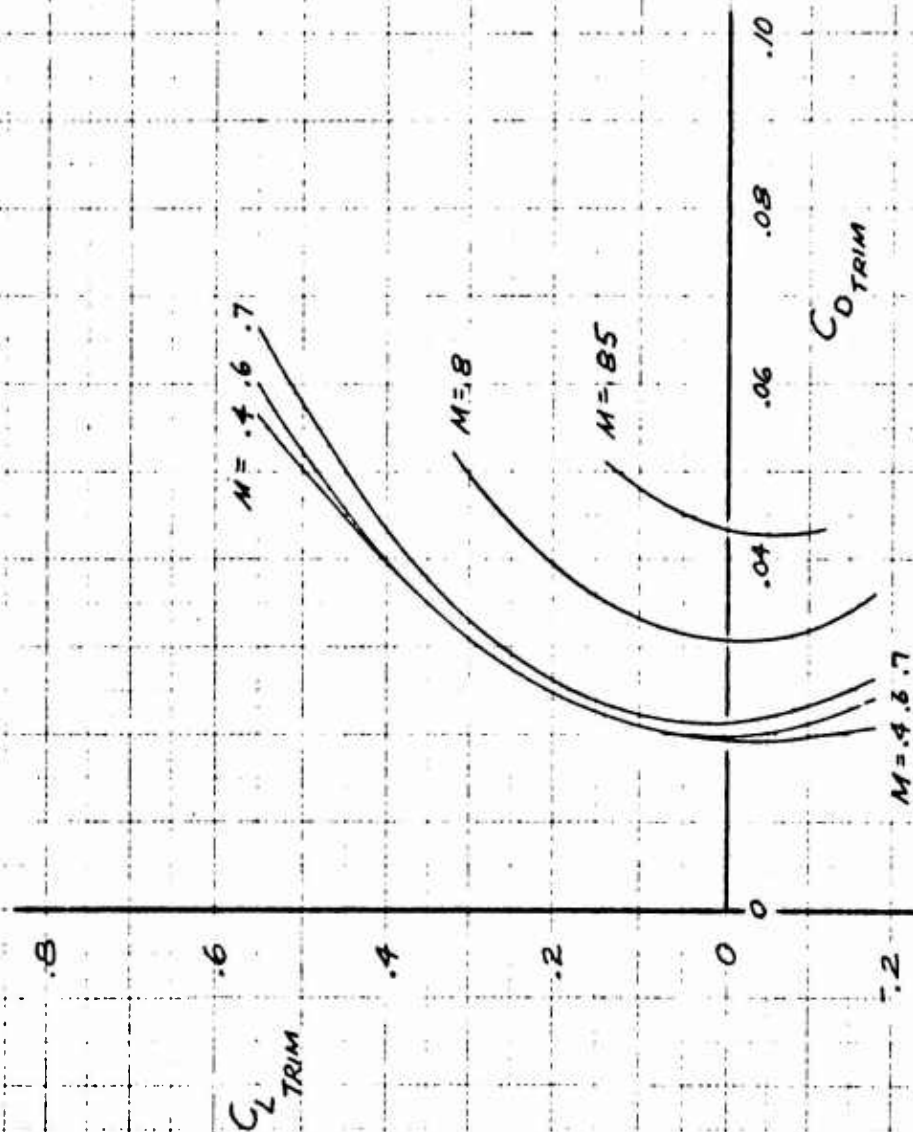


Figure 3.44

XV-5A
PITCHING MOMENT COEFFICIENT
DUE TO SIDESLIP.

HIGH SPEED

NOTE:

- 1 FLAPS UP
- 2 C.G. @ F.S. 240.0 - 244.0
- 3 $\alpha = 0^\circ - 5^\circ$
- 4 STABILITY AXES

$$C_{m_{\dot{\alpha}}} = (C_{m_{\dot{\alpha}}})_{\beta=0} + 0.05(1 - \sqrt{1 + K_{\dot{\alpha}} \beta^2})$$

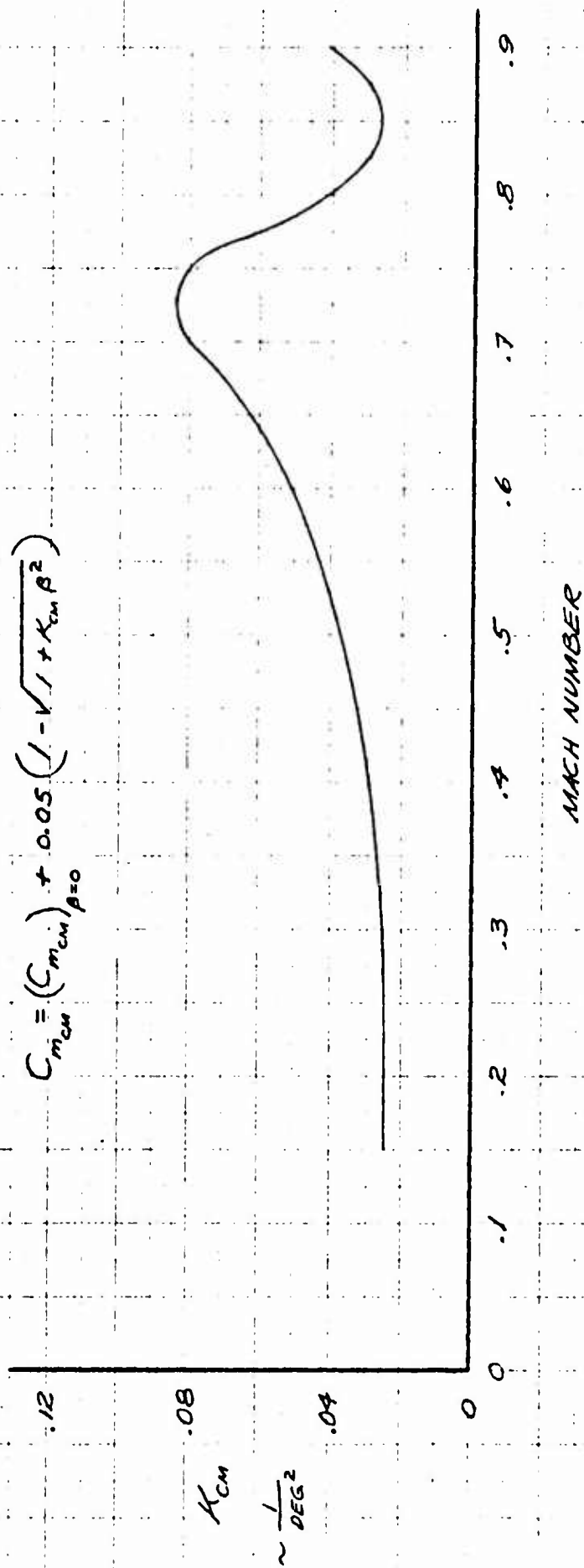


Figure 3.45

FLAPS UP

LEGEND α
0°, 4°, 8°
12°
16°

XV-5A
 $C_{Y_{PM-T}}$ vs. M

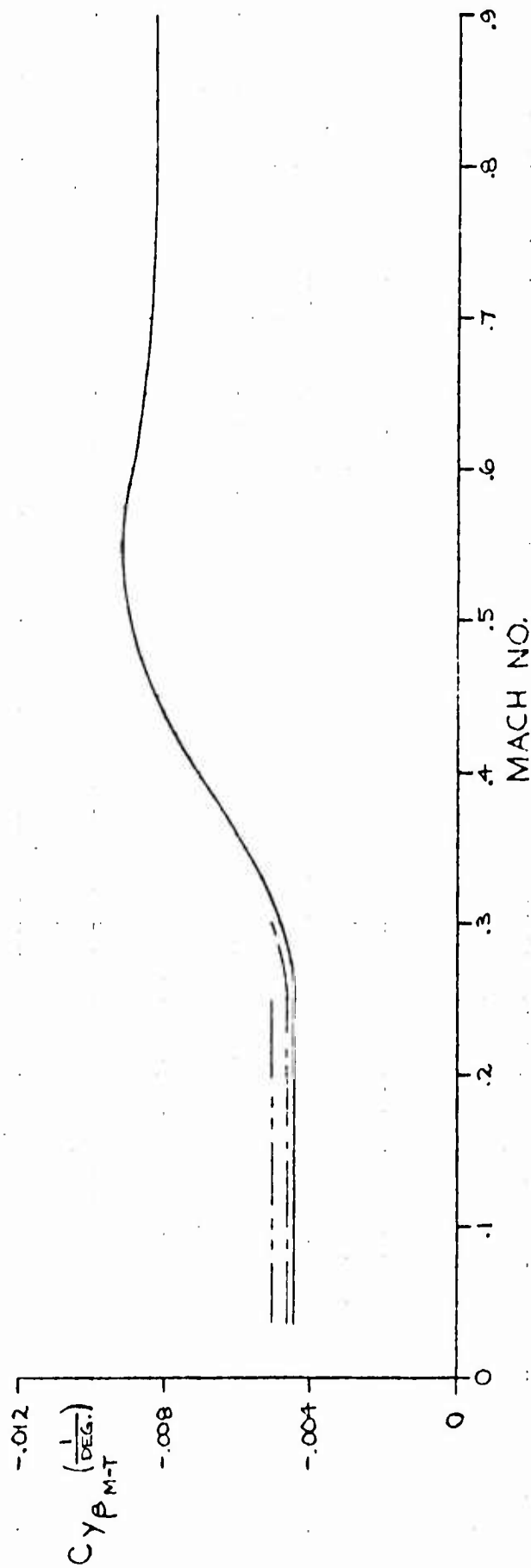


Figure 3.46

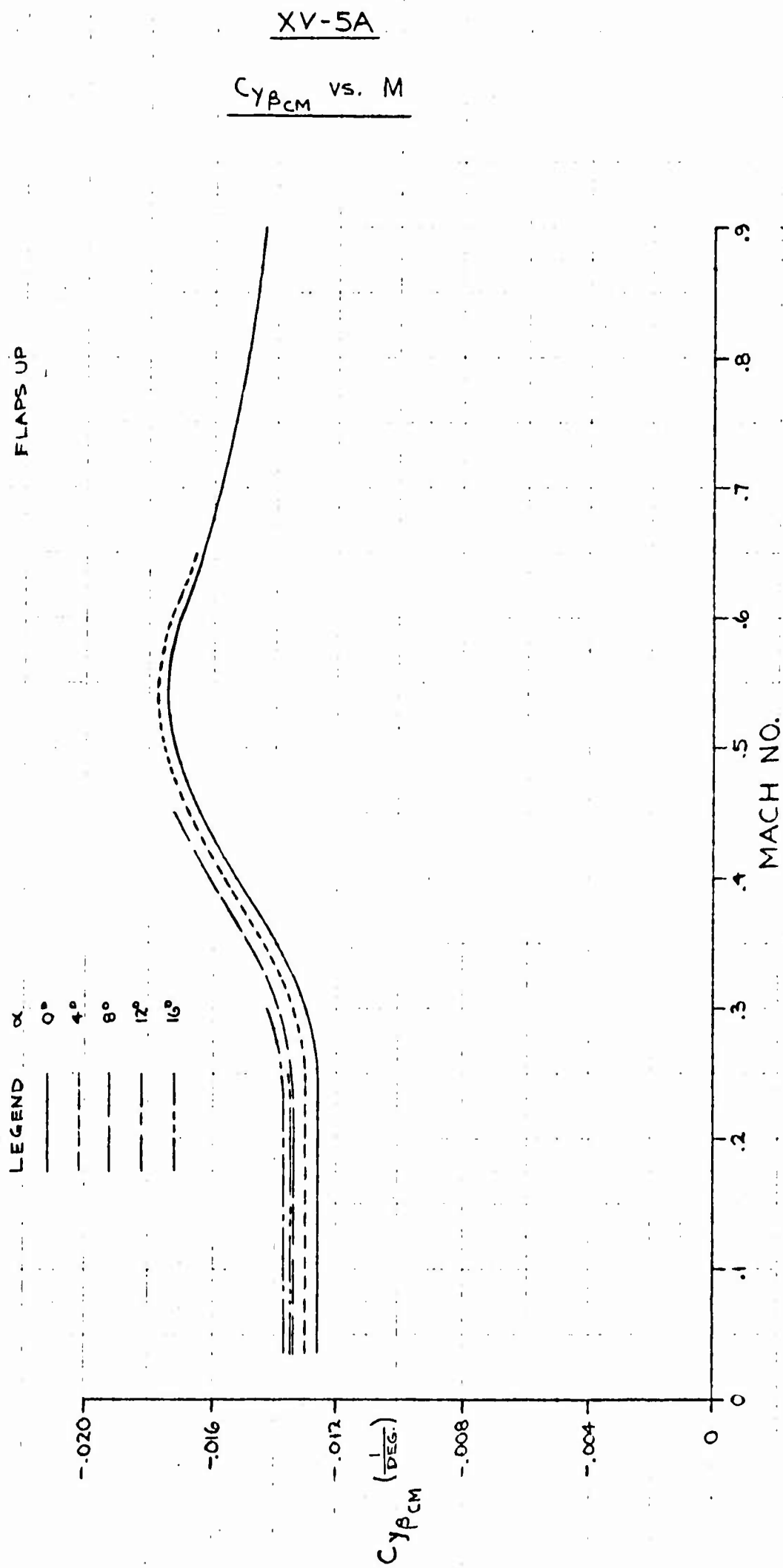


Figure 3.47

XV-5A

$C_{n\beta_{M-T}}$ vs. M

FLA'S UP
C.G. @ F.S. 246 - 240

LEGEND α
 ——— 0°, 4°, 8°
 - - - 12°
 - - - 16°

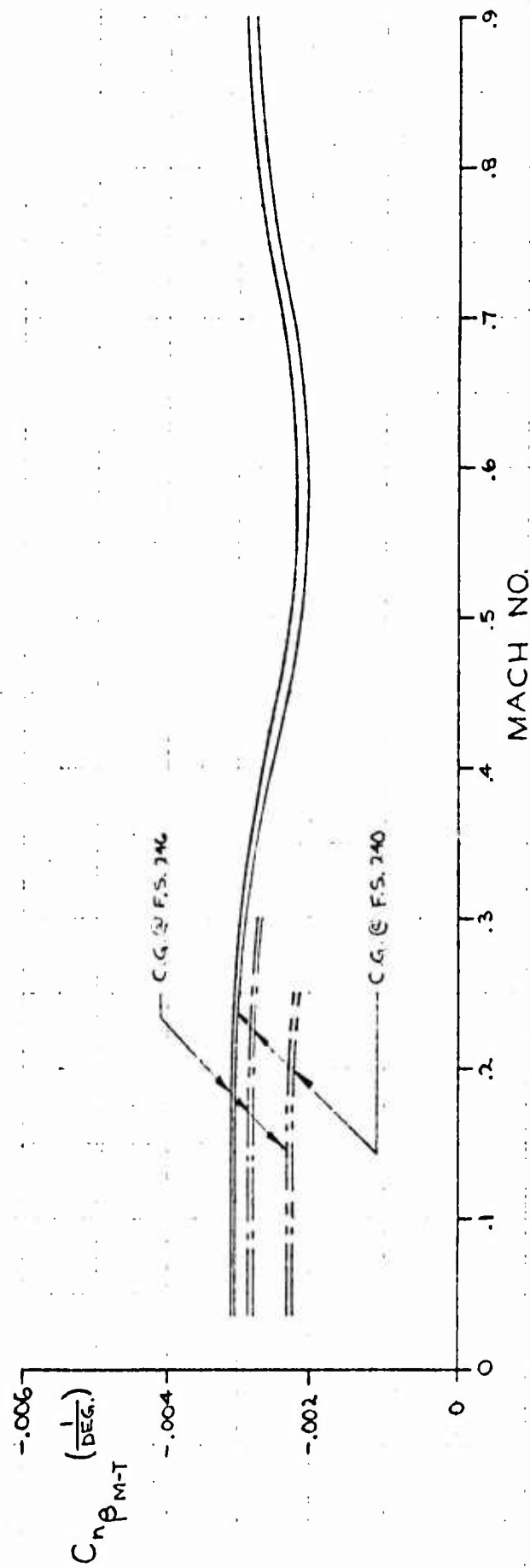


Figure 3.48

FLAPS UP
C.G. @ F.S. 240

XV-5A

$C_{n_{\beta CM}}$ vs. M

LEGEND

α	0°	4°	8°	12°	16°
	—	---	---	---	---

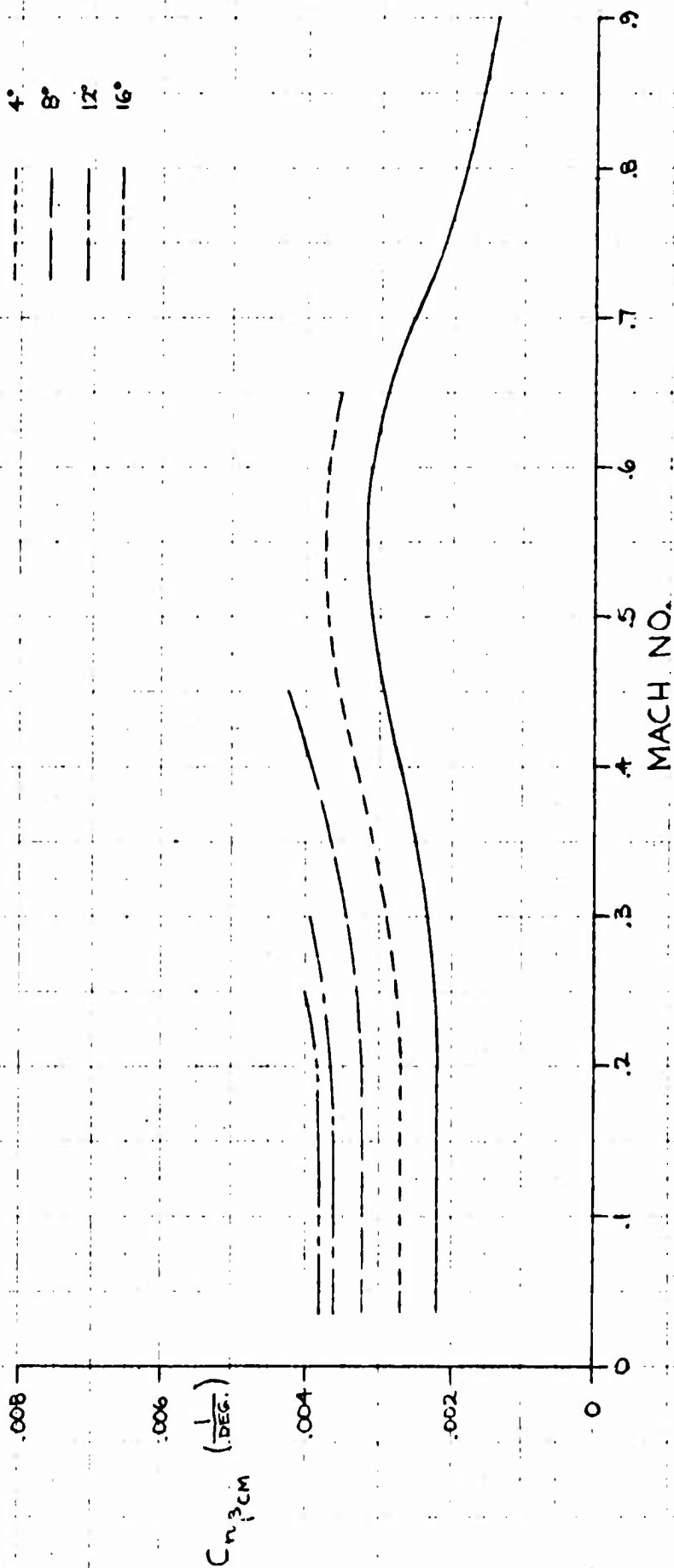


Figure 3.49

FLAPS UP
C.G. @ F.S. 24%

XV-5A
 $C_{n\beta_{cm}}$ vs. M.

LEGEND α
—— 0°
---- 4°
—— 8°
---- 12°
---- 16°

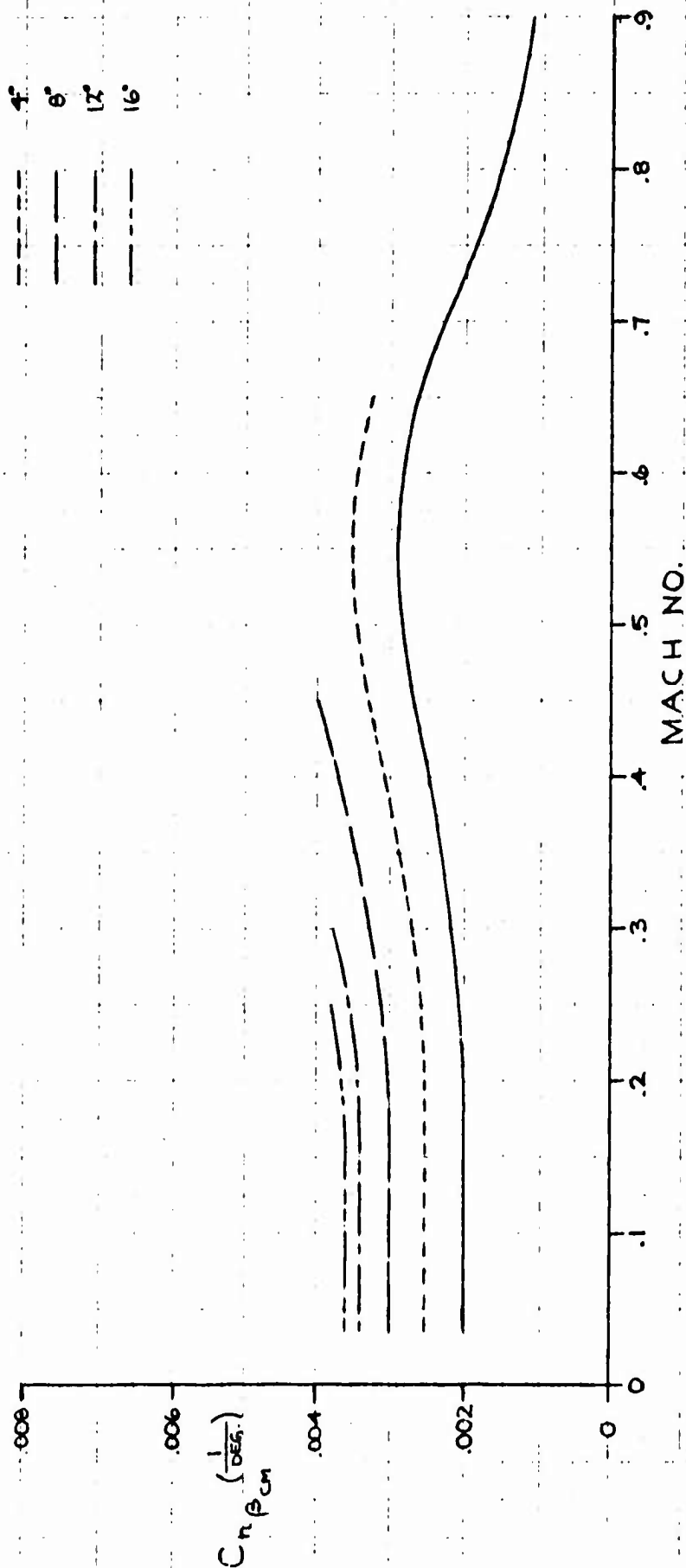


Figure 3.50

FLAPS UP
C.G. @ F.S. 246-240

XV-5A

$C_{L\beta_{M-T}}$ vs. M

LEGEND α

0°	---
4°	----
8°	----
12°	----
16°	----

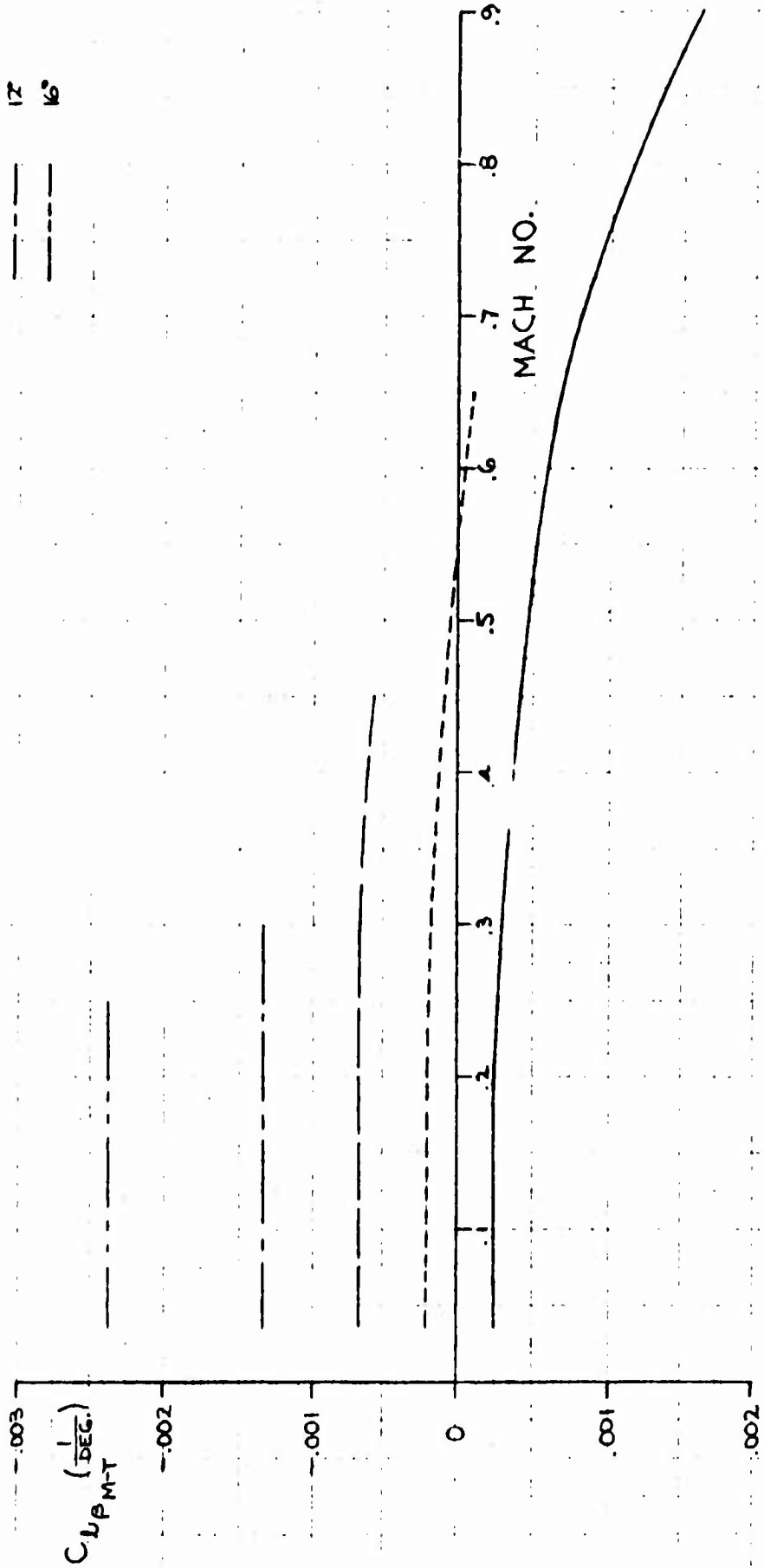


Figure 3.51

FLAPS UP
C.G. @ F.S. 146-240

LEGEND
 α
0° ———
4° - - -
8° ———
12° - - -
16° ———

XV-5A
 $C_{L\beta_{CM}}$ vs. M

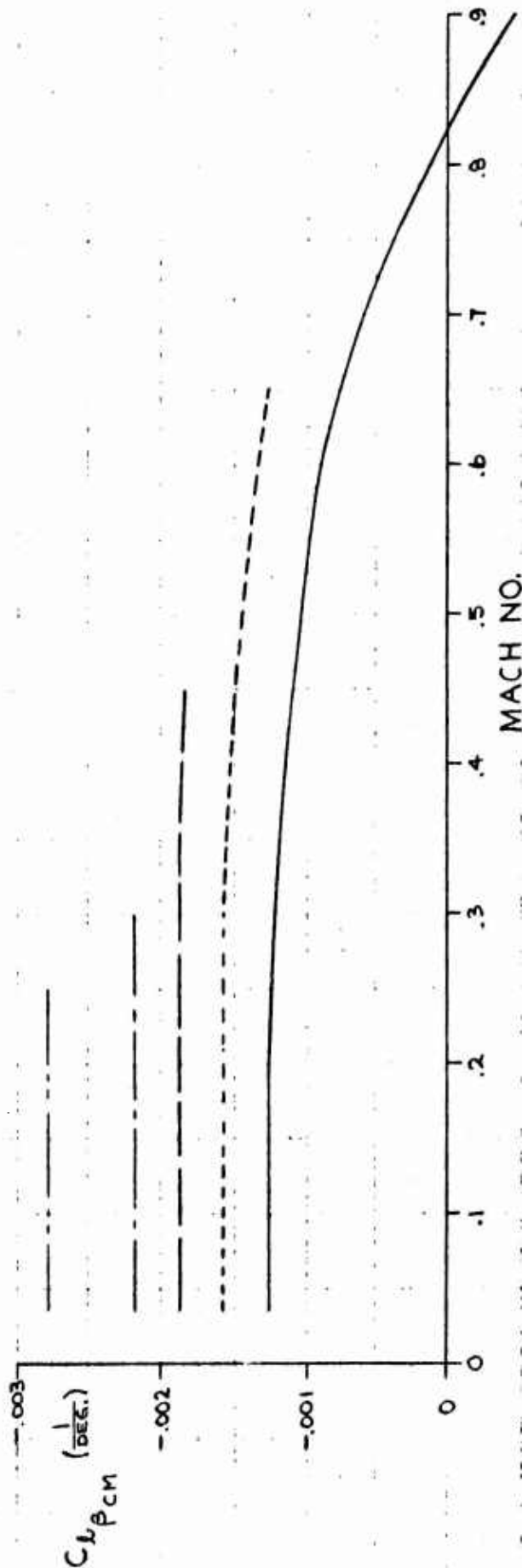


Figure 3.52

XV-5A AILERON DEFLECTION SCHEDULE

NOTE:
1. RIGID SYSTEM

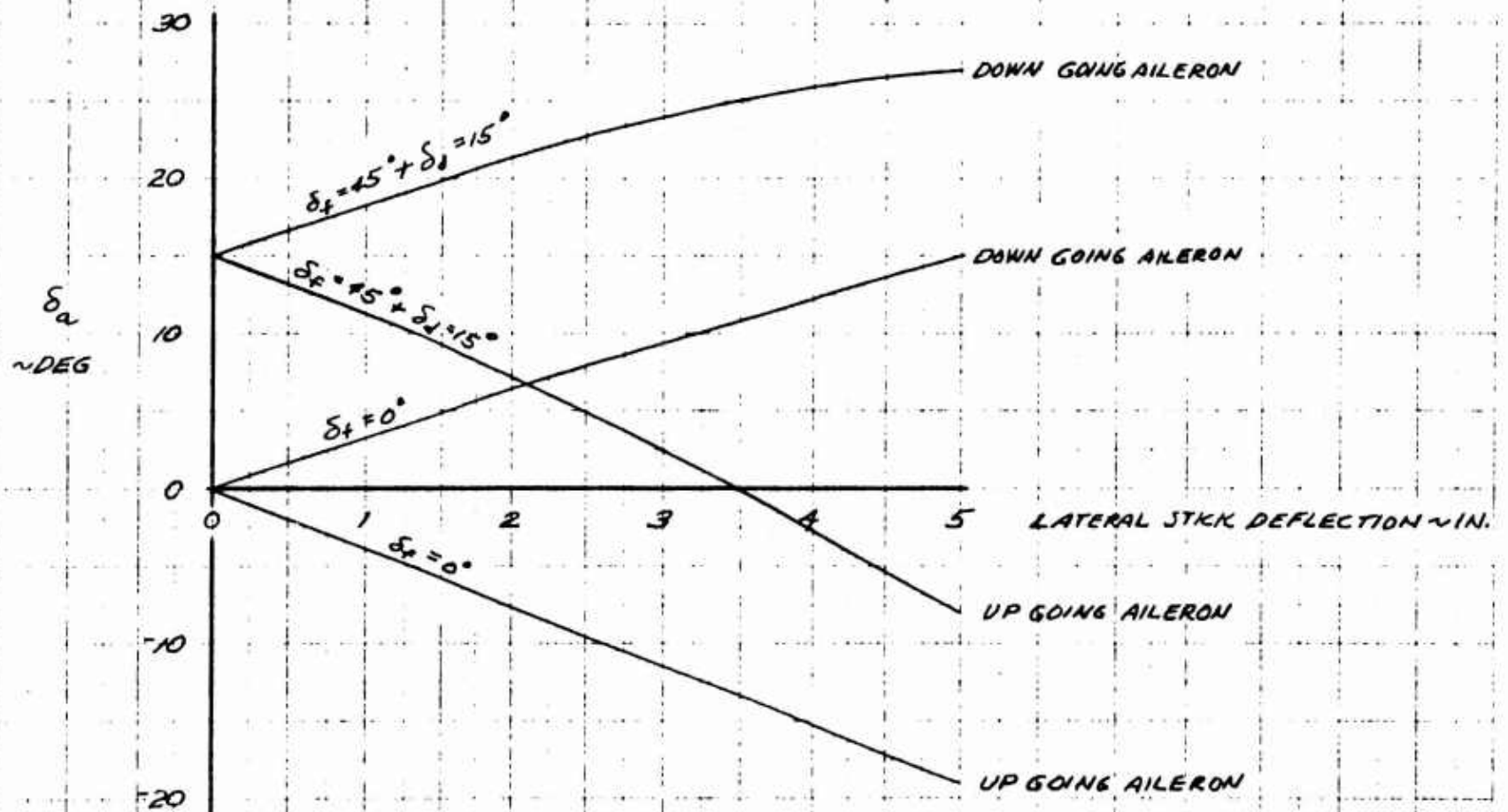


Figure 3.53

XV-5A AILERON DEFLECTION SCHEDULE

NOTE:
1. RIGID SYSTEM.

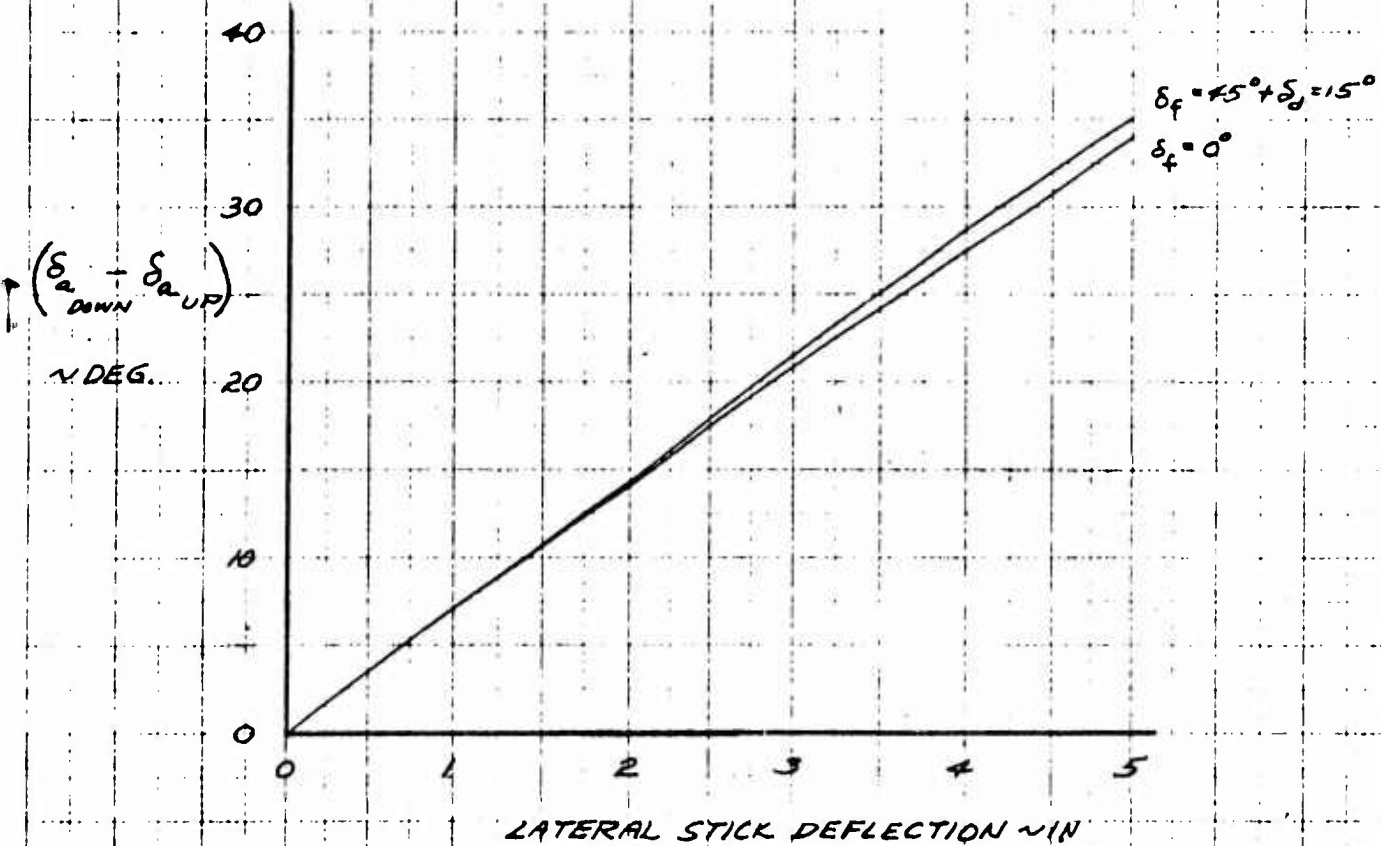


Figure 3.54

XV-5A
SIDE FORCE COEFFICIENT
DUE TO AILERON DEFLECTION

LOW SPEED

NOTE:

1. STABILITY AXES
2. POSITIVE AILERON DEFLECTION IS TRAILING EDGE DOWN
3. δ_a MEASURED WITH RESPECT TO THE WING CHORD PLANE

$$C_y = C_{y_{\delta_a}} (\delta_{a_L} - \delta_{a_R})$$

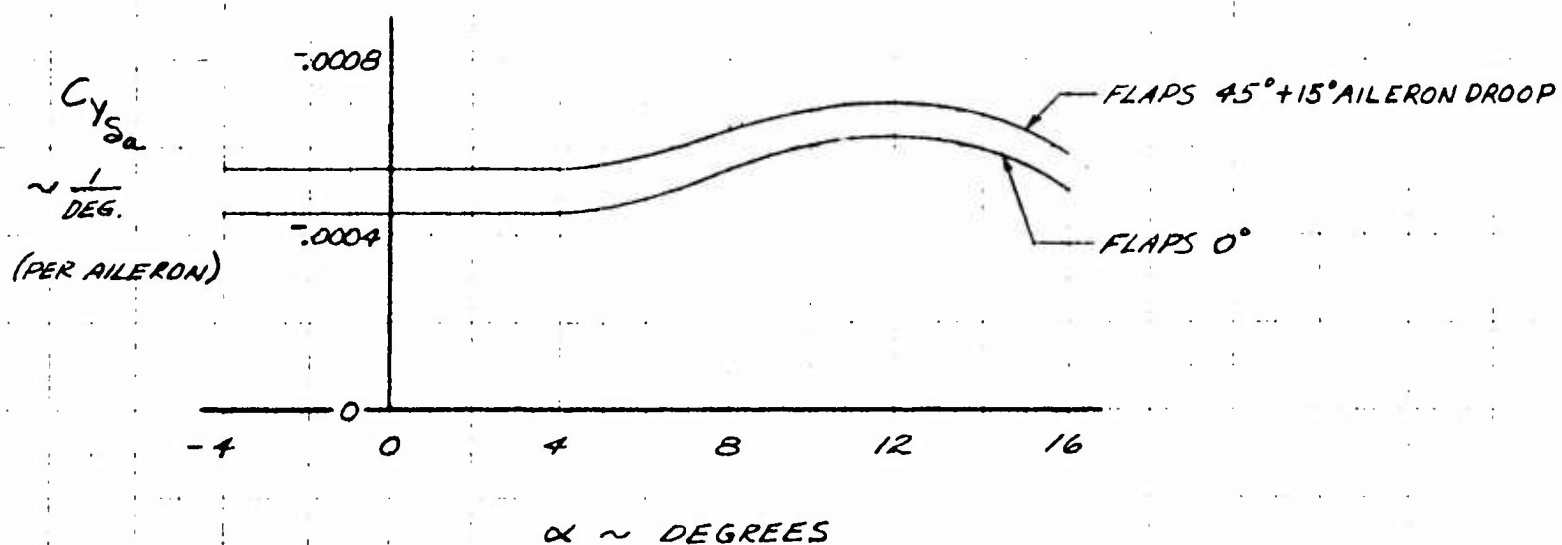


Figure 3.55

XV-5A
YAWING MOMENT COEFFICIENT
DUE TO AILERON DEFLECTION

LOW SPEED

NOTE:

1. FLAPS 45°+15°AILERON DROOP
2. STABILITY AXES
3. SIGN OF C_n IS FOR THE LEFT AILERON; FOR THE RIGHT AILERON REVERSE THE SIGN.
4. C.G. @ F.S. 246.0
5. δ_a MEASURED WITH RESPECT TO THE WING CHORD PLANE

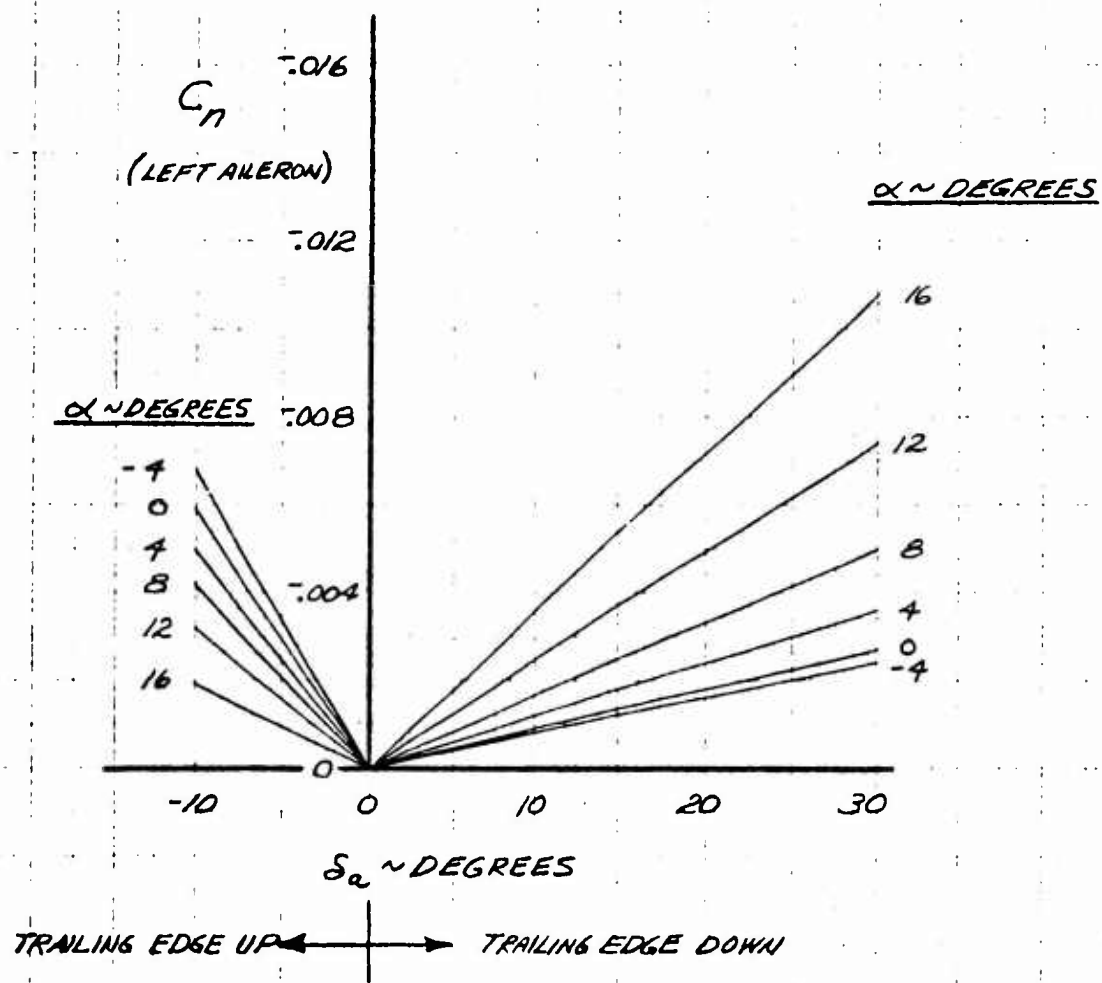


Figure 3.56

XV-5A

YAWING MOMENT COEFFICIENT DUE TO AILERON DEFLECTION, LOW SPEED

NOTE:

1. $\delta_4 = 45^\circ + \delta_4 = 15^\circ$
 2. RIGID DATA
 3. STABILITY AXES
 4. C.G. @ F.S. 246.0
 5. $C_n @ (\delta_4 - \delta_{4R}) = -C_n @ -(\delta_4 - \delta_{4R})$
 6. DATA VALID ONLY FOR DEFLECTION
- SCHEDULE SHOWN IN FIGS. 3.53 AND 3.54

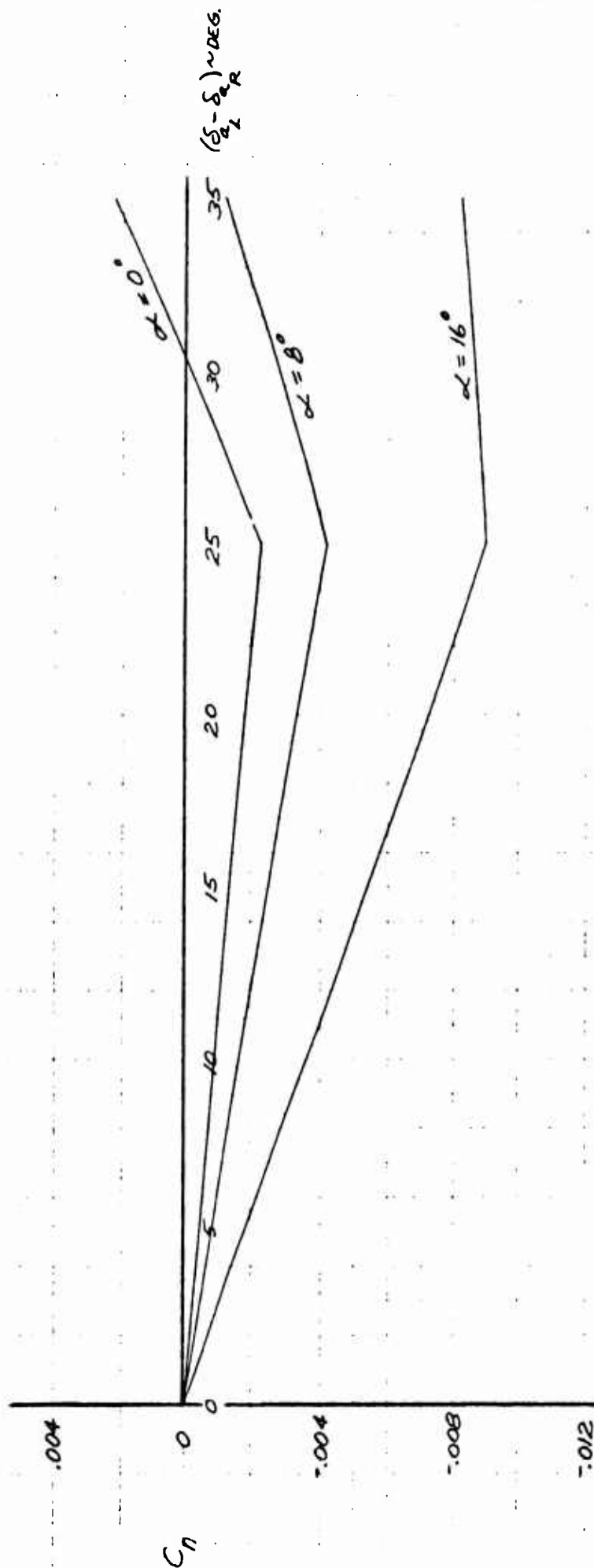


Figure 3.57

XV-5A
YAWING MOMENT COEFFICIENT
DUE TO AILERON DEFLECTION

LOW SPEED

NOTE:

1. RIGID DATA.
2. C.G. @ F.S. 246.0
3. STABILITY AXES
4. POSITIVE AILERON DEFLECTION IS TRAILING EDGE DOWN.
5. $\delta_f = 0^\circ$ BASED ON $\delta_{aL} = -\delta_{aR}$
6. $\delta_f = 45^\circ + \delta_d = 15^\circ$ VALID ONLY FOR THE DEFLECTION SCHEDULE SHOWN IN FIGS. 3.53 AND 3.54 AND FOR $|\delta_{aL} - \delta_{aR}| \leq 25^\circ$

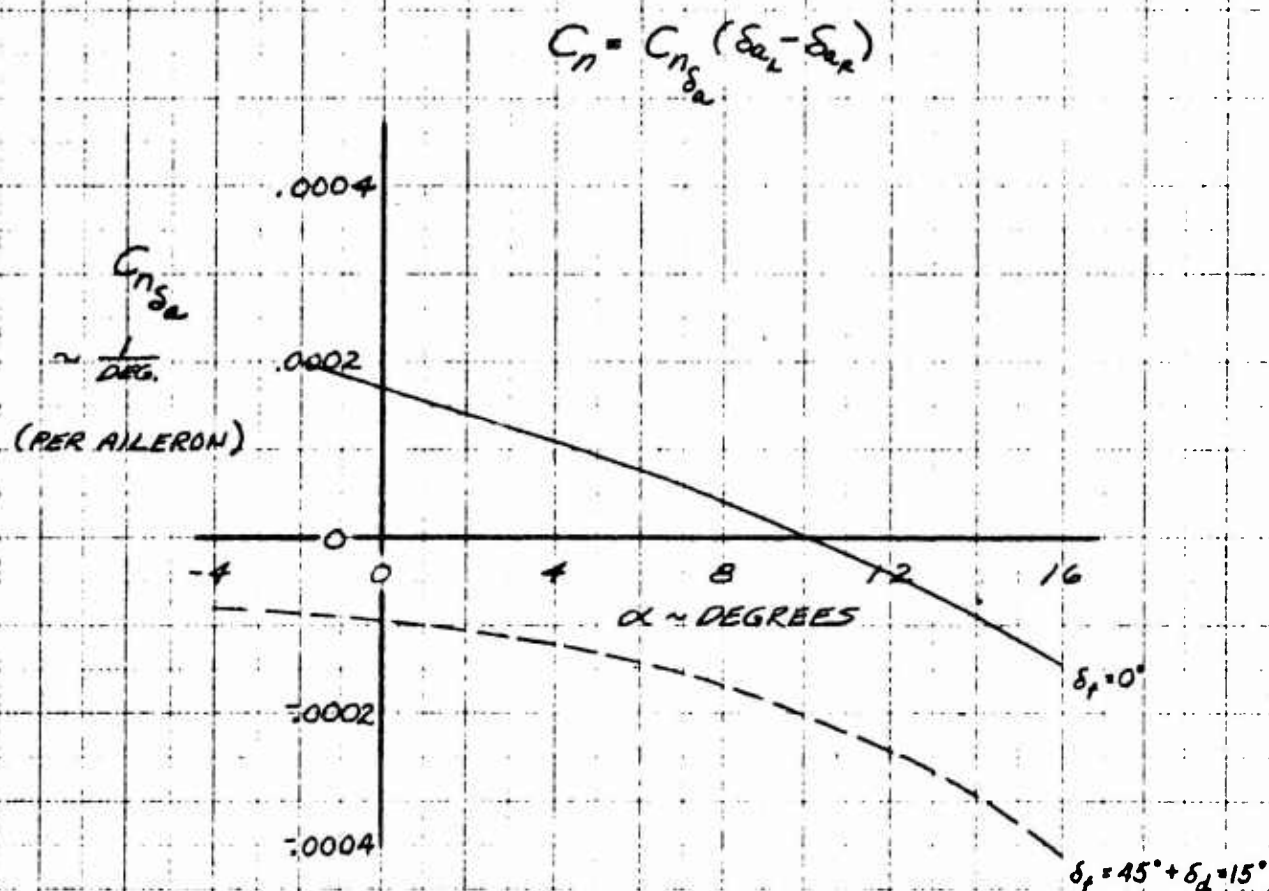


Figure 3.58

XV-5A
ROLLING MOMENT COEFFICIENT
DUE TO AILERON DEFLECTION

LOW SPEED

NOTE:

1. RIGID DATA
2. C.G. @ W.L. 112.0
3. STABILITY AXES
4. POSITIVE AILERON DEFLECTION IS TRAILING EDGE DOWN
5. ESTIMATED EFFECT OF AILERON TAB INCLUDED
6. $\delta_f = 0^\circ$ BASED ON $\delta_{aL} = -\delta_{aR}$ VALID TO $\delta_a = \pm 20^\circ$
7. $\delta_f = 45^\circ + \delta_d = 15^\circ$ VALID ONLY FOR THE DEFLECTION SCHEDULE SHOWN IN FIGS. 3.53 AND 3.54

$$C_l = C_{l_{\delta_a}} (\delta_{aL} - \delta_{aR})$$

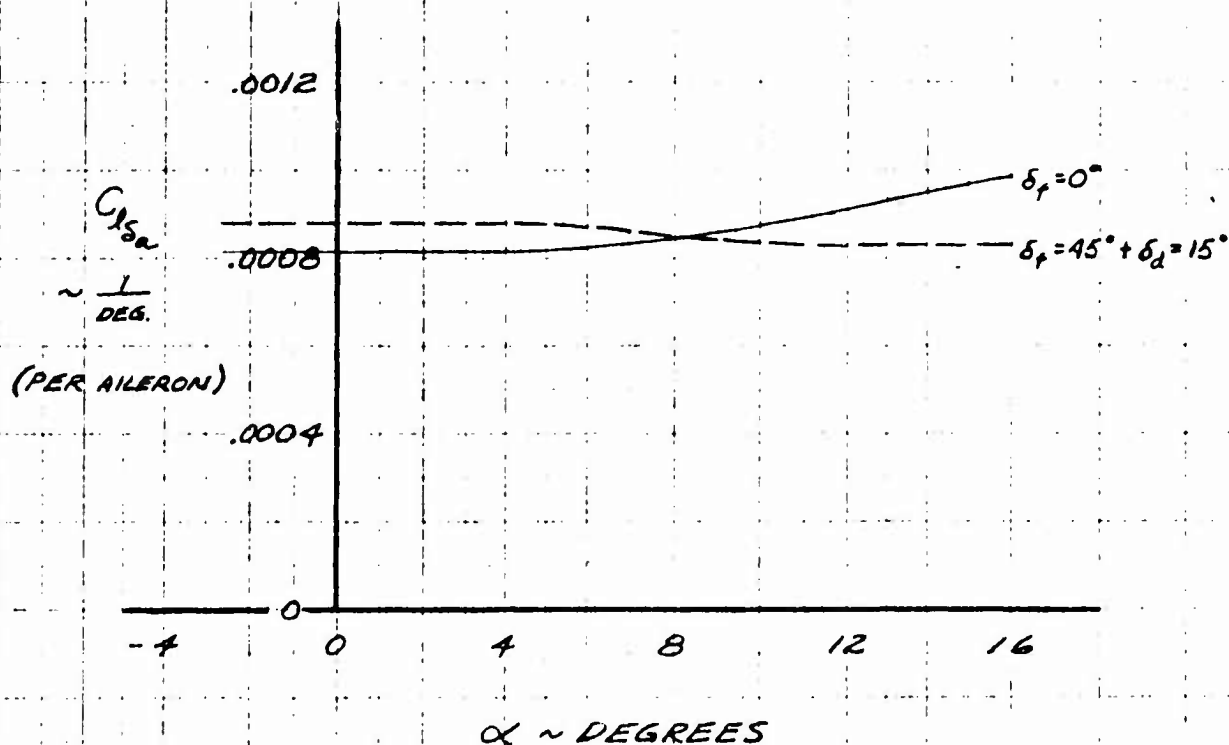


Figure 3.59

LOW SPEED

1. FLAPS $45^\circ + 15^\circ$ AILERON DROOP
2. C.G. @ W.L. 112.0
3. STABILITY AXES
4. ESTIMATED EFFECT OF AILERON TAB INCLUDED
5. SIGN OF C_L IS FOR THE LEFT AILERON; FOR THE RIGHT AILERON REVERSE THE SIGN.
6. δ_a MEASURED WITH RESPECT TO THE WING CHORD PLANE

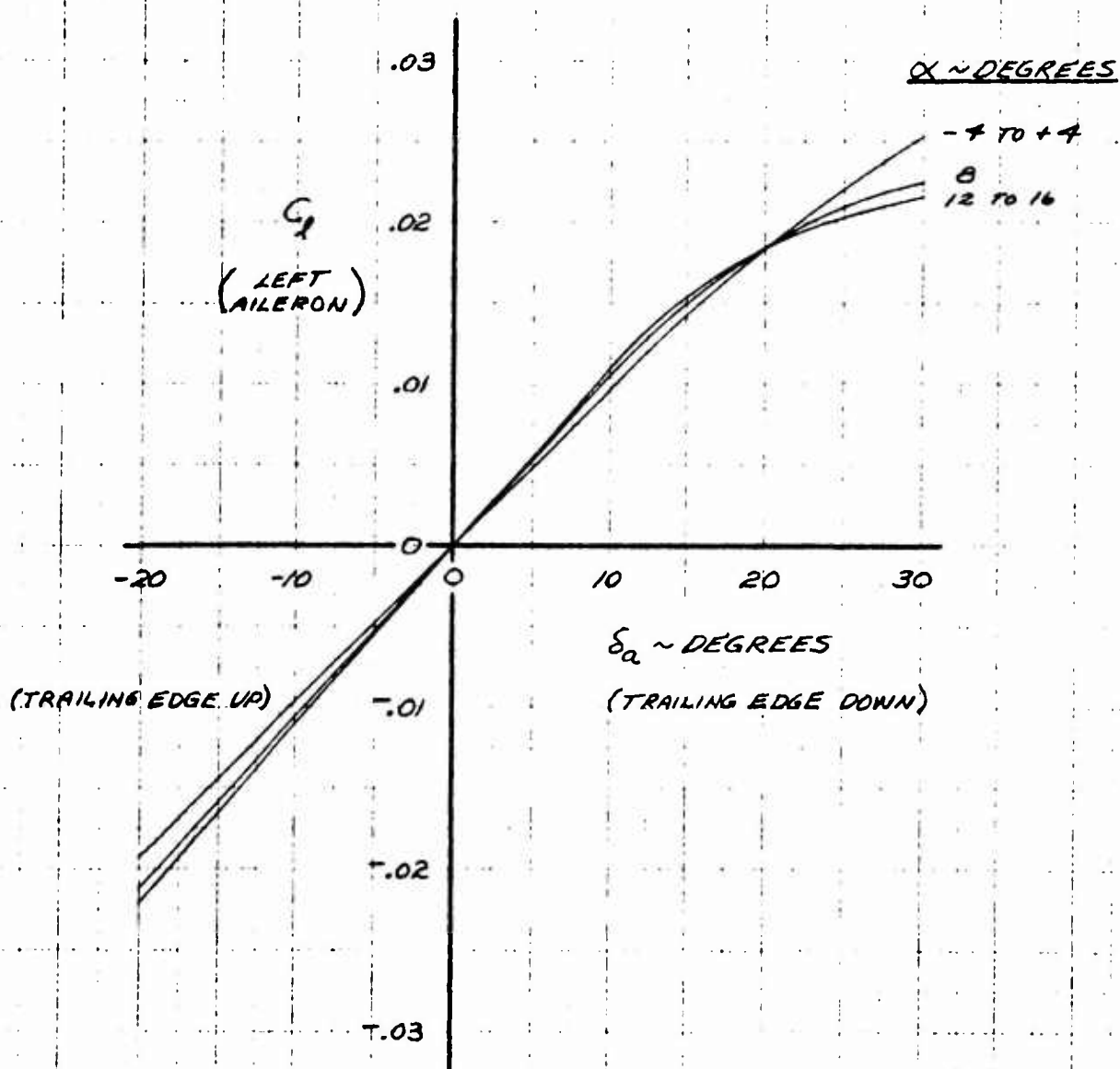


Figure 3.60

XV-5A
ELEVATOR EFFECTIVENESS PARAMETER, LOWSPEED

NOTE:

1. RIGID DATA
2. STABILITY AXES
3. $i_t = 0^\circ$

$$[\Delta C_m]_e = K_e [C_{m_{\delta_e}}]_{\alpha=0} \cdot \delta_e$$

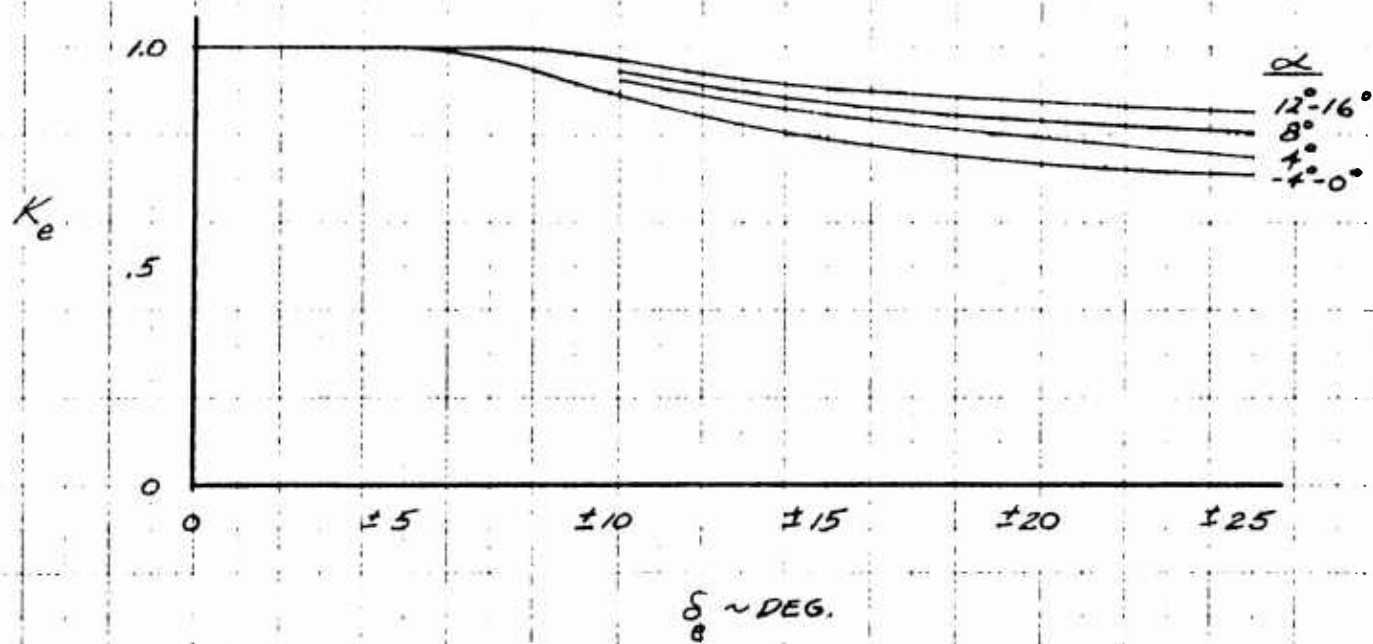


Figure 3.61

XV-5A

$C_{L\delta_e}$ vs. MACH NUMBER

NOTES:

1- RIGID DATA

2- FREE AIR

3- STABILITY AXES

4- $\delta_f = 0^\circ$

5- $S_{Y/S_0} = .203$

6- REFERENCE: 143

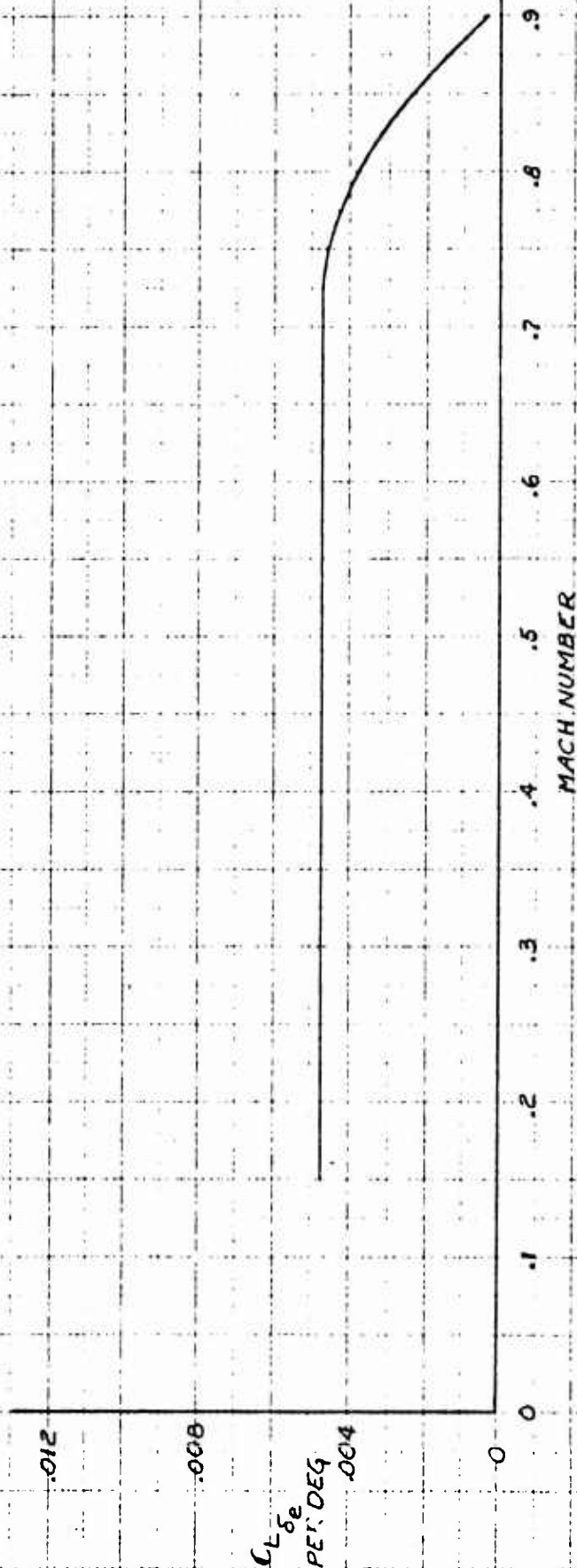


Figure 3.62

XV-5A
 $C_{m\delta_e}$ VS MACH. NUMBER.

NOTES:

- 1- RIGID DATA
- 2- FREE AIR
- 3- STABILITY AXES
- 4- C.G. @ FS. 240.0
- 5- $\delta_1 = 0^\circ$
- 6- $\delta_2/\delta_1 = .203$
- 7- REFERENCE: 143

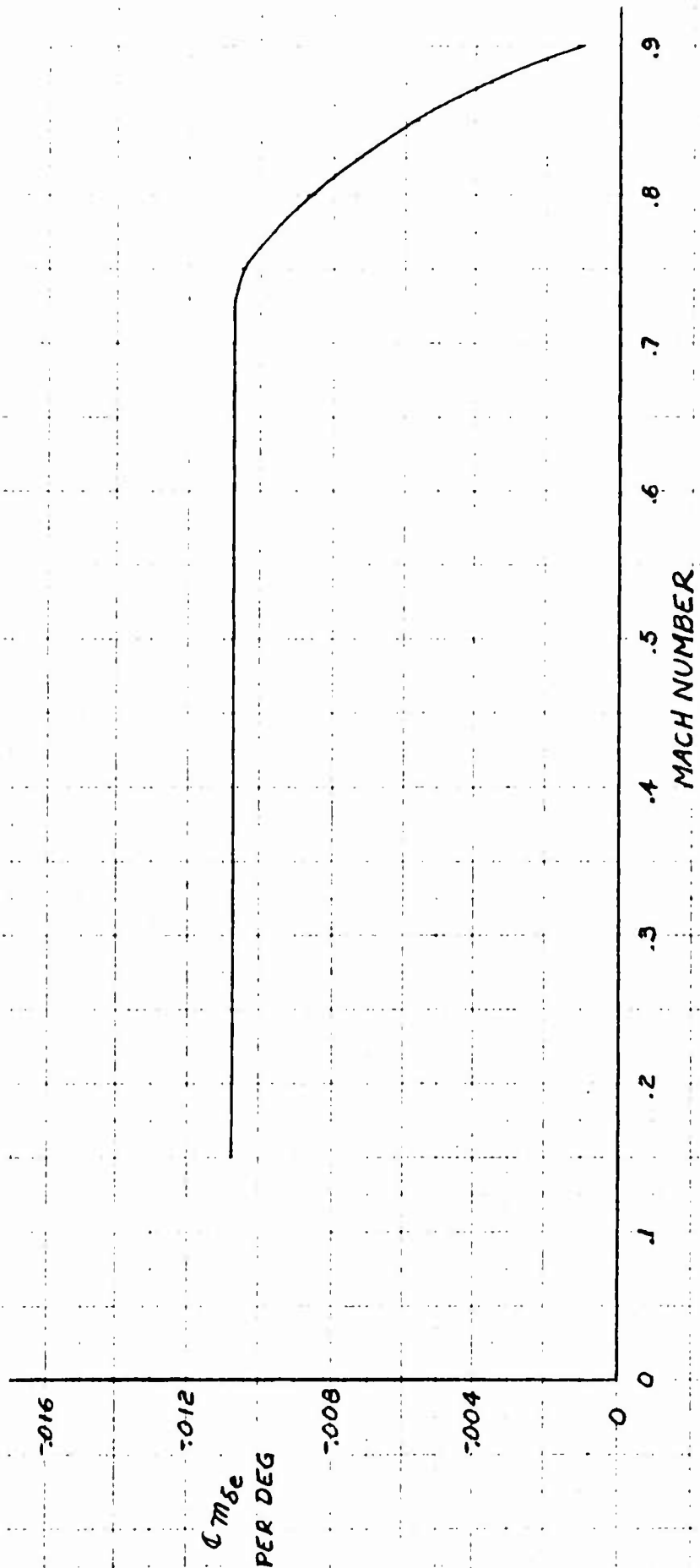


Figure 3.63

XV-5A

VS MACH NUMBER

Cm_{δ_e}

NOTES:

1- RIGID DATA

2- FREE AIR

3- STABILITY AXES

4- C.G. C.F.S. 246.0

5- $\delta_1 = 0^\circ$

6- $S_{\delta_1/S_2} = .203$

7- REFERENCE: 143

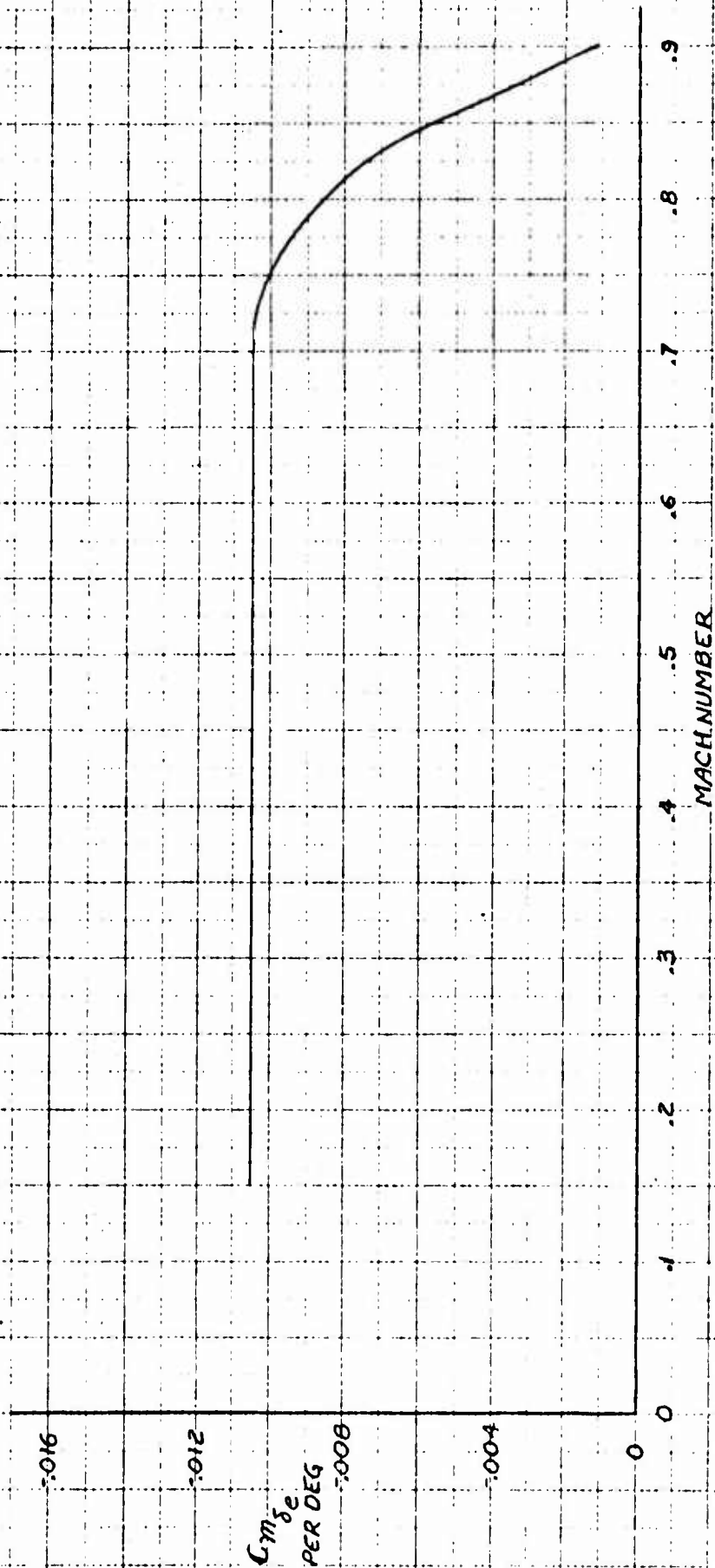


Figure 3.64

XV-5A
SIDE FORCE COEFFICIENT
DUE TO RUDDER DEFLECTION

HIGH SPEED

NOTE:

1. STABILITY AXES
2. POSITIVE RUDDER DEFLECTION
IS TRAILING EDGE LEFT.

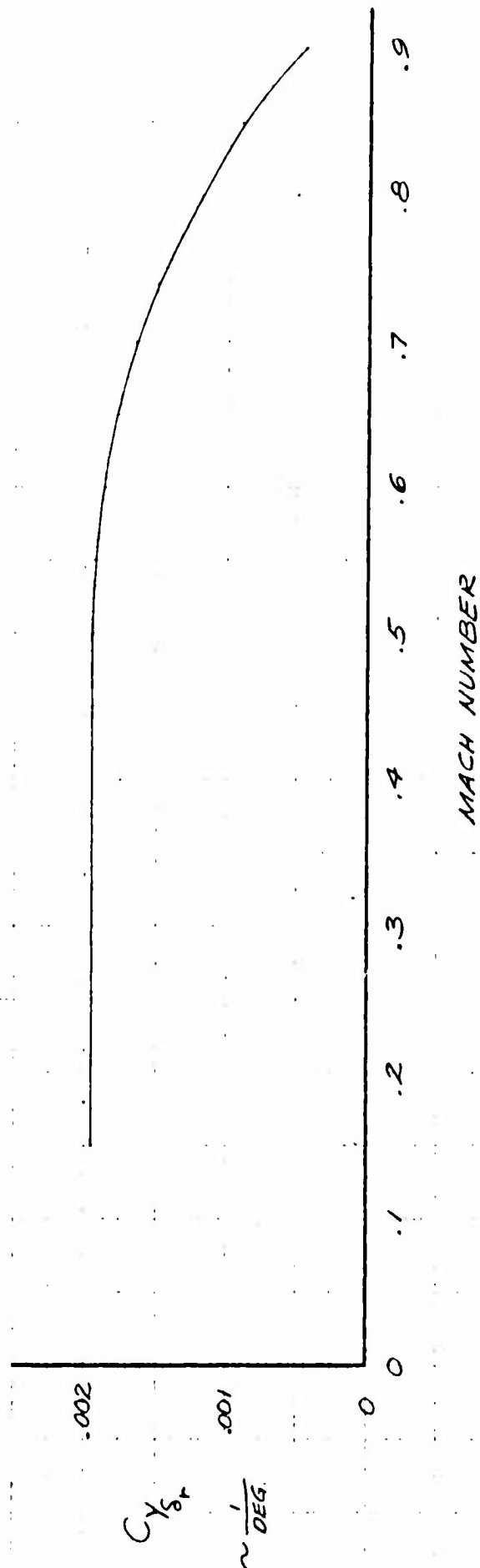


Figure 3.65

XV-5A
YAWING MOMENT COEFFICIENT
DUE TO RUDDER DEFLECTION

HIGH SPEED

NOTE:
 1. STABILITY AXES
 2. POSITIVE RUDDER DEFLECTION
 IS TRAILING EDGE LEFT
 3. LEGEND:
 — C.G. @ F.S. 246.0
 --- C.G. @ F.S. 240.0

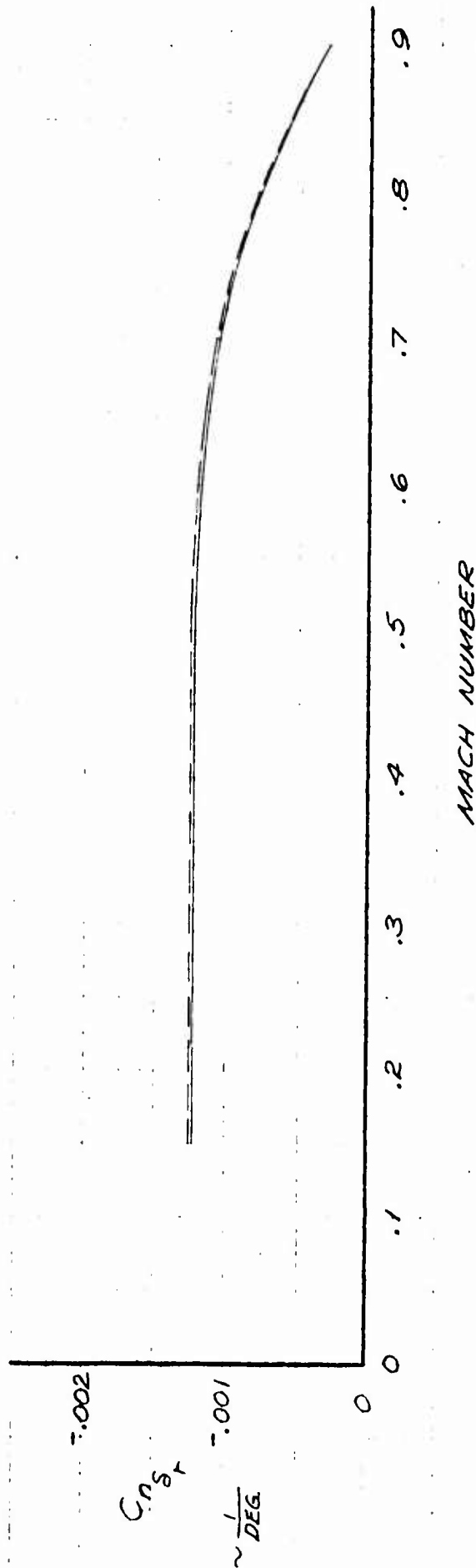


Figure 3.66

XV-5A
ROLLING MOMENT COEFFICIENT
DUE TO RUDDER DEFLECTION

HIGH SPEED

NOTE:
 1. STABILITY AXES
 2. POSITIVE RUDDER DEFLECTION
 IS TRAILING EDGE LEFT
 3. C.G. @ F.S. 240.0 - 296.0
 W.L. 112.0

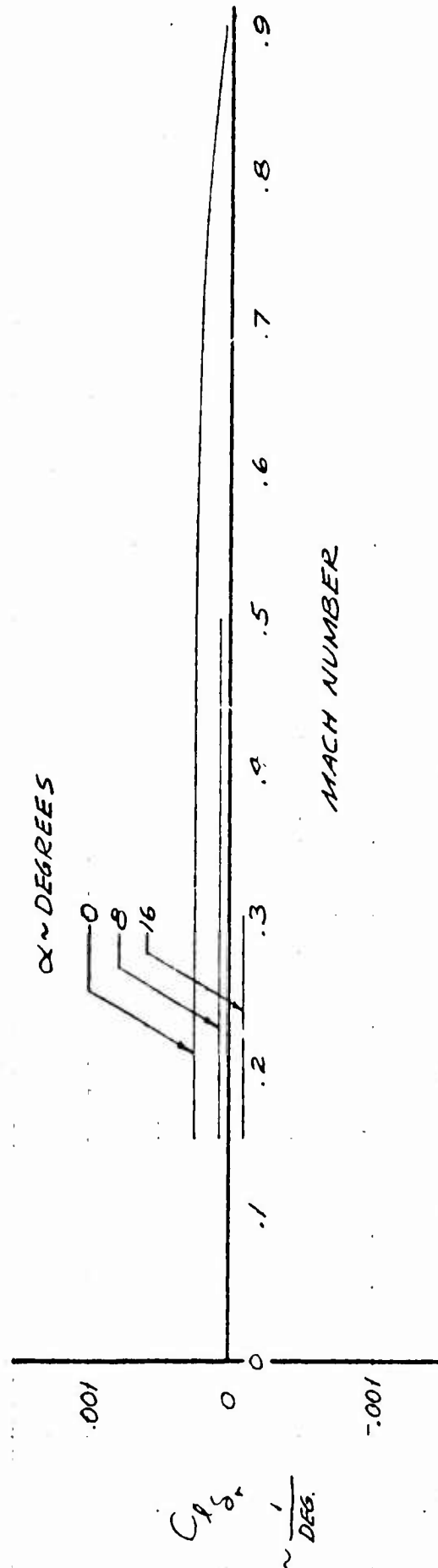


Figure 3.67

XV-5A
SIDE FORCE COEFFICIENT
DUE TO AILERON DEFLECTION

HIGH SPEED

NOTE:
 1. FLAPS UP
 2. STABILITY AXES
 3. POSITIVE AILERON DEFLECTION
 IS TRAILING EDGE DOWN

$$C_Y = C_{Y_{\delta_a}} (\delta_a - \delta_{a_e})$$

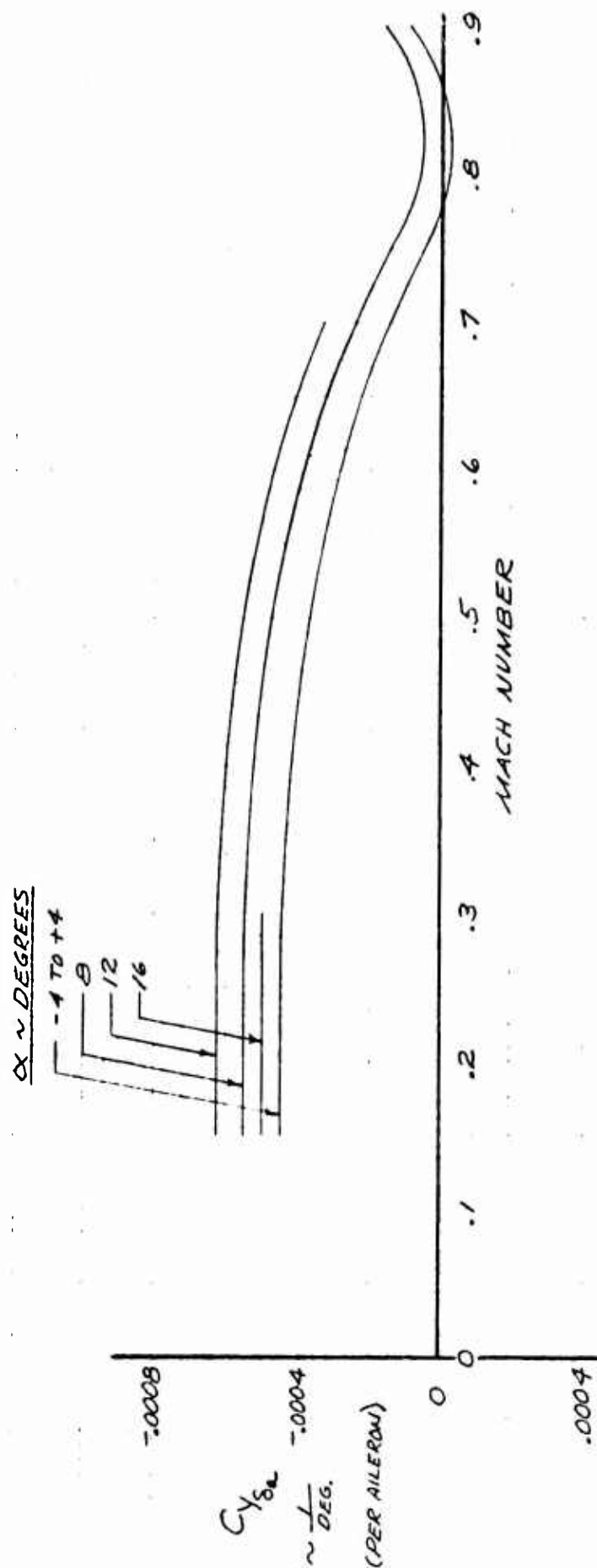


Figure 3.68

XV-5A

YAWING MOMENT COEFFICIENT
DUE TO AILERON DEFLECTION

HIGH SPEED

NOTE:

1. FLAPS UP
2. C.G. @ F.S. 246.0
3. STABILITY AXES
4. POSITIVE AILERON DEFLECTION
IS TRAILING EDGE DOWN

$$C_n = C_{n_{\delta_a}} (\delta_{a_L} - \delta_{a_R})$$

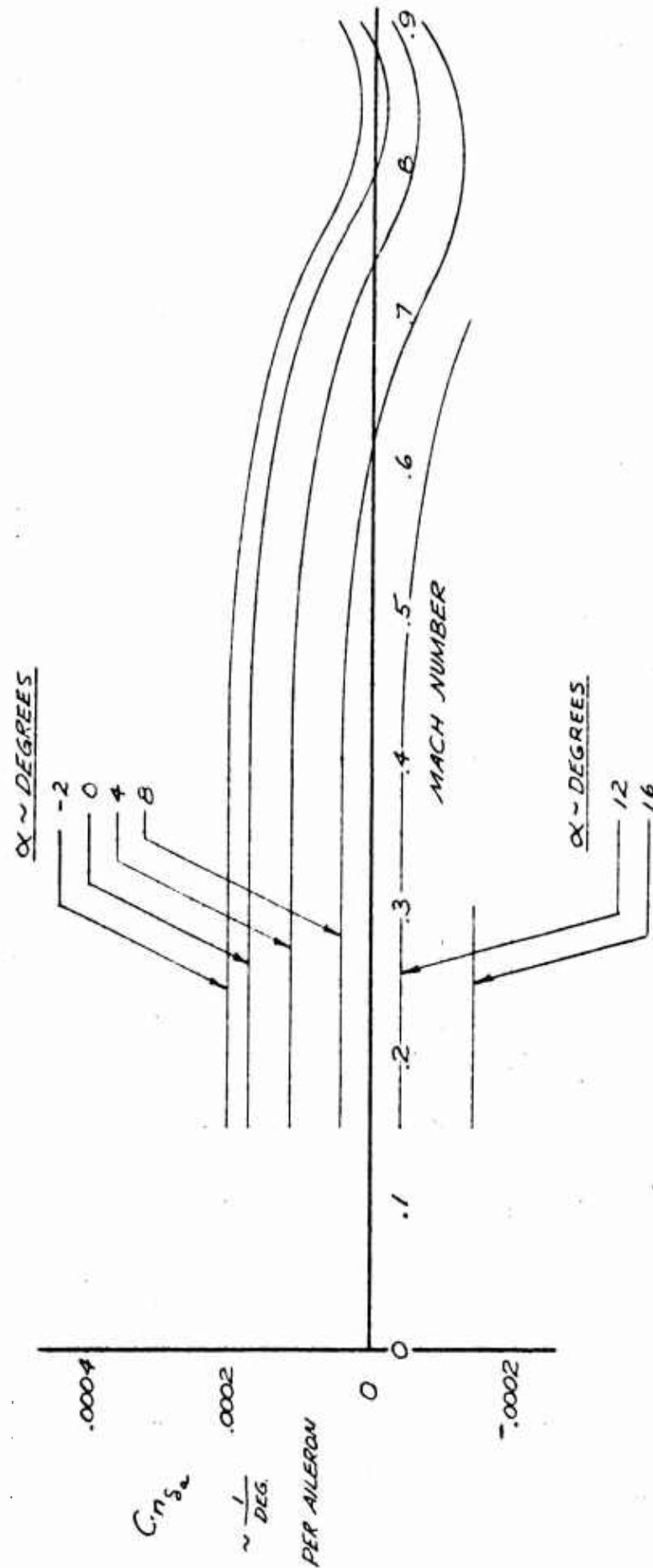


Figure 3.69

XV-5A
ROLLING MOMENT COEFFICIENT
DUE TO AILERON DEFLECTION

HIGH SPEED

NOTE:

1. FLAPS UP
2. C.G. @ W.L. 112.0
AND F.S. 246.0-240.0
3. STABILITY AXES
4. POSITIVE AILERON DEFLECTION
IS TRAILING EDGE DOWN.
5. ESTIMATED EFFECT OF
AILERON TAB INCLUDED

$$C_l = C_{l_{\delta_a}} (\delta_a - \delta_{a2})$$

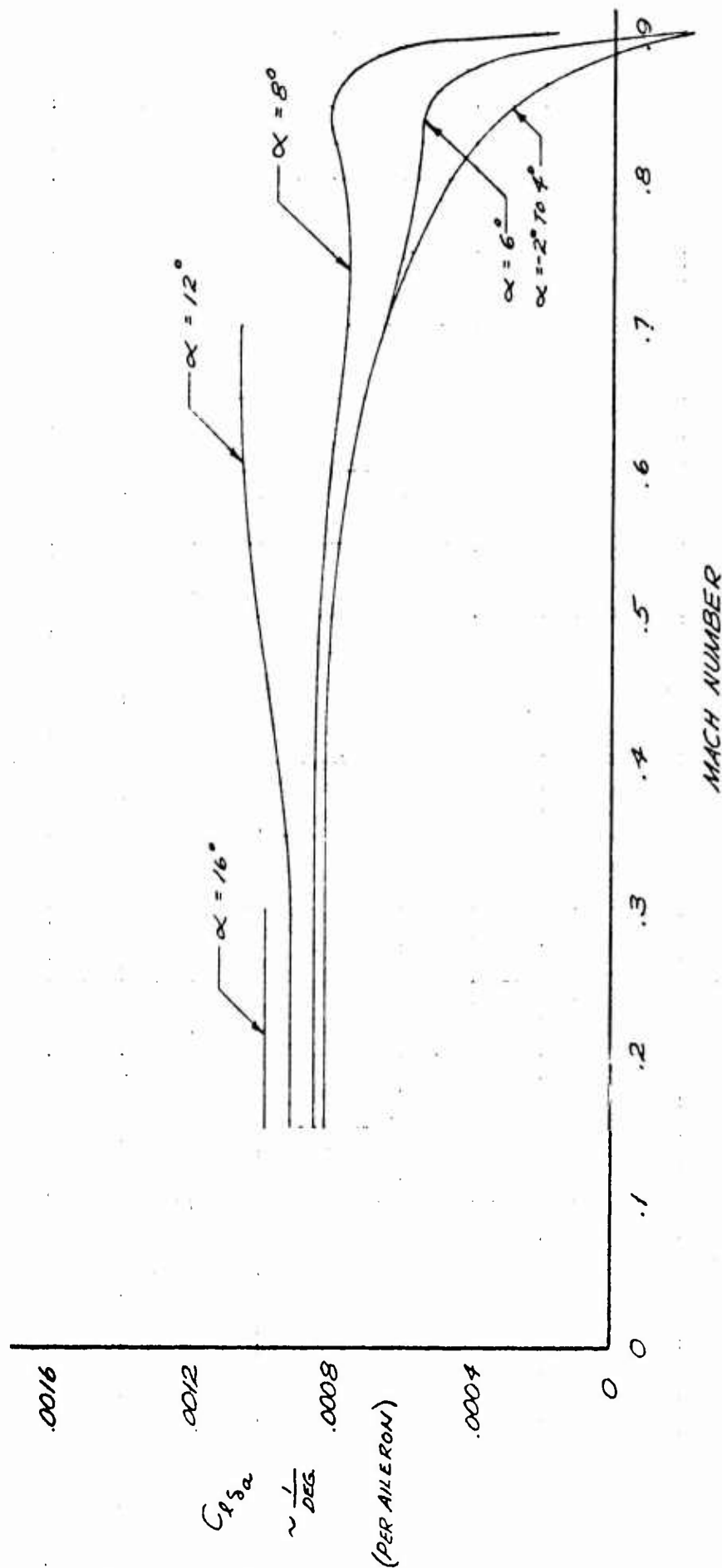


Figure 3.70

XV-5A
LOW SPEED C_{he} Vs δ_e
(BALANCED)

NOTES:

- 1- $\alpha_e = 0^\circ$
- 2- HINGE MOMENT IS BALANCED
- 3- RIGID DATA
- 4- FREE AIR
- 5- REF. $S_e = 11.970 \text{ FT}^2$ (TOTAL), $\bar{c}_e = 1.112 \text{ FT}$
- 6- REFERENCE: 1
- 7- INTERNALLY SEALED PRESSURE BALANCE
- 8- $(C_{he})_{\delta_e = \delta_{e1}} = - (C_{he})_{\delta_e = -\delta_{e1}}$

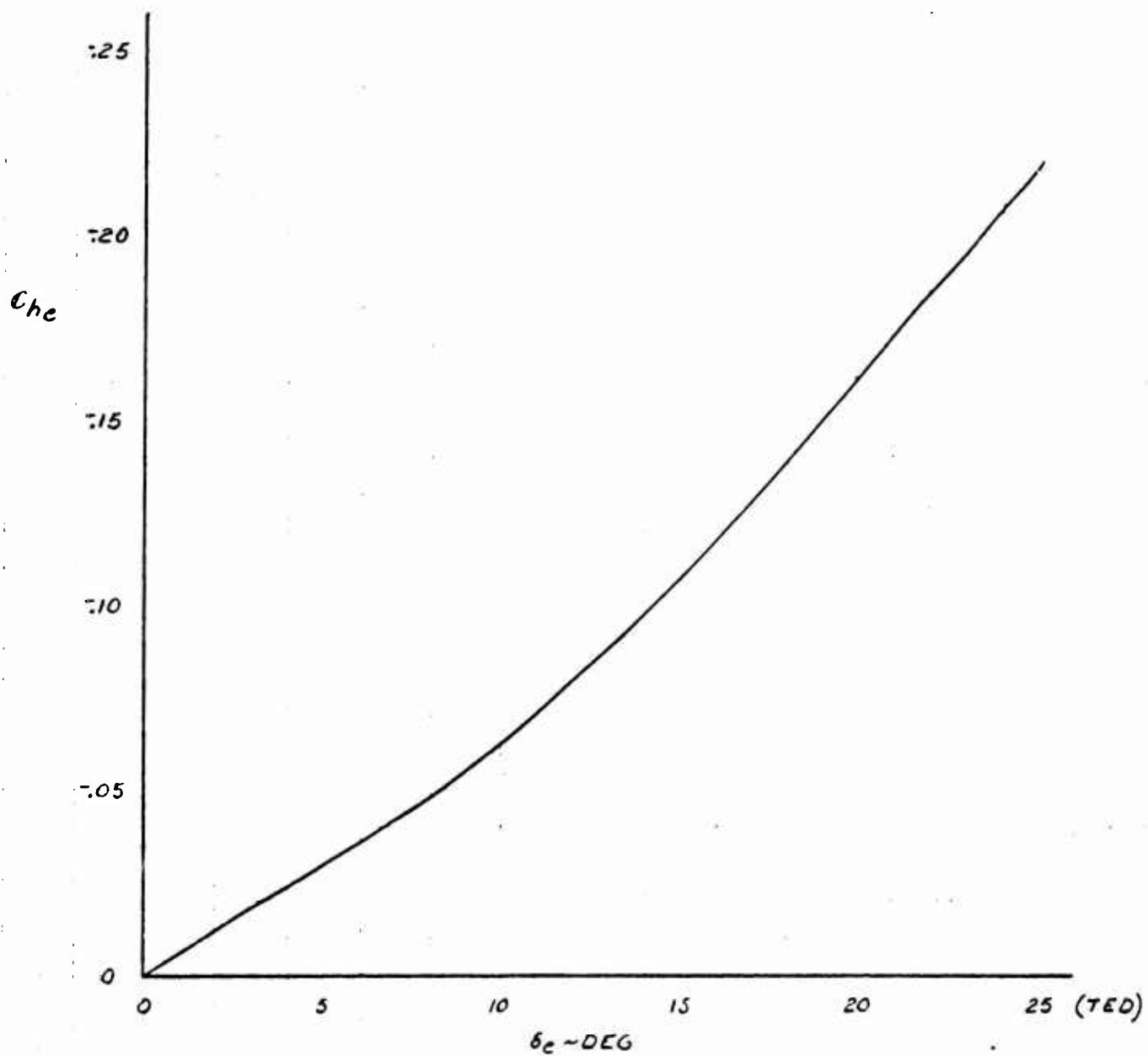


Figure 3.71

XV-5A
LOW SPEED C_{he} Vs α_e
(BALANCED)

NOTES:

- 1- $\delta_e = 0^\circ$
- 2- HINGE MOMENT IS BALANCED
- 3- RIGID DATA
- 4- FREE AIR
- 5- REF, $S_e = 11.970 \text{ FT}^2$ (TOTAL), $\bar{z}_e = 1.112 \text{ FT}$
- 6- REFERENCE: 1
- 7- INTERNALLY SEALED PRESSURE BALANCE

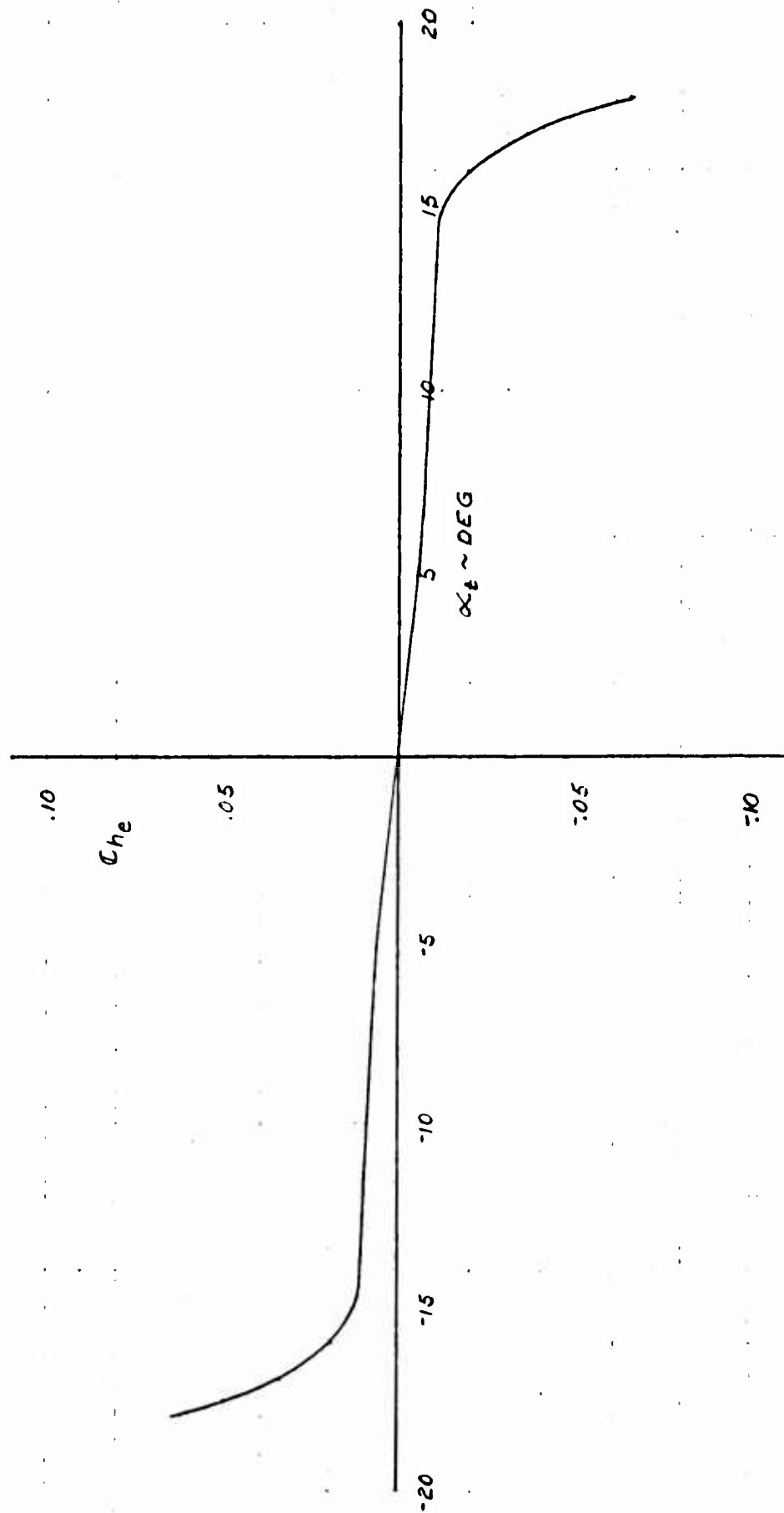


Figure 3.72

XV-5A
 LOW SPEED C_{he} VS α_e OR δ_e
 (UNBALANCED)

NOTES

1-HINGE MOMENT IS UNBALANCED

2-RIGID DATA

3-FREE AIR

4-REF, $S_e = 11.970 \text{ FT}^2$ (TOTAL), $\bar{c}_e = 1.112 \text{ FT}$

5-REFERENCE: 1

6- $(C_{he})_{\alpha_e = \alpha_{e1}, \delta_e = \delta_{e1}} = -(C_{he})_{\alpha_e = -\alpha_{e1}, \delta_e = -\delta_{e1}}$

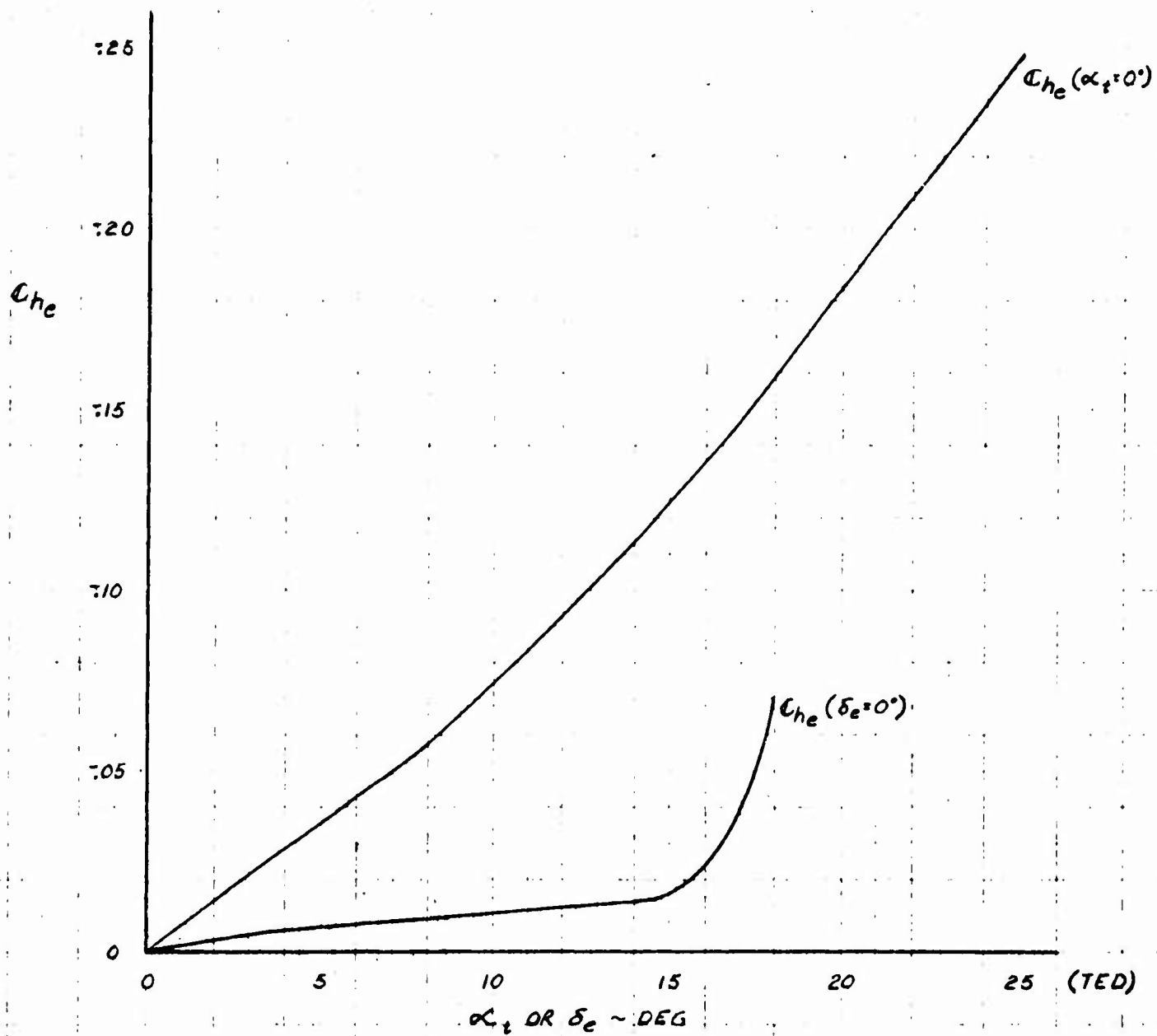


Figure 3.73

XV-5A
LOW SPEED C_{hr} VS δ_r (BALANCED)

NOTES:

- 1- $\beta = 0^\circ$
- 2- HINGE MOMENT IS BALANCED
- 3- NO TAB INCLUDED
- 4- RIGID DATA
- 5- REF. $S_r = 6.395 \text{ FT}^2$, $\bar{c}_r = 1.245 \text{ FT}$
- 6- INTERNALLY SEALED PRESSURE
BALANCE
- 7- $(C_{hr})_{\delta_r = \delta_{r1}} = -(C_{hr})_{\delta_r = -\delta_{r1}}$
- 8- REFERENCE: 1

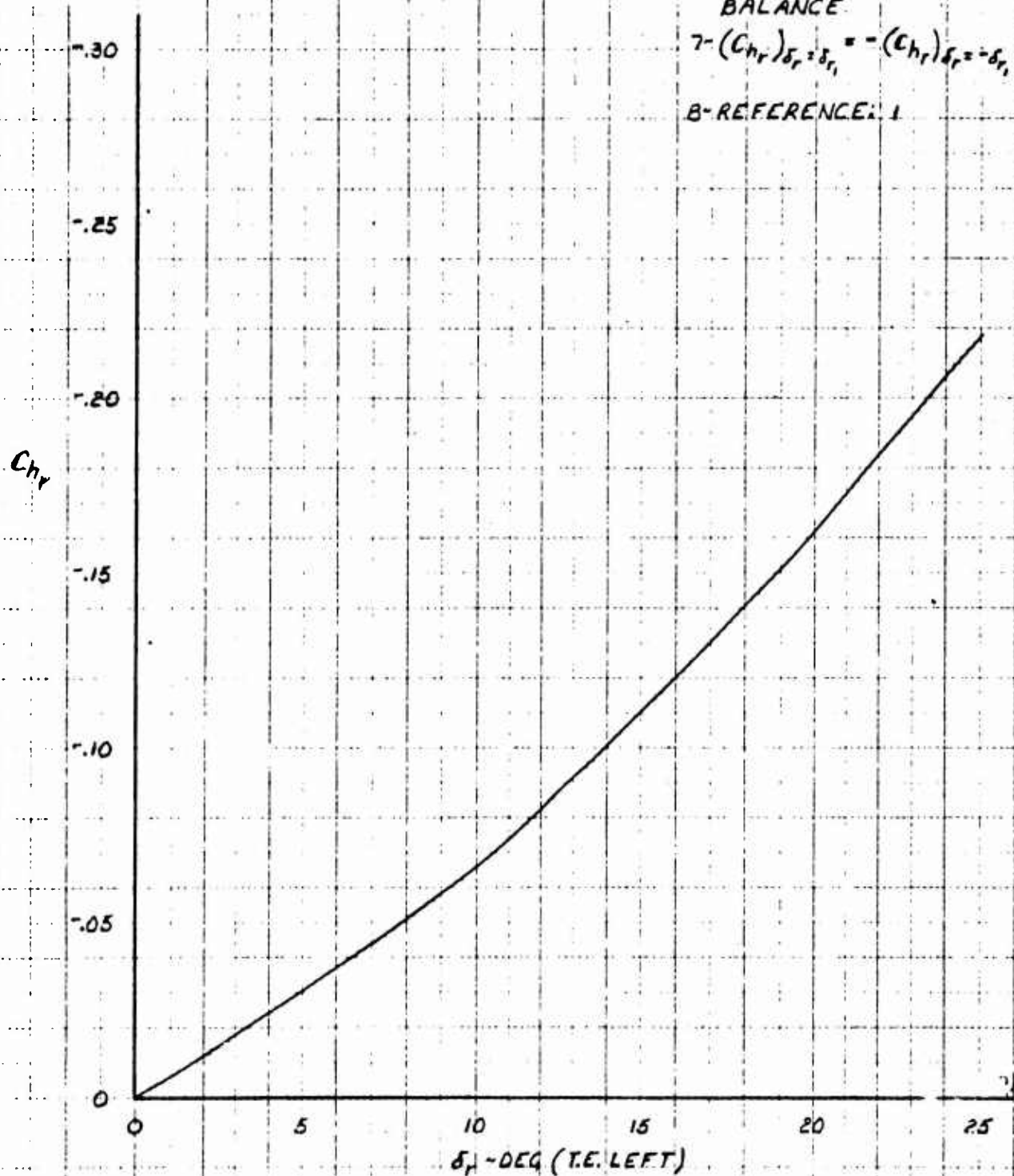


Figure 3.74

XV-5A
LOW SPEED C_{hr} VS β
(BALANCED)

NOTES

- 1- $\delta_r = 0^\circ$
- 2-HINGE MOMENT IS BALANCED
- 3-NO TAB INCLUDED
- 4-RIGID DATA
- 5-REF. $S_r = 6.395 \text{ FT}^2$, $\bar{z}_r = 1.245 \text{ FT}$
- 6-INTERNALLY SEALED PRESSURE BALANCE.
- 7-REFERENCE: 1

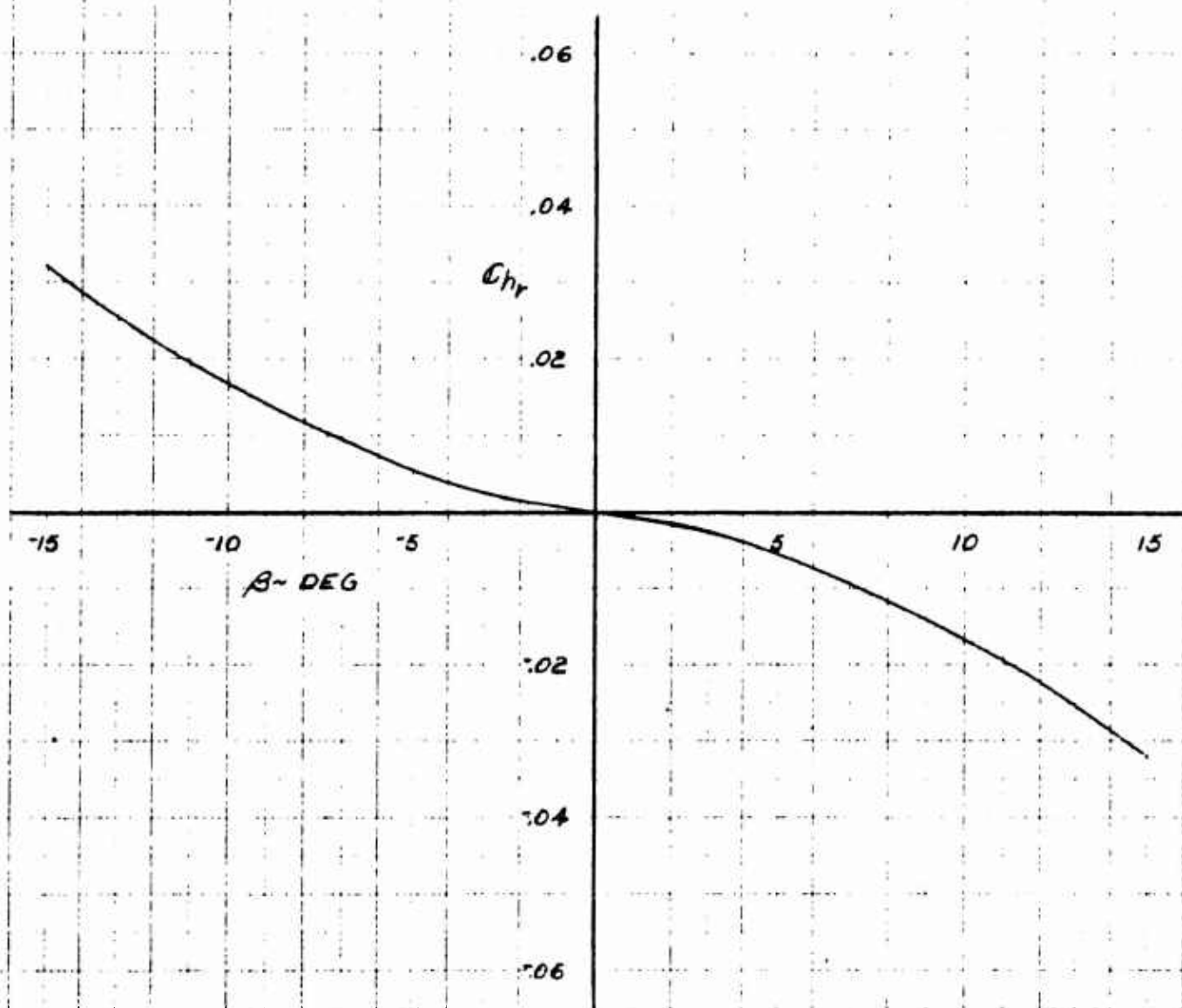


Figure 3.75

XV-5A
LOW SPEED C_{hr} Vs β OR δ_r
(UNBALANCED)

NOTES

1-HINGE MOMENT IS UNBALANCED

2-NO TAB INCLUDED

3-RIGID DATA

4-REF, $S_r = 6.395 \text{ FT}^2$, $\bar{z} = 1.245 \text{ FT}$

5- $(C_{hr})_{\beta=\beta_1, \delta_r=\delta_{r1}} = -(C_{hr})_{\beta=-\beta_1, \delta_r=-\delta_{r1}}$

6-REFERENCE: 1

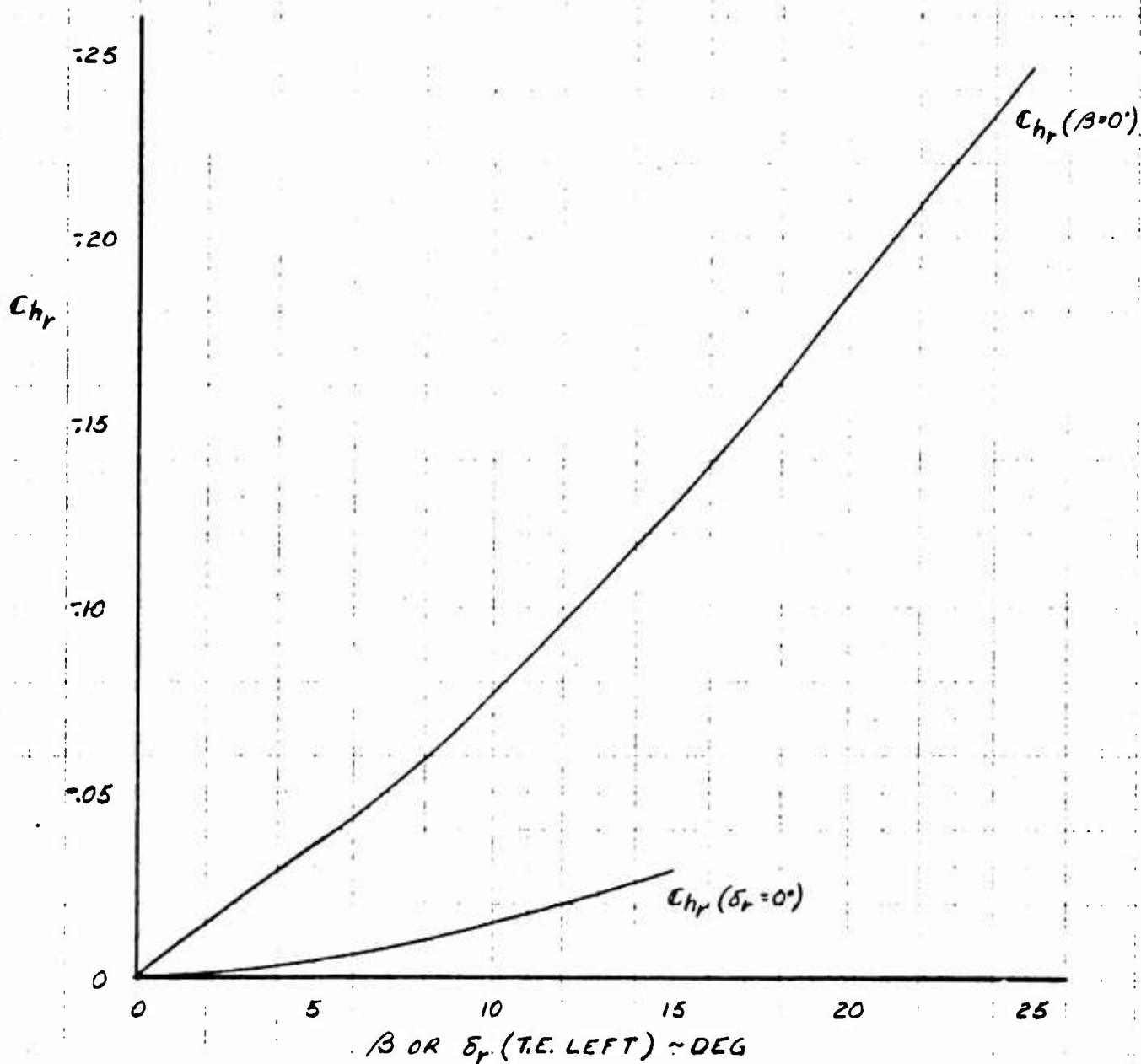


Figure 3.76

XV-5A

C_{ha} vs δ_a

LOW SPEED

NOTE:

1. RIGID DATA
2. $\alpha \approx 0$
3. REFERENCE DIMENSIONS:
 $S_a = 10.057 \text{ FT.}^2$ (AFT OF H , PER SIDE)
 $\bar{C}_a = 1.582 \text{ FT.}$
4. INTERNAL, SEALED PRESSURE BALANCE
5. $(C_{ha})_{\delta_a} = \delta_a^* - (C_{ha})_{\delta_a^*} - \delta_a$

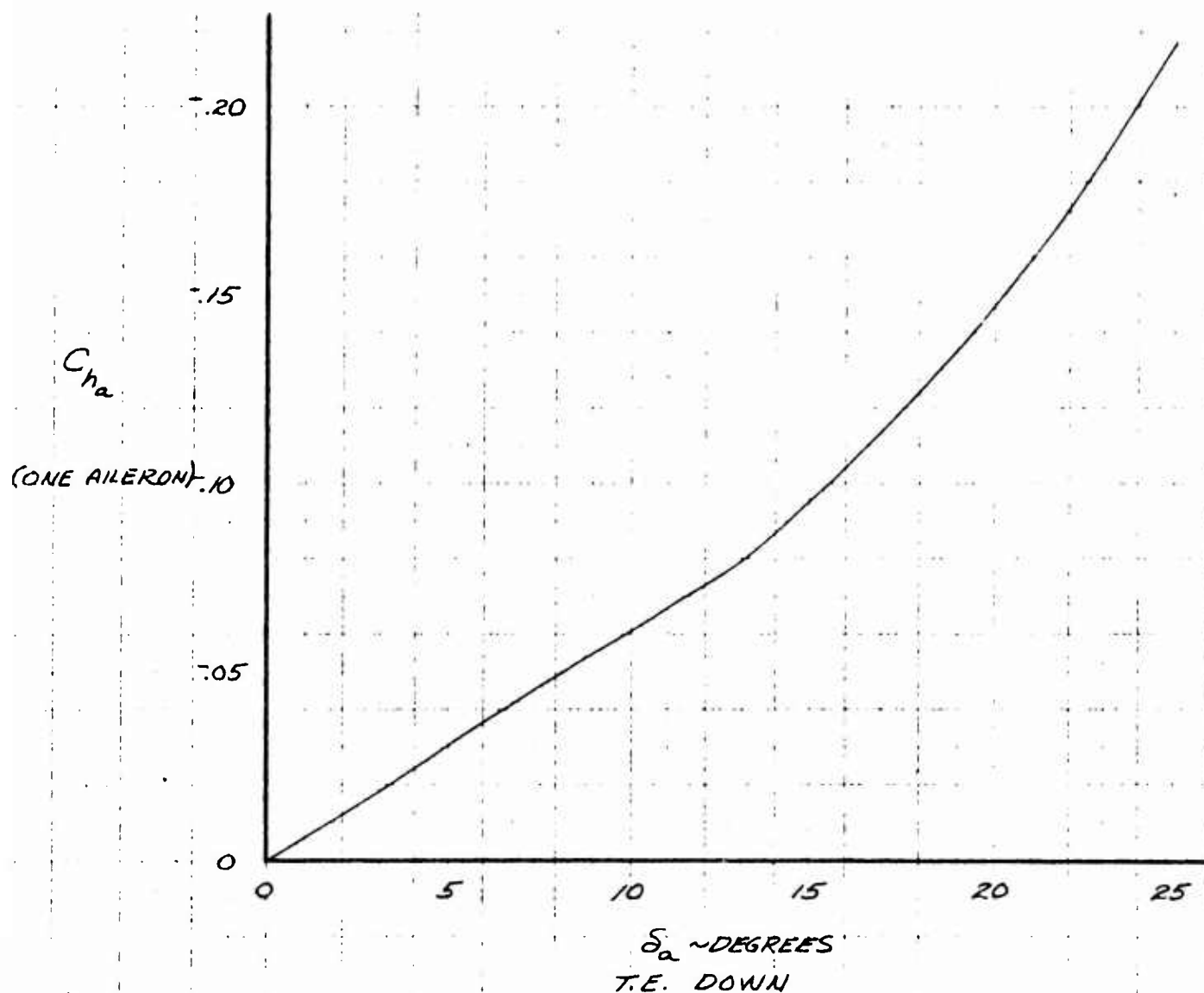


Figure 3.77

XV-5A
LOW SPEED C_{ha} VS α_w
(BALANCED)

NOTES:

- 1- $\delta_a = 0^\circ$
- 2-HINGE MOMENT IS BALANCED
- 3-RIGID DATA
- 4-FREE AIR
- 5-REF, $S_a = 10.057 \text{ FT}^2$ (PER SIDE, INCLUDING TAB), $\bar{c}_a = 1.582 \text{ FT}$
- 6-INTERNALLY SEALED PRESSURE BALANCE

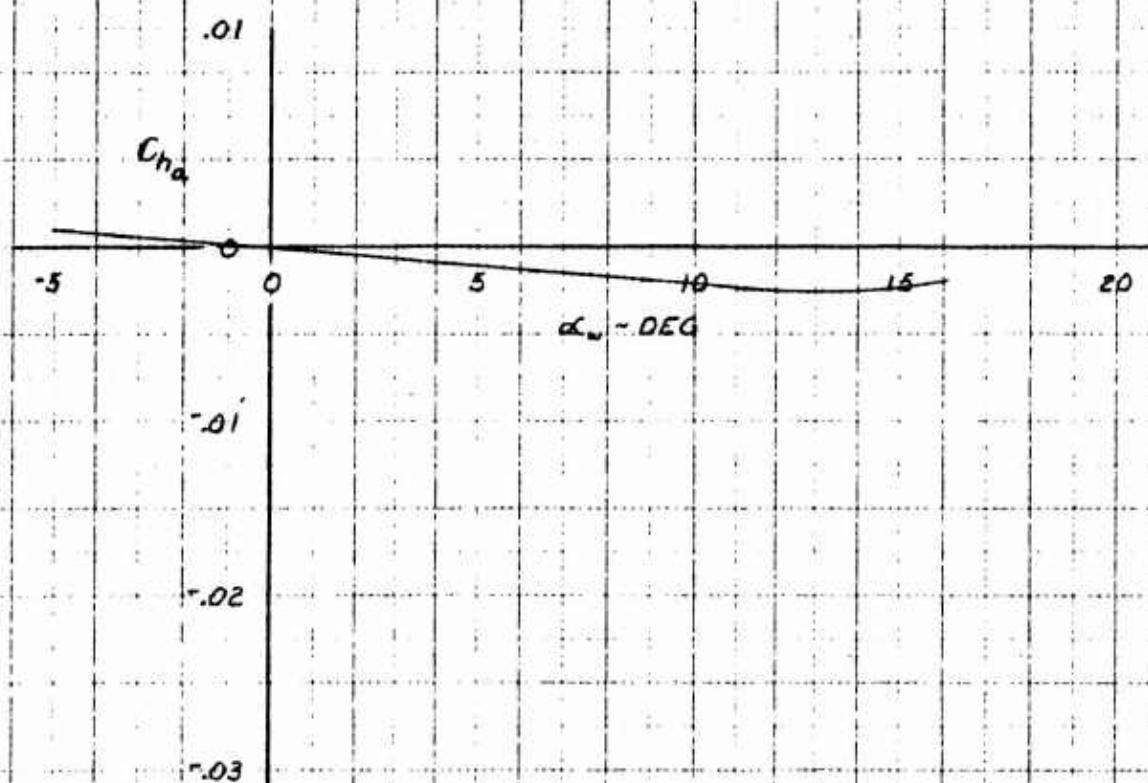


Figure 3.78

XV-5A
 LOW SPEED C_{ha} Vs α_w OR δ_a
 (UNBALANCED)

NOTES:

- 1- HINGE MOMENT IS UNBALANCED
- 2- RIGID DATA
- 3- FREE AIR
- 4- REF, $S_a = 10.057 \text{ FT}^2$ (PER SIDE, INCLUDING TAB), $\bar{c}_a = 1.582$
- 5- REFERENCE: 1
- 6- $(C_{ha})_{\alpha_w = \alpha_{w1}} = -(C_{ha})_{\alpha_w = -\alpha_{w1}}$
 $\delta_a = \delta_{a1}$ $\delta_a = -\delta_{a1}$

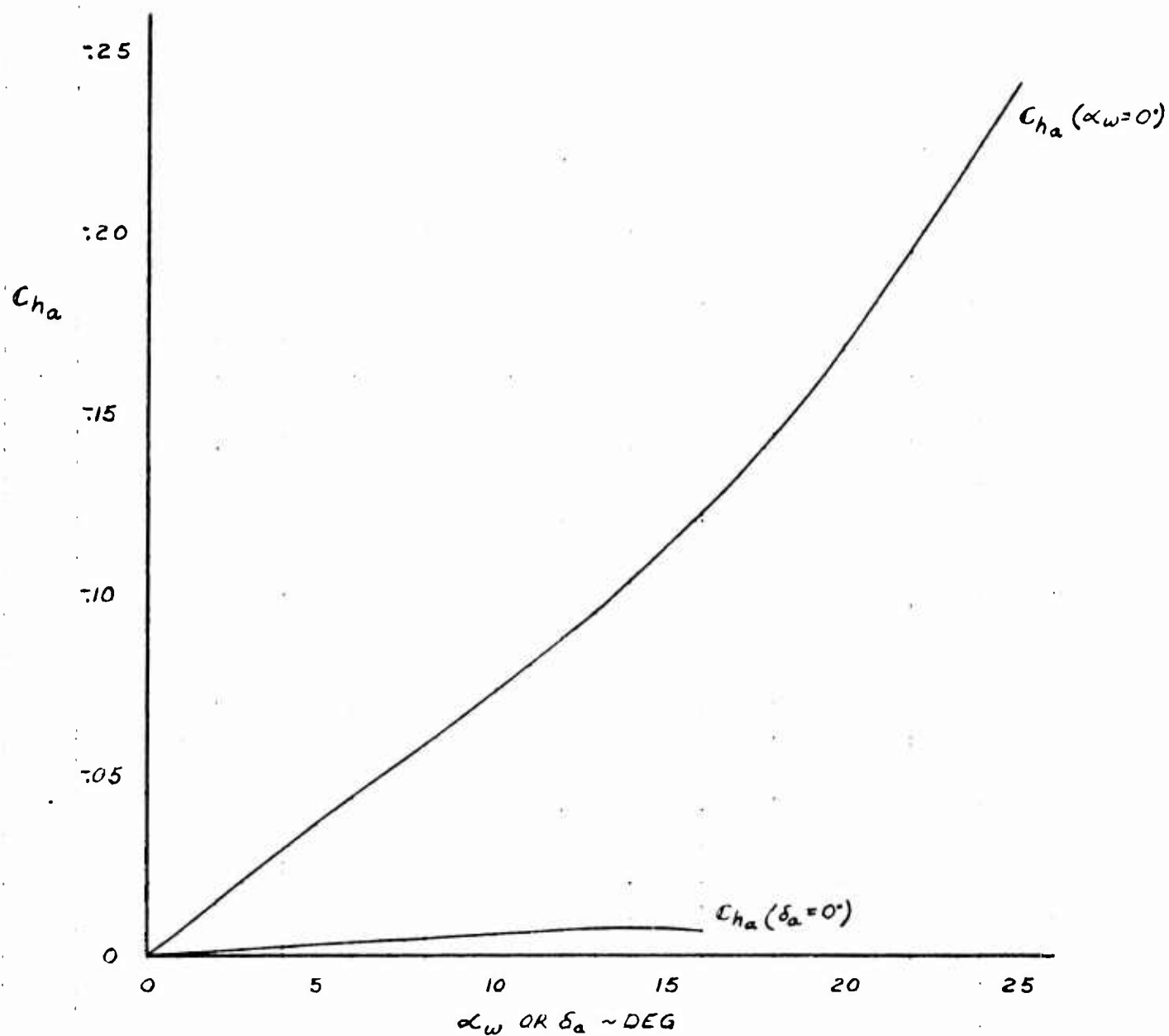


Figure 3.79

XV-5A
 C_{he} Vs MACH NUMBER
 (BALANCED)

NOTES:

- 1- $\alpha_0 = 0^\circ$
- 2- HINGE MOMENT IS BALANCED
- 3- RIGID DATA
- 4- REF, $S_0 = 11.970 \text{ FT}^2$ (TOTAL), $C_0 = 1.112 \text{ FT}$
- 5- REFERENCE: 143
- 6- INTERNALLY SEALED PRESSURE BALANCE
- 7- FREE AIR

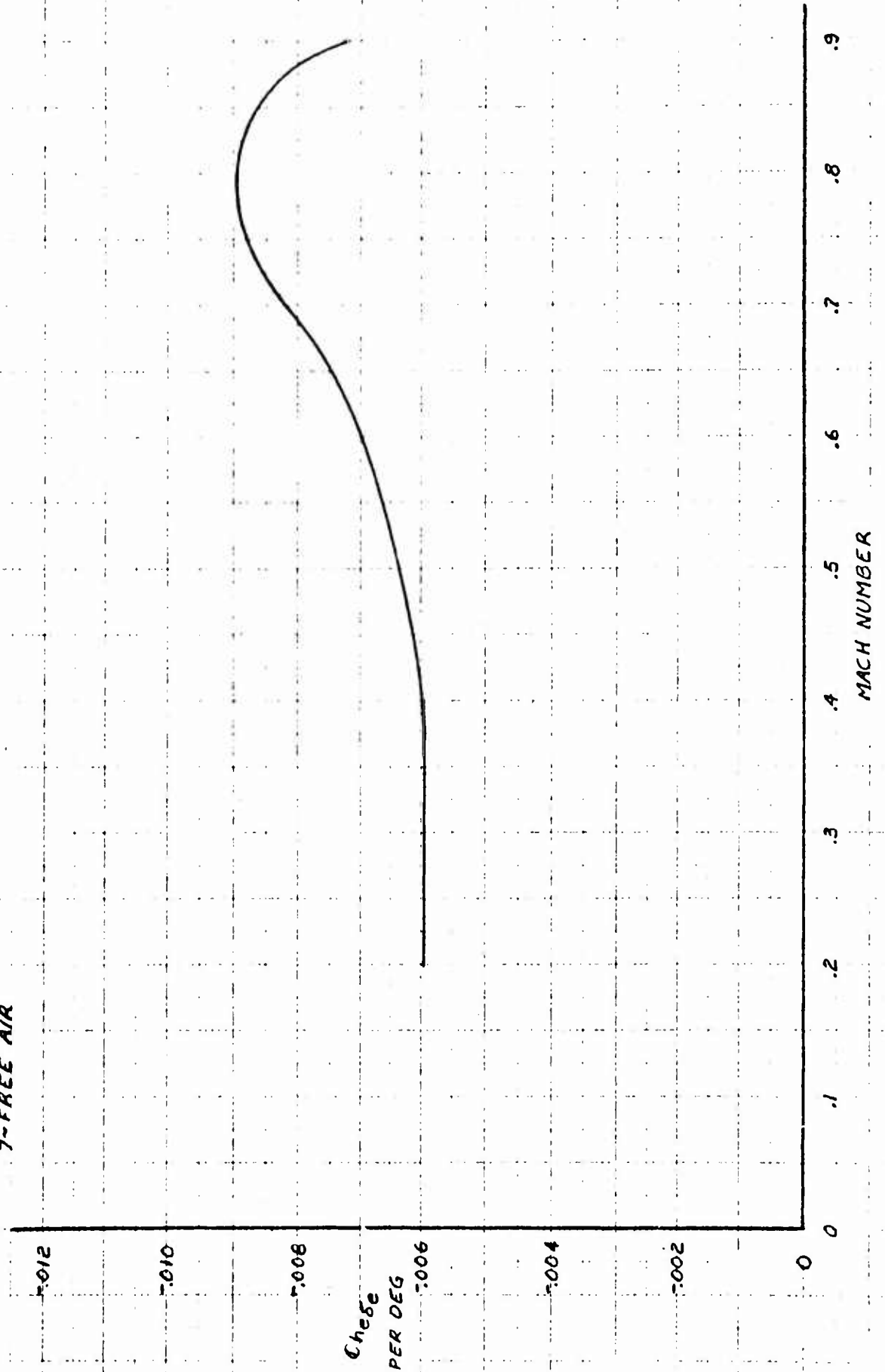


Figure 3.80

XV-5A
 $C_{he\alpha_e}$ Vs MACH NUMBER
 (BALANCED)

NOTES

- 1- $\delta_e = 0^\circ$
- 2- HINGE MOMENT IS BALANCED
- 3- RIGID DATA
- 4- REF. $S_e = 11.970 \text{ FT}^2$ (TOTAL); $\bar{c}_e = 1.112 \text{ FT}$
- 5- REFERENCE: 143
- 6- INTERNALLY SEALED PRESSURE BALANCE
- 7- FREE AIR

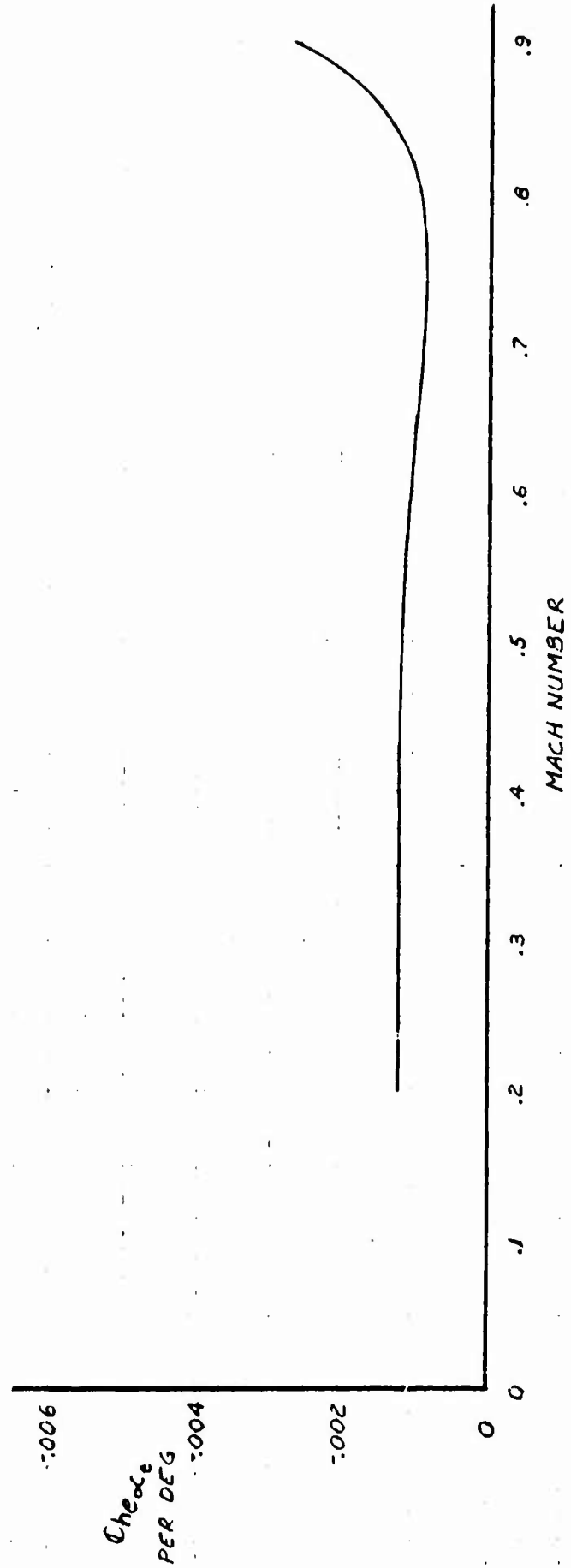


Figure 3.81

NOTES:

1- HINGE MOMENT IS UNBALANCED

2- RIGID DATA

3- REF. $S_e = 11.970 \text{ FT}^2$ (TOTAL), $\bar{c}_e = 1.112 \text{ FT}$

4- REFERENCE: 143

5- FREE AIR

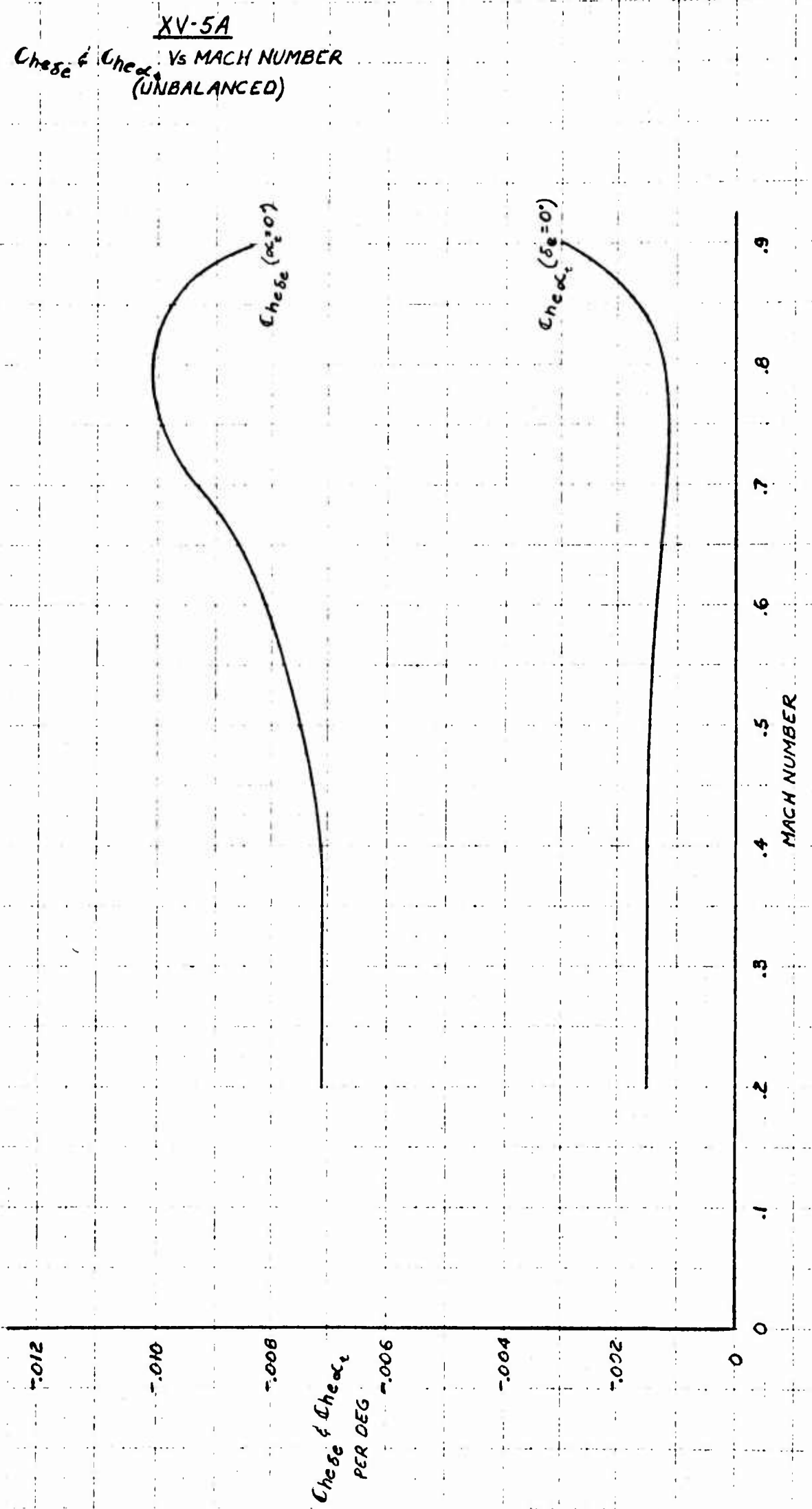


Figure 3.82

NOTES:

1- $\beta = 0^\circ$

2- HINGE MOMENT IS BALANCED

3- NO TAB INCLUDED

4- RIGID DATA

5- REF. $S_r = 6.395 \text{ FT}^2$, $\bar{c}_r = 1.245 \text{ FT}$

6- REFERENCE: 143

7- INTERNALLY SEALED PRESSURE BALANCE

XV-5A
 $C_{hr\delta_r}$ VS MACH NUMBER
 (BALANCED)

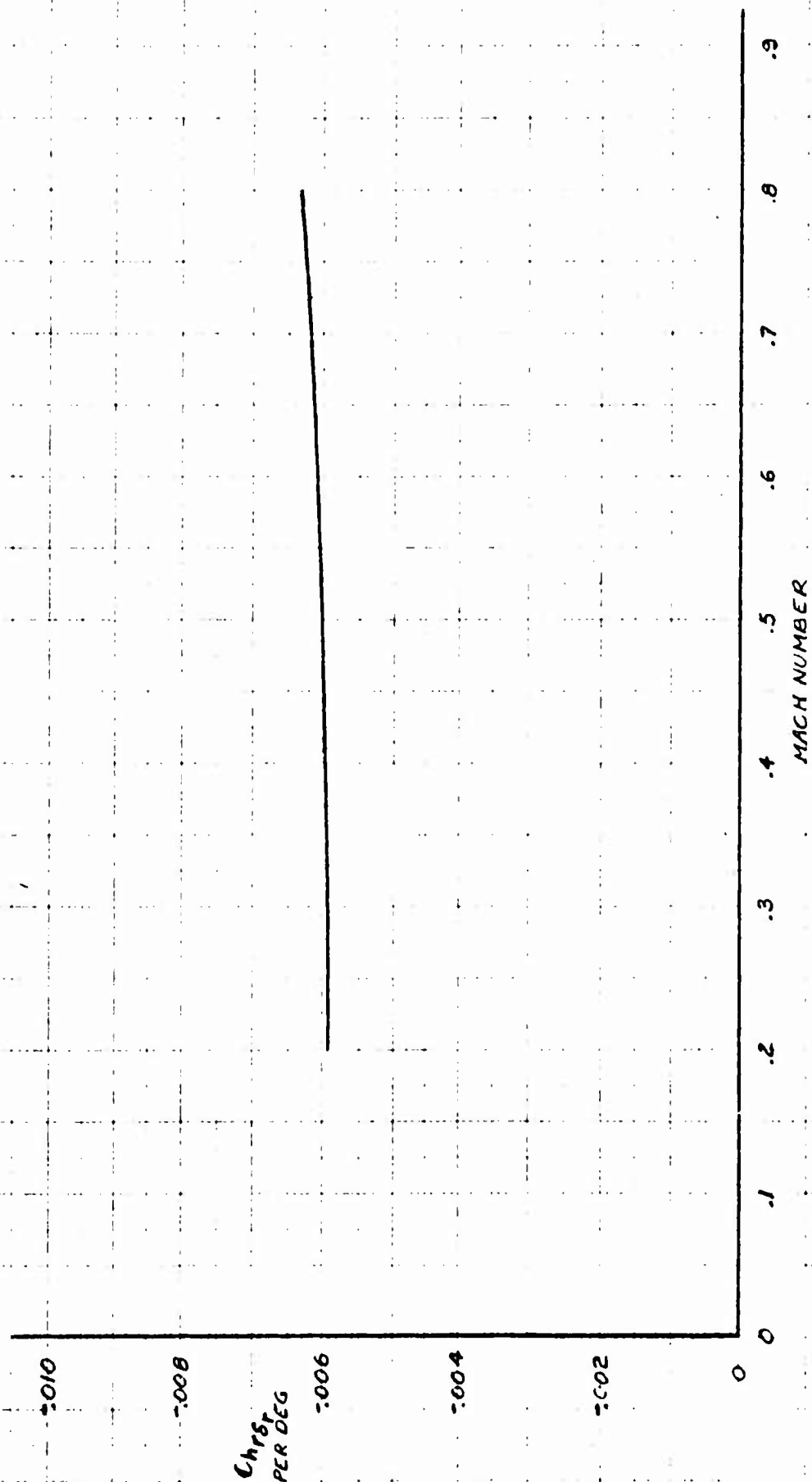


Figure 3.83

XV-5A
 C_{hrB} VS MACH NUMBER
 (BALANCED)

NOTES:

- 1- $\delta_r = 0^\circ$
- 2- HINGE MOMENT IS BALANCED
- 3- NO TAB INCLUDED
- 4- RIGID DATA
- 5- REF. $S_r = 6.395 \text{ FT}^2$, $\bar{C}_r = 1.245 \text{ FT}$
- 6- REFERENCE: 143
- 7- INTERNALLY SEALED PRESSURE BALANCE

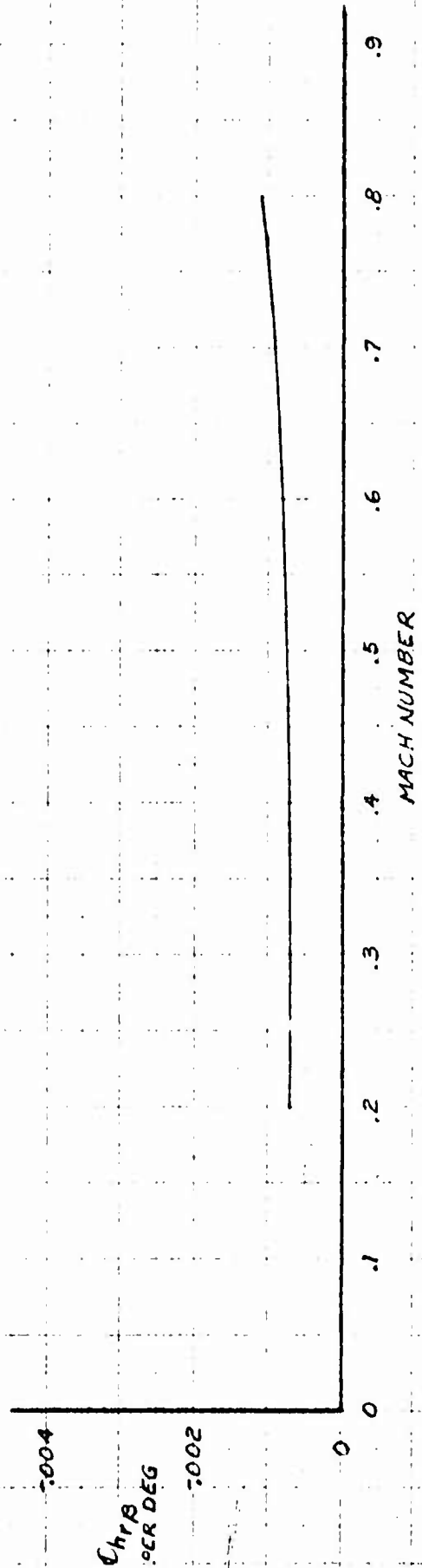


Figure 3.84

XV-5A
 $C_{hr\delta r}$ & $C_{hr\beta}$ VS MACH. NUMBER
 (UNBALANCED)

NOTES:

- 1- HINGE MOMENT IS UNBALANCED
- 2- NO TAB INCLUDED
- 3- RIGID DATA
- 4- REF. $S_r = 6.395 \text{ FT}^2$, $\bar{c}_r = 1.245 \text{ FT}$
- 6- REFERENCE: 143

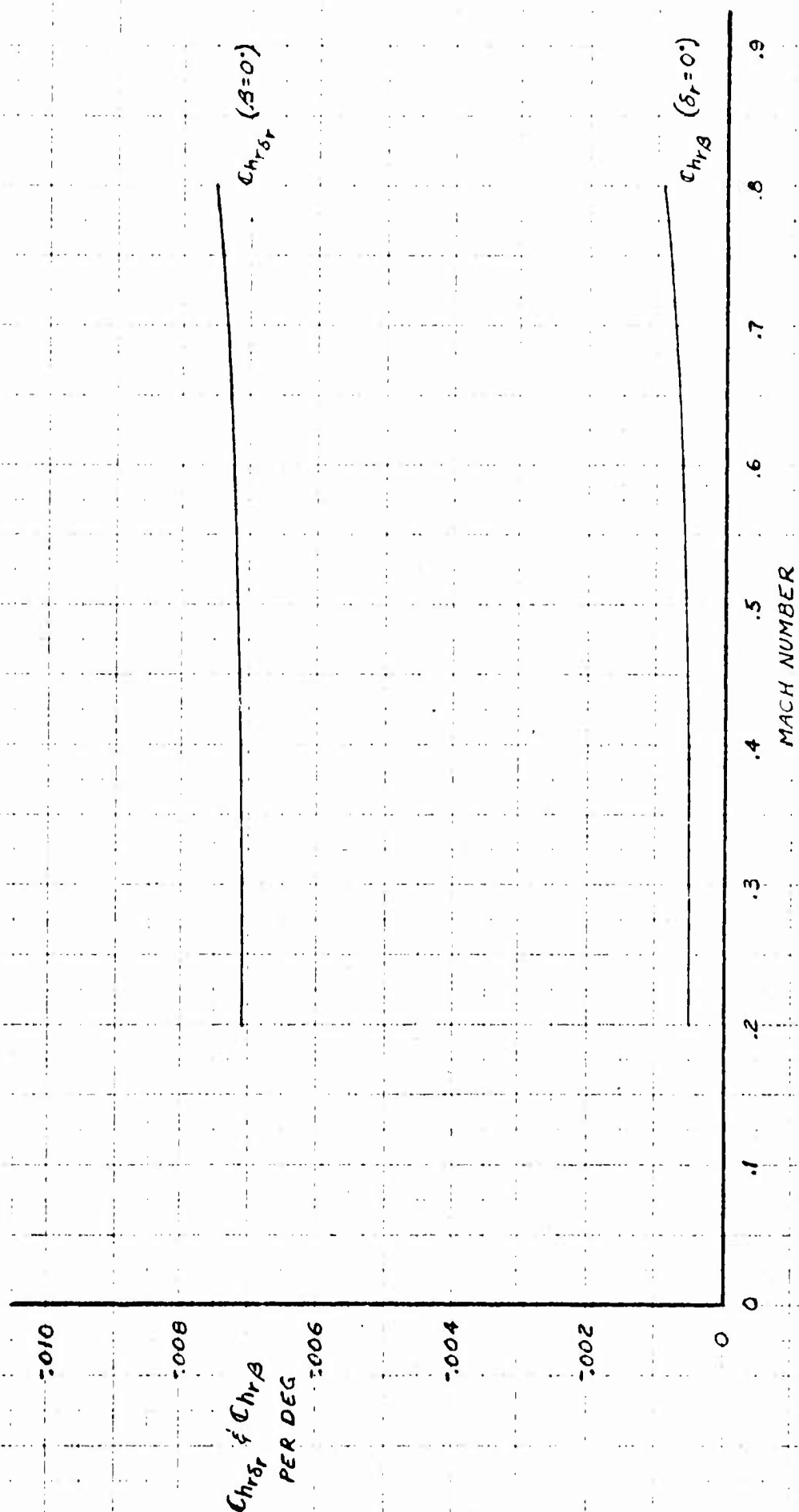


Figure 3.85

NOTE:

1. RIGID DATA
2. $\alpha \approx 0$
3. REFERENCE DIMENSIONS:
 $S_a = 10.057 \text{ FT.}^2$ (AFT OF H, PER SIDE)
 $\bar{c}_a = 1.582 \text{ FT.}$
4. INTERNAL, SEALED PRESSURE BALANCE
5. POSITIVE AILERON DEFLECTION
 IS TRAILING EDGE DOWN

XV-5A
 $C_{l_{aero}}$ & $C_{m_{aero}}$ VS. MACH NUMBER

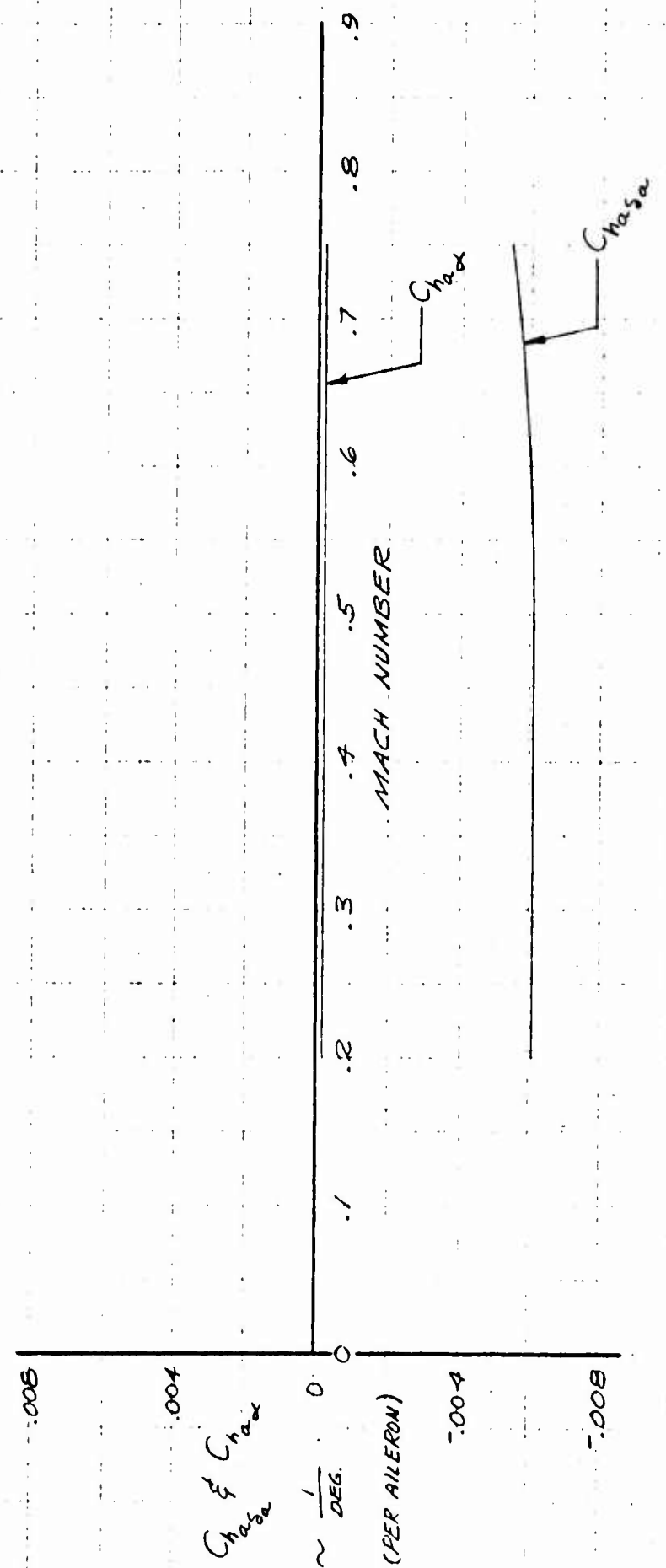


Figure 3.86

NOTE:

1. RIGID DATA

2. $\alpha \approx 0$

3. SEALED RADIUS NOSE TAB

4. POSITIVE TAB DEFLECTION

IS TRAILING EDGE DOWN

5. REFERENCE DIMENSIONS:

$S_t = 0.974 \text{ FT}^2$ (AFT OF H, PER SIDE)

$\bar{c}_t = 0.419 \text{ FT}$

6. C_{Hst} BASED ON AILERON AREA

AND CHORD.

XV-5A
 C_{Hst} , C_{Hsw} & C_{Hse} VS. MACH NUMBER

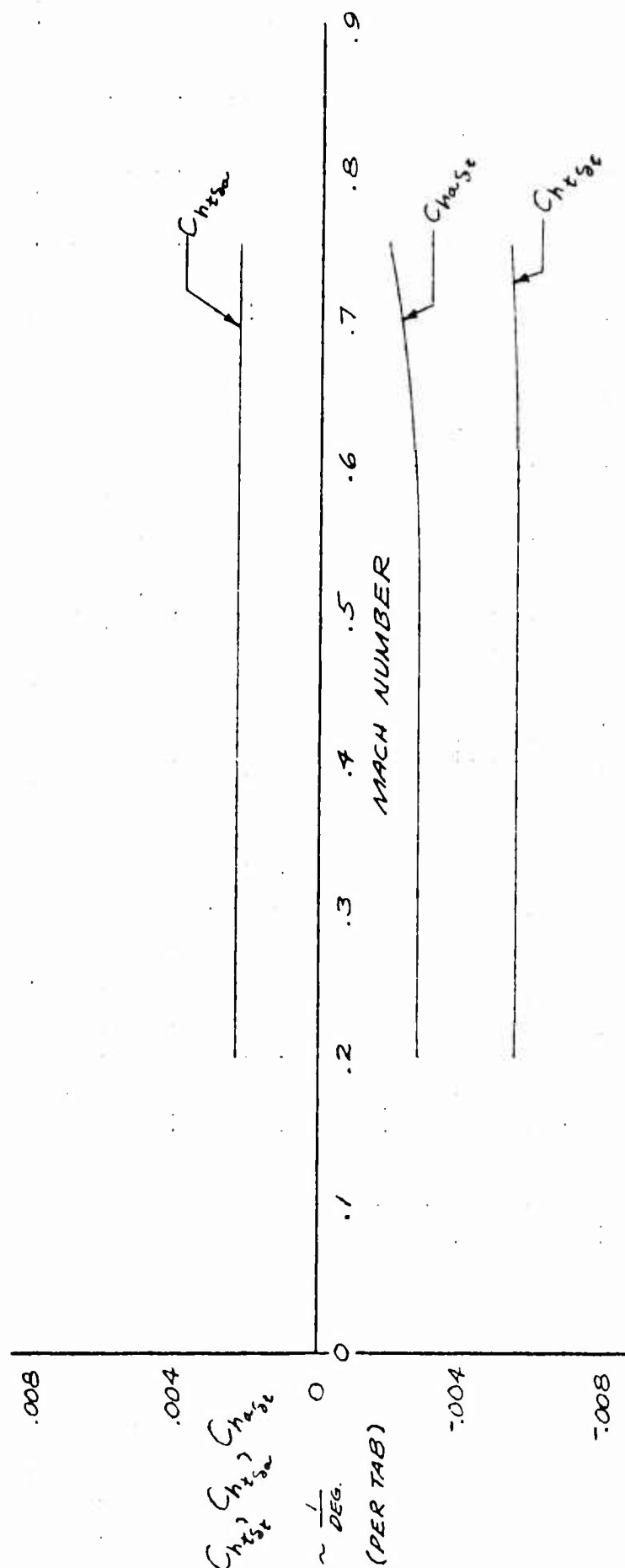


Figure 3.87

NOTES:

1~HINGE MOMENT IS UNBALANCED

2~RIGID DATA

3~REF. $S_a = 10.057 \text{ FT}^2$ (PER SIDE, INCLUDING TAB),
 $\bar{c}_a = 1.582 \text{ FT}$

4~REFERENCE: 1 & 3

5~FREE AIR

XV-5A
 $C_{ha\delta_a}$ & $C_{ha\alpha_w}$ VS MACH NUMBER
 (UNBALANCED)

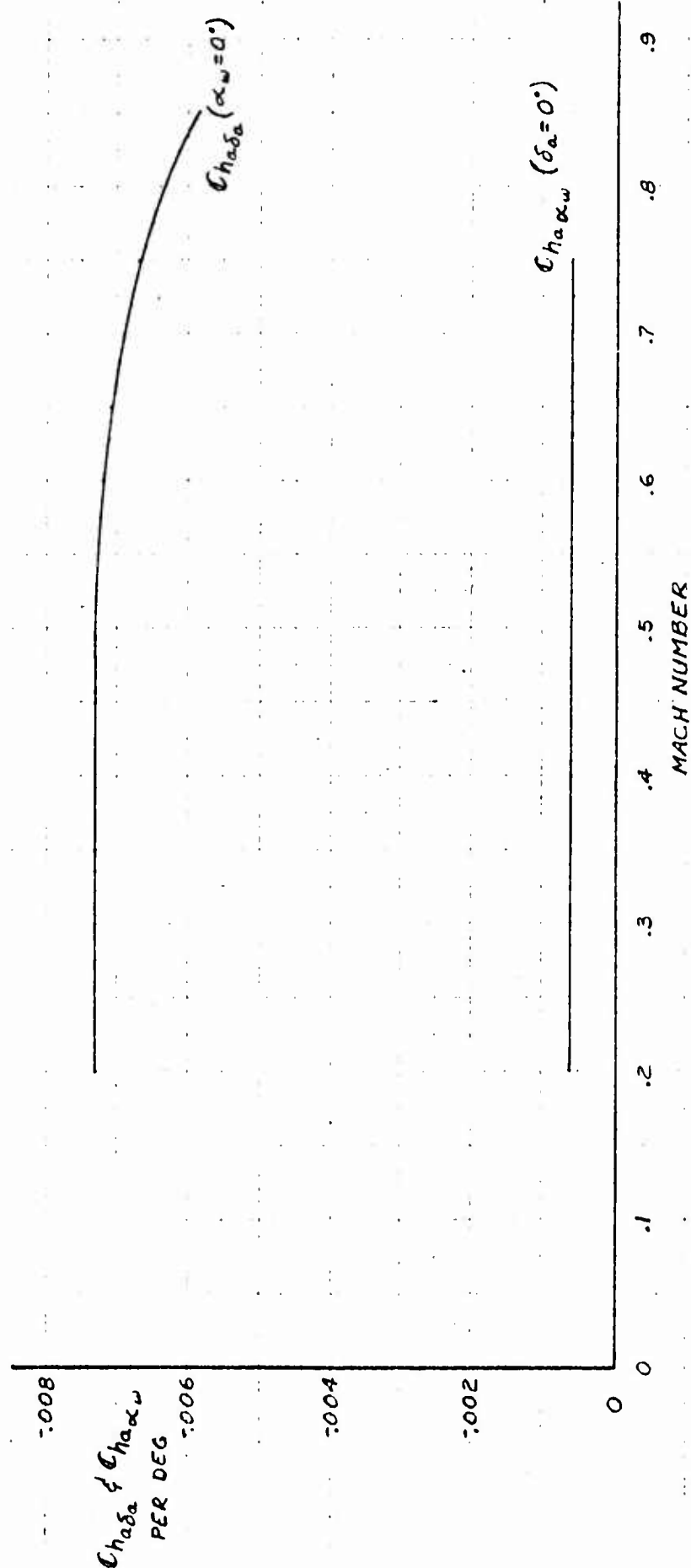


Figure 3.88

XV-5A

ELASTIC LIFT CURVE SLOPE PARAMETER VS MACH NUMBER, MODEL-TAIL

NOTE:

1. FREE AIR.
2. STABILITY AXES
3. $\delta_f = 0^\circ$
4. STANDARD DAY

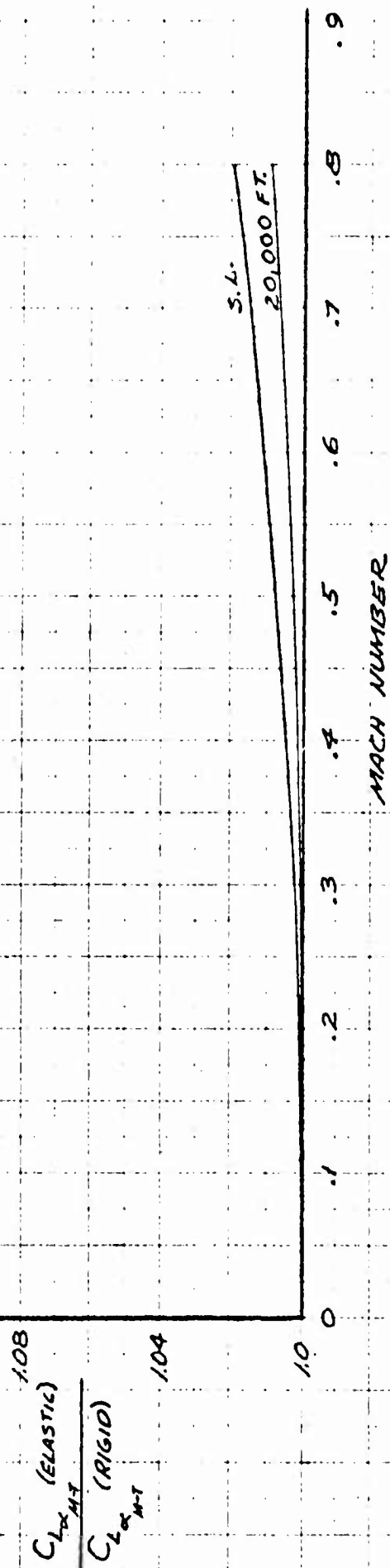


Figure 3.89

XV-5A

ELASTIC PITCHING MOMENT CURVE SLOPE PARAMETER VS MACH NUMBER, MODEL-TAIL

NOTE:

1. FREE AIR
2. STABILITY AXES
3. $\delta_f = 0^\circ$
4. STANDARD DAY

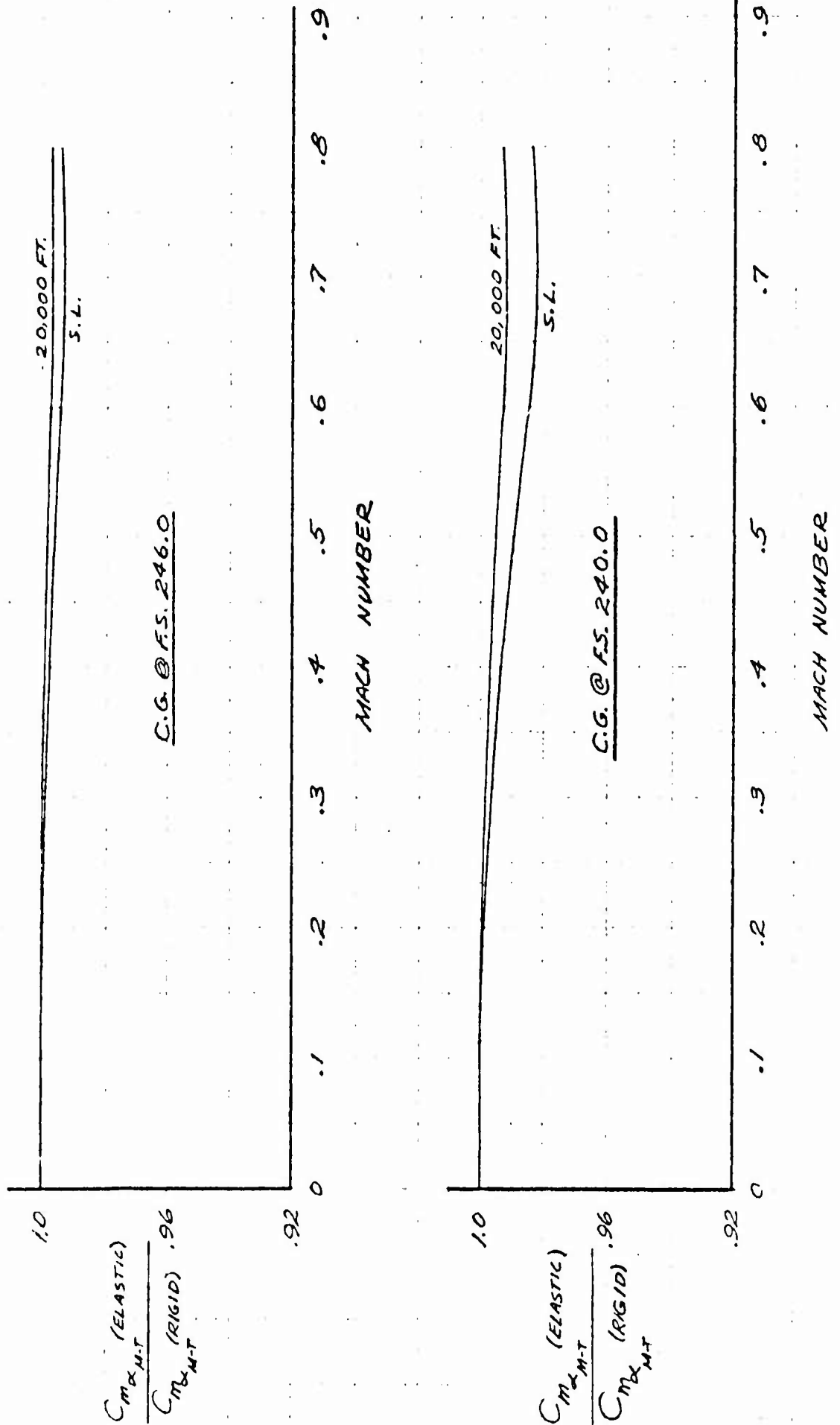


Figure 3.90

XV-5A

ELASTIC ANGLE OF ZERO LIFT AND PITCHING MOMENT COEFFICIENT AT ZERO LIFT PARAMETER
VS. MACH NUMBER, MODEL-TAIL

NOTE:

1. FREE AIR
2. STABILITY AXES
3. $\delta_4 = 0^\circ$
4. STANDARD DAY

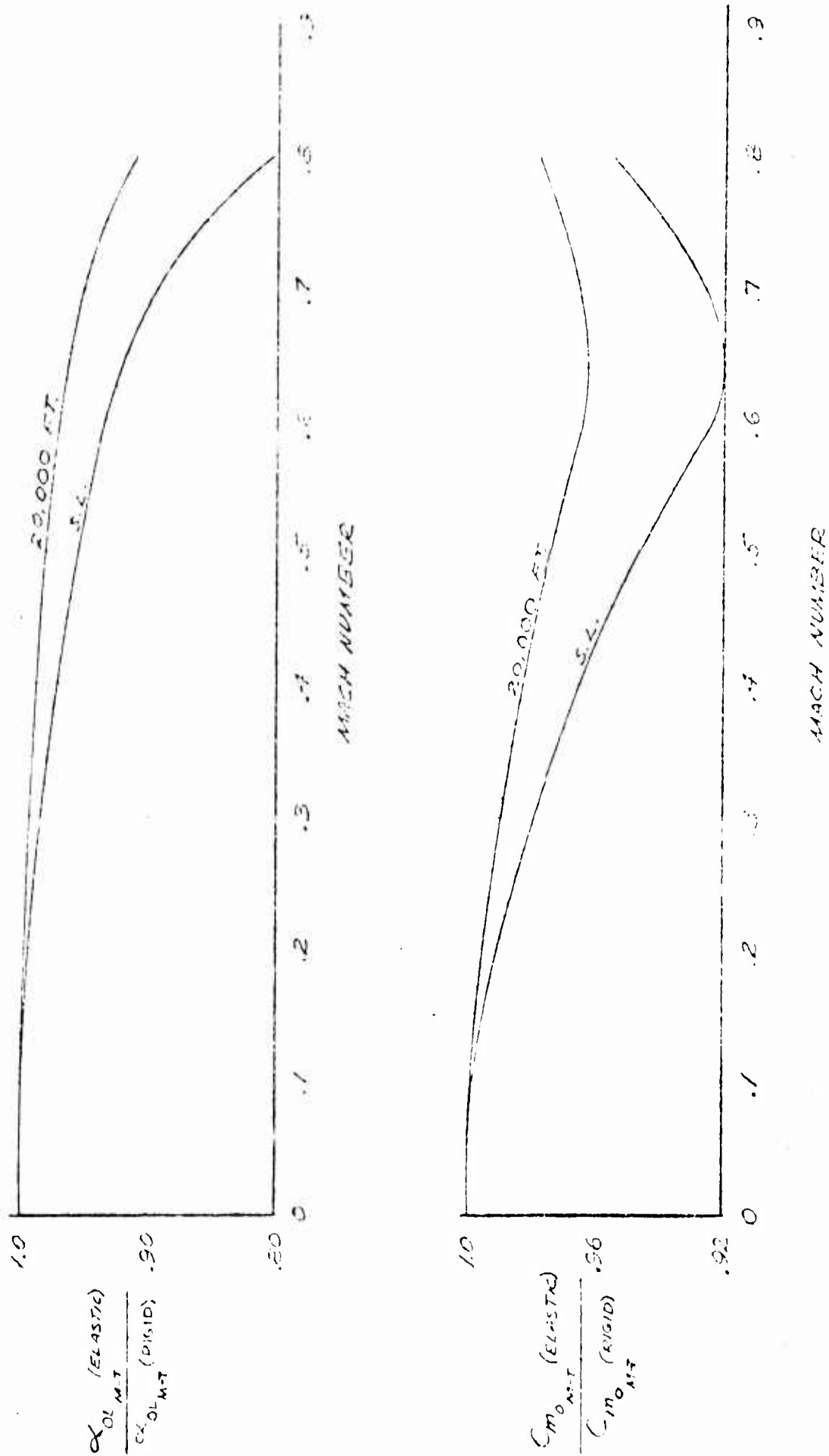


Figure 3.91

XV-5A

ELASTIC ROLLING MOMENT COEFFICIENT WITH AILERON DEFLECTION PARAMETER
VS MACH NUMBER

NOTE:

- 1. FREE AIR
- 2. STABILITY AXES
- 3. $\delta_f = 0^\circ$
- 4. STANDARD DAY

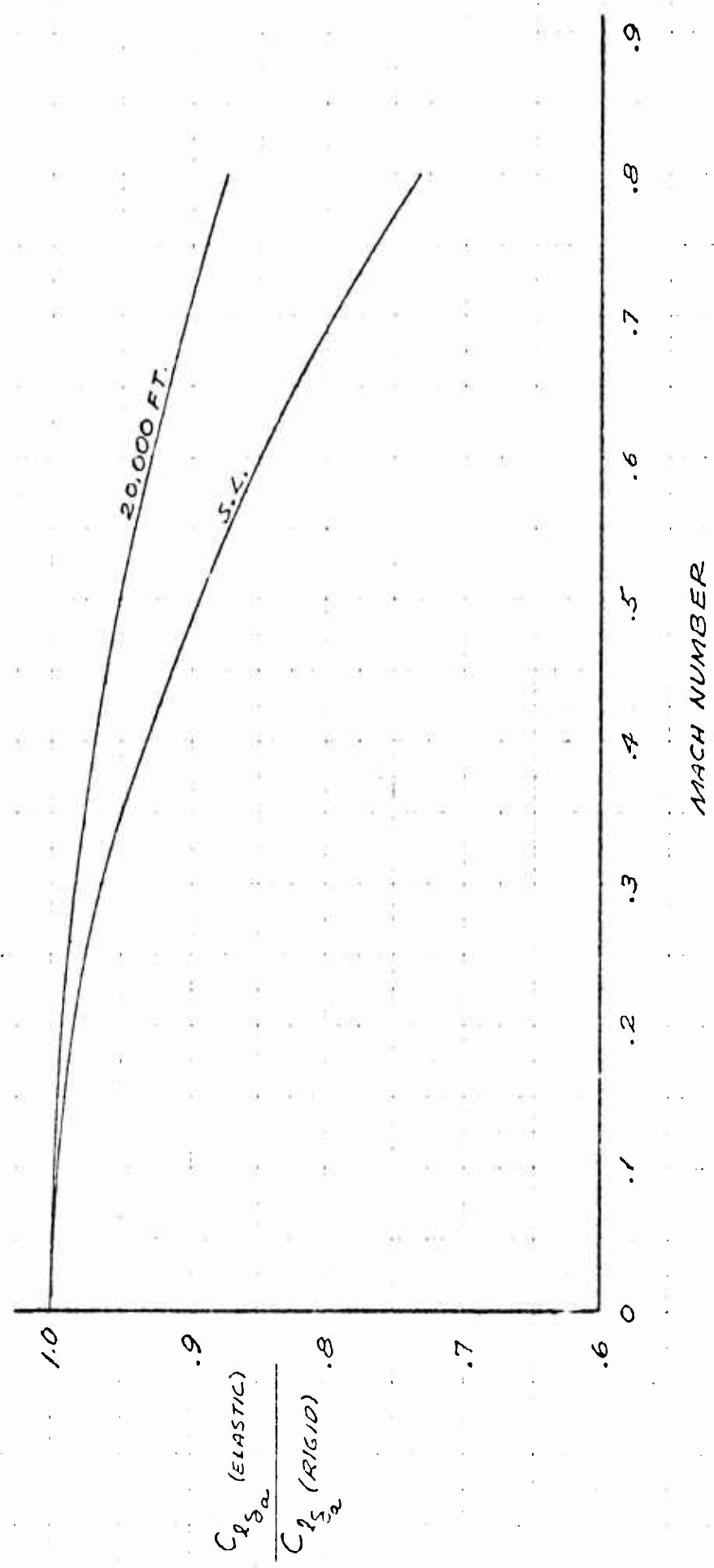


Figure 3.92

XV-5A
ELASTIC ROLL DAMPING PARAMETER VS MACH NUMBER

NOTE:
1. FREE AIR
2. STABILITY AXES
3. $\delta_f = 0^\circ$
4. STANDARD DAY

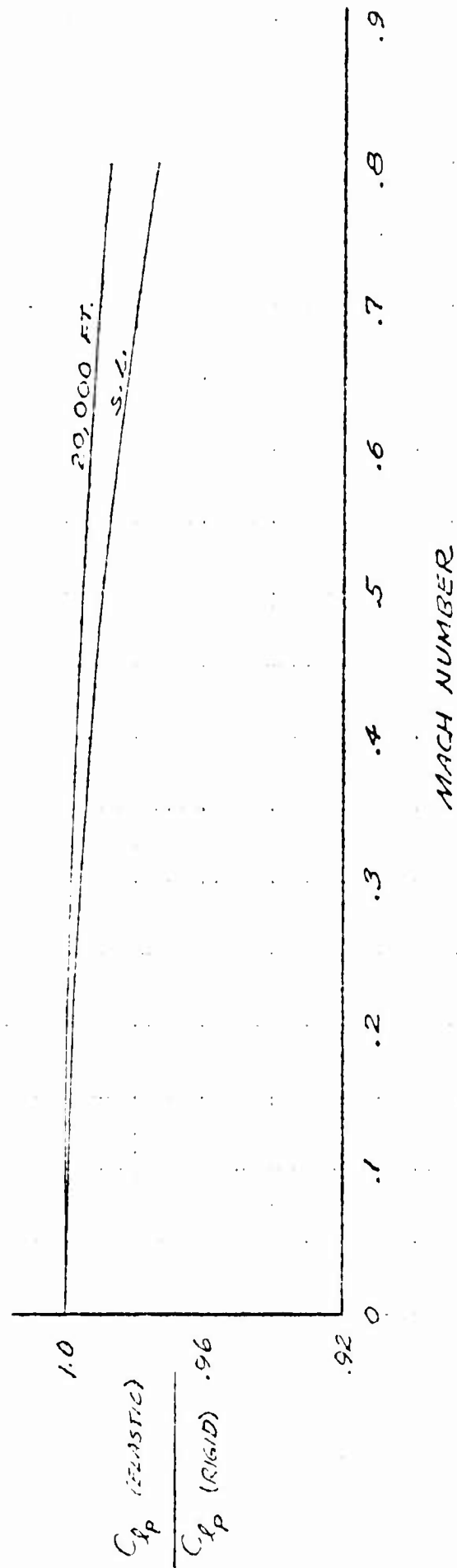


Figure 3.93

XV-5A

ELASTIC ROLL COEFFICIENT VS MACH NUMBER

Symbol	Altitude, ft.	Term
—○—	0	$(C_{l_{SA}})_{EW(B)} \div (C_{l_{SA}})_{RW(B)}$
- - Δ - -	20,000	"
—△—	0	$(C_{l_P})_{EW(B)} \div (C_{l_P})_{RW(B)}$
- - Δ - -	20,000	"

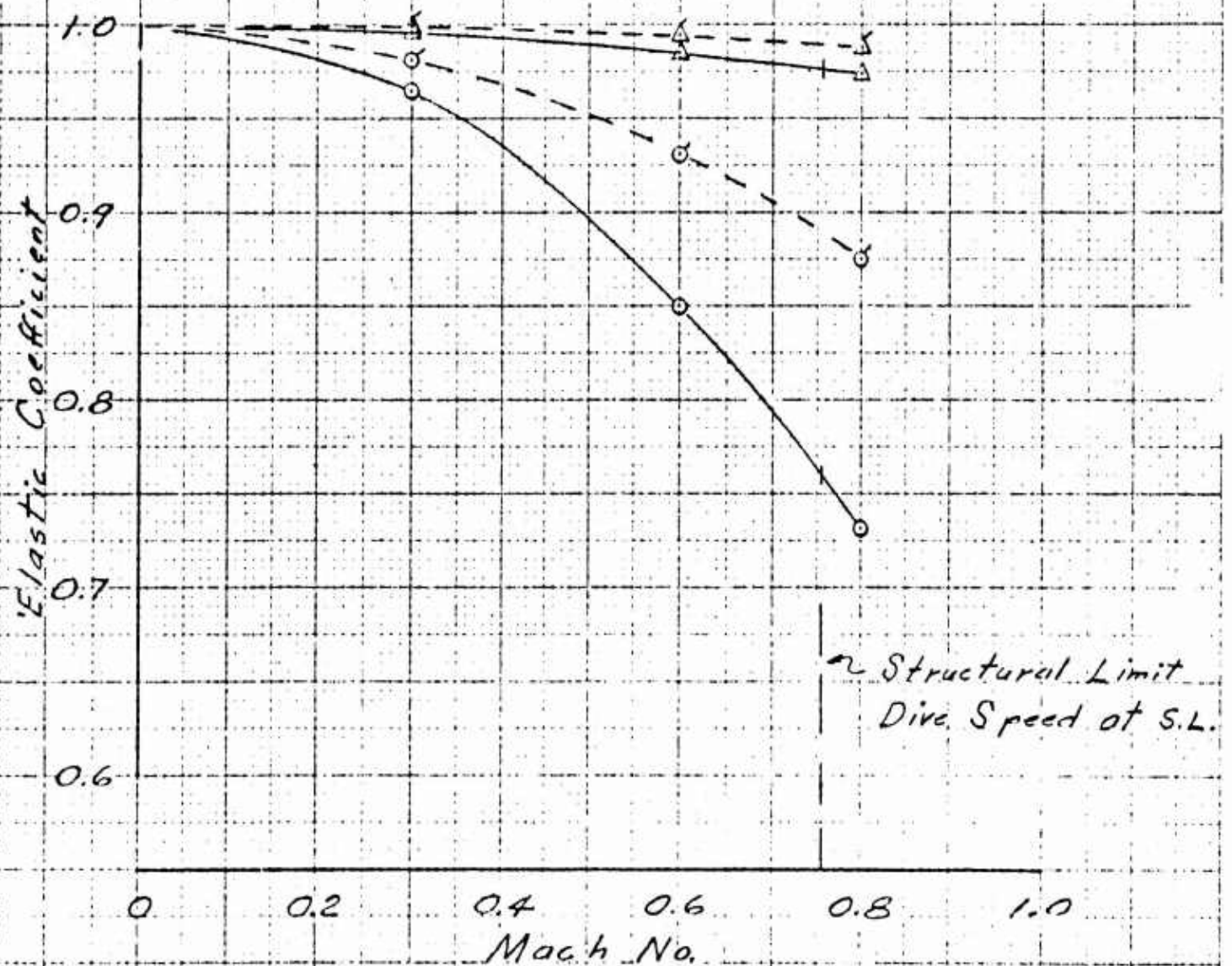


Figure 3.94

XV-5A

ELASTIC TAIL COEFFICIENT VS. MACH NUMBER

Symbol	Altitude, ft.	Term
—○—	0	$(C_{m_{\alpha}})_{ETEB} \div (C_{m_{\alpha}})_{RTTB}$
- -○- -	20,000	" "
—△—	0	$(C_{m_{\delta E}})_{ETEB} \div (C_{m_{\delta E}})_{RTTB}$
- -△- -	20,000	" "

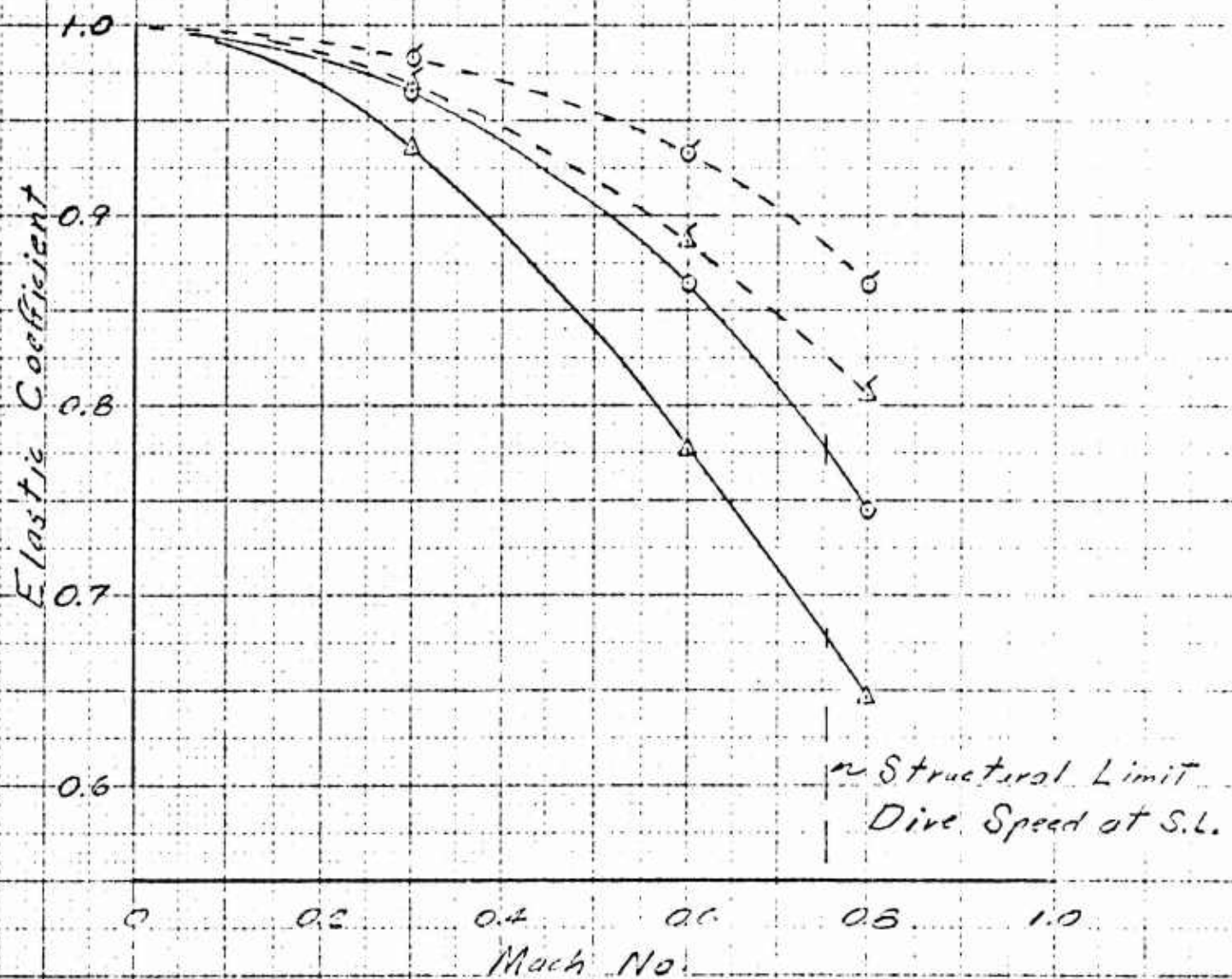


Figure 3.95

XV-5A

ELASTIC TRAIL COEFFICIENT VS. MACH NUMBER

Symbol	Altitude, ft.	Term
—○—	0	$(C_{n_p})_{ETEB} \div (C_{n_p})_{RTRB}$
- -○- -	20,000	"
—△—	0	$(C_{n_{\delta R}})_{ETEB} \div (C_{n_{\delta R}})_{RTRB}$
- -△- -	20,000	"

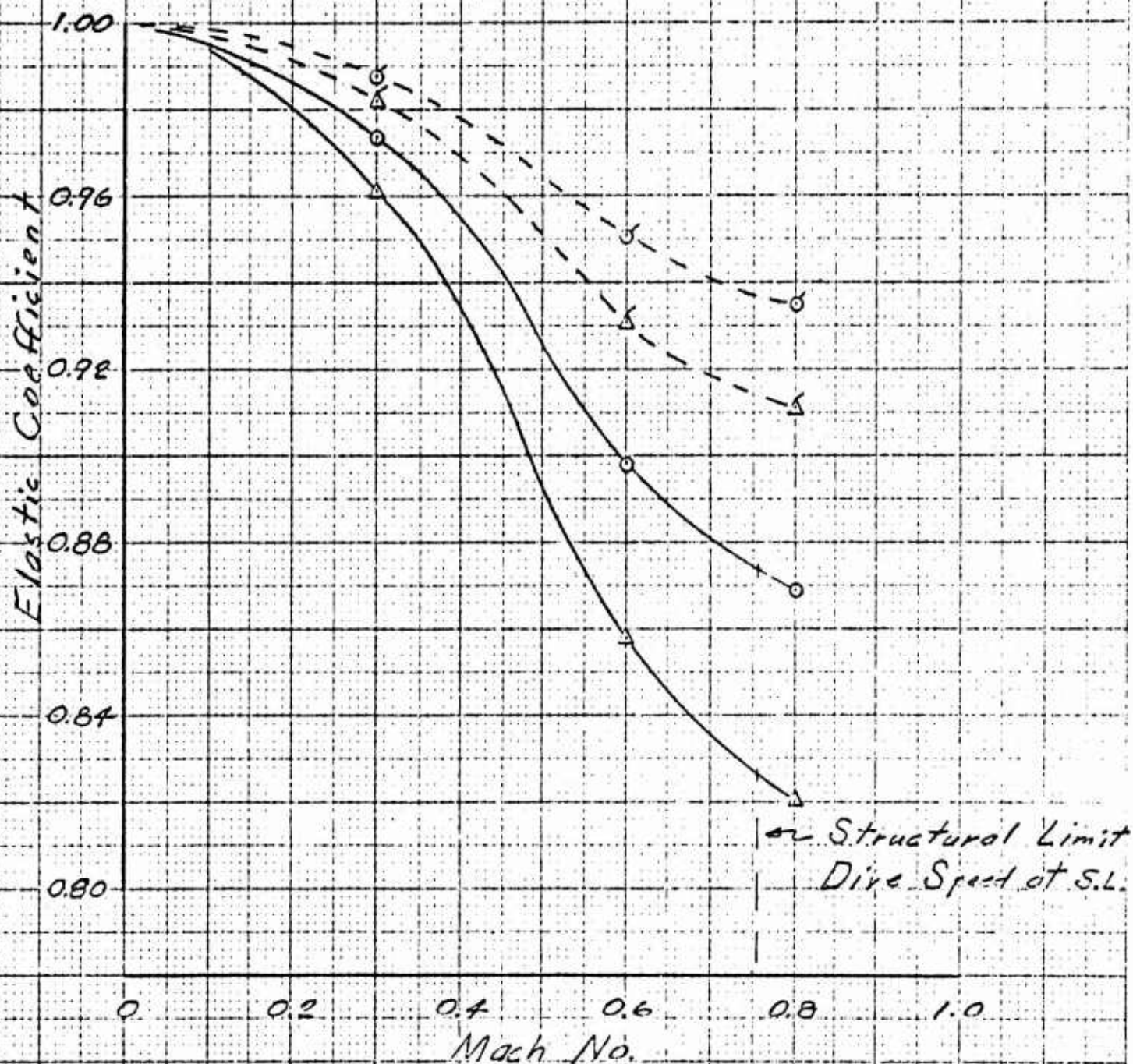


Figure 3.96

XV-5A

HORIZONTAL TAIL EFFECTIVE LIFT CURVE SLOPE
VS.

HORIZONTAL TAIL ASPECT RATIO

NOTE:

1. RIGID DATA
2. STABILITY AXES
3. ○ - WIND TUNNEL TEST DATA

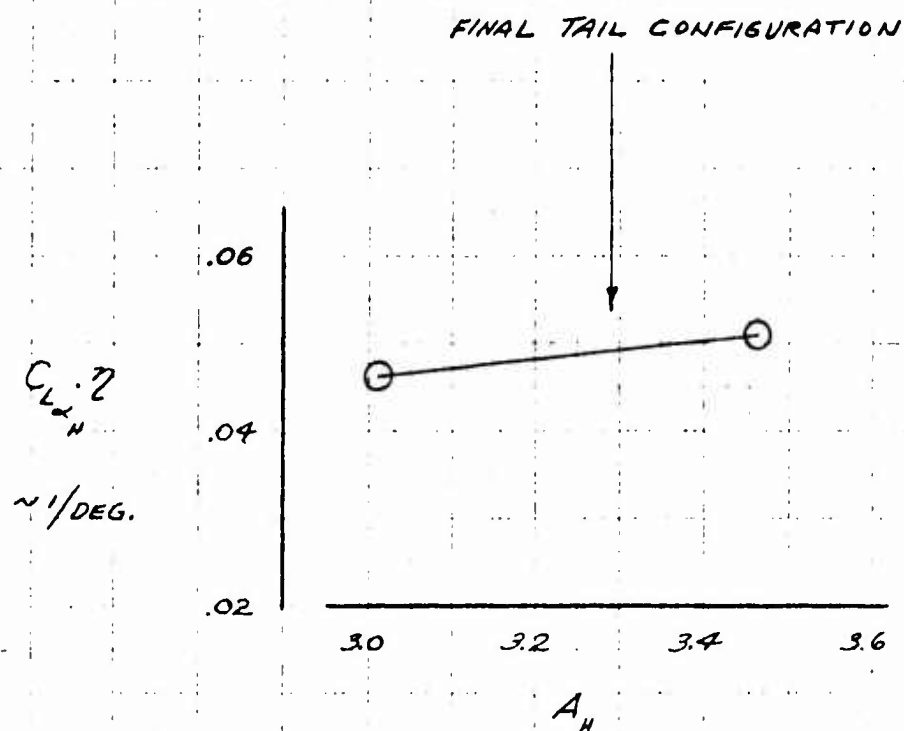


Figure 3.97

XV-5A

INCREMENTAL CHANGE IN ROLLING MOMENT WITH
SIDESHIP ANGLE COEFFICIENT VS. DIHEDRAL ANGLE

NOTE:

1. RIGID DATA
2. STABILITY AXES
3. $\delta_f = 0^\circ$

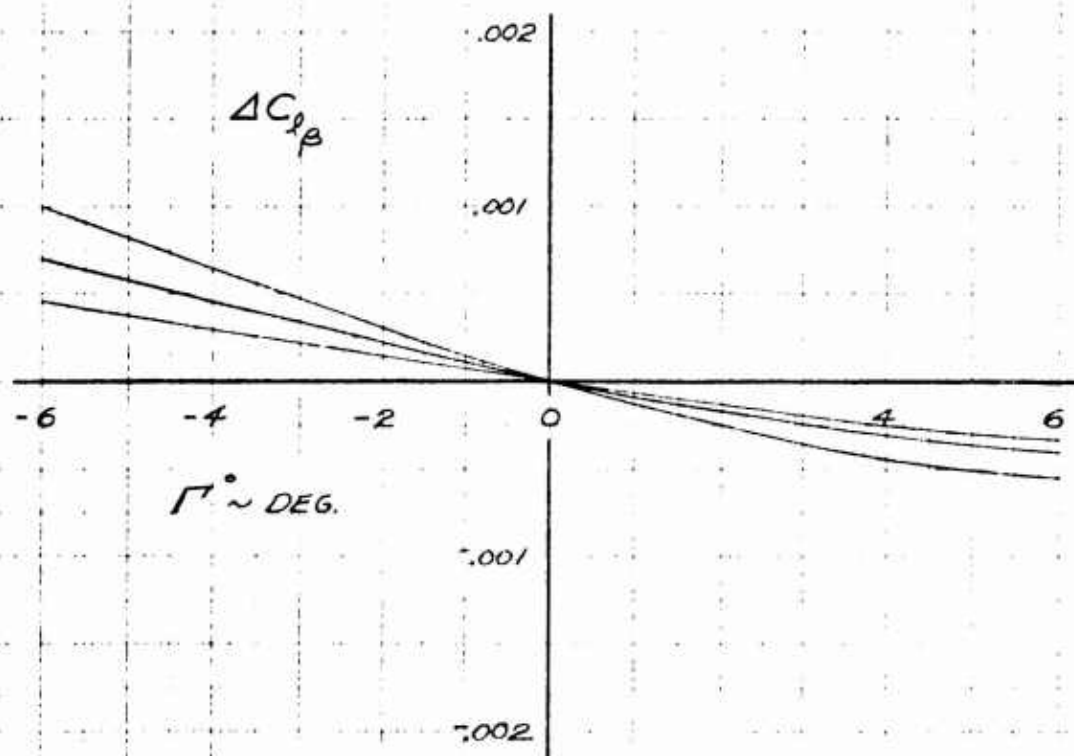


Figure 3.98

4.0 LIFT FAN MODE CHARACTERISTICS

4.1 FAN MODE, TRANSITION, LONGITUDINAL

The longitudinal characteristics in fan-powered flight have been developed from test data of the 1/6 scale powered wind tunnel model reported in Reference 2 and from unpublished test results of a full-scale facsimile of the XV-5A aircraft obtained at the NASA Ames Research Center's 40 x 80 wind tunnel and the test programs were designated as Tests 173 and 177. An incremental build-up method is used to develop the coefficients so that data from the various sources may be utilized.

Early inspection of the 1/6 scale model data and comparison with Ames full-scale data showed that the small-scale model fan power coefficient, C_P^S , increased with decreasing values of fan thrust coefficient, T_c^S , indicating an increase in fan power with increasing tunnel airspeed for a constant rotational fan speed. Observation of the full-scale propulsion system as tested in the Ames 40 x 80 wind tunnel has indicated an increase in fan rotational speed with increasing tunnel airspeed for constant gas generator power settings, resulting in a decrease in fan power with tunnel speed for a given fan speed.

Corrections were applied to the 1/6 scale thrust and power data which improved the correlation of the longitudinal data from the two test sources, but were not entirely satisfactory. Therefore, the full-scale data have been used to represent the basic level of lift, drag and pitching moment of the XV-5A in transition flight and incremental effects of flap deflection, exit louver angle, angle of attack, etc., have been obtained from the two sources. Other factors which possibly affect the correlation of the data from the two model tests are wind tunnel wall effects and differences in wing thickness ratio. The 1/6 scale model wing thickness was increased by 20% in order to accommodate the fans.

Due to the complex nature of the downwash variation at the horizontal tail and of the effects of operation of the nose fan, the basic data are presented for tail-off and nose fan inoperative configurations and the contributions of the tail and nose fan are added separately as described later.

4.1.1 Lift Characteristics

The zero angle of attack lift coefficient build-up is shown in Figure 4.1 using full-scale Ames data with the power-off lift deleted as the base. The power-off increment for the XV-5A, $\Delta C_{L_{po}}^s$, was taken from

Figure 3.1 for zero flap deflection and converted to the slipstream notation by

$$\Delta C_{L_{po}}^s = C_L \left(1 - T_c^s \right) \frac{S_w}{A_F} = .10 (1 - T_c^s) \frac{260}{42.6} = .61 (1 - T_c^s)$$

The increments due to flap and aileron droop deflection were obtained from 1/6 scale data and are shown in Figures 6.1 and 6.2. As shown in Figure 6.1 the power-on flap lift increments are considerably smaller than the power-off values for both the 1/6 scale and the full-scale data. Conversely, as shown in Figure 6.2, the power-on increments due to aileron droop are larger than the power-off value at high values of T_c^s , apparently due to fan-induced circulation on the wing outboard of the fans.

4.1.2 Drag Characteristics

The zero angle of attack drag coefficient build-up may be expressed as follows:

$$C_D^s = C_{D_{Basic}}^s - (\Delta C_{D_{Ames}}^s)_{PO, \delta_f = 0^\circ} + (\Delta C_{D_{XV-5A}}^s)_{PO, \delta_f = 0^\circ} + (\Delta C_{D_{Gear}}^s) + (\Delta C_{D_{Droop}}^s) + (\Delta C_{D_{Nose\ Fan\ Doors}}^s)$$

(1)
(2)
(3)
(4)

where

$$(1) C_{D_{Basic}}^s = \text{Full-scale data for } \beta_v = 0^\circ, \delta_f = 45^\circ$$

$$\textcircled{2} (\Delta C_D^S)_{\text{Ames}} = \text{Full-scale power-off data for } \delta_f = 0^\circ, \text{ louvers and fan inlet doors closed.}$$

$$= .05(1-T_c^s) \frac{S_w}{A_F} = .05(1-T_c^s) \frac{285}{42.6}$$

$$\textcircled{3} (\Delta C_D^S)_{\text{XV-5A}} = \text{Estimated XV-5A } C_{D_O} \text{ for } \delta_f = 0^\circ \quad (\text{Ref. 13})$$

$$= .02(1-T_c^s) \frac{260}{42.6}$$

$$\textcircled{4} (\Delta C_D^S)_{\text{Gear}} = C_{D_{\text{Gear}}} (1-T_c^s) \frac{260}{42.6} = .029(1-T_c^s) \frac{260}{42.6} \quad (\text{Ref. 13})$$

$$\textcircled{5} (\Delta C_D^S)_{\text{Aileron Droop}} \text{ from Figure 6.2}$$

$$\textcircled{6} (\Delta C_D^S)_{\text{Nose Doors}} = .017(1-T_c^s) \frac{260}{42.6} \quad (\text{Ref. 2})$$

The drag build-up is illustrated graphically in Figure 4.2. No correction was made for the difference in flap drag between the full-scale wind tunnel model and the XV-5A aircraft as this increment is small compared with the fan momentum drag.

4.1.3 Pitching Moment Characteristics

The zero angle of attack pitching moment coefficient was developed in a manner similar to the lift and drag as follows:

$$C_m^S = C_{m_{\text{Basic}}}^S - \textcircled{2} (\Delta C_m^S)_{\text{Ames}} + \textcircled{3} (\Delta C_m^S)_{\text{XV-5A}} + \textcircled{4}^{PO} (\Delta C_m^S)_{\delta_f} + \textcircled{5}^{PO} (\Delta C_m^S)_{\delta_d}$$

where

$$\textcircled{1} C_{m_{\text{Basic}}}^S = \text{Full-scale data for } \beta_v = 0^\circ, \delta_f = 0^\circ$$

$$\textcircled{2} (\Delta C_{m_{\text{Ames}}}^S) = \text{Full-scale power-off data for } \delta_f = 0^\circ, \text{ louvers and fan inlets closed.}$$

$$= C_{m_o} (1 - T_c^S) \frac{S_w}{A_F} \frac{\bar{c}}{D_F} = -.055(1 - T_c^S)$$

$$\frac{285}{42.6} \cdot \frac{10.14}{5.2}$$

$$\textcircled{3} (\Delta C_{m_{\text{XV-5A}}}^S) = \text{Estimated } C_{m_o} \text{ for XV-5A for } \delta_f = 0^\circ$$

$$= C_{m_o} (1 - T_c^S) \frac{S_w}{A_F} \frac{\bar{c}}{D_F} = -.04(1 - T_c^S)$$

$$\frac{260}{42.6} \times \frac{9.35}{5.2}$$

$$\textcircled{4} (\Delta C_{m_{\delta_f}}^S) = \text{Increment due to flap deflection, power-on (Figure 6.1)}$$

$$\textcircled{5} (\Delta C_{m_{\delta_d}}^S) = \text{Increment due to aileron droop, power-on (Figure 6.2)}$$

As shown in Figure 6.1 the power-on flap moment increment for the 1/6 scale model is approximately 70% of the power-off value, whereas the power-on increment for the full-scale model has an average value equal to the power-off increment. The trend of the full-scale data was assumed to apply and the power-off increment for the 1/6 scale model was applied to the pitching moment build-up for the effect of flap deflection. The estimated pitching moment coefficients are shown in Figure 4.3.

All of the pitching moment increments discussed above were measured with respect to or corrected to a/cg location at aircraft fuselage station 246, W.L. 112.

4.1.4 Effect of Angle of Attack

The effect of angle of attack on the tail-off lift, drag and pitching moment coefficients is shown in Figures 4.4 through 4.8 as functions of thrust coefficient and vector angle.

The lift curve slopes were measured from angle of attack polars in Ref. 2. Typical variations of the lift curve slope with exit louver vector angle at constant thrust coefficients are illustrated in Figure 6.3. As shown in Figure 4.4, the nearly linear variation of $dC_L^s/d\alpha$ with

T_c^s in the transition speed range shows that the power-off lift curve slope $dC_L/d\alpha$, is not largely affected by fan operation although $dC_L^s/d\alpha$

is lower at most values of thrust coefficient than for the inlet doors and exit louvers open configuration at $T_c^s=0$.

The variation of drag coefficient with angle of attack is not sufficiently linear to represent as a slope; therefore, it is shown as an increment from $\alpha = 0^\circ$ in Figures 4.5, 4.6 and 4.7. The zero vector data were obtained by correcting full-scale drag data for the additional effect of aileron droop determined from Ref. 2 and shown in Figure 6.5. The 50° vector drag data were determined exclusively from 1/6 scale data.

As an aid in determining the drag coefficient for other vector angles, the variation of the incremental drag coefficient due to angle of attack is shown in Figure 6.4 as a function of β_v for two values of thrust coefficient.

The estimated pitching moment curve slope, $dC_m^s/d\alpha$, with the tail-off is shown in Figure 4.8 for the entire range of thrust coefficient. Values for the various conversion configurations with power-off are also indicated. $dC_m^s/d\alpha$ for the high range of T_c^s was determined from full-scale data and faired into 1/6 scale data at the lower values of T_c^s .

A comparison of the pitching moment curve slopes as determined from full-scale and 1/6 scale tests is given in Figure 6.6. The 1/6 scale pitching moment curve slope is of the order of 10 to 20 percent higher than the full-scale value and both models show a destabilizing effect of the fans compared with the power-off stability level with the inlet doors and exit louvers closed.

The limiting angle of attack for wing stall is indicated in Figure 4.4 and the limiting angle of attack for linear variation of pitching moment coefficient with angle of attack is included on Figure 4.8. A stable break in the tail-off pitching moment curves occurs prior to the stall angle and accounts for the lower angle of attack envelope for the pitching moment data.

4.1.5 Exit Louver Control System

The wing fan exit louver system is utilized for fan-flight propulsion, hovering lift control, and for hovering and transition lateral-directional control. Collective vectoring with equal louver angles of each wing fan provides propulsion and differential vectoring between the left and right hand fans provides directional or yaw control. Collective staggering of the louvers is used for hovering altitude control and differential stagger of the louvers for roll control. Combinations of both collective and differential vector and stagger angles as a result of control commands are provided by the mechanical mixer box within the aircraft control system.

The majority of the test data obtained to describe the effectiveness of the exit louver system has been for collective vector and stagger angles only. These data, when non-dimensionalized in terms of fan static thrust, may be used to predict the rolling and yawing moments developed by differential louver deflections for any fan thrust level.

4.1.5.1 Exit Louver Vector Effectiveness

The incremental lift, drag and pitching moment coefficients due to collective exit louver vector angle are presented in Figures 4.9 and 4.10 for the range of thrust coefficient defining the transition speed range. The lift and drag increments were obtained by cross-plotting the data of Figure 6.7, which were obtained from full-scale and 1/6 scale tests. By plotting the incremental coefficients versus thrust coefficient, as in Figure 6.7, data comparisons are more easily made and the trends with thrust coefficient are evident.

At high values of thrust coefficient the 1/6 scale data show larger lift changes and smaller longitudinal force changes than the full-scale data, with improved agreement at intermediate thrust coefficients. The data in Figure 6.7 were faired in favor of the full-scale values to reflect the full-scale variation with thrust coefficient.

The incremental pitching moment coefficient due to exit louver vector angle, as shown in Figure 4.10, was taken from Figure 6.8 which shows both full-scale and 1/6 scale test data. The pitching moment coefficient increments are in generally good agreement for the two test sources. At high values of T_c^s (low flight speeds) vectoring is shown to produce positive (nose-up) pitching moments which decrease significantly as the thrust coefficient decreases (flight speed increases).

4.1.5.2 Exit Louver Stagger Effectiveness

Collective exit louver stagger effectiveness is shown in Figure 4.11. These curves were obtained from cross plots of a compilation of force and moment data presented in Figure 6.9. Due to the scarcity of louver stagger data, some results are included in Figure 6.9 from full-scale tests of a research fan in wing model reported in detail in Ref. 12.

The change in sign of the pitching moment coefficient due to stagger angle between $1.0 > T_c^s > .96$ is not clearly defined. Compared with the data from the 1/6 scale model and from Ref. 12, the Ames Test 173 data is subject to question in this range of thrust coefficient.

The stagger effectiveness data of Figure 4.11 was obtained for various louver vector settings approximating trimmed flight conditions. The schedule of vector settings with thrust coefficient for the various tests is included on the Figure. For the hovering condition, Figure 4.11 indicates a range of collective stagger from 13° to 37° provides a thrust change of 22% for lift control.

4.1.5.3 Longitudinal Trim in Transition

The basic tail-off longitudinal coefficients for zero angle of attack are presented in Figure 4.12 as functions of thrust coefficient and vector angle for the transition speed range. The intersection of the drag curves with the zero origin defines the trim values of thrust coefficient for zero longitudinal force. Corresponding available lift coefficients and the pitching moment coefficient representing the untrimmed pitching moment are then determined. Corrections to the coefficients due to the contributions of the horizontal tail, the nose fan, and stagger angle give the final trim values of the coefficients which are used to predict the longitudinal characteristics of the aircraft for the transition speed range.

4.1.6 Contribution of the Horizontal Tail

The horizontal tail was treated as an isolated surface with characteristics determined from wind tunnel test data. The tail lift, drag and moment referred to the airplane stability axes are given by:

$$L_t = \left[\left(\frac{dC_L}{d\alpha} \right)_t (\alpha - \epsilon + i_t) + \frac{dC_{L_t}}{d\delta_e} \delta_e - C_{D_t} \sin \epsilon \right] \eta_t \rho / 2 V^2 S_t$$

$$D_t = \left\{ C_{D_t} + \left[\frac{dC_{L_t}}{d\delta_e} \delta_e + \left(\frac{dC_L}{d\alpha} \right)_t (\alpha - \epsilon + i_t) \right] \sin \epsilon \right\} \eta_t \rho / 2 V^2 S_t$$

$$M_t = -L_t (\ell_t + Z_t \sin \alpha) + D_t (Z_t - \ell_t \sin \alpha)$$

where

$$\left(\frac{dC_L}{d\alpha} \right)_t = .053 \quad \text{(Figure 3.15)}$$

$$C_{D_t} = C_{D_{0_t}} + \frac{C_{L_t}^2}{e \pi A} \quad \text{(Figure 3.16)}$$

$$\frac{dC_{L_t}}{d\delta_e} = .023$$

$$\eta_t = f(\alpha) \quad \text{(Figure 3.14)}$$

$$\ell_t = 20.6 \text{ ft.}$$

$$Z_t = 7.82 \text{ ft.}$$

$$\bar{c} = 9.4 \text{ ft.} \quad S_t = 52.86 \text{ ft.}^2$$

In coefficient form based on wing geometry the tail expressions become:

$$\Delta C_{L_t} = \left[\left(\frac{dC_L}{d\alpha} \right)_t (\alpha - \epsilon + i_t) + \frac{dC_{L_t}}{d\delta_e} \delta_e - C_{D_t} \sin \epsilon \right] \eta_t \frac{S_t}{S_w}$$

$$\Delta C_{D_t} = \left\{ C_{D_t} + \left[\left(\frac{dC_L}{d\alpha} \right)_t (\alpha - \epsilon + i_t) + \frac{dC_{L_t}}{d\delta e} \delta e \right] \sin \epsilon \right\} \eta_t \frac{S_t}{S_w}$$

$$\Delta C_{m_t} = \left[\left(\frac{dC_L}{d\alpha} \right)_t (\alpha - \epsilon + i_t) + \frac{dC_{L_t}}{d\delta e} \delta e - C_{D_t} \sin \epsilon \right] \eta_t \frac{S_t}{S_w}$$

$$\frac{(\ell_t + \frac{Z_t \sin \alpha}{c})}{c} + \left\{ C_{D_t} + \left[\frac{dC_{L_t}}{d\delta e} \delta e + \left(\frac{dC_L}{d\alpha} \right)_t (\alpha - \epsilon + i_t) \right] \right.$$

$$\left. \sin \epsilon \right\} \eta_t \frac{S_t}{S_w} \left(\frac{Z_t - \ell_t \sin \alpha}{c} \right)$$

These coefficients may, in turn, be expressed in slipstream coefficient form as follows:

$$\Delta C_{L_t}^S = \Delta C_{L_t} \frac{S_w}{A_F} (1 - T_c^S)$$

$$\Delta C_{D_t}^S = \Delta C_{D_t} \frac{S_w}{A_F} (1 - T_c^S)$$

$$\Delta C_{m_t}^S = \Delta C_{m_t} \frac{S_w}{A_F} \frac{\bar{c}}{D_F} (1 - T_c^S)$$

Horizontal tail effectiveness, $\frac{dC_{m_t}^S}{d i_t}$, as determined from Ref. 2 is

shown in Figure 4.3. The linear variation with thrust coefficient shows that the effectiveness of the tail is unaltered by the wing fans. The effect of the horizontal tail modification made subsequent to the wind tunnel tests is indicated in Figure 4.13.

The variation of average downwash angle at the horizontal tail with angle of attack and thrust coefficient is shown in Figure 4.14. The downwash angle was determined from tail-on and tail-off pitching moment data from Ref. 2 from

$$\alpha_t = \alpha + i_t - \epsilon = 0$$

where α is the value common to tail-off and tail-on pitching moment for a given tail incidence angle. The downwash points were determined for 0° and 50° vector angle, with and without 15° aileron droop and with the nose fan inoperative. The effect of the variations due to vector angle and aileron droop appeared to be within 1 or 2 degrees downwash which is probably of the order of the accuracy in the data.

The estimated longitudinal stability of the XV-5A in the transition flight mode, shown in Figure 4.15, was calculated from the data of Figure 4.8 and the horizontal tail equations of this section. The contribution of the nose fan was derived from the data of Figure 6.10. While the absolute magnitude is not well defined, the available test data indicate a destabilizing influence due to nose fan operation. From Figure 4.15, the airplane is statically stable at thrust coefficients less than approximately .92 which corresponds to a flight speed of approximately 70 knots.

4.1.7 Contribution of the Nose Fan

The estimated installed static thrust characteristics of the nose fan are presented in Figure 4.21 for the nose fan thrust reverser doors at the maximum lift position. The control effectiveness of the reverser doors is shown in Figure 4.16 along with wind tunnel test data obtained on the full-scale and 1/6 scale models. The reference door angle for the full-scale Ames data has been referred from 0° for maximum lift to the 115° door position in order to correspond with the XV-5A door travel designation.

Attempts to define the actual lift and drag characteristics of the nose fan in forward flight were not successful due to apparent interference increments obtained when comparing nose fan-off and nose fan-on test data. The simplest approach is to assume constant nose fan thrust with flight speed and to calculate the pitching moment by using the static thrust reverser door effectiveness. This assumption is borne out reasonably well by the pitching moment data of Figure 6.11 obtained with the wing fans inoperative. The corresponding reduction in lift is apparently occurring to a large degree on the wing. Tests conducted with the wing fans operating do not show lift reductions as large as those with the wing fans off.

Nose fan lift coefficient for constant nose fan thrust and nose fan drag coefficient based on theoretical momentum drag are shown in Figure 4.17 versus nose fan thrust coefficient. From simple momentum theory,

$$\frac{D}{L} = \frac{\rho A V_j V}{\rho A V_j^2} = \frac{V}{V_j}$$

Assuming lift is equal to the static thrust, the jet velocity for the static condition is

$$V_{j_s} = \sqrt{\frac{L}{\rho A}}$$

and

$$V = \sqrt{\frac{2q}{\rho}}$$

from which

$$\frac{V}{V_{j_s}} = \sqrt{\frac{2qA}{L}}$$

Making use of slipstream terminology,

$$L = T = T_c^s q^s A$$

and

$$q^s = q + \frac{T}{A}$$

From which

$$\frac{V}{V_{j_s}} = \sqrt{\frac{2qA}{T_c^s q^s A}} = \sqrt{\frac{2(1-T_c^s)}{T_c^s}}$$

$$\therefore \frac{D}{L} = \frac{C_D^s}{T_c^s} = \sqrt{\frac{2(1-T_c^s)}{T_c^s}}$$

or

$$C_D^s = T_c^s \sqrt{\frac{2(1-T_c^s)}{T_c^s}} = \sqrt{2T_c^s (1-T_c^s)}$$

which is plotted in Figure 4.17.

The nose fan drag may be expressed as an incremental coefficient based on the wing fan geometry as follows:

$$\Delta C_D^S = \frac{C_{D_{NF}}^S q_{NF}^S A_{NF}^S}{q^S A_F^S} = C_{D_{NF}}^S \left(\frac{T_{NF}^S}{A_{NF}^S T_{c_{NF}}^S} \right) \left(\frac{A_F^S T_c^S}{T_{\infty}^S} \right) \times$$

$$\frac{A_{NF}^S}{A_F^S} = C_{D_{NF}}^S \frac{T_{NF}^S}{T_{\infty}^S} \frac{T_c^S}{T_{c_{NF}}^S}$$

Thus, the incremental drag coefficient of the nose fan is a function of the ratio of nose fan static thrust to the total wing fan static thrust and of the ratio of the thrust coefficients.

Substituting for $C_{D_{NF}}^S$,

$$\Delta C_D^S = T_{c_{NF}}^S \sqrt{\frac{2(1-T_{c_{NF}}^S)}{T_{c_{NF}}^S}} \left[\frac{T_{NF}^S}{T_{\infty}^S} \cdot \frac{T_c^S}{T_{c_{NF}}^S} \right] \sqrt{\frac{2(1-T_{c_{NF}}^S)}{T_{c_{NF}}^S}} \times$$

$$\left[\frac{T_{NF}^S}{T_{\infty}^S} T_c^S \right]$$

The nose fan thrust coefficient may be eliminated by use of the following relationship:

$$\frac{1-T_{c_{NF}}^S}{T_{c_{NF}}^S} = \frac{1-T_c^S}{T_c^S} \frac{T_{\infty}^S}{A_F^S} \frac{A_{NF}^S}{T_{NF}^S}$$

Therefore,

$$\Delta C_D^S = \sqrt{\frac{2(1-T_c^S)}{T_c^S} \frac{T_{\infty}^S}{A_F^S} \frac{A_{NF}^S}{T_{NF}^S}} \left[\frac{T_{NF}^S}{T_{\infty}^S} T_c^S \right]$$

which reduces to

$$\Delta C_D^S = T_c^S \sqrt{\frac{2(1-T_c^S)}{T_c^S} \frac{T_{NF}}{T_{000}} \frac{A_{NF}}{A_F}}$$

This incremental drag coefficient is compared in Figure 6.12 with experimental data obtained in the Ames 40 x 80 wind tunnel (Test 177). The reference wing fan thrust coefficient for the wing fans-off data is the equivalent value based on the average ratio of nose fan thrust to wing fan thrust for the fan speeds obtained in the tests.

4.2 CONVERSION, LONGITUDINAL

The transient condition of conversion between the fan-flight lift mode and the conventional flight mode is represented by slipstream coefficients in order to fair smoothly into the transition flight data. The magnitude of the equivalent static fan thrust, upon which the coefficients are based, is governed by the time response of fan speed following engine diverter valve actuation.

Longitudinal characteristics for zero angle of attack are shown in Figure 4.18 for the thrust coefficient range representing conversion ($0 < T_c^S \lesssim .88$). The effects of the various conversion configurations are indicated for the power-off condition ($T_c^S = 0$). The configuration with the wing inlet doors open at zero T_c^S does not represent a true flight condition as the doors are fully closed prior to complete fan speed run-down when conversion is made from fan powered flight to conventional flight.

The effects of angle of attack on the tail-off lift, drag and pitching moment coefficients during conversion are included with the transition data of Figures 4.4, 4.7 and 4.8. The estimated tail-on pitching moment curve slope as a function of thrust coefficient is shown in Figure 4.19.

4.3 FAN THRUST AND POWER CHARACTERISTICS

Estimated installed static thrust characteristics of the wing fans and nose fan for sea level standard day and 2500' hot day atmospheres are shown in Figures 4.20 and 4.21 as a function of gas generator throttle setting. Inasmuch as the fan thrust and rotational speed are known as a function of throttle setting, the knowledge of the actual gas horsepower available to the fan turbines is not required. It is convenient, however,

to express the fan thrust or disk loading in terms of some function of power in order to account for changes in fan static thrust with fan speed at a given power setting, as occurs at forward speeds. This is accomplished by the use of a fan power coefficient defined as

$$C_P^S = \frac{P_F \rho^{1/2}}{\left(\frac{T_{000}}{A_F}\right)^{3/2} A_F}$$

Where P_F is a hypothetical power available to the fans which varies only with throttle setting. For convenience, a value of unity is chosen for the static power coefficient and the variation of P_F with throttle setting as shown in Figure 4.20 is calculated from the known fan thrust.

Variations in power coefficient with thrust coefficient and exit louver angle are shown in Figures 4.22 and 4.23. These variations were determined from measured variations in fan speed at constant gas generator throttle settings during the full-scale wind tunnel tests. Assuming a constant power, P_F , the ratio of the power coefficient at any condition in transition flight to the static value is

$$\frac{C_P^S}{C_{P_o}^S} = \frac{\frac{P_F \rho^{1/2}}{\left(T_{000}/A_F\right)^{3/2} A_F}}{\frac{P_{F_o} \rho^{1/2}}{\left(T_{000}/A_F\right)_o^{3/2} A_F}} = \left[\frac{\left(T_{000}/A_F\right)_o}{\left(T_{000}/A_F\right)} \right]^{3/2}$$

Since the fan thrust is a linear function of the square of the fan speed,

$$\frac{C_P^S}{C_{P_o}^S} = \left\{ \frac{\left(T_{000}/A_F\right)_o}{\left(T_{000}/A_F\right)} \right\}^{3/2} = \left\{ \left(\frac{N_o}{N} \right)^2 \right\}^{3/2} = \left(\frac{N_o}{N} \right)^3 = \left(\frac{1}{N/N_o} \right)^3$$

Percentage changes in fan speed as determined during Ames Test 177 are shown in Figure 6.13. The power coefficient variation with exit louver vector angle at a thrust coefficient of unity was determined from the measured power data of Ref. 2.

The reference static thrust may be calculated from the power coefficient equation, for any exit louver angle and thrust coefficient, for a given value of P_F . If the flight speed which influences the magnitude of the thrust coefficient is a factor, the thrust must be calculated by iteration. In the above procedure, any increase in available fan power due to the gas generator ram recovery is assumed to be reflected in the fan speed increase with airspeed.

4.4 FAN MODE, LATERAL-DIRECTIONAL

The lateral-directional static stability derivatives with sideslip for the fan flight mode were determined from the test data of Ref. 2. Cross plots were made of angle of attack polars obtained at constant angles of yaw and the coefficients were converted from slipstream notation to conventional notation for comparison with data from Ref. 1, and for correction for the change in wing dihedral. The variation of the derivatives with thrust coefficient, angle of attack and for vector angles of 0° and 50° is shown in Figures 6.14, 6.15 and 6.16. The effect of fan operation is stabilizing in that the derivatives increase with increasing thrust coefficient.

The effect of the nose fan on the lateral-directional derivatives was determined from increments obtained from nose fan-on and nose fan-off tests. These increments are shown in Figures 6.17, 6.18, and 6.19. Inasmuch as the nose fan employed on the 1/3 scale model was not dynamically similar to the full-scale nose fan, a correction based on the nose fan drag was applied to the nose fan incremental effects on the lateral-directional stability derivatives. It was shown in Section 4.1.7 that the incremental drag coefficient of the nose fan when referred to the wing fan thrust coefficient, is a function of the ratio of the nose fan thrust to the wing fan thrust.

Therefore,

$$\frac{(\Delta C_D)_{\text{Full Scale}}}{(\Delta C_D)_{\text{Model}}} = \frac{(\Delta C_D^S)_{\text{FS}}}{(\Delta C_D^S)_{\text{Model}}} = \left\{ \frac{\left(T_{\text{NF}}/T_{\text{ooo}} \right)_{\text{FS}}}{\left(T_{\text{NF}}/T_{\text{ooo}} \right)_{\text{Model}}} \right\}^{1/2}$$

$$= \left(\frac{.122}{.240} \right)^{1/2} = .71$$

The increments of Figures 6.17, 6.18 and 6.19 were multiplied by this factor. It is conceivable that the influence of the nose fan on the lateral-directional characteristics results from flow interference as well as from the direct forces developed on the nose fan, but the principal factor affecting $C_{y\beta}$ and $C_{n\beta}$ is probably the nose fan drag force.

An additional correction was applied to $C_{\ell\beta}$ to account for the change in wing dihedral angle from -6° to $+4^\circ$ which was obtained from Ref. 1.

The increments applied due to the dihedral effect were:

α	$C_{\ell\beta}$
0°	-.00083
8°	-.00116
16°	-.00162

The final values of the estimated derivatives with the nose fan on were converted back to slipstream notation to permit extrapolation to the zero speed condition and are shown in Figures 4.24, 4.25, and 4.26. The effect of β_v as a variable was removed by using a trim schedule of T_c^s versus β_v and interpolating between the 0° and 50° vector data of Figures 6.14, 6.15 and 6.16. The values of the derivatives at zero T_c^s were taken from Ref. 1 for the wing dihedral angle of $+4^\circ$.

Only a limited amount of lateral-directional data was available from the full-scale Ames tests and is shown in comparison with 1/6 scale data in Figure 6.20. Considering the differences in the geometry of the two models and of the axes systems used, the data show good agreement.

The cross-coupling effect of pitching moment with sideslip angle in fan flight is shown in Figure 4.27 for 0° and 50° vector angle settings. The linear character of these curves with thrust coefficient permits represent-

ing the pitching moment coefficient in conventional notation which is independent of thrust coefficient as shown in Figure 4.28. The data for the 50° vector configuration agrees reasonably well with that for the power-off test of Ref. 1 (see Figure 3.21).

4.5 FAN-MODE, LATERAL-DIRECTIONAL CONTROL EFFECTIVENESS, CONVENTIONAL CONTROLS

The conventional flight control system is operable during all phases of flight and is thus independent of the fan exit louver control system utilized for the hovering and transition flight conditions. The contributions of the aileron and rudder to the lateral-directional control power are, therefore, additive to that of the fan system.

4.5.1 Aileron

In transition flight with the flaps deflected 45° , the ailerons are deflected differentially from the 15° droop position according to the aileron deflection schedule of Figure 3.53. The lateral control derivative shown in Figure 3.59 was developed for the deflection schedule from test data of Ref. 1 and 2 and includes the effect of the aileron force-feel tabs. Aileron effectiveness data obtained from the powered model tests of Ref. 2 are shown in Figure 6.21. These data show that the effectiveness of the ailerons is independent of fan operation and the control derivative in conventional notation remains constant with speed.

The differential aileron deflection schedule requires that the yawing moment due to aileron deflection be calculated separately for each aileron surface. Since the deflection schedule was not duplicated during the wind tunnel tests, this was accomplished by utilizing data obtained for single aileron deflection and for equal and opposite deflections. The total yawing moment coefficient was then determined and plotted versus the differential aileron deflection as in Figure 6.22. The resulting variation of yawing moment coefficient with differential deflection is linear to 25° and, according to the limited data available, increases with increasing thrust coefficient. This effect on the resulting yawing moment is not large, however, as the free stream dynamic pressure diminishes with increasing thrust coefficient. The final derivative of yawing moment coefficient with aileron deflection is shown in Figure 4.29.

The side force due to aileron deflection was too small to be discernible in the data scatter of the powered model tests and is, therefore, assumed to be the same as for the power-off condition as shown in Figure 3.55.

4.5.2 Rudder

The yawing moment derivative with rudder deflection, $C_{n\delta_r}$, is shown

in Figure 4.30 versus thrust coefficient. As in the case of the ailerons, the rudder effectiveness is unaffected by fan operation and may be considered a constant. Rolling moment and side force due to rudder deflection are given in Figures 3.65 and 3.67.

4.6 FAN MODE, HOVERING STABILITY

4.6.1 Vertical Flight

The effect of velocity in vertical ascent and descent as would occur in hovering flight is shown in Figure 4.31. The data in this figure, as determined from Ref. 2, are presented with the nose fan off in order to illustrate the relative damping of the wing fans and the aircraft proper. The change in pitching moment with vertical velocity from the static condition is seen to be largely due to the vertical drag forces developed on the wing-body-tail.

The estimated damping effect due to the nose fan, as shown in Figure 4.32, was determined from the data of Ref. 2 by putting nose fan only lift data in non-dimensional form, subtracting the vertical drag component and adding the resulting values as an increment to the nose fan off data of Figure 4.31. This procedure eliminates the off-design nose fan to wing fan thrust ratio which in the case of the 1/6 scale model was approximately 64% larger than for the full-scale airplane. While admittedly the nose fan used on the 1/6 scale model is not dynamically similar to full-scale, the data of Figure 4.32 represent the only information available on axial flow with the nose fan thrust reverser door system of the XV-5A represented.

4.6.2 Lateral Translation

The variations of the coefficients with thrust coefficient for low translational velocities along the Y axis are shown in Figure 4.33. These curves are presented for the nose-fan off as the effects of the nose fan could not be rationalized in the 1/6 scale data. For the model attitude tested, the trend of the nose fan effect was for a positive yawing moment increment which is opposite to that predicted. This is further complicated by the fact that the nose fan static thrust calibration indicated a negative yawing moment coefficient, C_n^S , of approximately $-.0010$. (See also Figure 4.4, Reference 2.) The yawing moment due to side velocity is relatively

small, however, with a coefficient of .0020 representing approximately 25% of the static directional control power available from the exit louver control system. The effects of roll angle in lateral translation are also small and are illustrated in Ref. 2.

Flight velocities of 10, 20 and 35 knots are indicated on Figure 4.33. These speeds were calculated for a wing fan disk loading of 210 lbs./ft.² which is representative of a trimmed lift condition for 9200 pounds gross weight.

4.6.3 Rearward Flight

The variation of the longitudinal coefficients for zero pitch attitude in rearward flight is shown in Figure 4.34. The data presented are for the nose fan off to permit comparison with forward flight characteristics at low speeds. The nose fan incremental effects may be added as explained in the section on transition longitudinal characteristics. Nose fan control effectiveness obtained at a thrust coefficient of .992 with the 1/6 scale model compares favorably with that obtained statically.

The drag coefficient of Figure 4.34 has been reduced by an increment determined from comparisons of Ames data and 1/6 scale data for forward speeds. This correction amounts to a reduction of approximately 25% in the small-scale data.

The effect of negative vectoring in rearward flight is shown in Figure 4.35 for various combinations of T_c^S and β_v . These curves were converted to stability axes from the body axes data of Ref. 2, to show the aircraft pitch angle required to trim the drag force in rearward flight or for hovering in a tail wind. At a thrust coefficient of .994 the ratio of vector angle to pitch angle for trim is approximately 2 to 1. The drag data of Figure 4.35 have been corrected as discussed above.

Also shown in Figure 4.35 is the estimated condition with the nose fan supplying the required pitching moment for trim at a rearward speed of 10 knots. The nose fan thrust reverser door setting is that required for 45% of the maximum nose fan thrust capability compared with 37% for the static condition. The data of Figure 4.35 indicate that speeds greater than 10 knots may be trimmed for $-5^\circ \beta_v$. For example, a rearward flight speed of 20 knots requires a nose up pitch angle of approximately 4° and 60% of the maximum nose fan thrust for moment trim. The maximum nose fan thrust is assumed to be 14.6% of the wing fan thrust for these calculations.

Full-scale flight velocities of 10 and 20 knots are indicated on Figure 4.35 for reference and are based on a wing fan disk loading of 210 lbs./ft.².

XV-5A

ESTIMATED LIFT CHARACTERISTICS IN FAN MODE

$\alpha = 0^\circ$ $\beta_1 = 0^\circ$ $\beta_2 = 0^\circ$ TAIL-OFF NOSE FAN OFF

○ ANES TEST 173 $\alpha = 0^\circ$ $\beta_1 = 0^\circ$ $\beta_2 = 0^\circ$ POWER-OFF LIFT DELETED, TAIL-OFF 1.6

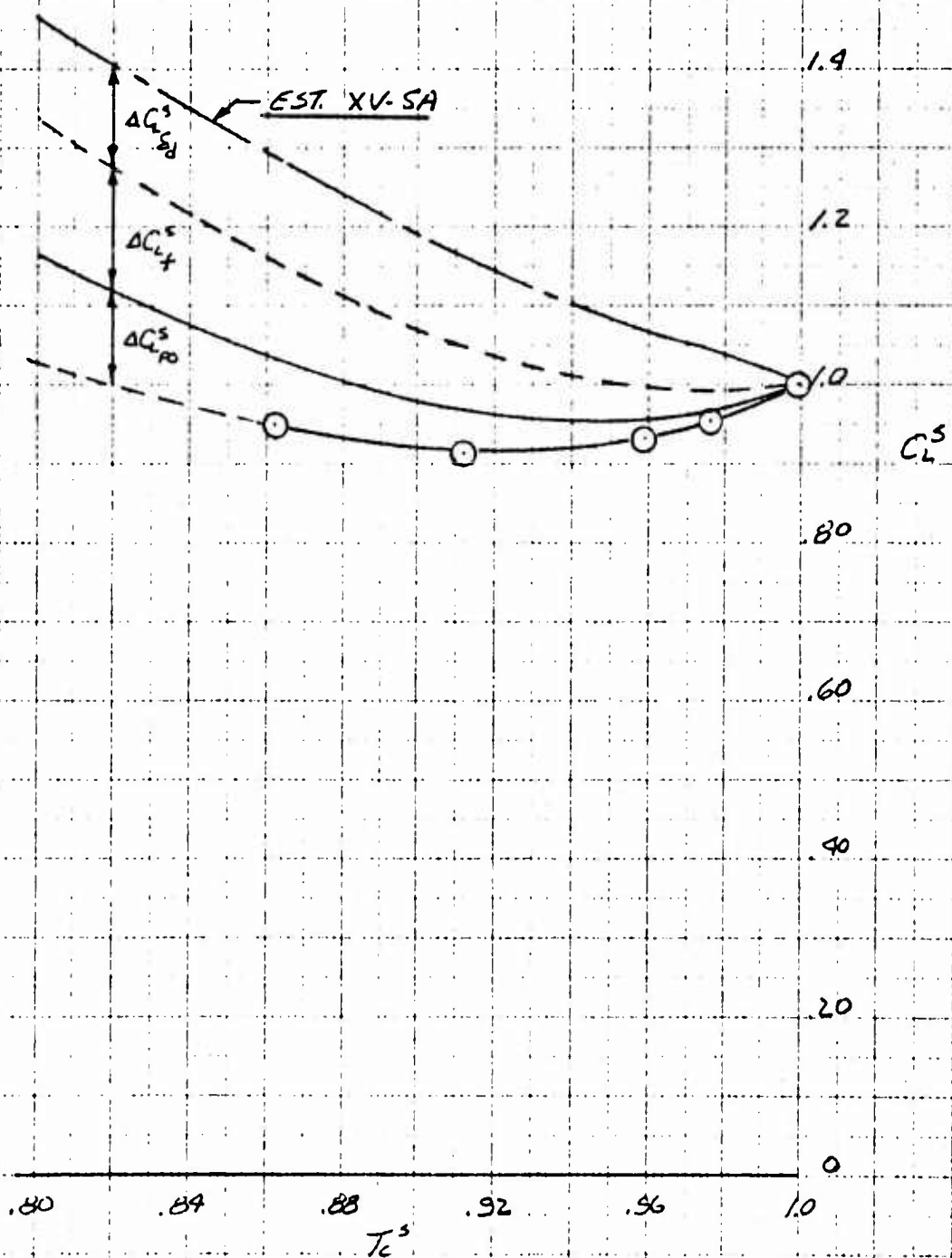


Figure 4.1

XV-5A

ESTIMATED DRAG CHARACTERISTICS IN FAN MODE

$\alpha = 0^\circ$ $\delta_f = 45^\circ$ $\beta_f = 0^\circ$ $\beta_s = 0^\circ$ TAIL OFF NOSE FAN OFF

○ AMES TEST 173 $\alpha = 0^\circ$ $\delta_f = 45^\circ$ $\beta_f = 0^\circ$ $\beta_s = 0^\circ$ TAIL OFF

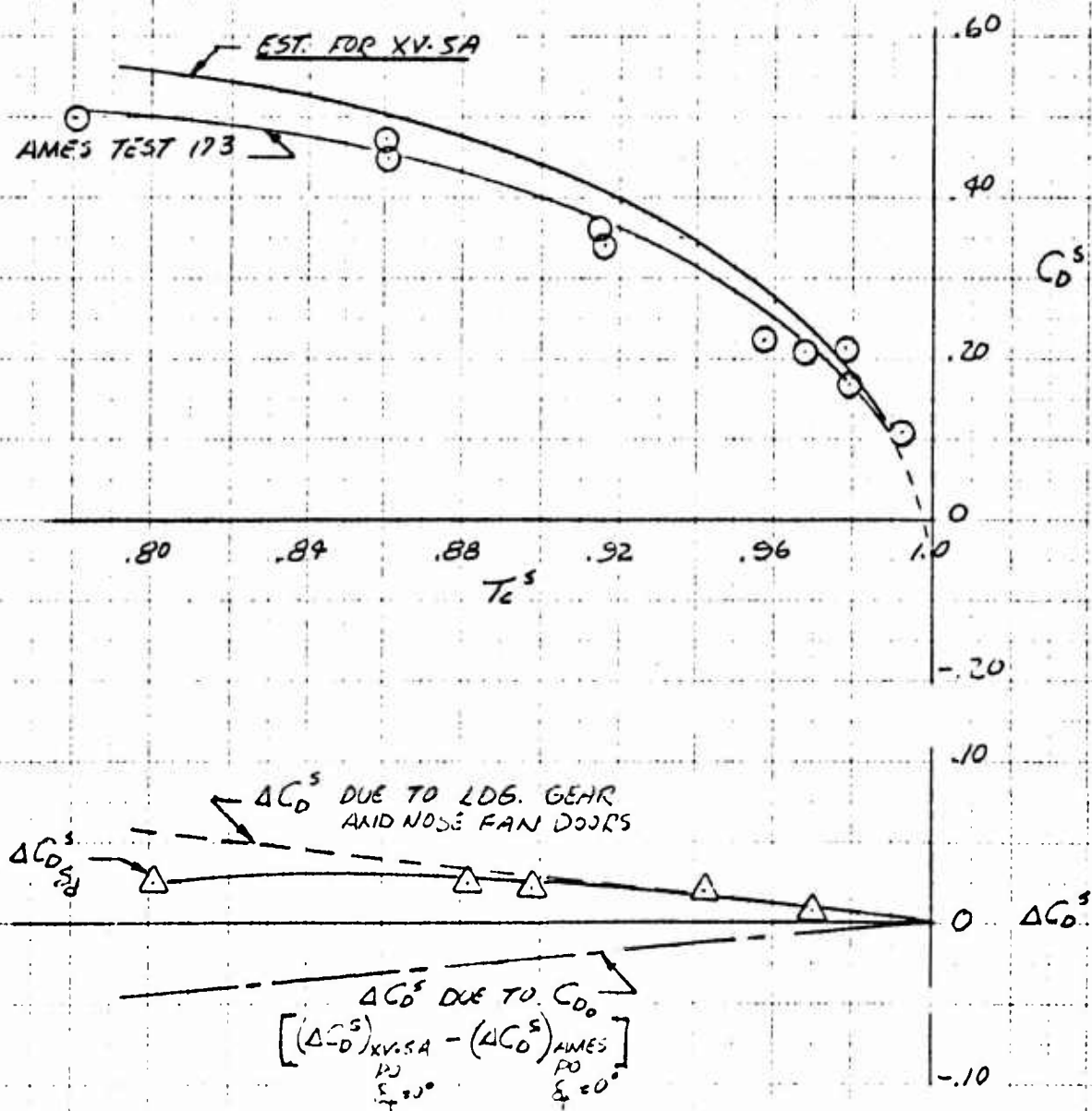


Figure 4.2

XV-5A

ESTIMATED PITCHING MOMENT CHARACTERISTICS IN FAN MODE

$\alpha = 0^\circ$ $\beta_v = 0^\circ$ $\beta_s = 0^\circ$ TAIL-OFF NOSE FAN OFF

CG AT STA 246 WL 112

○ ANES TEST 173 $\alpha = 0^\circ$ $\beta_v = 0^\circ$ $\beta_s = 0^\circ$ TAIL OFF

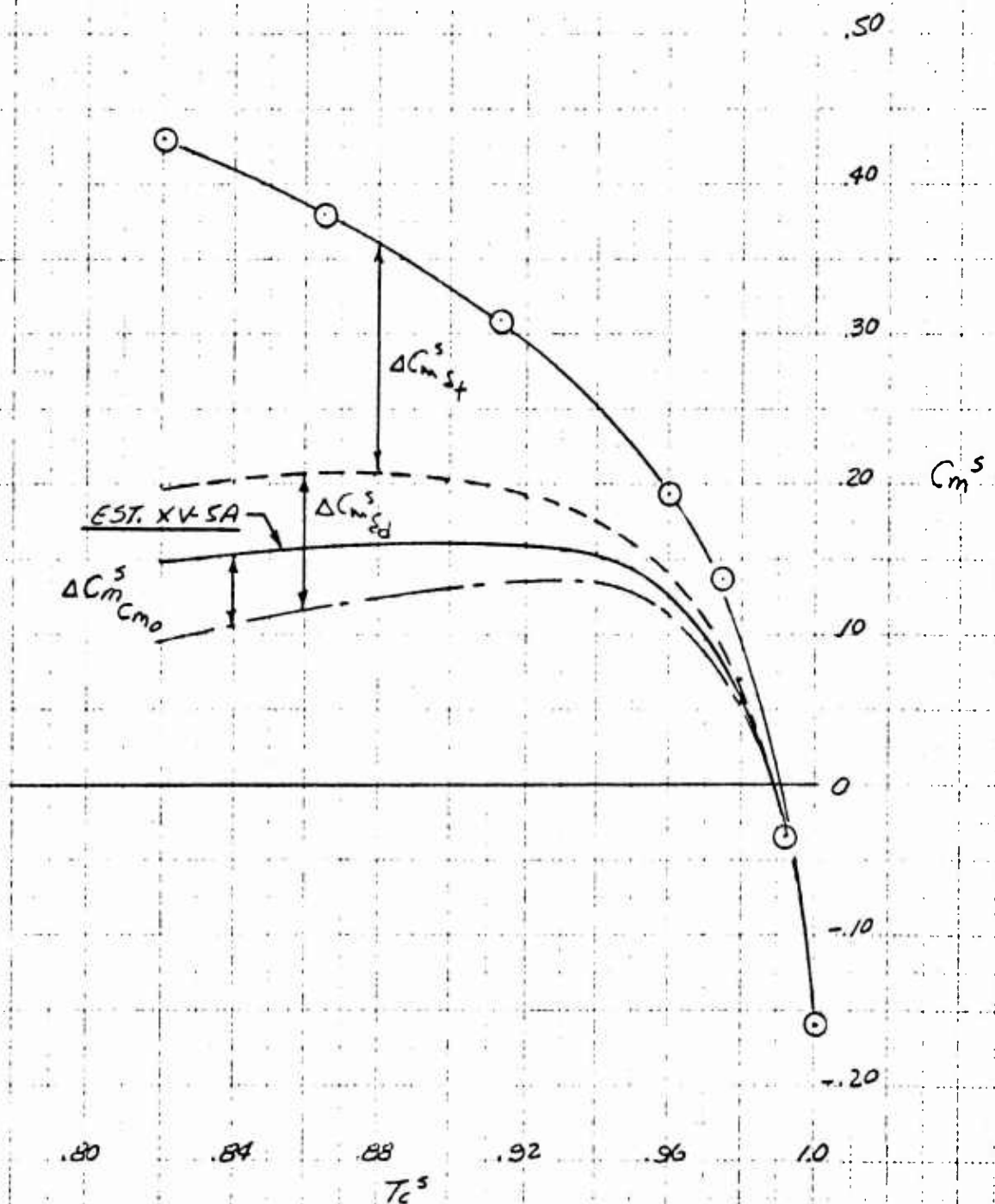


Figure 4.3

XV-5A

VARIATION OF LIFT CURVE SLOPE WITH
THRUST COEFFICIENT AND VECTOR ANGLE

WING DOORS $\delta_f = 45^\circ$, $\delta_r = 0^\circ$, TAIL OFF, CG @ FUS STA 246
WL 112

WING DOORS	δ_f	δ_r
CLOSED	77°	—
CLOSED	50°	16°
OPEN	50°	—

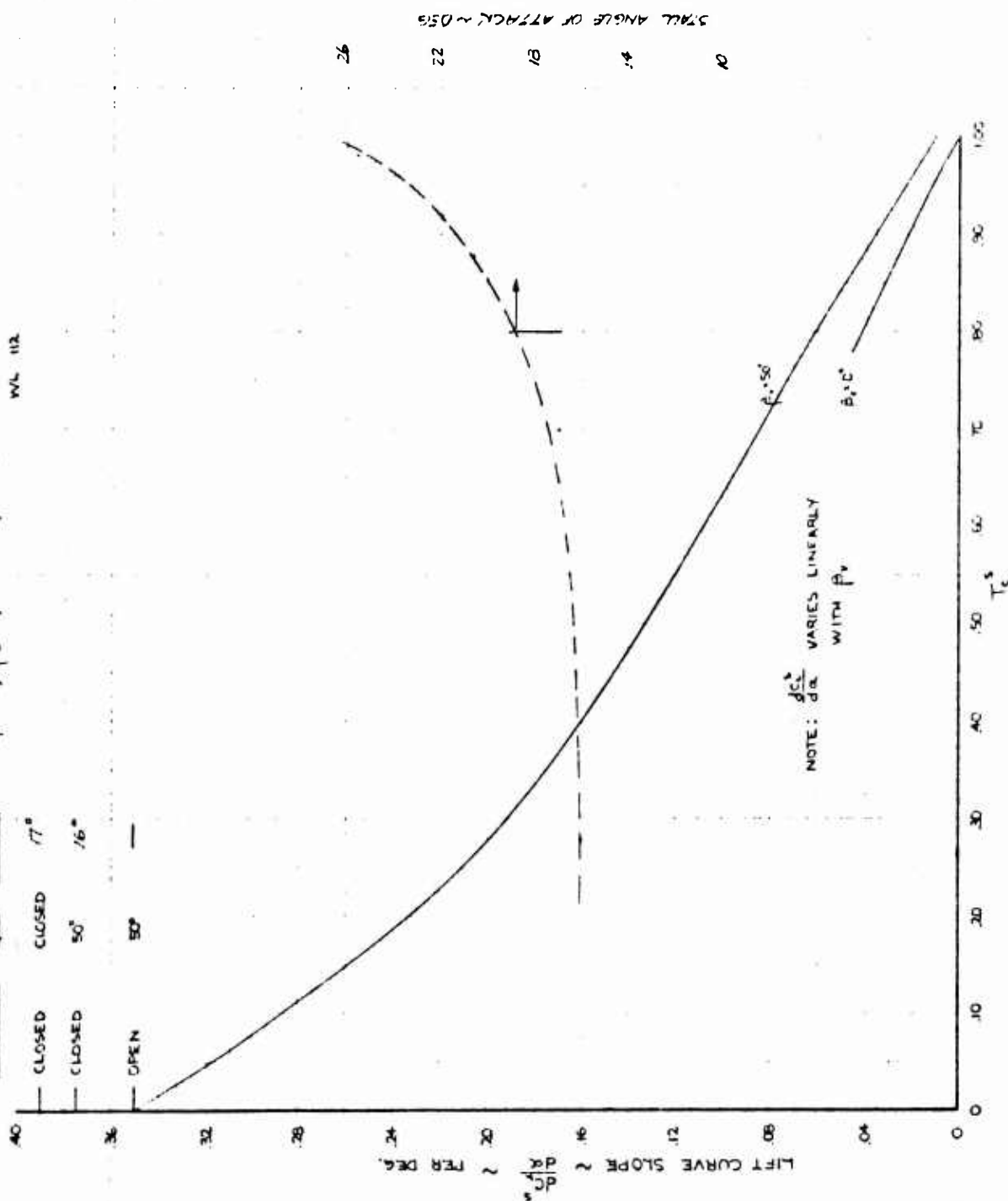


Figure 4.4

XV-5A

ESTIMATED ΔC_D^s DUE TO ANGLE OF ATTACK

TAIL-OFF, $\delta_f = 45^\circ$, $\delta_d = 15^\circ$, $\beta_v = 0^\circ$, $\beta_s = 0^\circ$

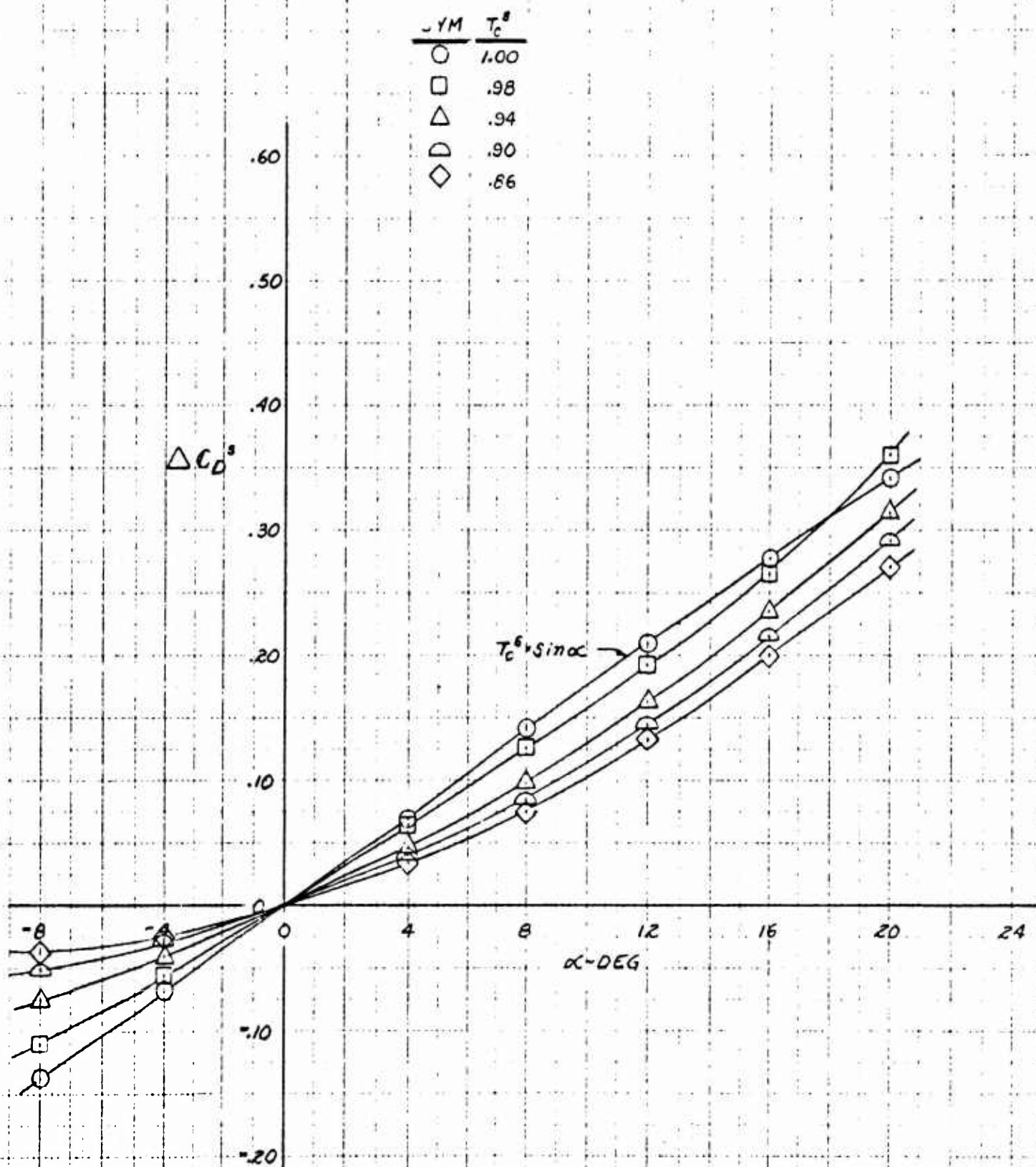


Figure 4.5

XV-5A

ESTIMATED ΔC_D^s DUE TO ANGLE OF ATTACK

TAIL-OFF, $\delta_f = 45^\circ$, $\delta_d = 15^\circ$, $\beta_v = 50^\circ$, $\beta_s = 0^\circ$

SYM	T_C^s
○	1.00
□	.98
△	.94
◐	.90
◇	.86
◓	.80

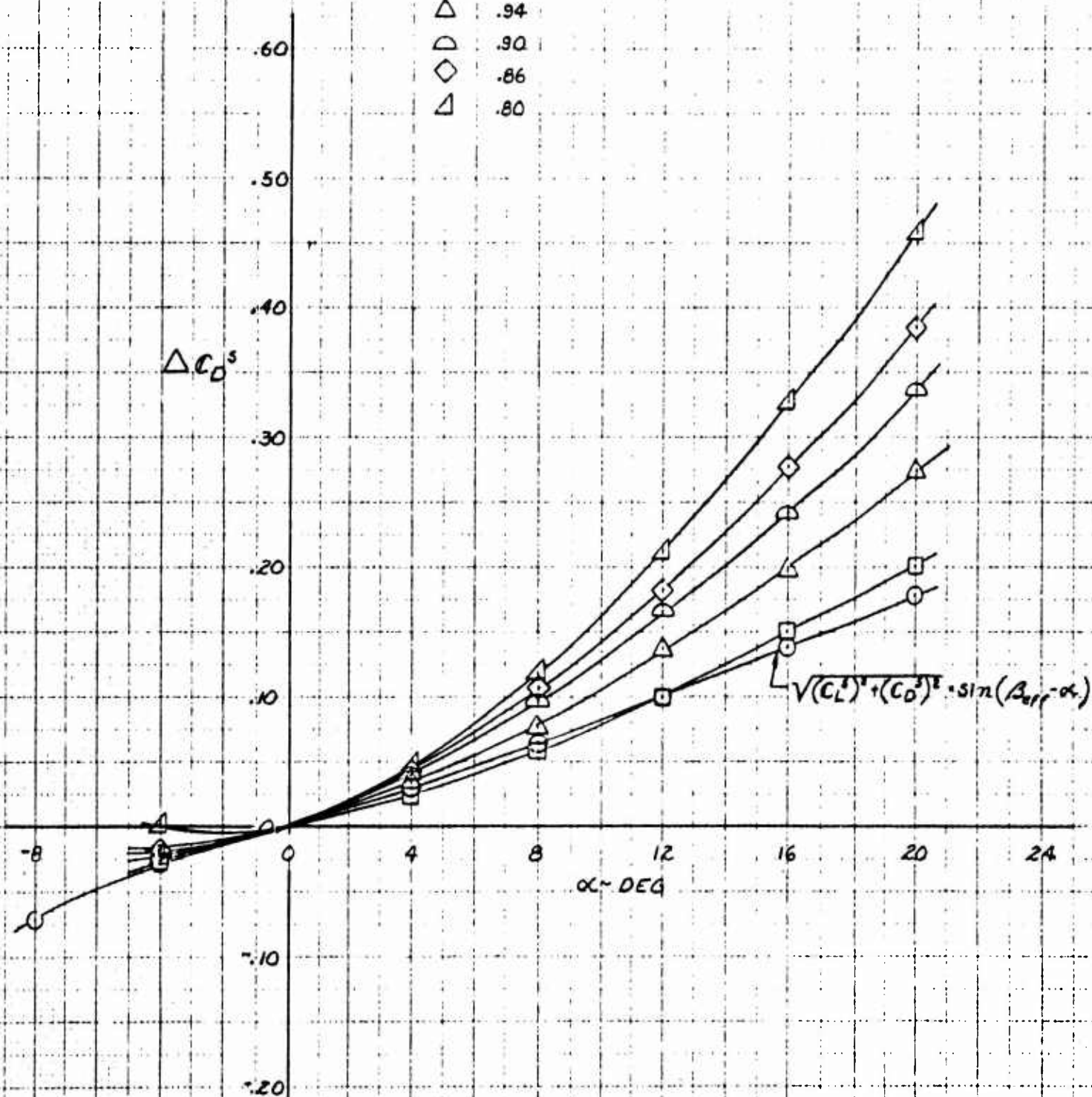


Figure 4.6

XV-5A

ESTIMATED ΔC_D^s DUE TO ANGLE OF ATTACK

TAIL-OFF, $\delta_f = 45^\circ$, $\delta_d = 15^\circ$, $\beta_v = 50^\circ$, $\beta_s = 0^\circ$

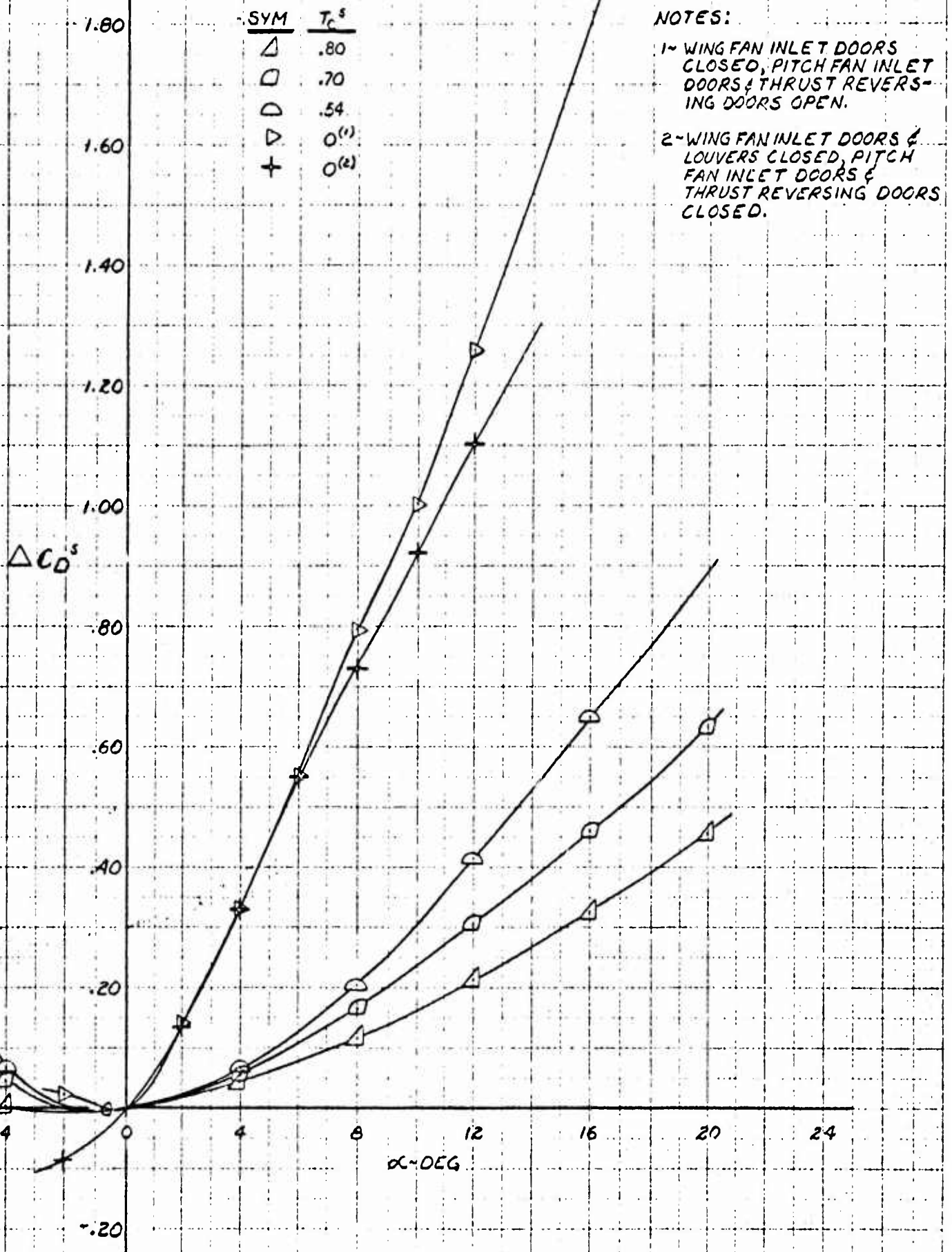


Figure 4.7

XV-5A

VARIATION OF PITCHING MOMENT CURVE SLOPE WITH THRUST COEFFICIENT

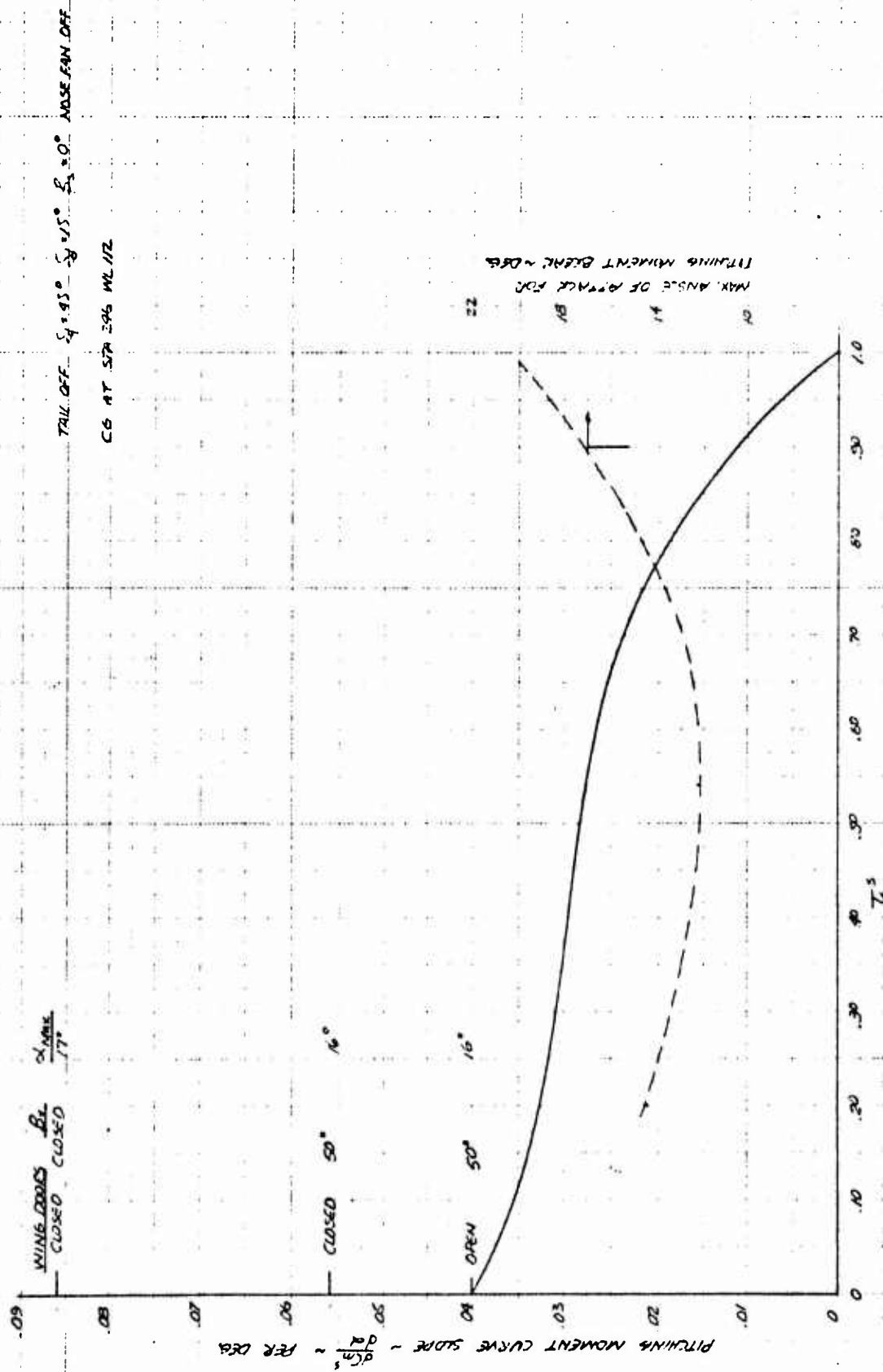
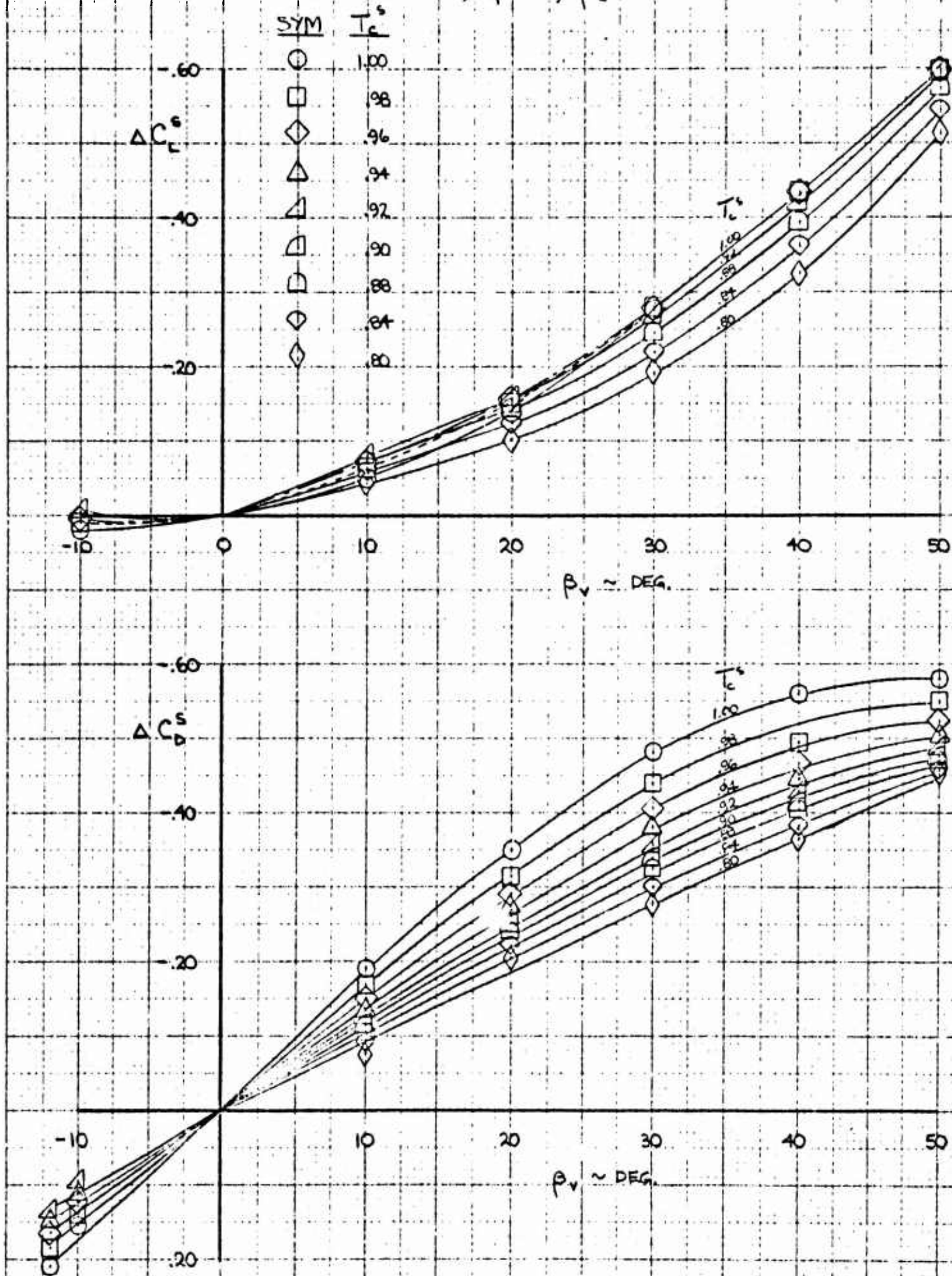


Figure 4.8

XV-5A

INCREMENTAL LIFT AND DRAG COEFFICIENTS DUE TO EXIT LOUVER VECTOR ANGLE

$\alpha = 0^\circ, \delta_f = 45^\circ, \beta_s = 0^\circ$



CH 9-11-63

Figure 4.9

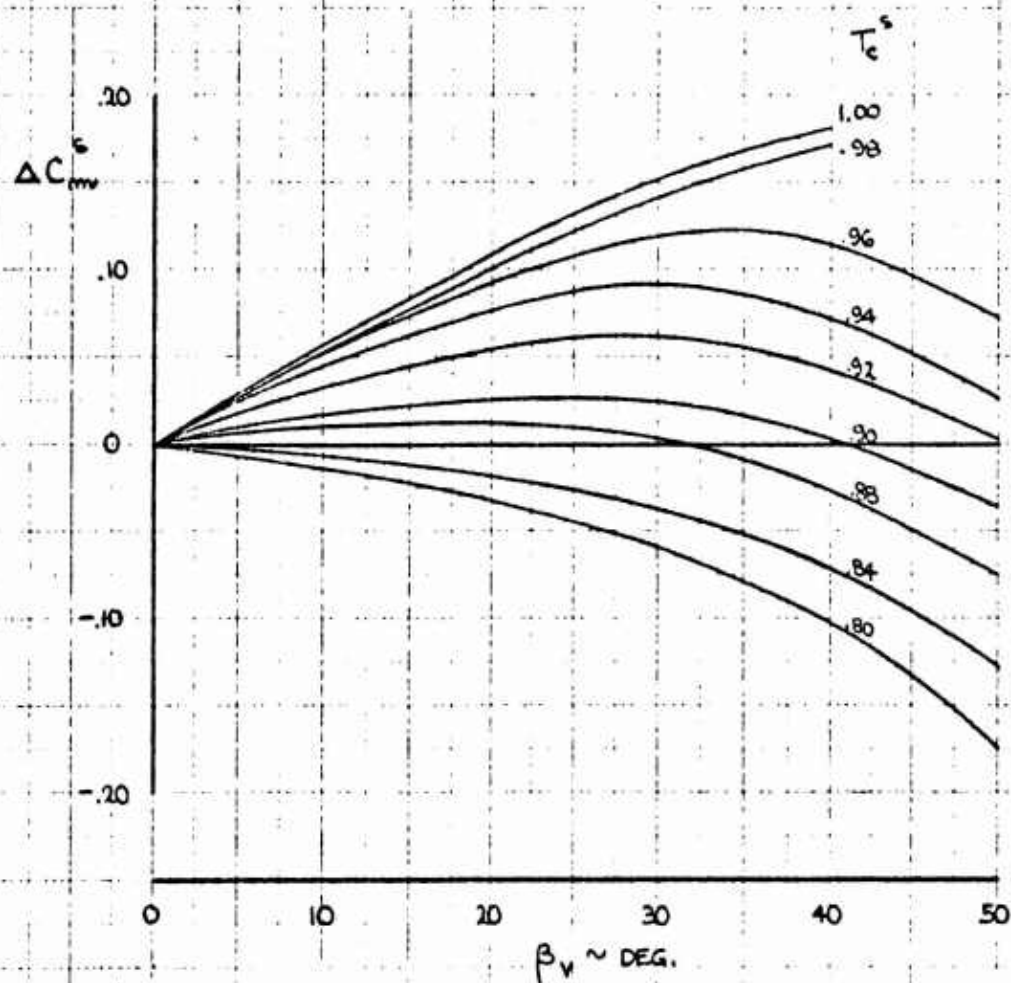
XV-5A

INCREMENTAL PITCHING MOMENT COEFFICIENT DUE TO EXIT LOUVER VECTOR ANGLE

$\alpha = 0^\circ$, $\delta_f = 45^\circ$, $\delta_d = 15^\circ$, $\rho_s = 0^\circ$

CG, @ FUS. STA. 246

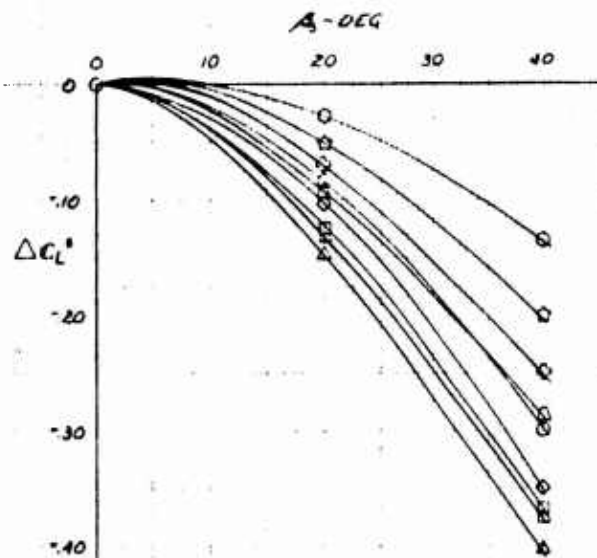
WL 112



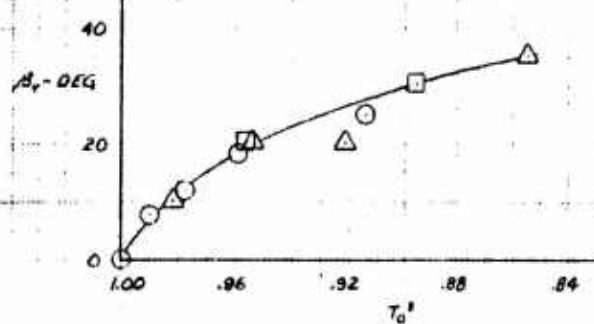
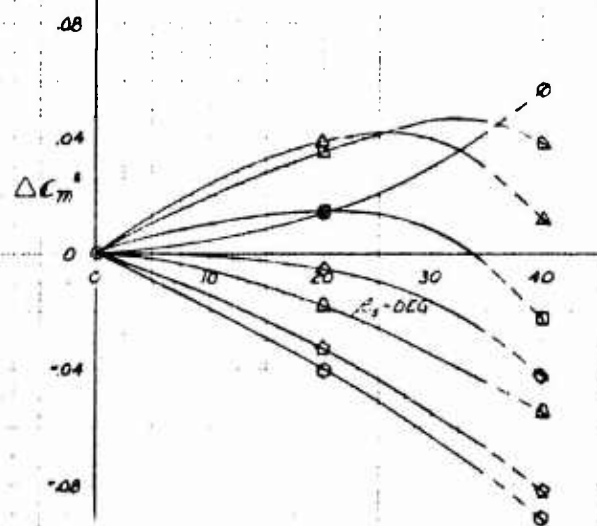
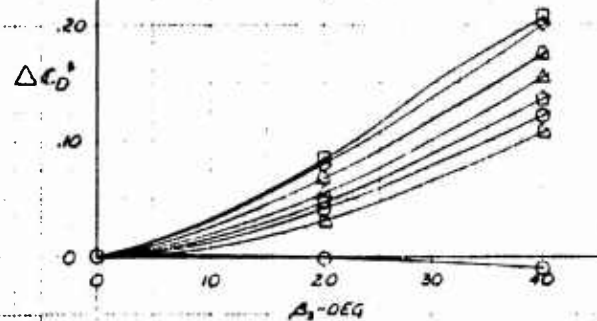
XV-5A

EFFECT OF EXIT ADJUSTER STAGGER ON LONGITUDINAL CHARACTERISTICS

$\alpha = 0^\circ, \delta_f = 45^\circ$



SYM	T_e
○	1.00
□	.99
△	.98
◇	.96
◇	.94
△	.92
◇	.90
☆	.88
○	.86



VECTOR ANGLE SETTINGS FOR
STAGGER EFFECTIVENESS DATA

SYM.	SOURCE
○	AMES XV-5A MODEL
△	AMES TEST 158
□	1/6 SCALE MODEL DATA

Figure 4.11

XV-5A

LONGITUDINAL COEFFICIENTS
IN
TRANSITION SPEED RANGE

$\delta_f = 45^\circ, \delta_d = 15^\circ, \beta_s = 0^\circ, \alpha = 0^\circ$

TAIL OFF
NOSE FAN OFF

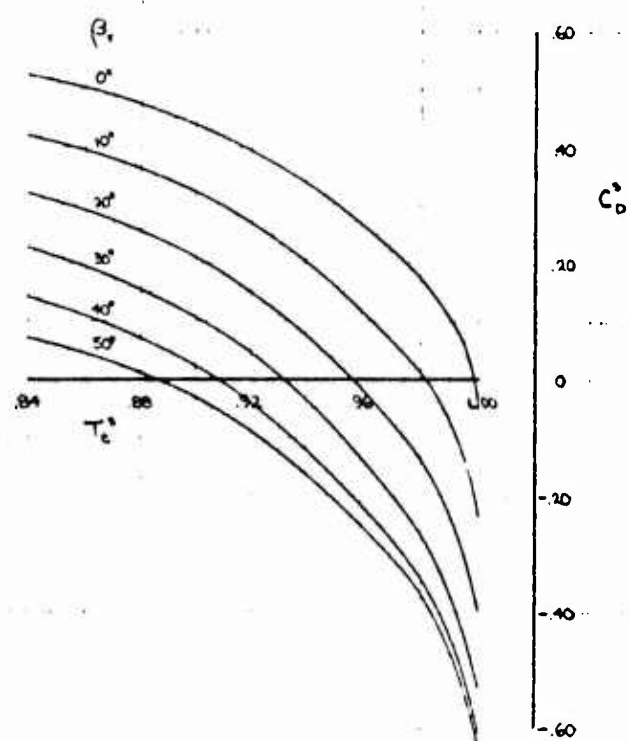
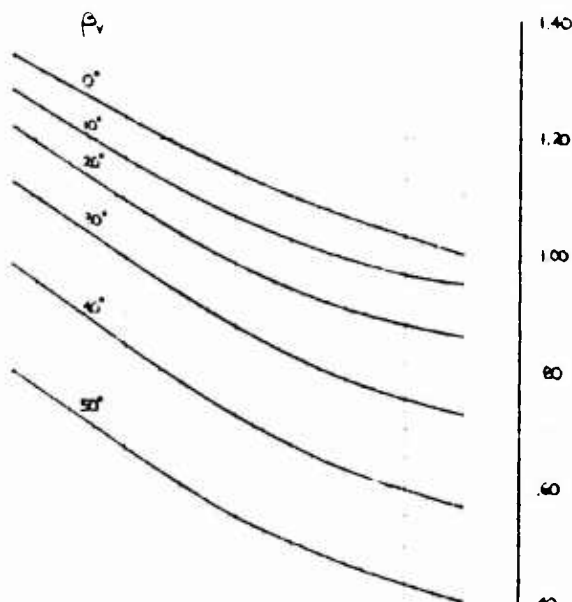
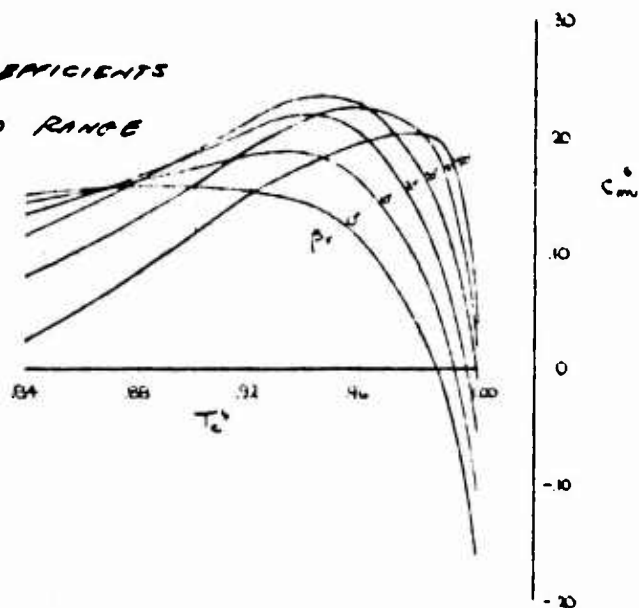
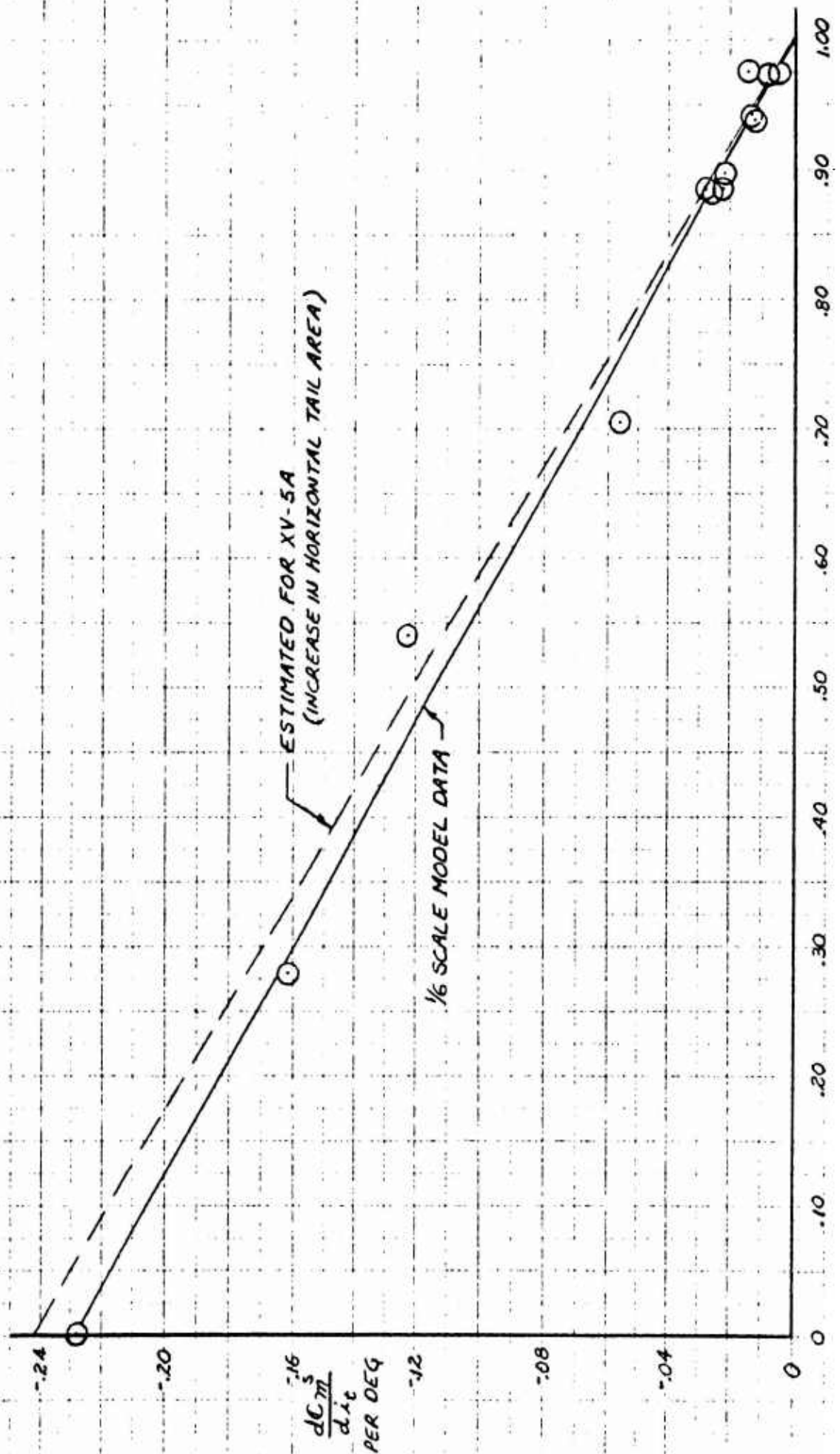


Figure 4.12

XV-5A

HORIZONTAL TAIL EFFECTIVENESS
IN
FAN POWERED FLIGHT MODE

$\alpha = 0^\circ, \delta_f = 45^\circ, \beta_s = 0^\circ, \text{C.G. C.F.S. 246}$



XV-5A

DOWNWASH AT HORIZONTAL TAIL
VS

AIRCRAFT ANGLE OF ATTACK

$\delta_f = 45^\circ, \delta_2 = 15^\circ, \beta_3 = 0^\circ$

SOURCE
AMES XV-5A MODEL
1/6 SCALE MODEL DATA

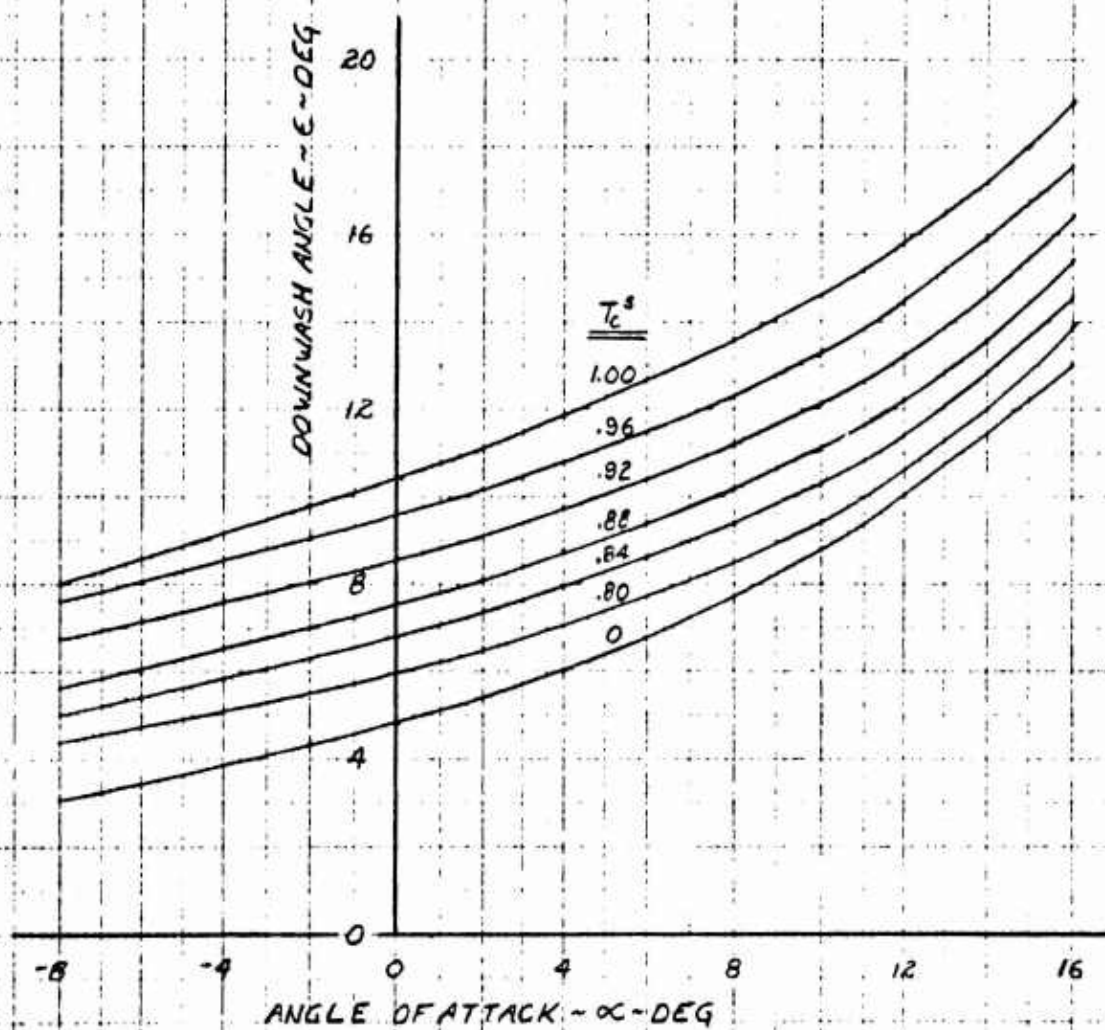


Figure 4.14

XV-5A

ESTIMATED LONGITUDINAL STATIC STABILITY
IN TRANSITION SPEED RANGE

$\delta_f = 45^\circ$, $\beta_s = 0^\circ$, TAIL-ON, C.G. @ F.S. 246.

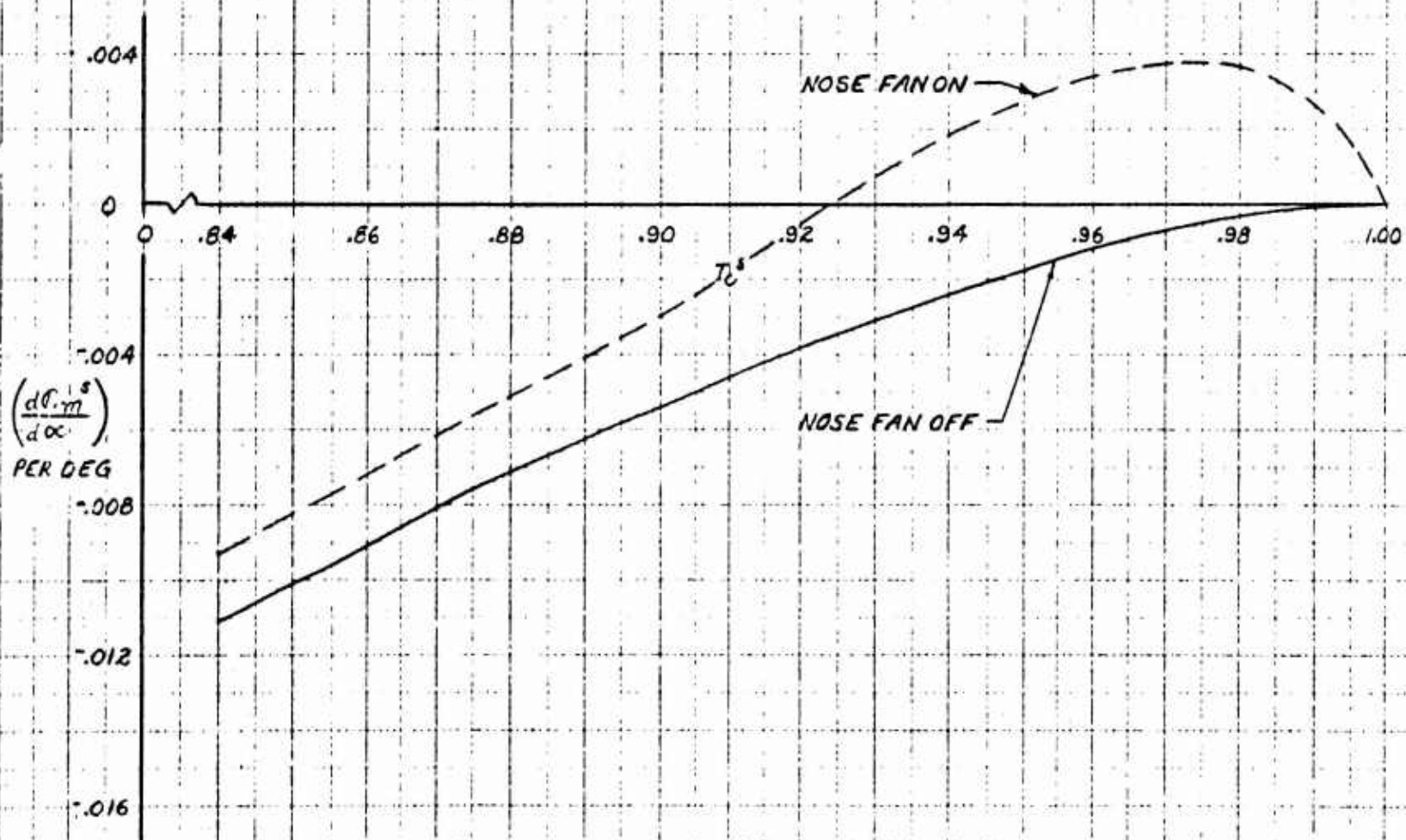


Figure 4.15

XV-5A

NOSE FAN STATIC LIFT VARIATION WITH THRUST REVERSER DOOR POSITION

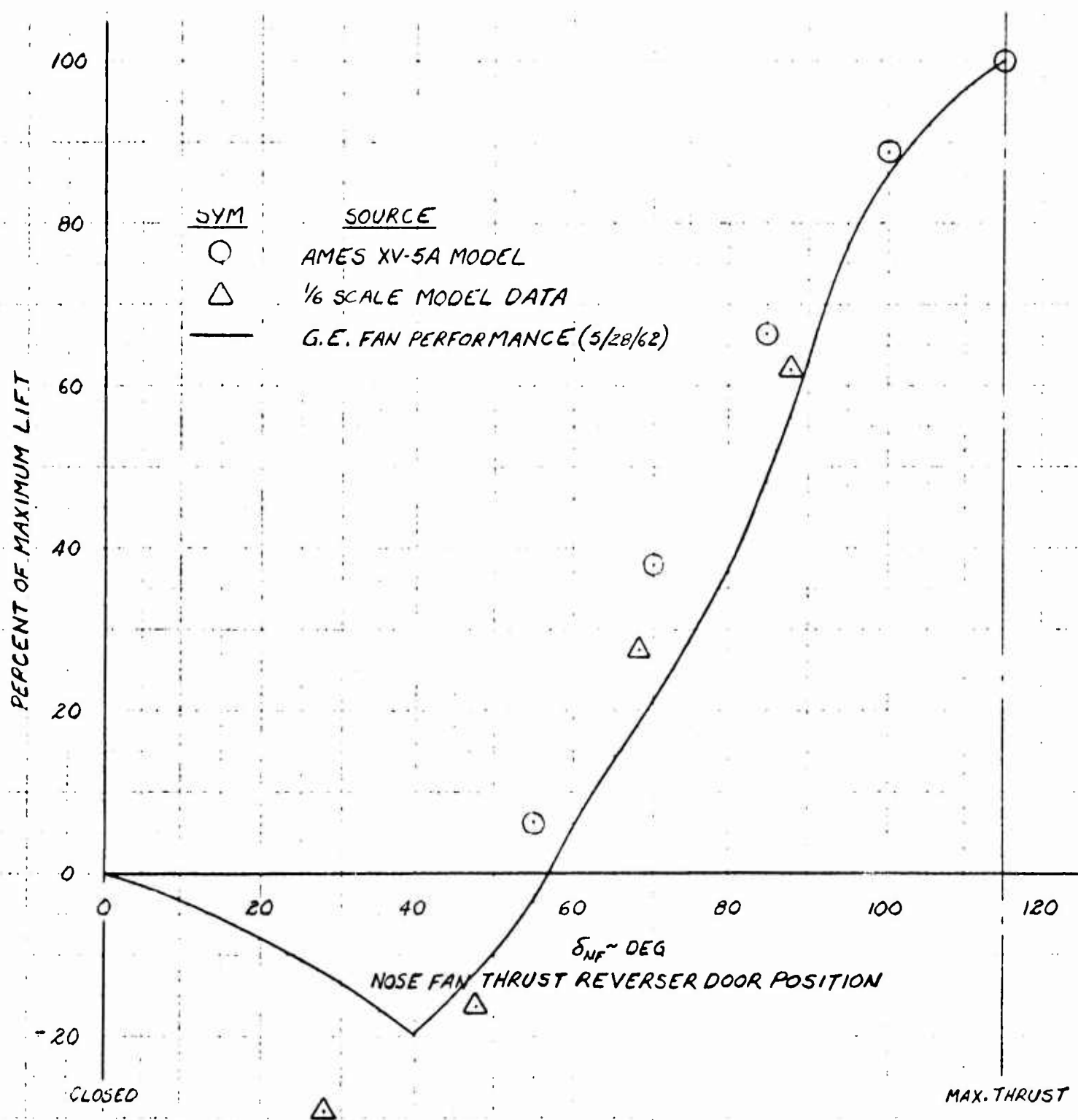


Figure 4.16

XV-5A

ESTIMATED NOSE FAN LIFT & DRAG
COEFFICIENTS

$\alpha = 0^\circ$

$C_{D_{NF}}^s$ = ESTIMATED THEORETICAL RAM DRAG

$C_{L_{NF}}^s$ = BASED ON CONSTANT THRUST WITH THRUST REVERSER
DOORS AT MAXIMUM LIFT POSITION

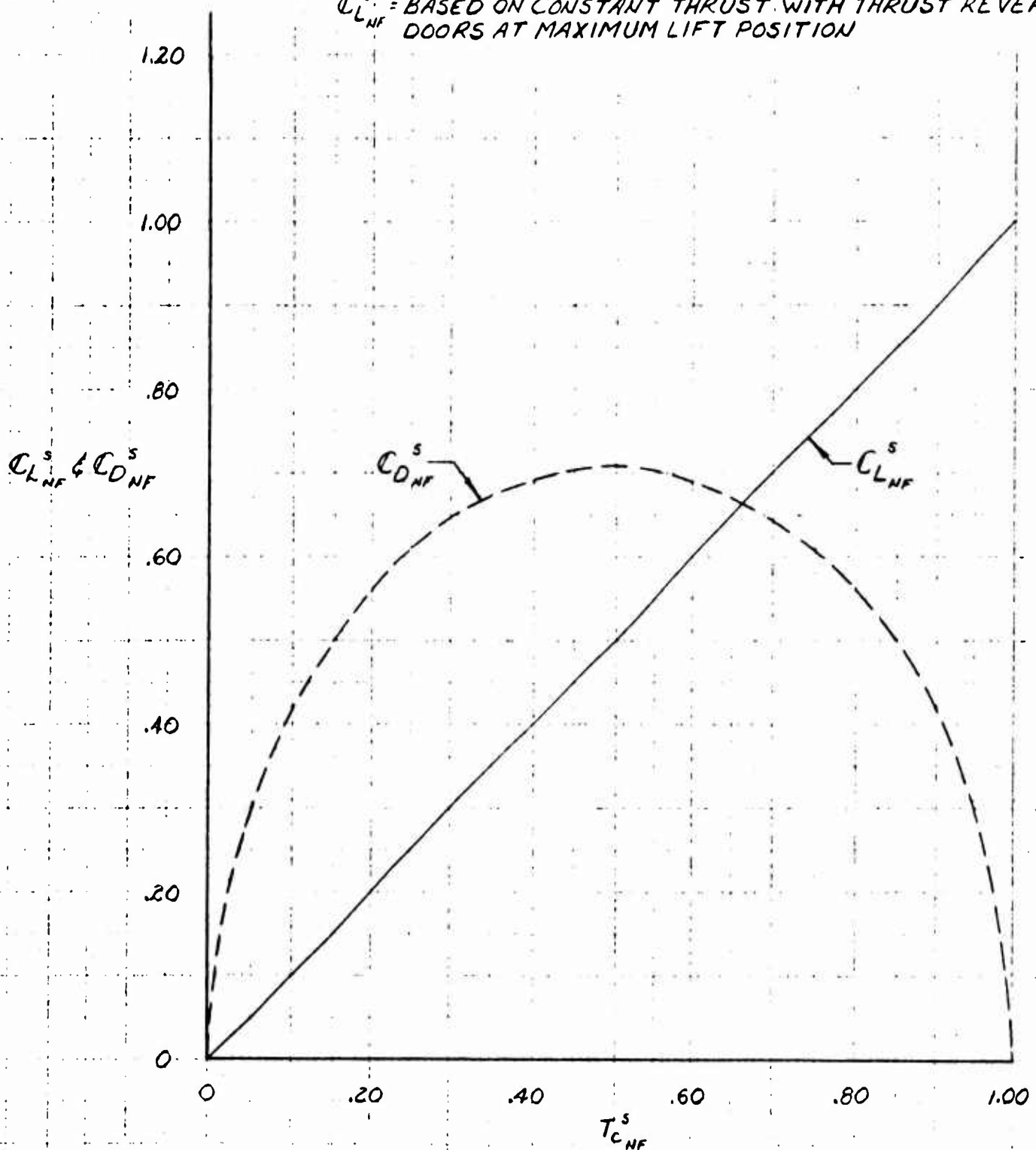


Figure 4.17

XV-5A

ESTIMATED TAIL-OFF LONGITUDINAL CHARACTERISTICS
FOR
CONVERSION

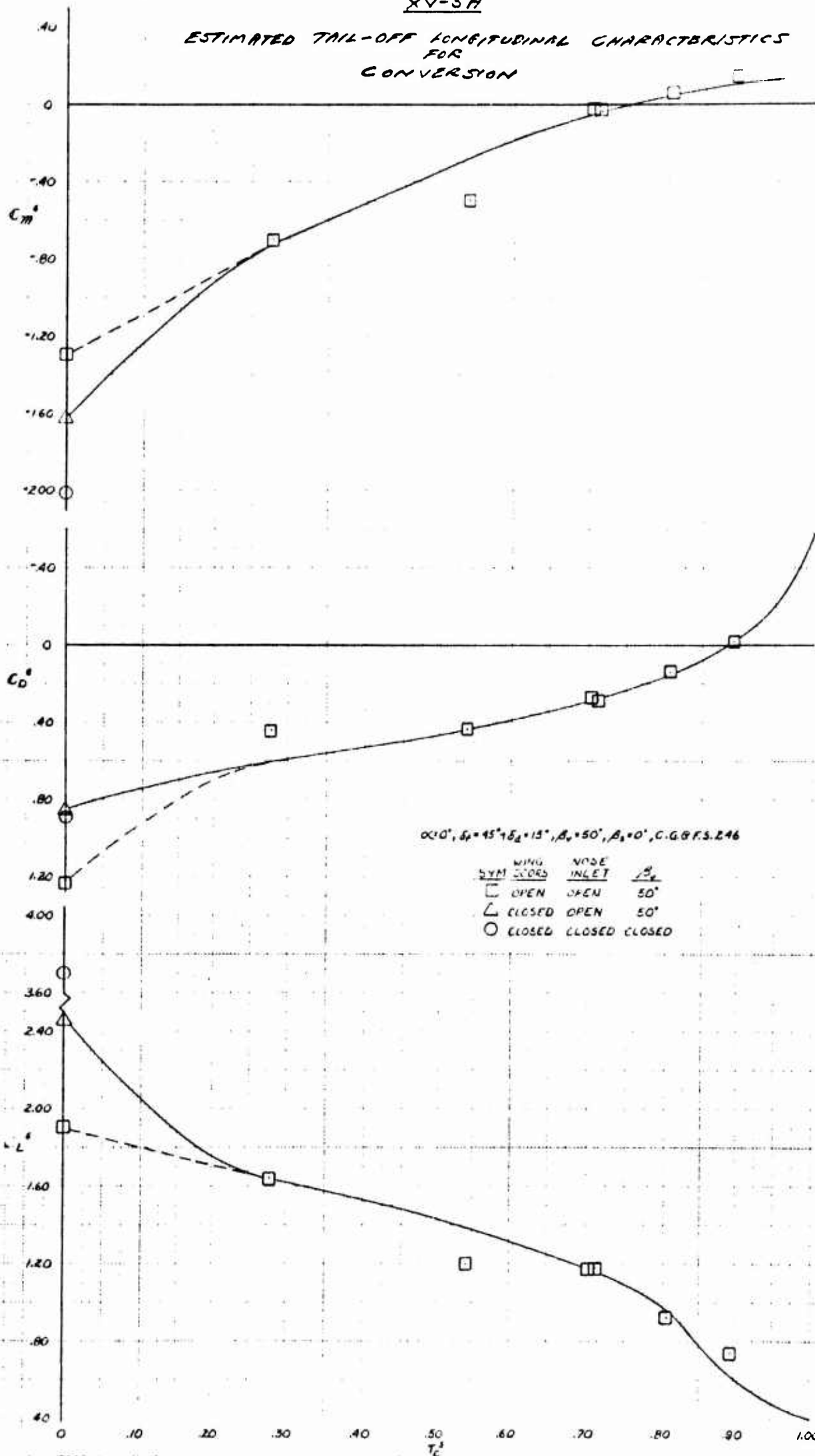


Figure 4.18

XV-5A

ESTIMATED TRAIL-ON PITCHING MOMENT CURVE SLOPE FOR CONVERSION

$\delta_f = 45^\circ$; $\delta_d = 15^\circ$; C.G. @ F.S. 246, NOSE FAN OFF

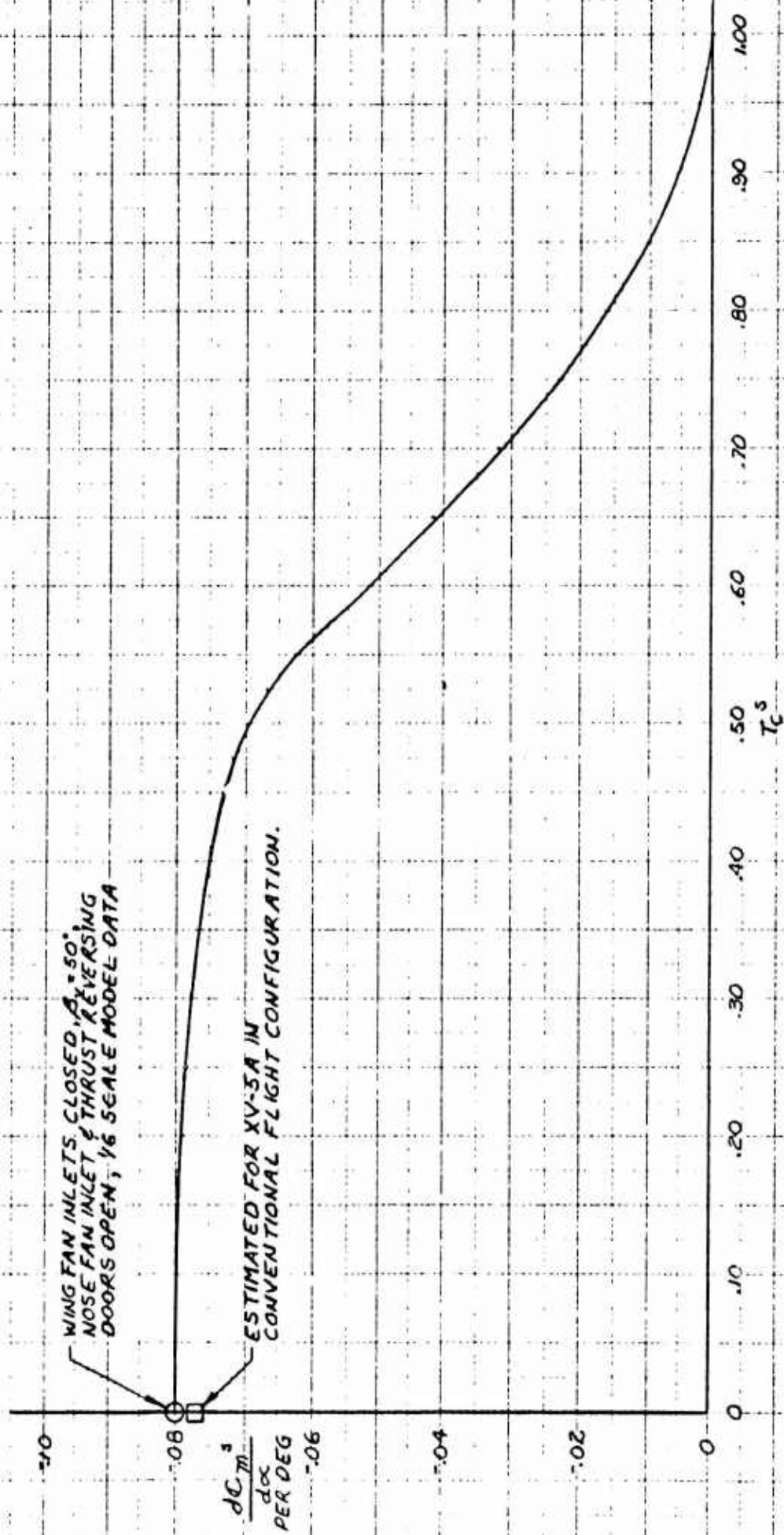


Figure 4.19

XV-5A

WING FAN STATIC LIFT AND POWER

SYM CONDITIONS

○ STANDARD DAY, SEA LEVEL

□ ANA421 STANDARD HOT DAY, 2500 FT. ALTITUDE

THRUST BASED ON 12.3% BLEED FOR NOSE FAN

$$C_{P_0}^s = \frac{P_F \rho^{1/2}}{\left(\frac{T_{000}}{A_F}\right)^{3/2} A_F} = 1.0$$

$$A_F = 42.6 \text{ FT}^2$$

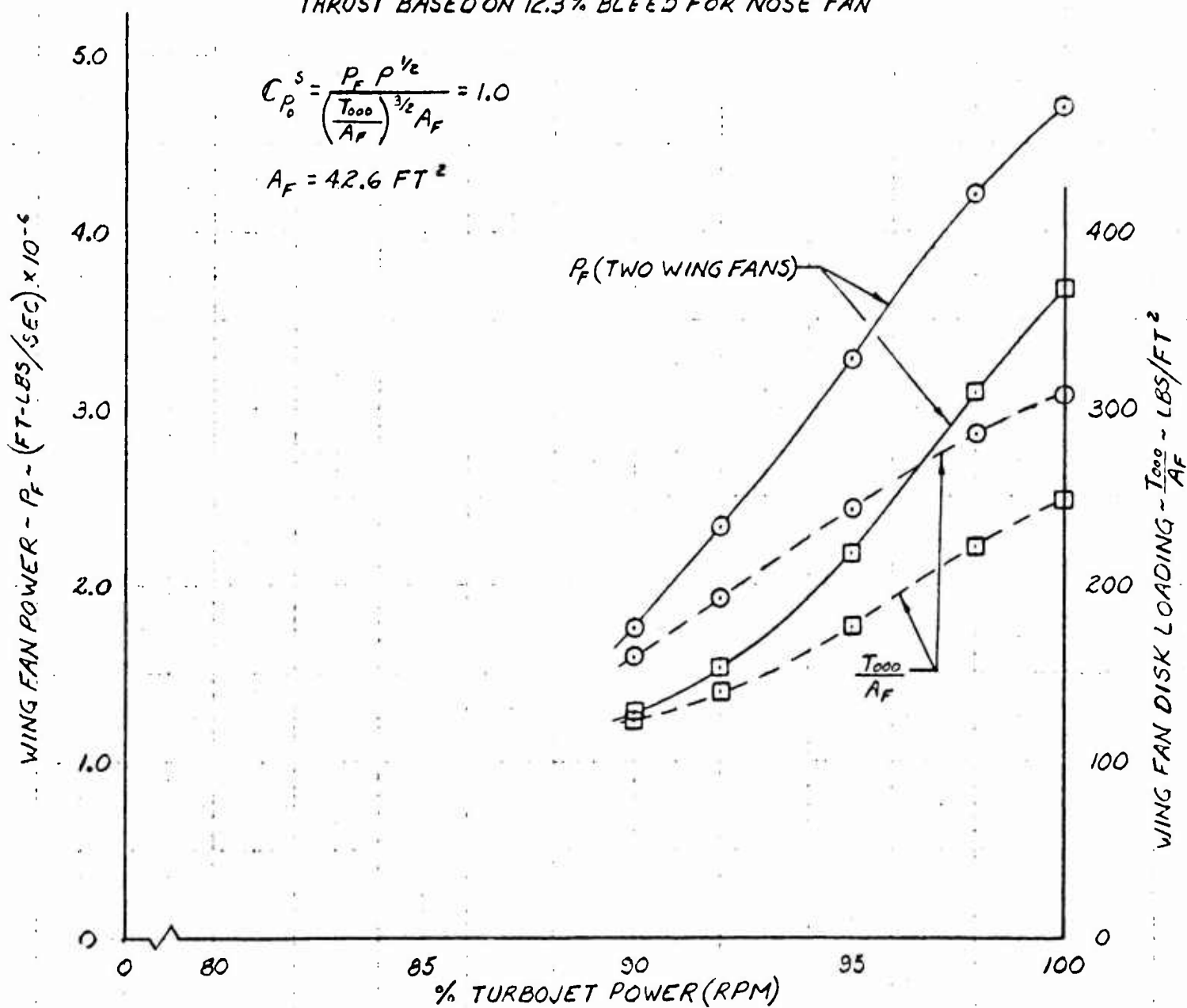


Figure 4.20

XV-5A
NOSE FAN STATIC LIFT
AND
POWER

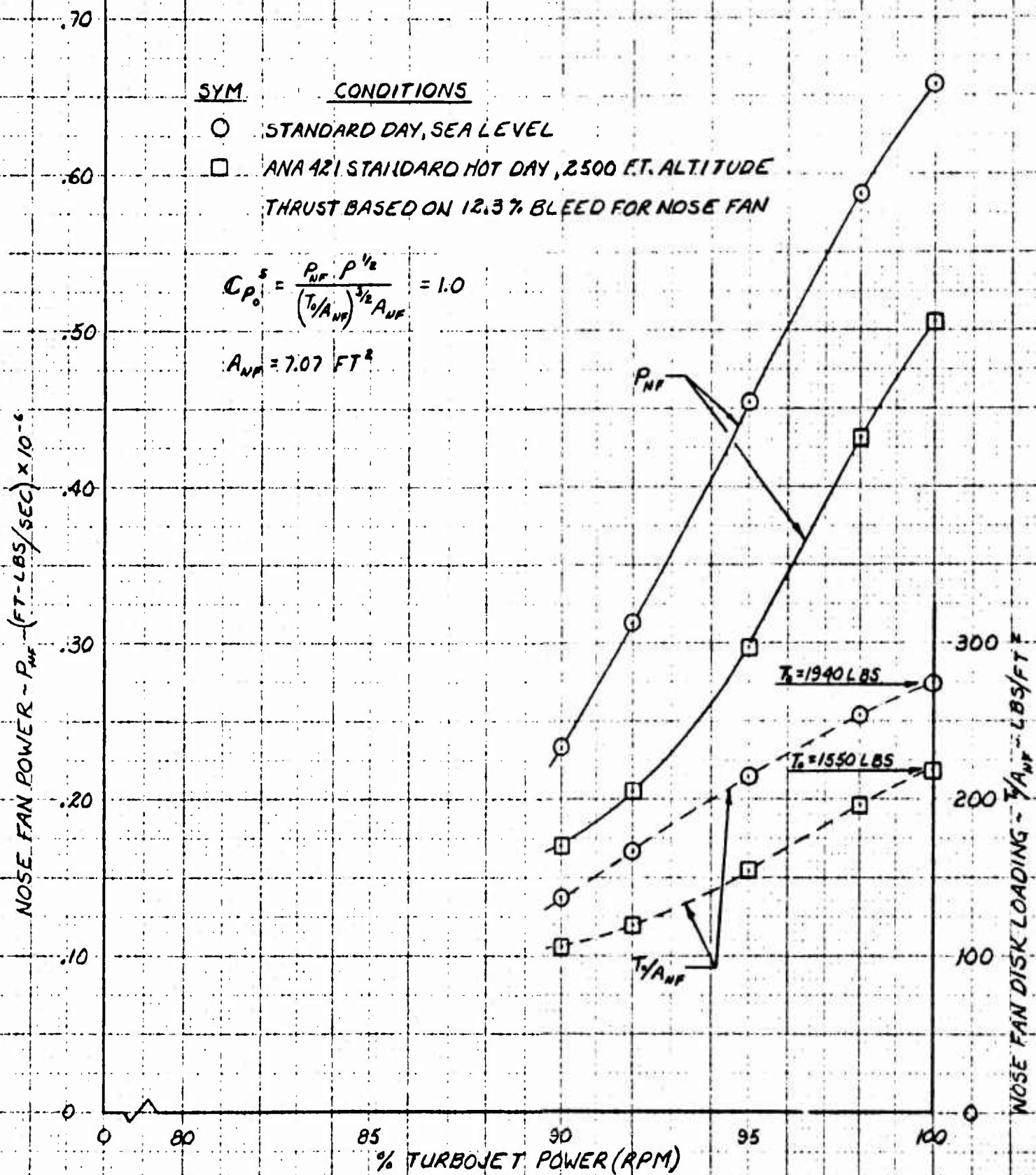


Figure 4.21

XV-5A

VARIATION OF POWER COEFFICIENT
WITH
EXIT LOUVER ANGLE

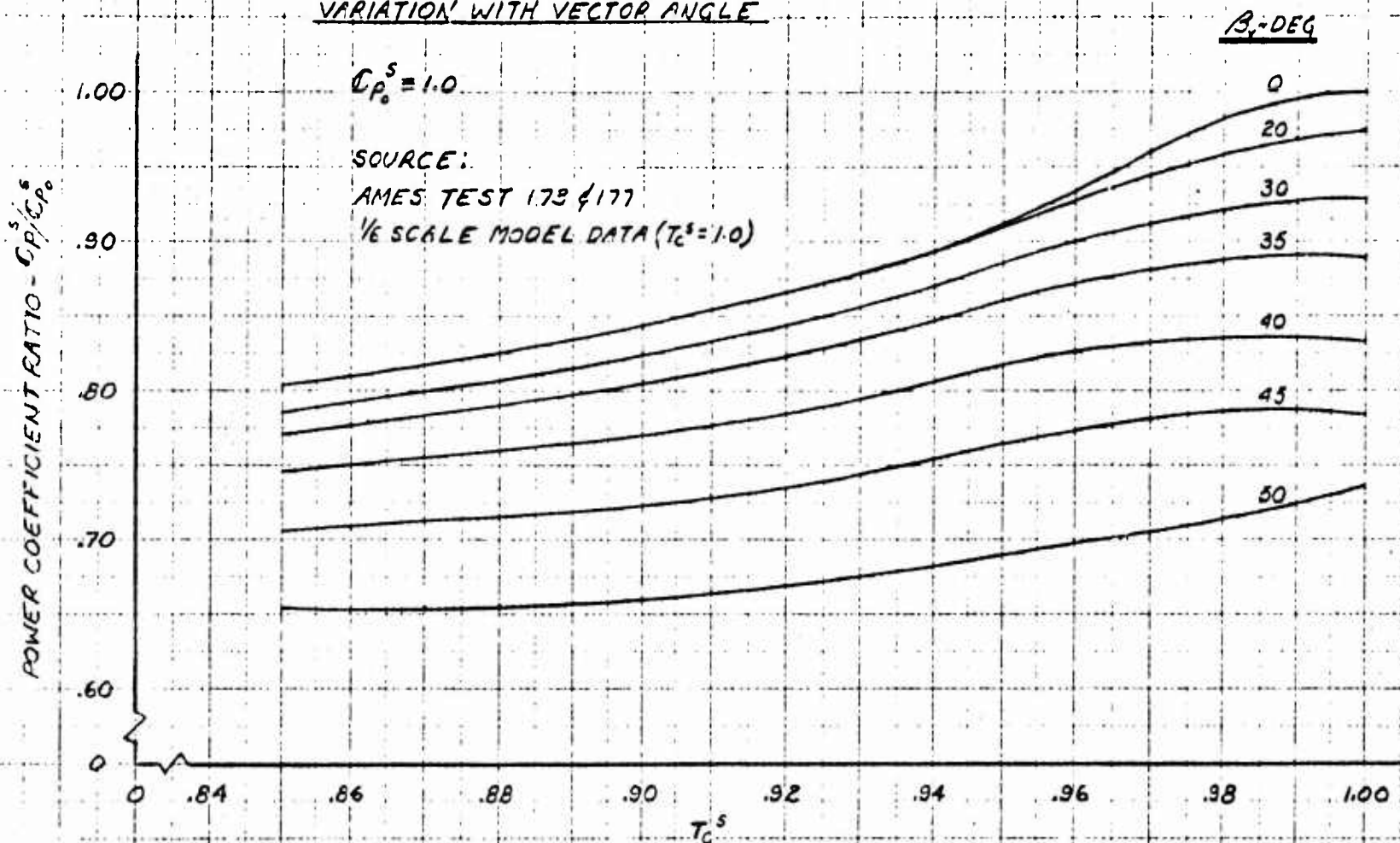
VARIATION WITH VECTOR ANGLE

$$C_{P_0}^S = 1.0$$

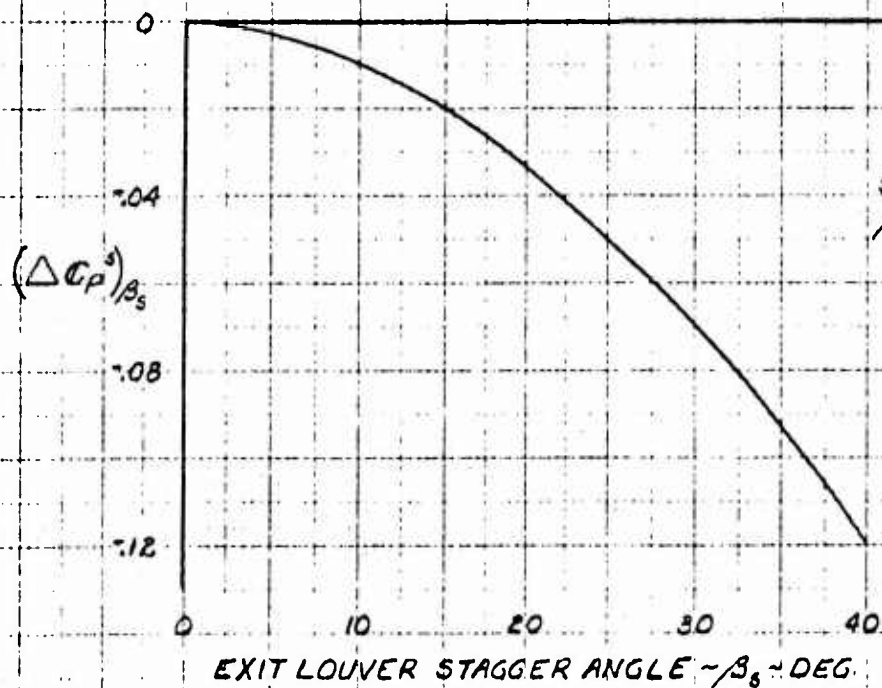
SOURCE:

AMES TEST 173 & 177

1/8 SCALE MODEL DATA ($T_C^S = 1.0$)



INCREMENTAL CHANGE DUE TO STAGGER ANGLE



SOURCE:

AMES TEST 173

Figure 4.22

XV-5A

VARIATION OF NOSE FAN POWER COEFFICIENT
RATIO IN TRANSITION

$$C_{p_0}^s \approx 1.0$$

SOURCE:
AMES TEST 177

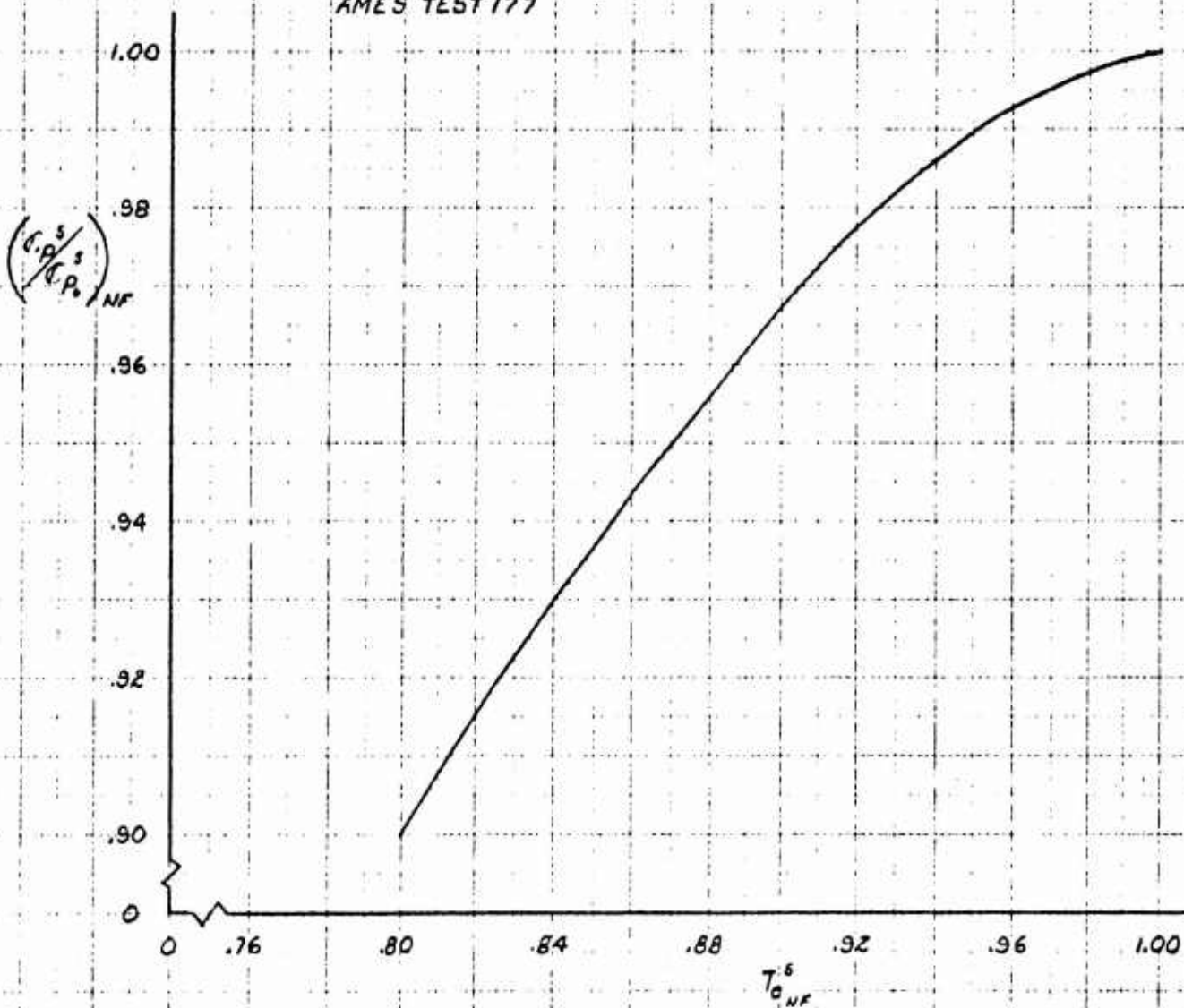


Figure 4.23

XV-5A
ESTIMATED SIDE FORCE DERIVATIVE WITH
NOSE FAN

SIDESHIP IN FAN POWERED FLIGHT

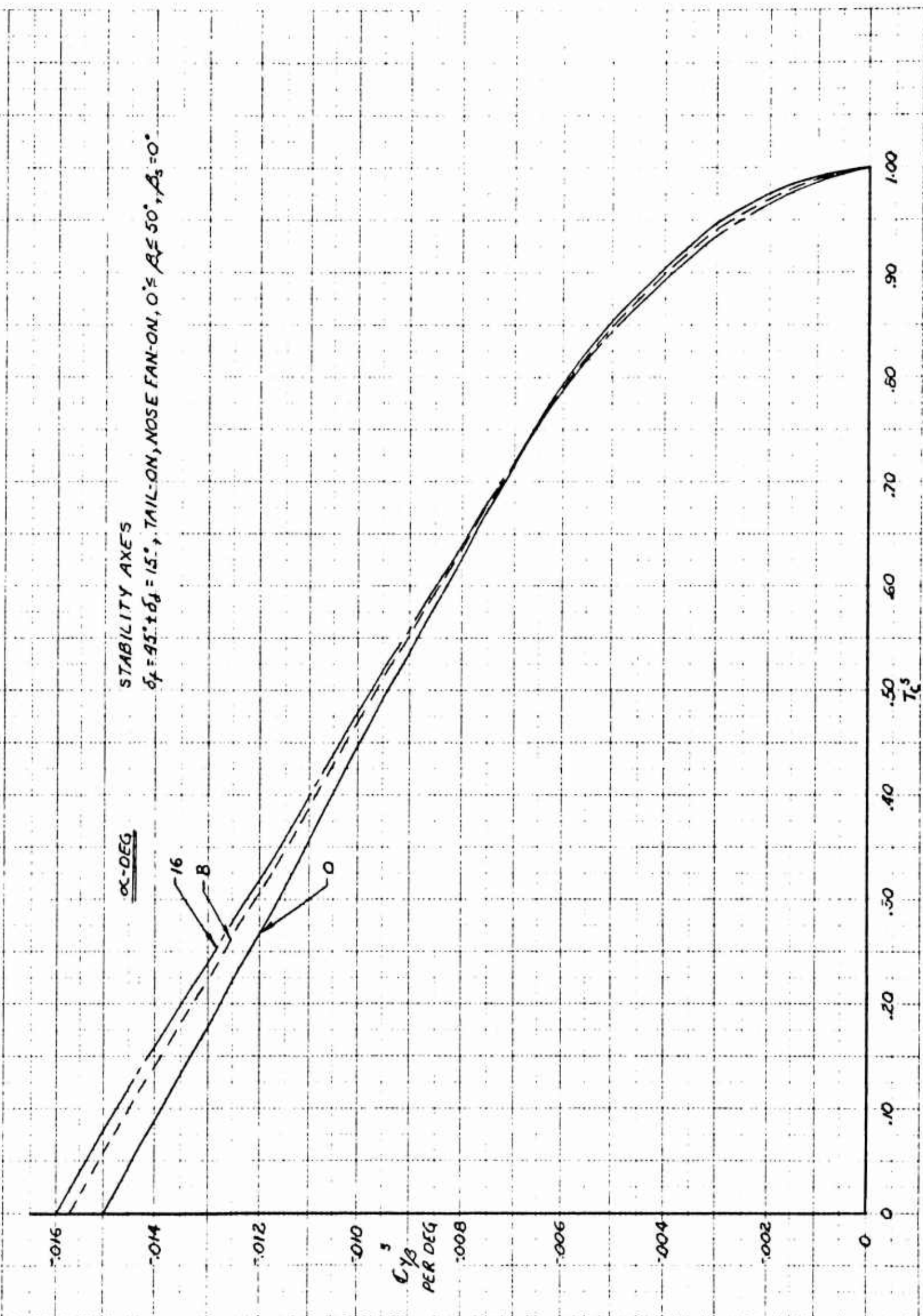


Figure 4.24

XV-5A

ESTIMATED YAWING MOMENT DERIVATIVE WITH
SIDESLIP IN FAN POWERED FLIGHT

STABILITY AXES, CG, C.F.S. 246, W.L. 118.
 $\delta_f = 45^\circ + \delta_d = 15^\circ$, TAIL-ON, NOSE FAN-ON, $0^\circ \leq A_e \leq 50^\circ$, $A_d = 0^\circ$

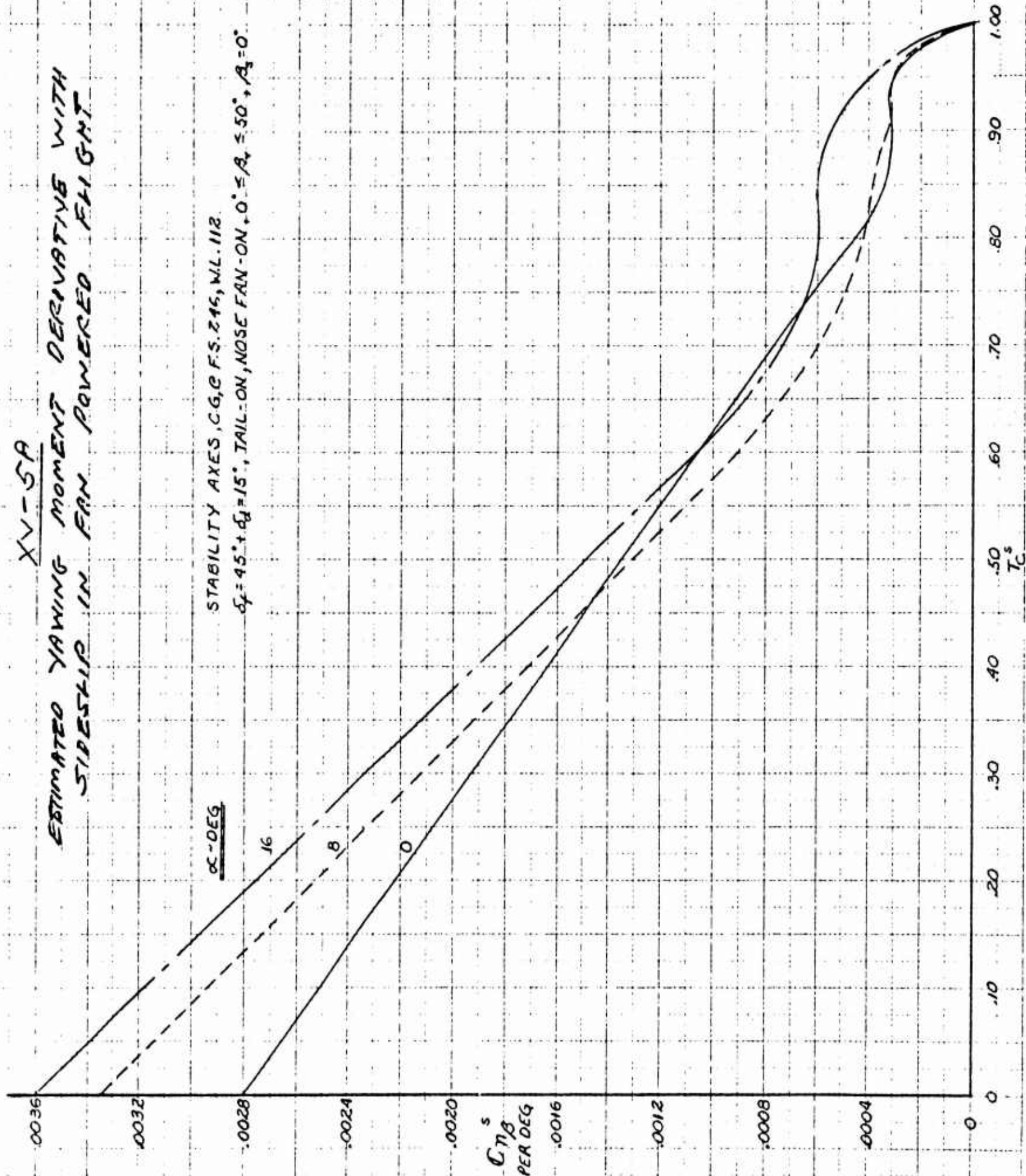


Figure 4.25

XV-5A
ESTIMATED ROLLING MOMENT WITH SIDESHIP
IN
FAN POWERED FLIGHT

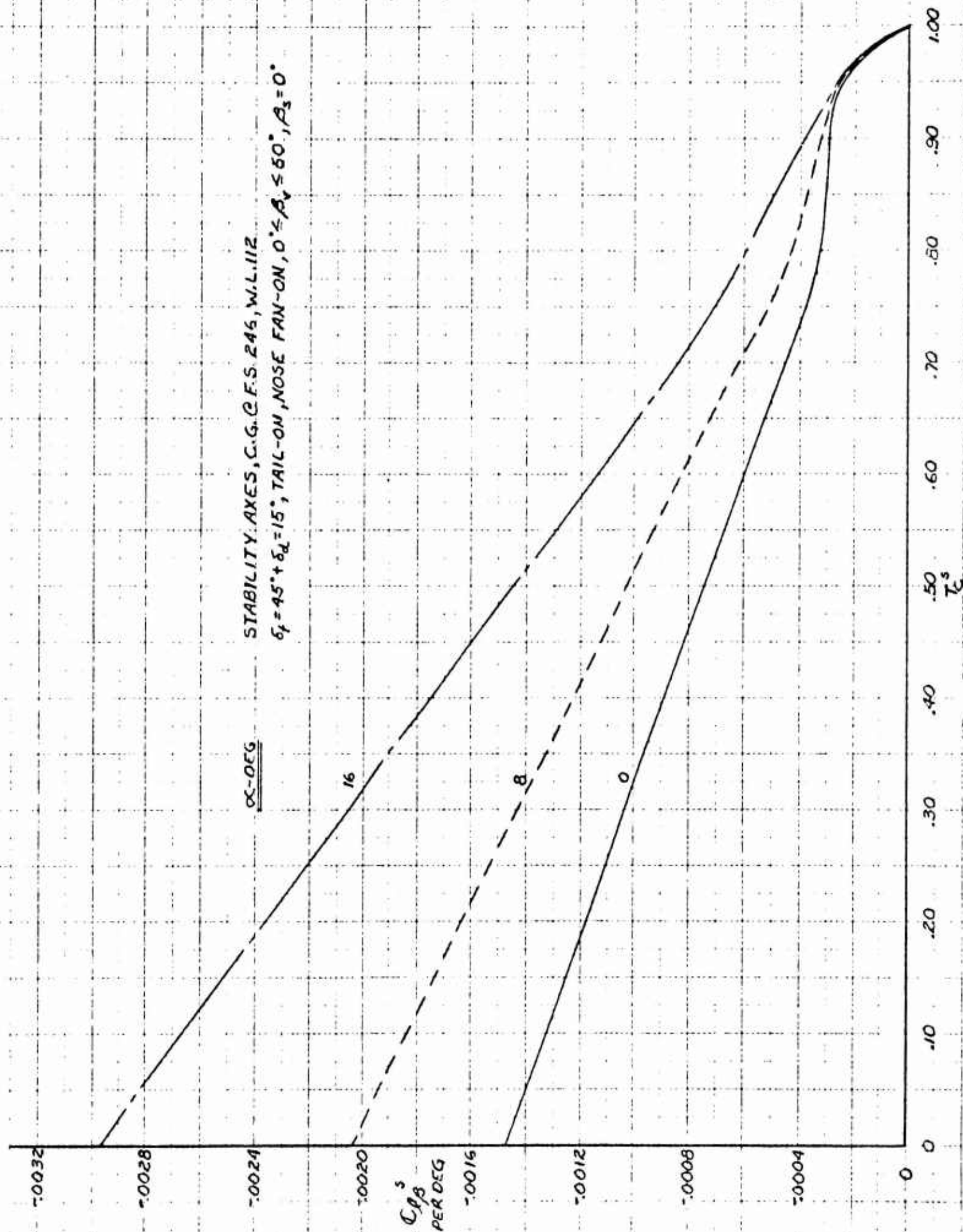


Figure 4.26

XV-5A

CROSS COUPLING OF PITCHING MOMENT
WITH SIDESHIP IN FAN FLIGHT

$\delta_f = 45^\circ + \delta_d = 15^\circ$, TAIL-ON, C.G. @ F.S. 246, W.L. 112

SYM	β_f	β_d	α
○	0°	0°	0°
△	50°	0°	0°

OPEN SYMBOLS NOSE FAN-OFF
SHADED SYMBOLS NOSE FAN-ON

$$dC_m/d|\beta| = m(1 - T_c^2)$$

$$dC_m/d|\beta| = m \frac{A_F}{S} \frac{D_F}{C}$$

SOURCE:
1/6 SCALE MODEL DATA

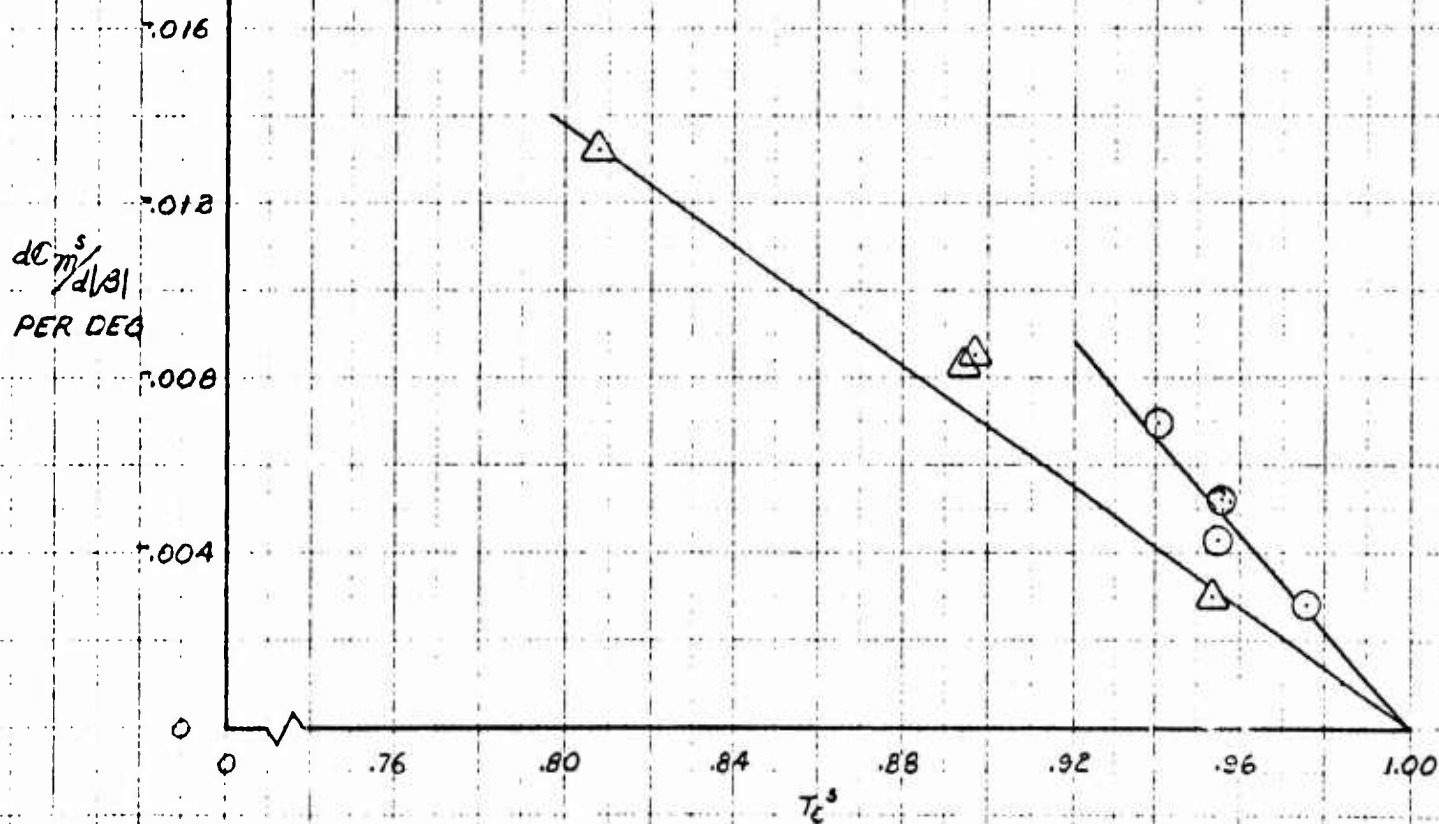


Figure 4.27

XV-5A

CROSS COUPLING DERIVATIVE OF PITCHING
MOMENT DERIVATIVE WITH SIDESHIP IN
FAN POWERED FLIGHT

$\delta_f = 45^\circ + \delta_d = 15^\circ$, TAIL-ON, C.G. @ F.S. 246, W.L. 112

$$\frac{dC_m^s}{d\beta} = \frac{dC_m}{d\beta} (1 - T_c^s) \frac{S}{A_F} \frac{\bar{c}}{D_F}$$

SOURCE:

1/6 SCALE MODEL DATA

β , -DEG

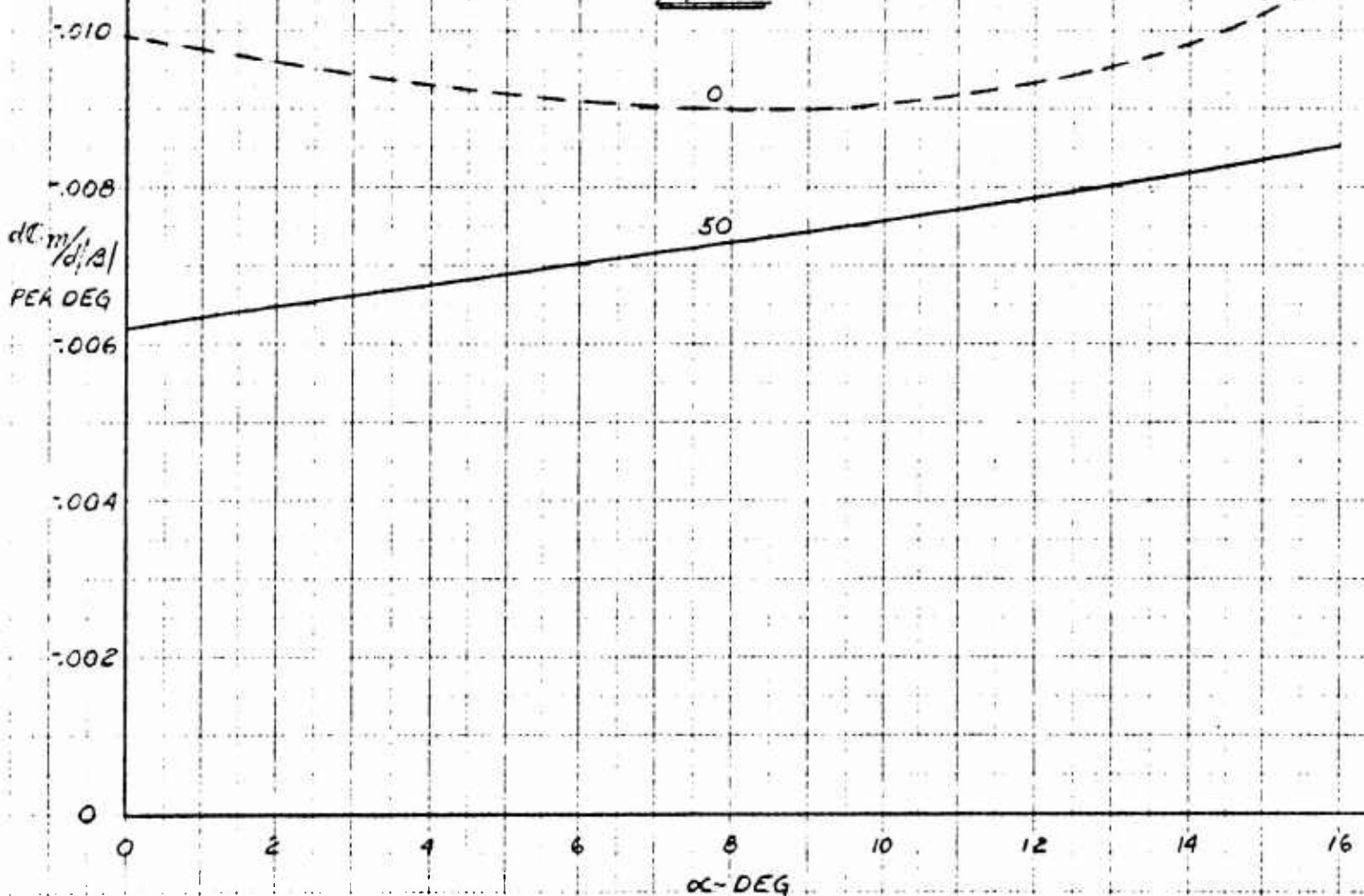


Figure 4.28

XV-5A

YAW VS. MOMENT DERIVATIVE WITH AILERON DEFLECTION IN FAN POWERED FLIGHT

$\delta_f = 45^\circ + \delta_a = 15^\circ$, TAIL-ON, C.G. @ F.S. 246, W.L. 112

$$C_{\eta} = (C_{\eta_{\delta_a}} + \Delta C_{\eta_{\delta_a}})(\delta_{a_L} - \delta_{a_R})$$

NOTE:

- 1- POSITIVE AILERON DEFLECTION IS TRAILING EDGE DOWN.
- 2- DATA VALID FOR DIFFERENTIAL AILERON DEFLECTION SCHEDULE FOR 15° AILERON DROOP.
- 3- DATA NOT VALID FOR $|\delta_{a_L} - \delta_{a_R}| > 25^\circ$
- 4- STABILITY AXES

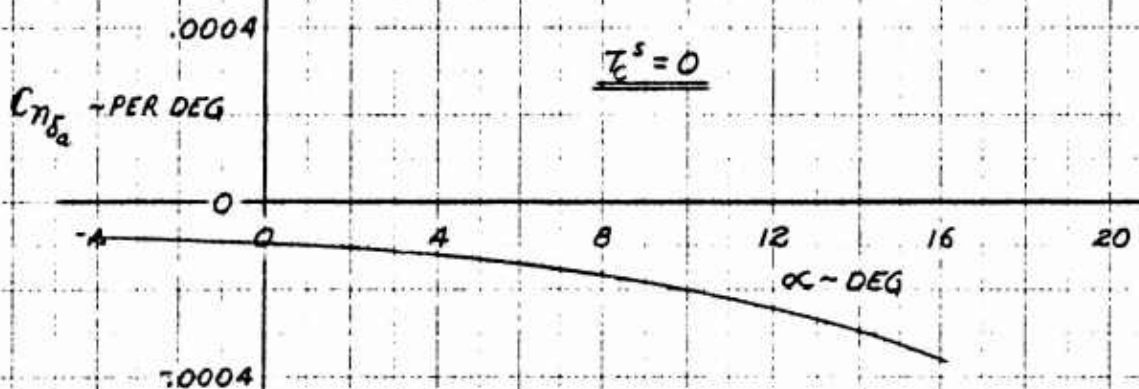
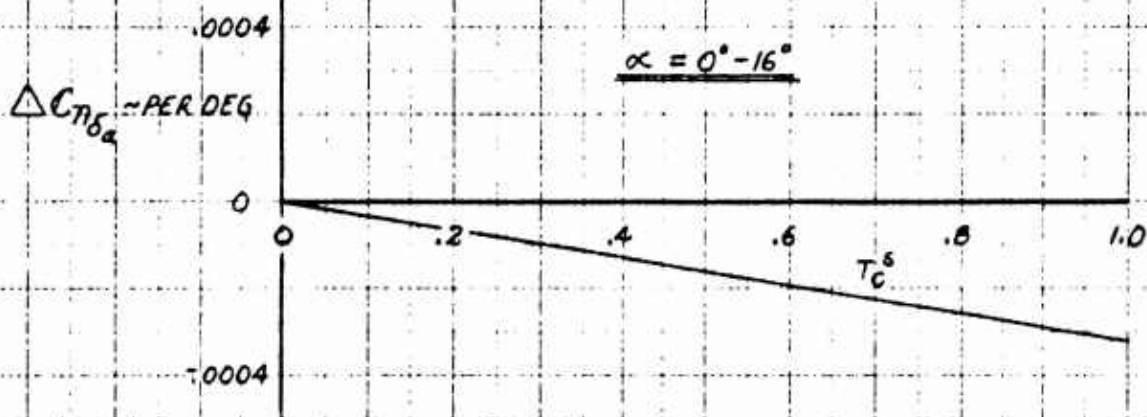


Figure 4.29

XV-5A
 RUDDER CONTROL EFFECTIVENESS
 DERIVATIVE IN FAN POWERED FLIGHT

$\alpha=0^\circ, \psi=0^\circ, \text{C.G. @ F.S. 216, W.L. 112}$

SYM	SOURCE	δ_F
○	1/8 SCALE MODEL DATA	0°
□	1/6 SCALE MODEL DATA	45°

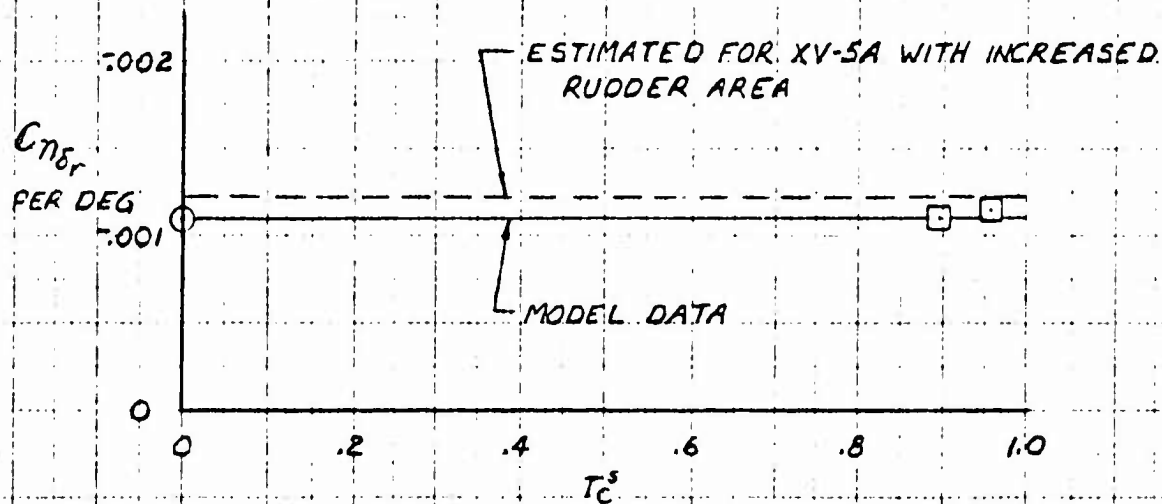


Figure 4.30

XV-5A

EFFECT OF VERTICAL VELOCITY ON
LIFT AND PITCHING MOMENT COEFFICIENTS

$\beta_v = 0^\circ$, $\beta_v = 0^\circ$ DATA SOURCE: 1/6 SCALE MODEL
NOSE FIN OFF

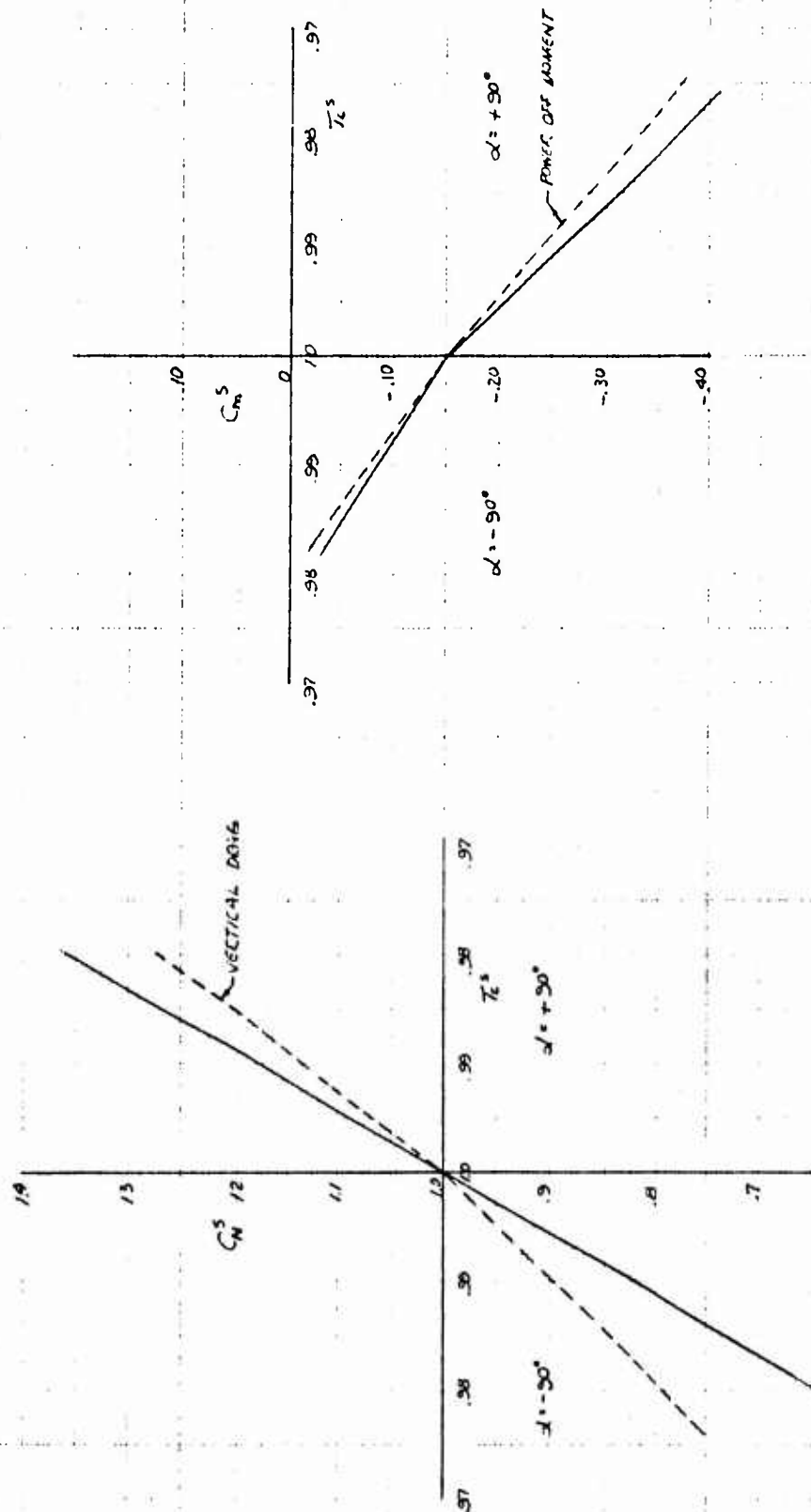


Figure 4.31

XV-5A

GRAPHING IN VERTICAL FLIGHT WITH THE NOSE FAN AT VARIOUS THRUST LEVELS

$\delta_1 = 45^\circ, \delta_2 = 0^\circ, \delta_3 = 0^\circ, \delta_4 = 0^\circ$
CG OF S246, N. 12

$\delta_1 = 0^\circ$
NOSE FAN THRUST REVERSER
DOOR POSITION

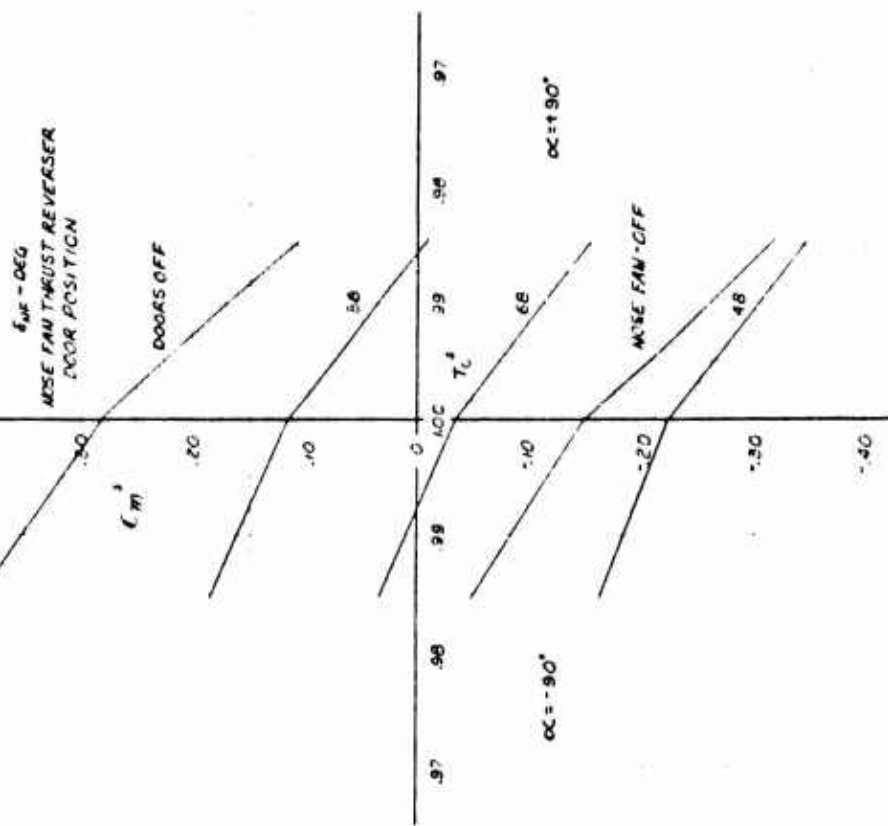
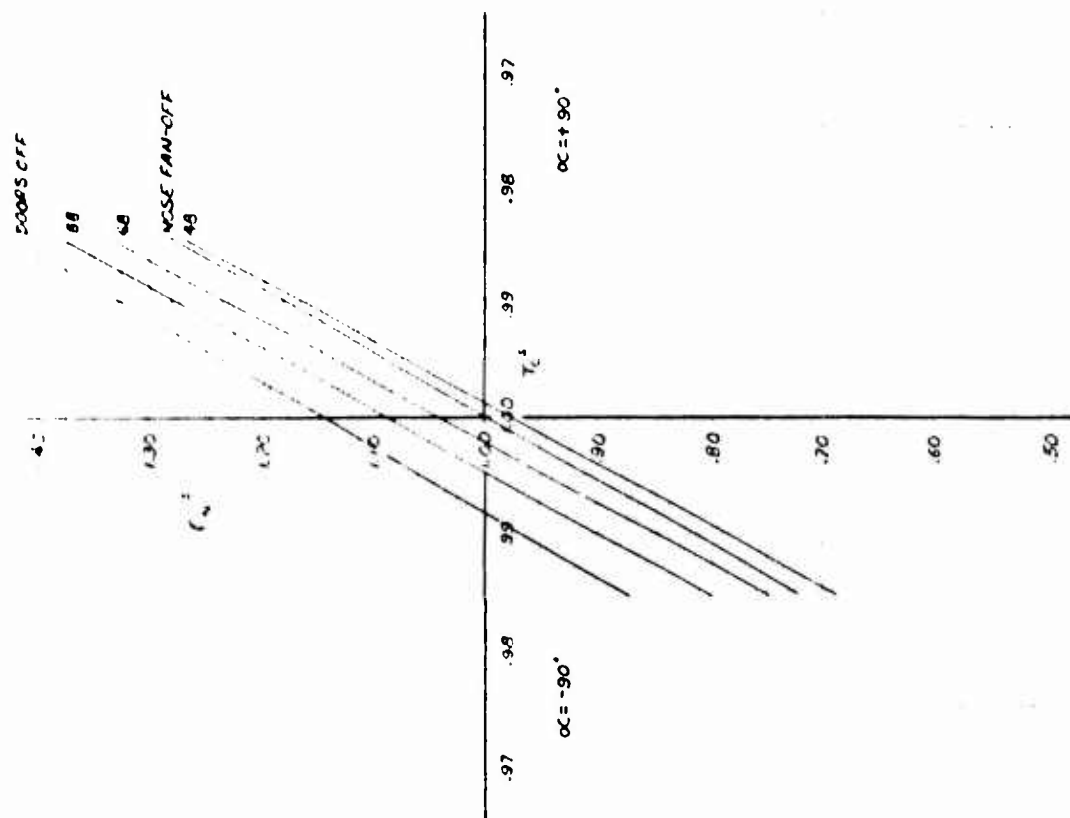


Figure 4.32

N-5H

LONGITUDINAL AND LATERAL FLIGHT CHARACTERISTICS
IN LATERAL TRANSITION

$\alpha=0^\circ, \beta=90^\circ, \phi=0^\circ, A_1=0^\circ, A_2=0^\circ, \delta_1=45^\circ$, TAIL-ON, NOSE FAN-OFF
CGEFS 246, VLL12

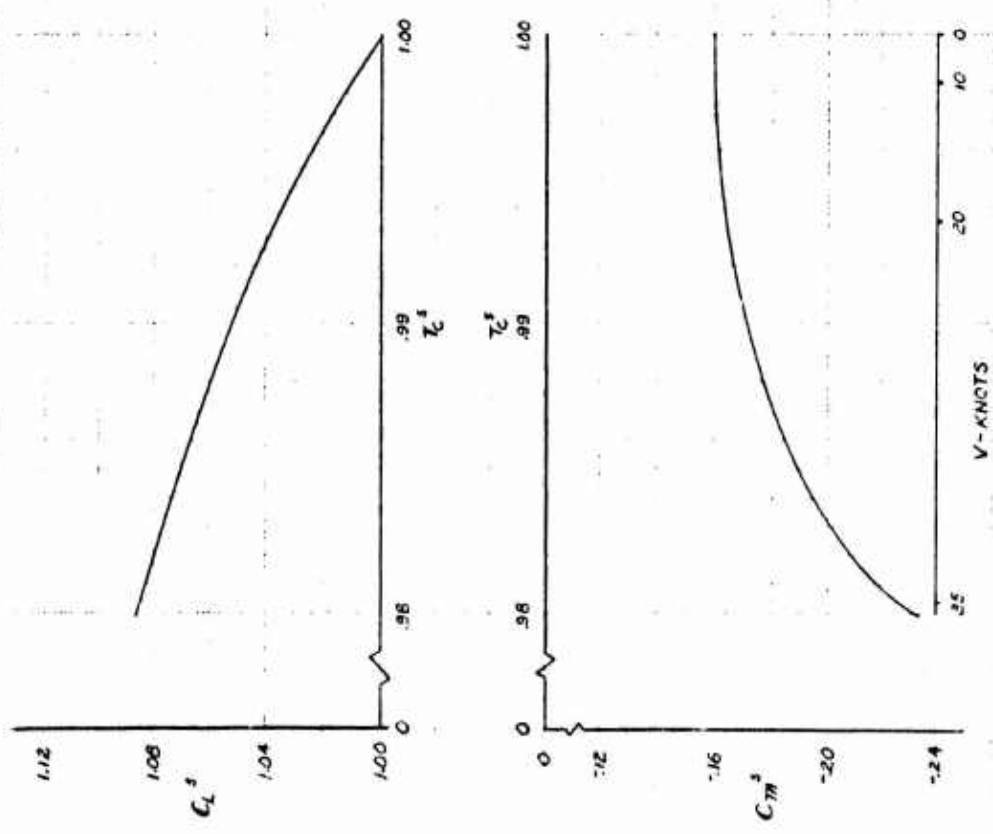
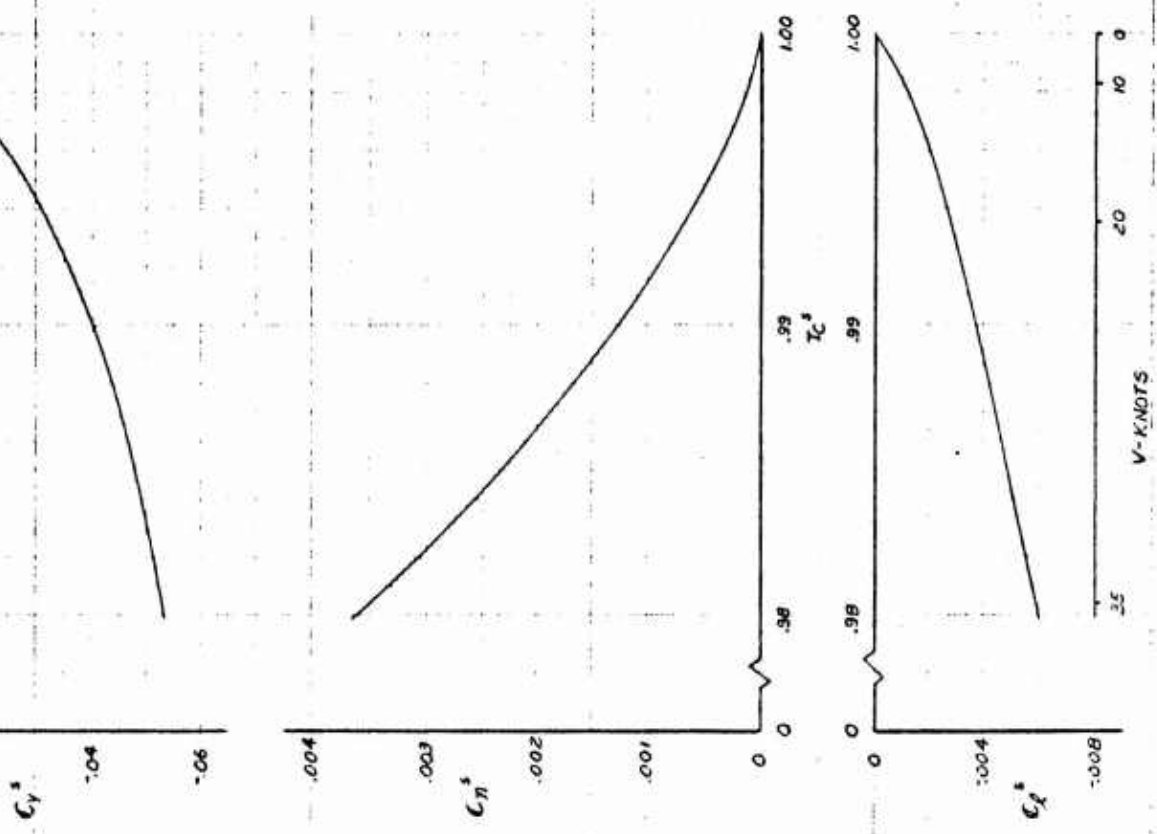


Figure 4.33



XV-5A

LONGITUDINAL CHARACTERISTICS IN REARWARD FLIGHT

$\theta = 0^\circ, \delta_f = 45^\circ, \beta_r = 0^\circ, \beta_s = 0^\circ, \alpha_e = 0^\circ, \text{NOSE FAN-OFF}$
C.G. @ F.S. 246, W.L. 112

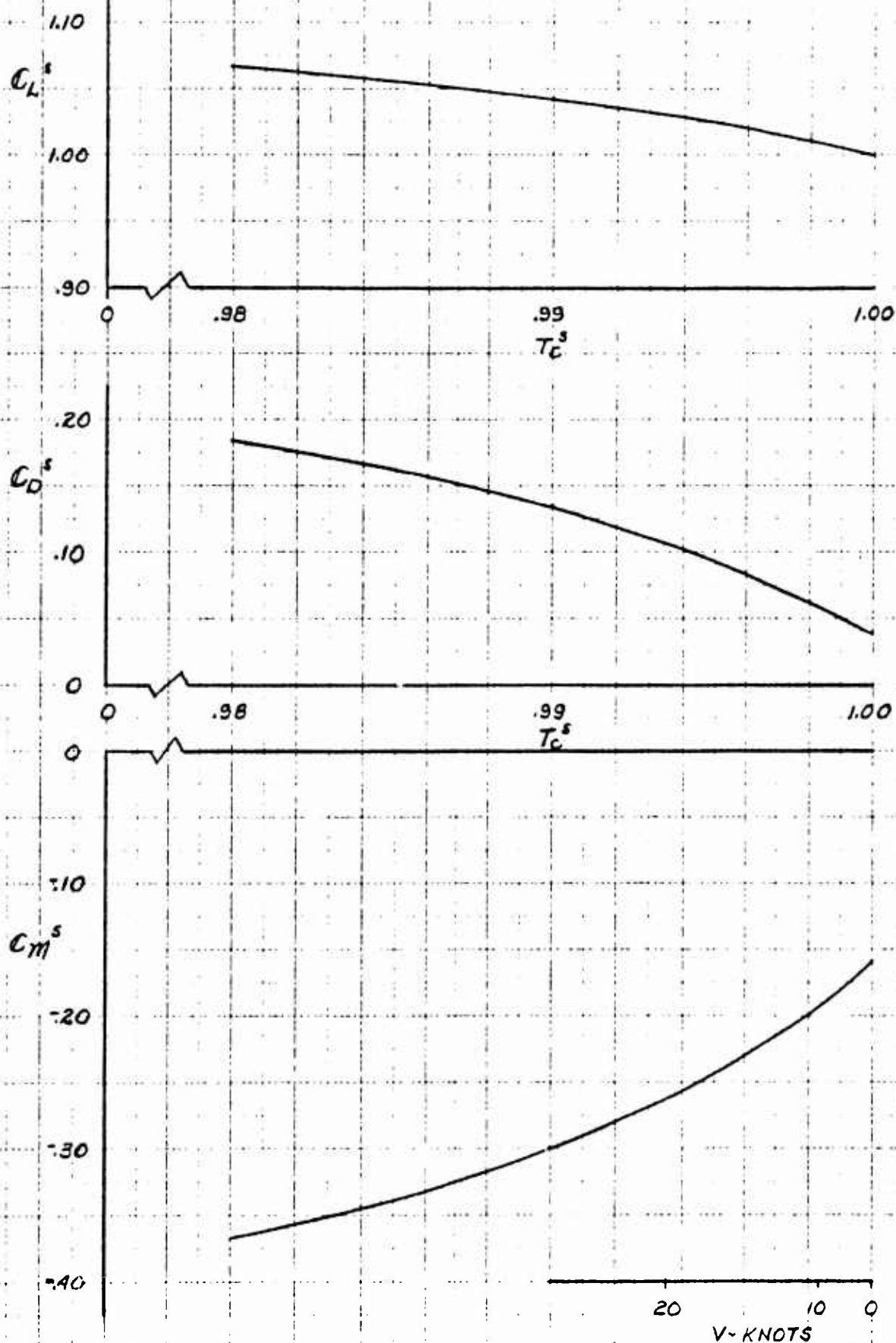


Figure 4.34

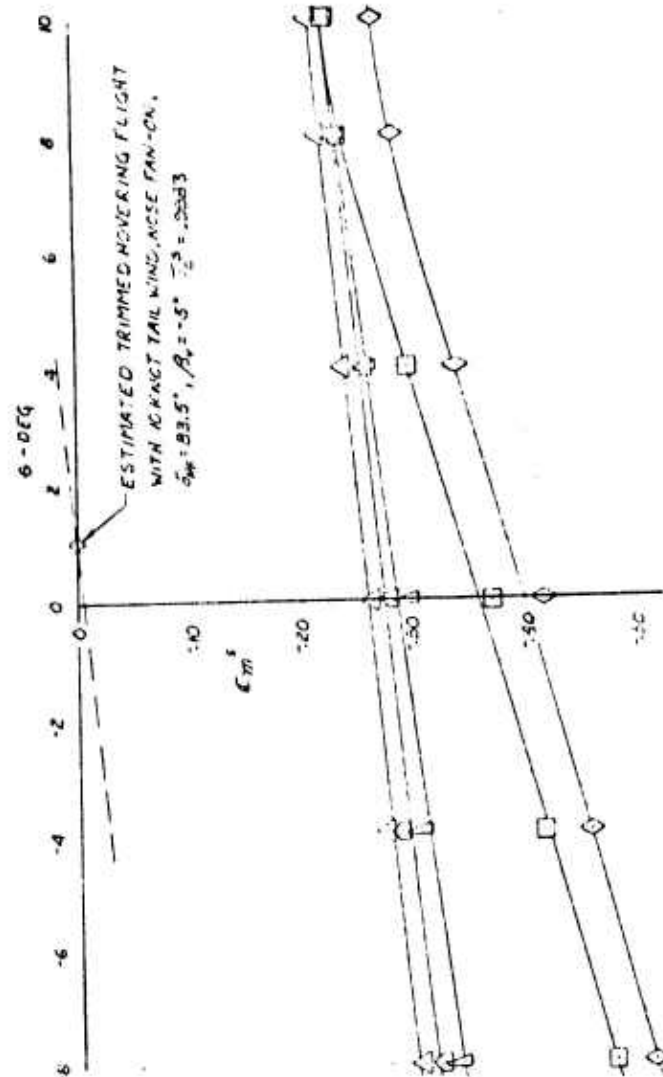
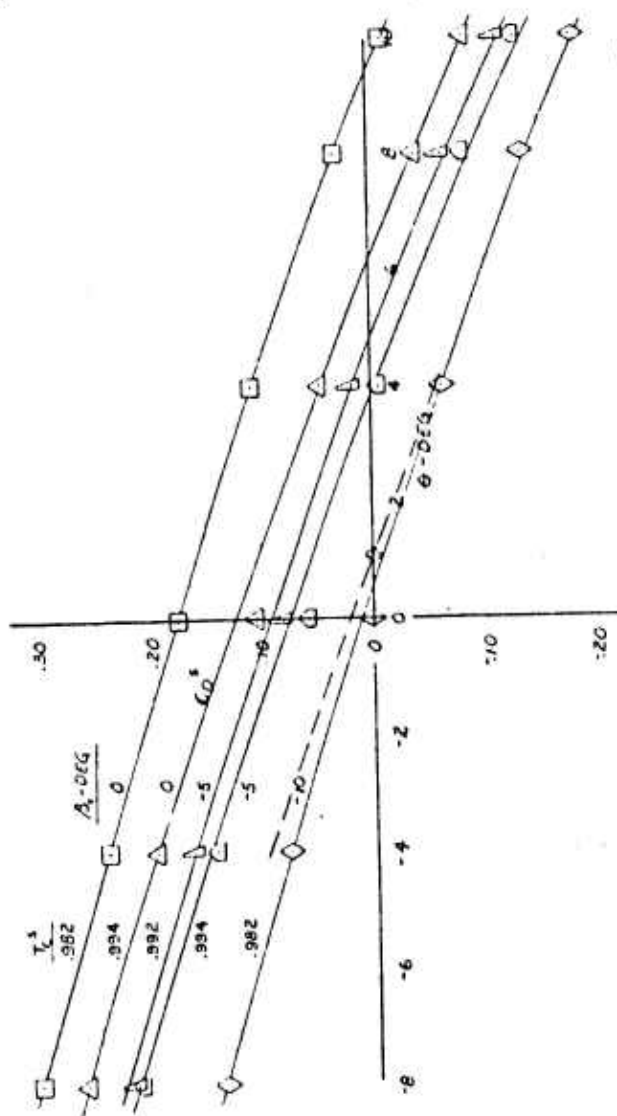
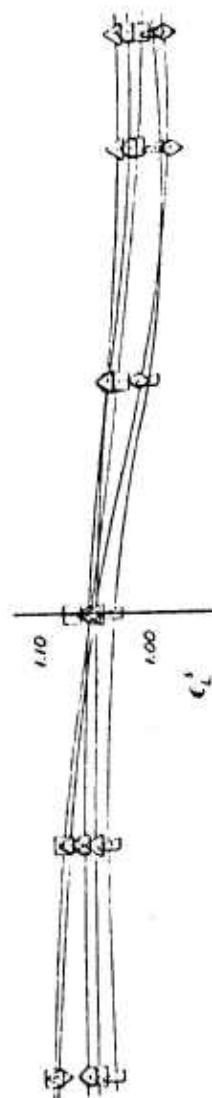
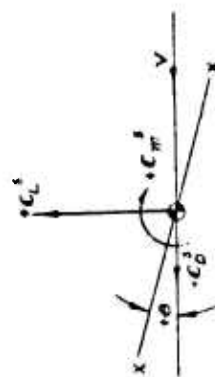
XY-5A

EFFECT OF NEGATIVE VECTERING AND PITCH ANGLE IN REARWARD FLIGHT

$\delta_t = 45^\circ, \beta_t = 0^\circ, \alpha_t = 0^\circ$ NOSE FAN-OFF (OR NOTED)

C.G. FS 246, VL 112

SYM	T_c	β_c
\triangle	.994	0°
\square	.994	-5°
\diamond	.992	-5°
\square	.982	0°
\diamond	.982	-10°



ESTIMATED TRIMMED HOVERING FLIGHT
WITH NOSE TAIL WING, NOSE FAN-ON,
 $\delta_m = 93.5^\circ, \beta_t = -5^\circ, \alpha_t = -20.33^\circ$

Figure 4.35

5.0 CONCLUSIONS

- The estimated basic zero angle of attack and zero flap deflection lift, drag, and pitching moment of the XV-5A airplane in fan-powered flight are based upon data from model tests with the full-scale propulsion system, rather than the 1/6 scale model, due to an increase in fan power absorption with tunnel speed for the small-scale model. Other factors which possibly affect correlation of the characteristics of the two models are differences in wing thickness ratio and wind tunnel wall effects.
- The wing-fans and the nose fan contribute destabilizing pitching moments with respect to angle of attack, as determined by comparison of longitudinal stability with fan power on and off.
- The aircraft with the nose fan operating is statically unstable in pitch with the most aft cg location for thrust coefficients greater than approximately .92 or for speeds less than approximately 70 knots and stable for all speeds greater than this condition.
- The drag of the nose fan can be predicted by simple momentum theory and the control effectiveness of the nose fan at forward speeds can be estimated from the static-thrust and reverser door effectiveness.
- The aircraft possesses positive lateral and directional static stability with sideslip at all forward speeds in fan-powered flight. The effect of wing fan operation is stabilizing in that the derivatives $C_{l\beta}$ and $C_{n\beta}$ increase with increasing thrust coefficient. The nose fan produces destabilizing increments in $C_{l\beta}$ and $C_{n\beta}$ but the net stability level is as high or higher at all values of thrust coefficient than at the power-off condition, for angles of attack less than 8°.
- The effectiveness of the conventional flight control system is not affected by fan operation in the fan flight mode and the control derivatives in conventional coefficient notation are therefore independent of flight speed.

- The exit louver vector control system is capable of providing the required propulsive forces to accelerate the airplane from a minimum of 10 knots rearward to the forward flight speed for conversion to conventional flight.
- The exit louver stagger control system in the hovering flight condition provides a total wing fan thrust degradation for lift control of 22% of the static installed thrust between the limits of 13° and 37° stagger angle.
- Conventional flight, nonlinear low speed, flap down static longitudinal stability of the complete aircraft is a result of nonlinear downwash and tail dynamic pressure ratio in the vicinity of the tail at high angles of attack.
- Satisfactory low speed lateral-directional characteristics were achieved by increasing wing outboard panel dihedral from -6° to $+4^\circ$ and verified by subsequent low speed tests.
- Additional horizontal tail area was required to account for aeroelastic effect at high Mach numbers to insure adequate static longitudinal stability.
- Loss in static longitudinal stability at high speed due to angle of attack at high altitude or high normal load factor at low altitude results in a limit lift coefficient versus Mach number which is presented in Figure 3.35.
- Despite discrepancies between high and low speed wind tunnel directional stability data, satisfactory lateral-directional stability characteristics are predicted.
- Low speed control effectiveness has been estimated including the nonlinear characteristics at higher deflections and found satisfactory.
- Deterioration of high speed control effectiveness beyond Mach 0.75 warrants consideration before flight in this area is attempted.

6.0 APPENDIX

6.1 REFERENCES

1. Wind Tunnel Test Report Conventional Model, Volumes I and II, General Electric Co., Report Number 141, January, 1964.
2. Wind Tunnel Test Report Lift Fan-Powered Scale Model, General Electric Co., Report Number 137, November, 1963.
3. Wind Tunnel Test Report Conventional Model, Volume III, General Electric Co., Report Number 141, January, 1964.
4. Malthan, L. V. et al.: USAF Stability and Control Handbook; Douglas Aircraft Co., October, 1960.
5. Recant, Isidore G.: Wind Tunnel Investigation of Ground Effect on Wings with Flaps; NACA TN704, May, 1939.
6. Decker, J. et al.: USAF Stability and Control Handbook; M-03671, 1956, (Title Unclassified)
7. Toll, Thomas A., and Schneiter, Leslie E.: Approximate Relations for Hinge-Moment Parameters of Control Surfaces on Swept Wings at Low Mach Numbers; NACA TN1113, October, 1948.
8. Dads, Jules B., Jr.: Estimation of Low-Speed Lift and Hinge-Moment Parameters for Full-Span Trailing-Edge Flaps on Lifting Surfaces with and without Sweepback, NACA TN2288, February, 1951.
9. Toll, Thomas A.: Summary of Lateral Control Research; NACA TN1245, March, 1947.
10. Purser, Paul E., and Cook, Charles B.: Collection and Analysis of Hinge-Moment Data on Control-Surface Tabs; NACA TN1113, April, 1947.
11. Structural Design Loads, General Electric Co., Report Number 143, March, 1964.

12. Hickey, D.H. and Hall, L.P.: Aerodynamic Characteristics of a Large Scale Model with Two High Disk Loading Fans Mounted in the Wing; NASA TN-D-1650, February, 1963.
13. Priestley, R.T.: Estimated Performance Characteristics, U.S. Army XV-5A Lift-Fan Research Aircraft; Ryan Report (Unpublished).

6.2 SYMBOLS AND NOMENCLATURE

General Symbols

A Aspect ratio, b^2/S . With no subscript, refers to Wing

A Fan area, $\frac{2\pi D^2}{4}$, ft² total

b Span, ft. Unsubscripted symbol refers to the wing

C_D Drag coefficient, $D/q S$

C_D^s Drag coefficient, $D/q^s A_F$

C_L Lift coefficient, $L/q S$

C_L^s Lift coefficient, $L/q^s A_F$

C_m Pitching moment coefficient, $M/q S \bar{c}$

C_m^s Pitching moment coefficient, $M/q^s A_F D_F$

C_Y Sideforce coefficient, $Y/q S$

C_Y^s Sideforce coefficient, $Y/q^s S$

C_N^s Normal force coefficient, Normal Force/ $q^s A_F$

C_n Yawing moment coefficient, $N/q S b$

C_n^s Yawing moment coefficient, $N/q^s S b$

C_l Rolling moment coefficient, $R/q S b$

C_l^s Rolling moment coefficient, $R/q^s S b$

C_p^s Fan power coefficient, $\frac{P \rho^{1/2}}{\left(\frac{T_{000}}{A_F} \right)^{3/2}} A_F$

C_h	Hinge moment coefficient, $HM/q S_{ref} \bar{c}_{ref}$
\bar{c}	Mean aerodynamic chord, ft., unsubscripted symbol refers to wing
D	Drag, lb. or fan diameter, ft.
HM	Hinge moment, ft. -lb.
i	Horizontal stabilizer incidence angle, deg., positive trailing edge down
L	Lift force, lb.
ℓ_H	Distance along the stability X axis from the c.g. to the a.c. of the horizontal tail, ft.
M	Pitching moment, ft. -lb., or Mach number
N	Yawing moment, ft. -lb., or fan rotational speed, revolutions per minute
P	Hypothetical power delivered to the fans from both engines, ft. -lb./sec.
q	Free stream dynamic pressure, $(\rho/2) V^2$
q^s	Slipstream dynamic pressure, $q + T_{000}/A_F$
R	Rolling moment, ft. lb.
S	Reference area, ft ² . Unsubscripted symbol refers to wing area. Control surface areas are aft of the hinge line.
T	Static fan thrust, lb.
T_{000}	Wing fan static lift force with $\beta_v = 0^\circ$, $\beta_s = 0^\circ$
T_C^s	Fan thrust coefficient, $T_{000}/q^s A_F$ or $T_{NF}/q^s_{NF} A_{NF}$
V	Velocity, ft./sec.

x	Distance aft of the leading edge of the wing mac.
Y	Sideforce, lb.
z_H	Distance along the stability z axis between the horizontal tail a. c. and the c. g., ft.
α	Angle of attack, deg.
β	Sideslip angle, deg.
β	Wing fan exit louver angle in degrees, measured between louver aft surface tangent plane and a plane parallel to fan axis, positive trailing edge aft.
β_s	Exit louver stagger angle, measured between any even numbered louver and the adjacent odd numbered louver, i. e., $\beta_s = \beta_2 - \beta_1$ where β_2 is the most forward and alternate louvers.
β_v	Exit louver vector angle determined from the average angle formed by adjacent louvers, i. e., $\beta_v = \frac{\beta_2 + \beta_1}{2}$
Γ	Wing outboard panel dihedral angle, deg.
δ	Flap or control surface deflection, deg. Trailing edge down positive; rudder deflection trailing edge left positive.
δ_{NF}	Nose fan thrust reverser door deflection, measured from the closed position, deg.
ϵ	Average downwash angle at the horizontal tail, deg.
$d\epsilon/d\alpha$	Rate of change of downwash angle with wing angle of attack.
η	Dynamic pressure ratio at the horizontal tail, q_H/q
θ	Pitch angle, deg. positive nose up
μ	Wing fan blade tip advance ratio, $V/\frac{\pi ND}{60}$
ρ	Air mass density, slug/ft ³ .

Derivatives

$C_{L\alpha}$	$\partial C_L / \partial \alpha$		1/deg.
$C_{m\alpha}$	$\partial C_m / \partial \alpha$		1/deg.
C_{mC_L}	$\partial C_m / \partial C_L$		
$C_{L\alpha_H}$	$\partial C_{LH} / \partial \alpha_H$	(based on tail area)	1/deg.
$C_{Y\beta}$	$\partial C_Y / \partial \beta$		1/deg.
$C_{n\beta}$	$\partial C_n / \partial \beta$		1/deg.
$C_{l\beta}$	$\partial C_l / \partial \beta$		1/deg.
C_{Li_H}	$\partial C_L / \partial i_H = C_{L\alpha_H} \frac{S_H}{S} \eta$		1/deg.
C_{mi_H}	$\partial C_m / \partial i_H = C_{Li_H} \frac{l_H}{\bar{c}}$		1/deg.
$C_{L\delta_e}$	$\partial C_L / \partial \delta_e = C_{L\alpha_H} \frac{\partial \alpha_H}{\partial \delta_e} \frac{S_H}{S} \eta$		1/deg.
$C_{m\delta_e}$	$\partial C_m / \partial \delta_e = C_{L\delta_e} \frac{l_H}{\bar{c}}$		1/deg.
$C_{Y\delta_r}$	$\partial C_Y / \partial \delta_r$		1/deg.
$C_{n\delta_r}$	$\partial C_n / \partial \delta_r$		1/deg.
$C_{l\delta_r}$	$\partial C_l / \partial \delta_r$		1/deg.

$C_Y \delta_a$	$\partial C_Y / \partial (\delta_{aL} - \delta_{aR})$	1/deg.
$C_n \delta_a$	$\partial C_n / \partial (\delta_{aL} - \delta_{aR})$	1/deg.
$C_l \delta_a$	$\partial C_l / \partial (\delta_{aL} - \delta_{aR})$	1/deg.
$C_{h_e} \delta_e$	$\partial C_{h_e} / \partial \delta_e$	1/deg.
$C_{h_e} \alpha_H$	$\partial C_{h_e} / \partial \alpha_H$	1/deg.
$C_{h_r} \delta_r$	$\partial C_{h_r} / \partial \delta_r$	1/deg.
$C_{h_r} \beta$	$\partial C_{h_r} / \partial \beta$	1/deg.
$C_{h_r} \delta_t$	$\partial C_{h_r} / \partial \delta_t$	1/deg.
$C_{h_a} \delta_a$	$\partial C_{h_a} / \partial \delta_a$	1/deg.
$C_{h_a} \alpha$	$\partial C_{h_a} / \partial \alpha$	1/deg.
$C_{h_a} \delta_t$	$\partial C_{h_a} / \partial \delta_t$	1/deg.
$C_{h_t} \delta_t$	$\partial C_{h_t} / \partial \delta_t$	1/deg.
$C_{h_t} \delta_a$	$\partial C_{h_t} / \partial \delta_a$	1/deg.

Subscripts

a	Aileron
CM	Complete model
d	Aileron droop
e	Elevator
F	Wing fans
f	Wing trailing edge flap
G	In ground effect
H	Horizontal tail
j	Fan exit
L	Left hand
M-T	Model minus tail
NF	Nose fan
o	Zero angle of attack or zero velocity
OL	Zero lift
PO	Power-off
R	Right hand
r	Rudder
s	Stagger
TRIM	Trimmed condition ($C_m = 0$)
t	Horizontal tail
v	Vector
W	Wing

Abbreviations

a. c.	Aerodynamic center
c g	Center of gravity
eff	Effective
F. S.	Fuselage station

mac Mean aerodynamic chord

max Maximum

W. L. Water line

SUPPLEMENTARY DATA

Data presented in Section 6.3 are included as a supplement to the body of the report and are used to illustrate the development of the aerodynamic characteristics of the aircraft as described therein.

XV-5A
LIFT & MOMENT INCREMENTS
DUE TO FLAP DEFLECTION

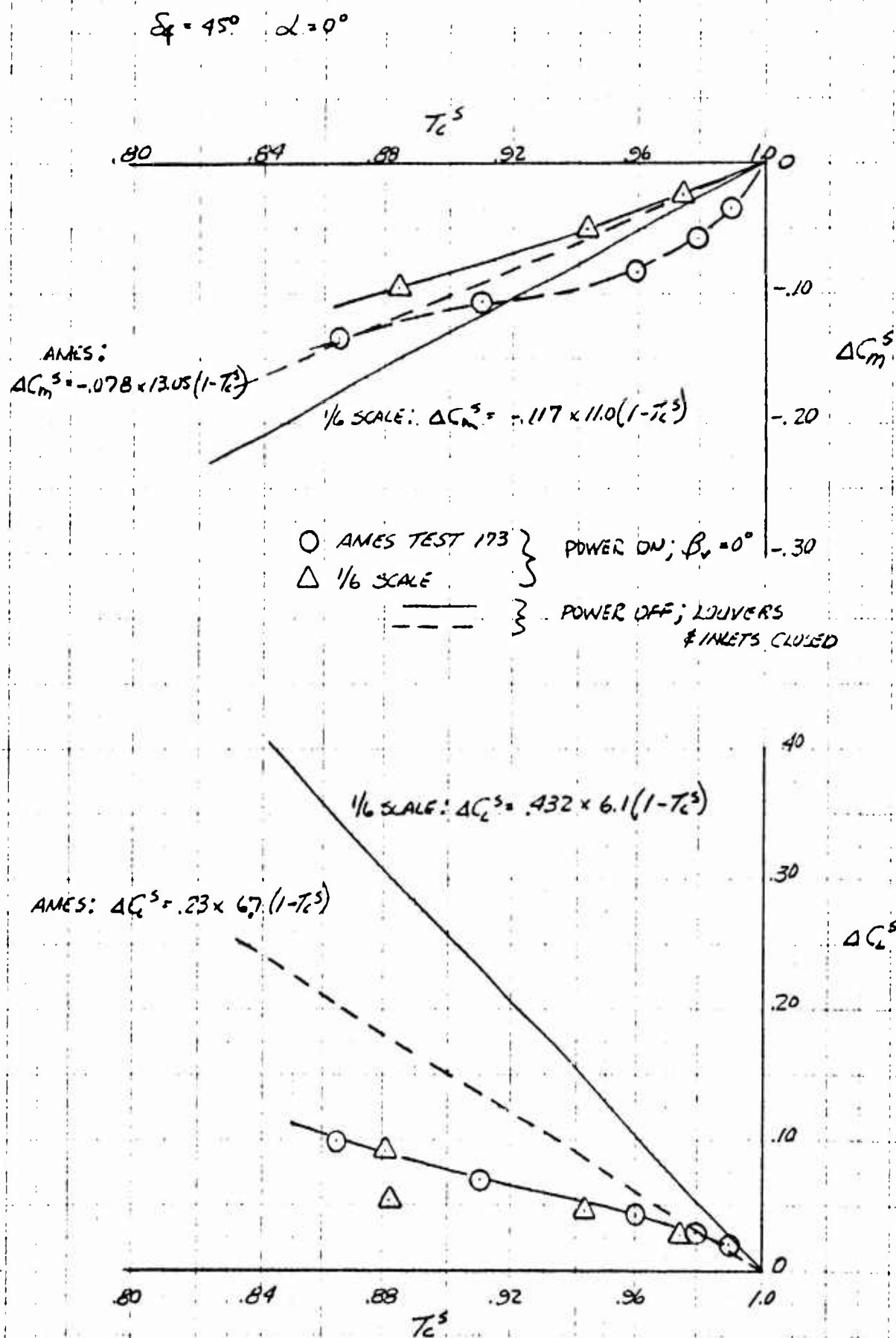


Figure 6.1

XV-5A EFFECT OF AILERON DECOOP ON LONGITUDINAL CHARACTERISTICS

$\alpha = 0^\circ$ $\delta_H = 15^\circ$

SOURCE: 1/6 SCALE MODEL

- POWER ON $\delta_V = 0^\circ$
- - - POWER OFF LOUVERS & INLETS CLOSED

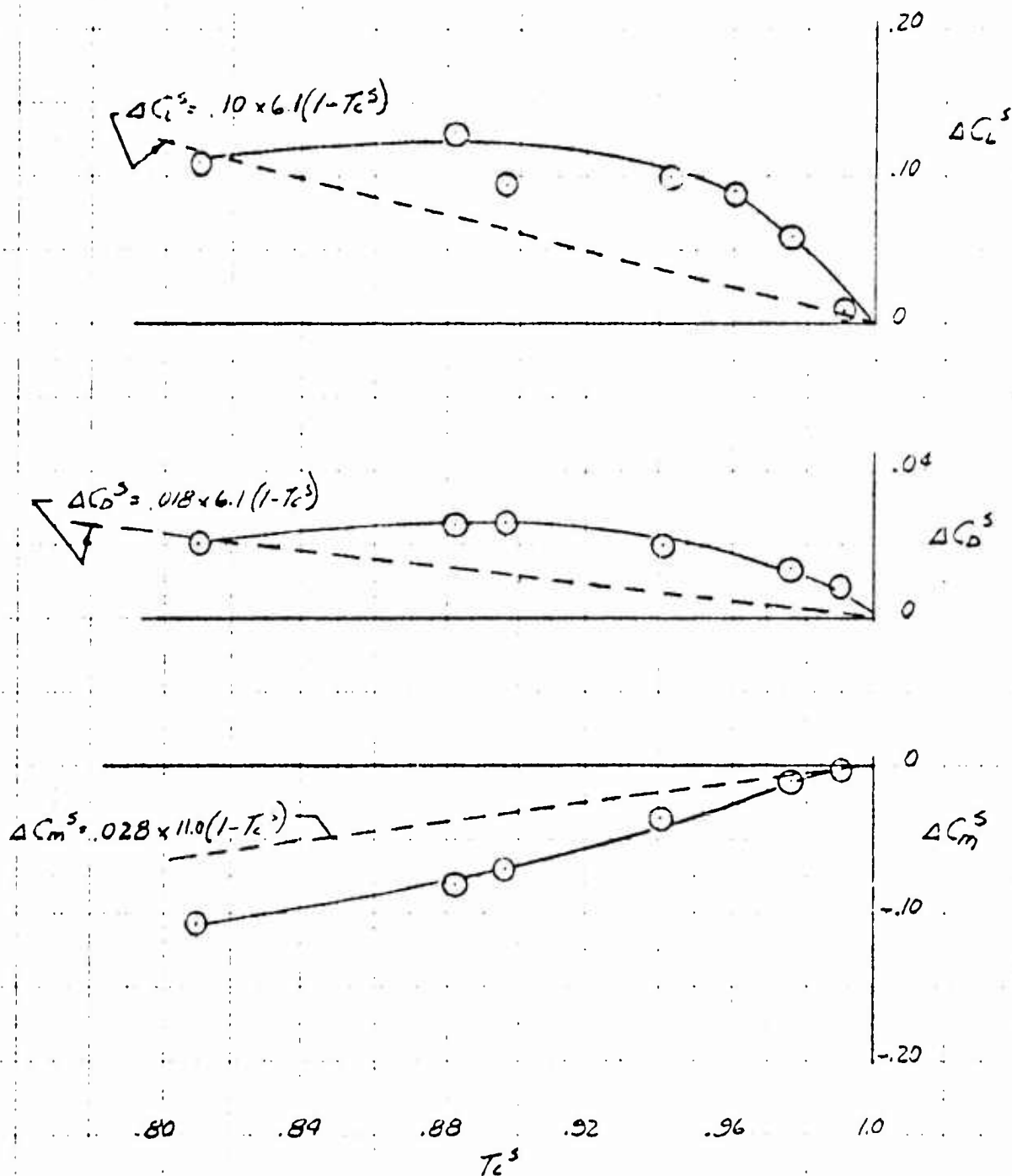


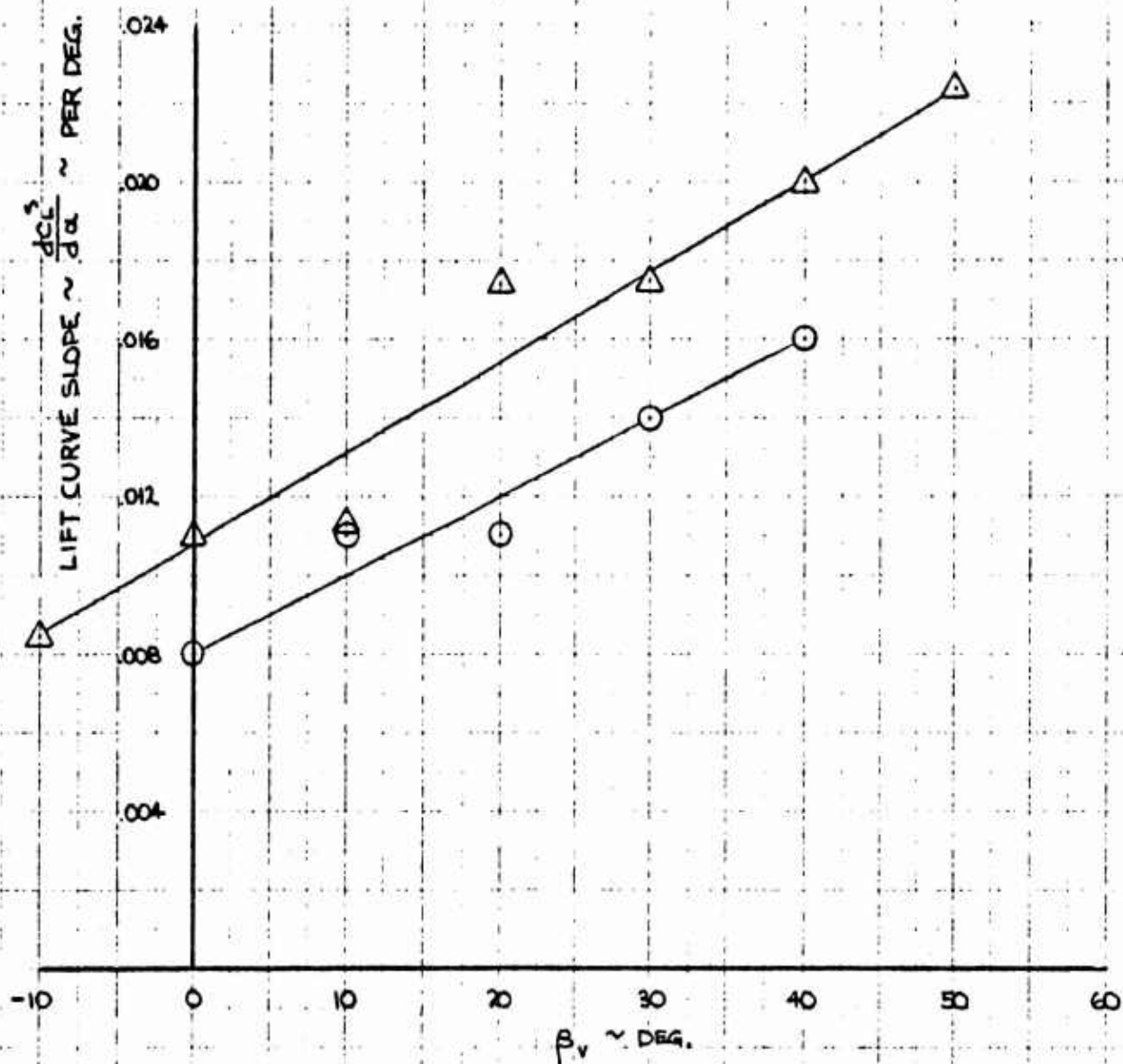
Figure 6.2

XV-5A

TYPICAL VARIATION OF LIFT CURVE SLOPE WITH VECTOR ANGLE

SOURCE: 1/6 SCALE MODEL

Sym	T_c^*	i_c^*
○	.975	15°
△	.956	OFF



YV-5A
 VARIATION OF INCREMENTAL DRAG
 COEFFICIENT DUE TO ANGLE OF ATTACK WITH
 VECTOR ANGLE

$\delta_f = 45^\circ, \beta_s = 0^\circ$
 1/6 SCALE TEST DATA

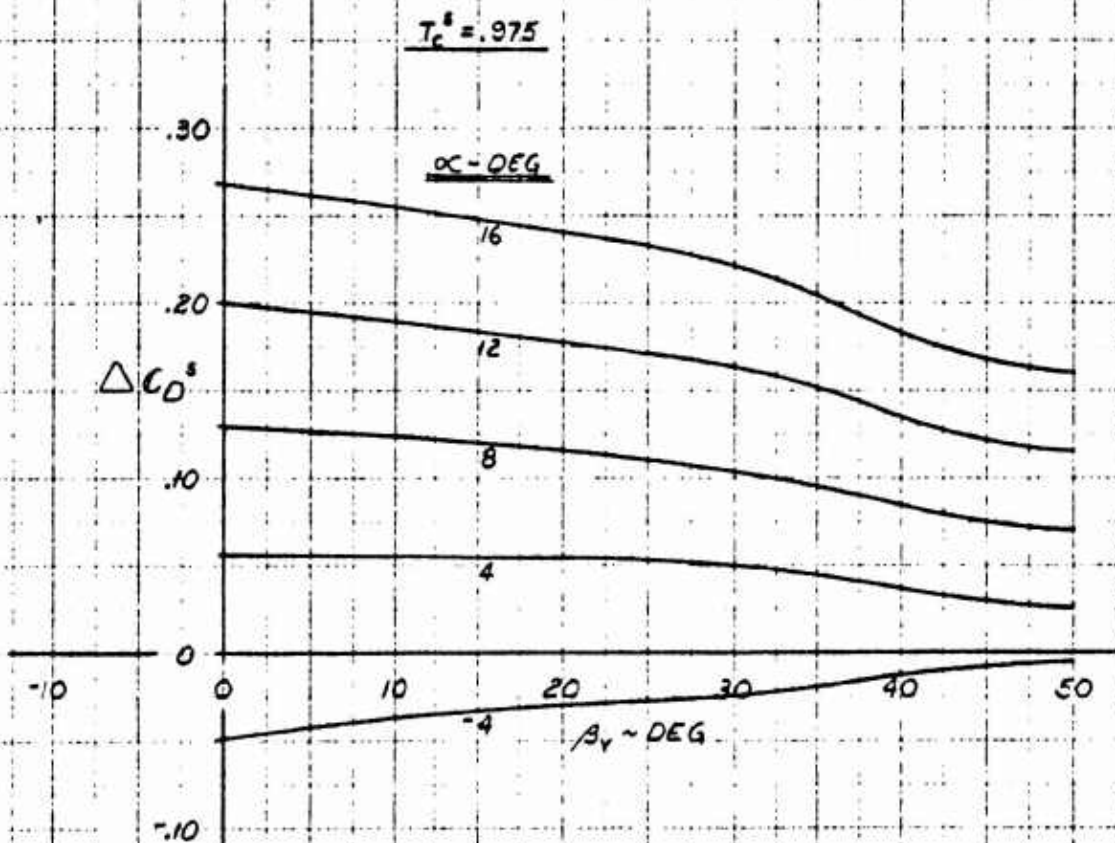
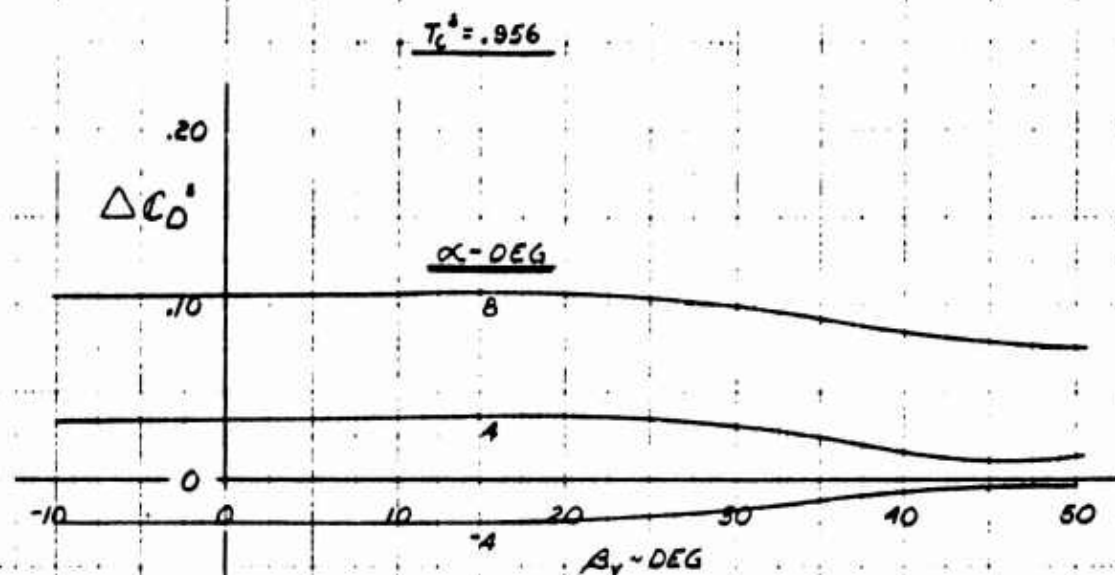


Figure 6.4

XU-5A
INCREASE IN THE INCREMENTAL DRAG
COEFFICIENT DUE TO ANGLE OF ATTACK
WITH 15° AILERON DROOP

TAIL-OFF, $\delta_t = 45^\circ$, $\beta_s = 0^\circ$
1/6 SCALE TEST DATA

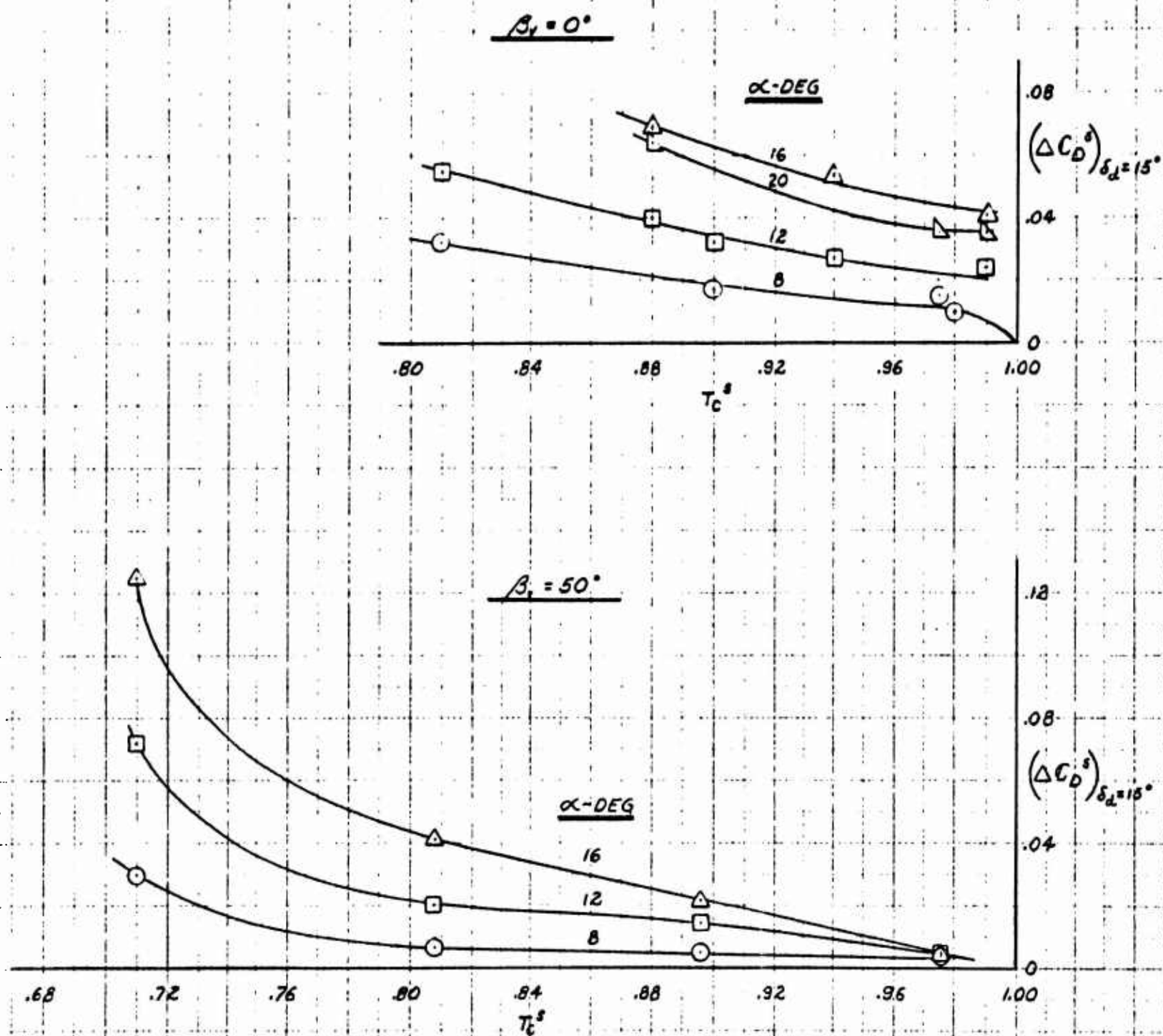


Figure 6.5

XU-5A
COMPARISON OF FULL-SCALE AND
1/6 SCALE STATIC STABILITY WITH
THE TAIL OFF

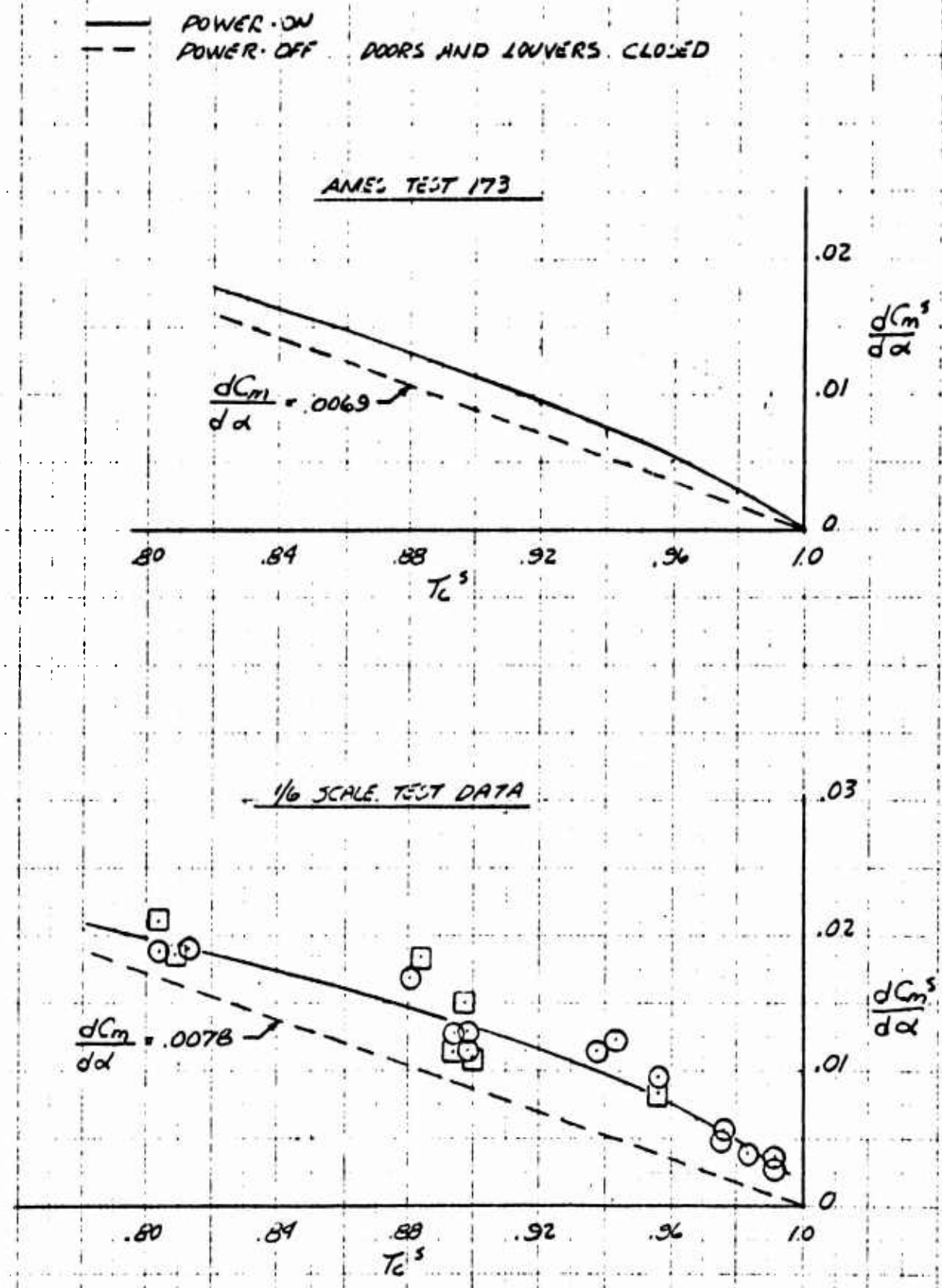


Figure 6.6

XV-5B
 INCREMENTAL LIFT AND COEFFICIENT
 DUE TO VECTOR ANGLE

$\alpha = 0^\circ$ $\delta_1 = 45^\circ$ $\delta_2 = 0^\circ$

SYMBOLS	SOURCE
SOLID	1/6 SCALE MODEL
HALF-SOLID	AMES TEST 173
FLASSED	AMES Q-AND TESTS
	1/6 SCALE (15° DOWN)

β°

\circ	-12
\circ	-10
\circ	10
\circ	15
Δ	20
\square	30
\diamond	40
\triangle	50

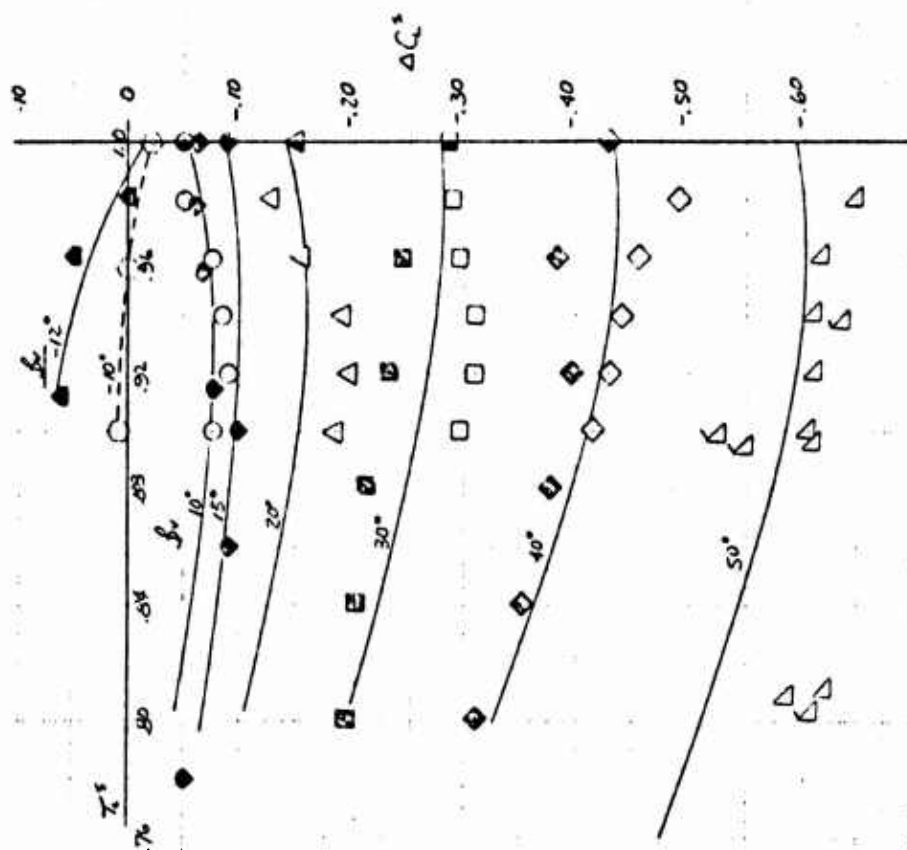
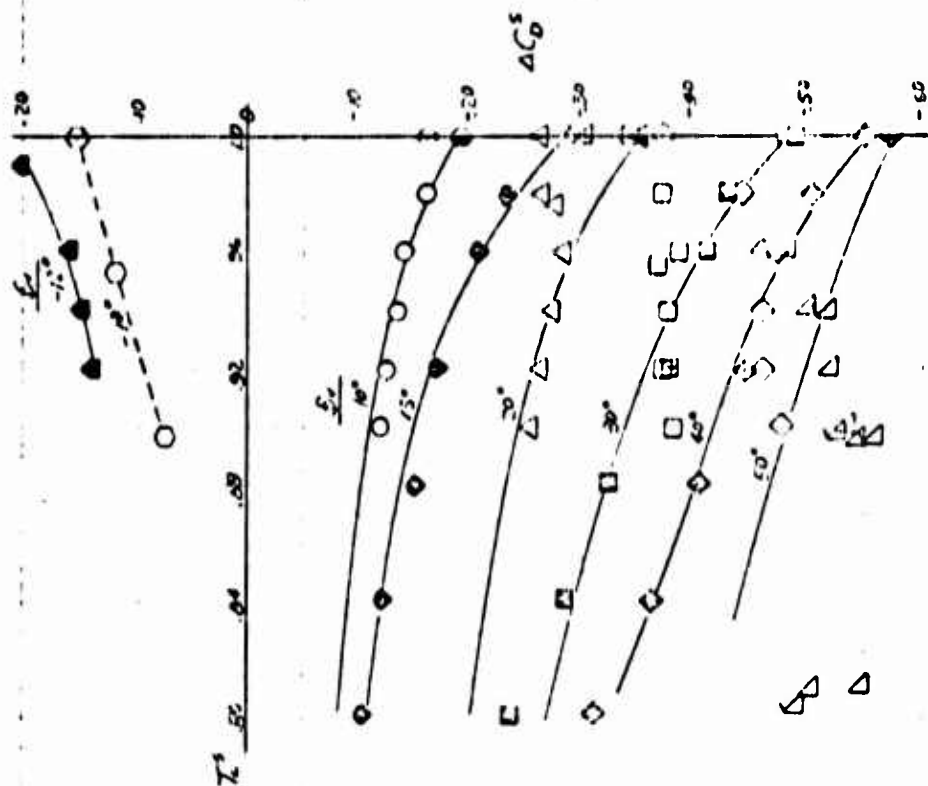


Figure 6.7

XV-5A
INCREMENTAL PITCHING MOMENT
COEFFICIENT DUE TO VECTOR ANGLE

$\alpha = 0^\circ$, $\delta_f = 45^\circ$, $\beta_0 = 0^\circ$, CG @ FUS. STA. 246, WL 112

SYMBOL	T_c^s	SYMBOLS	SOURCE
○	1.00	OPEN	1/6 SCALE MODEL
⌒	.98	SOLID	AMES TEST 173
□	.96	FLAGGED	1/6 SCALE MODEL (15° DROOP)
◇	.94		
▴	.92		
◻	.90		
▾	.88		
◊	.84		
○	.80		

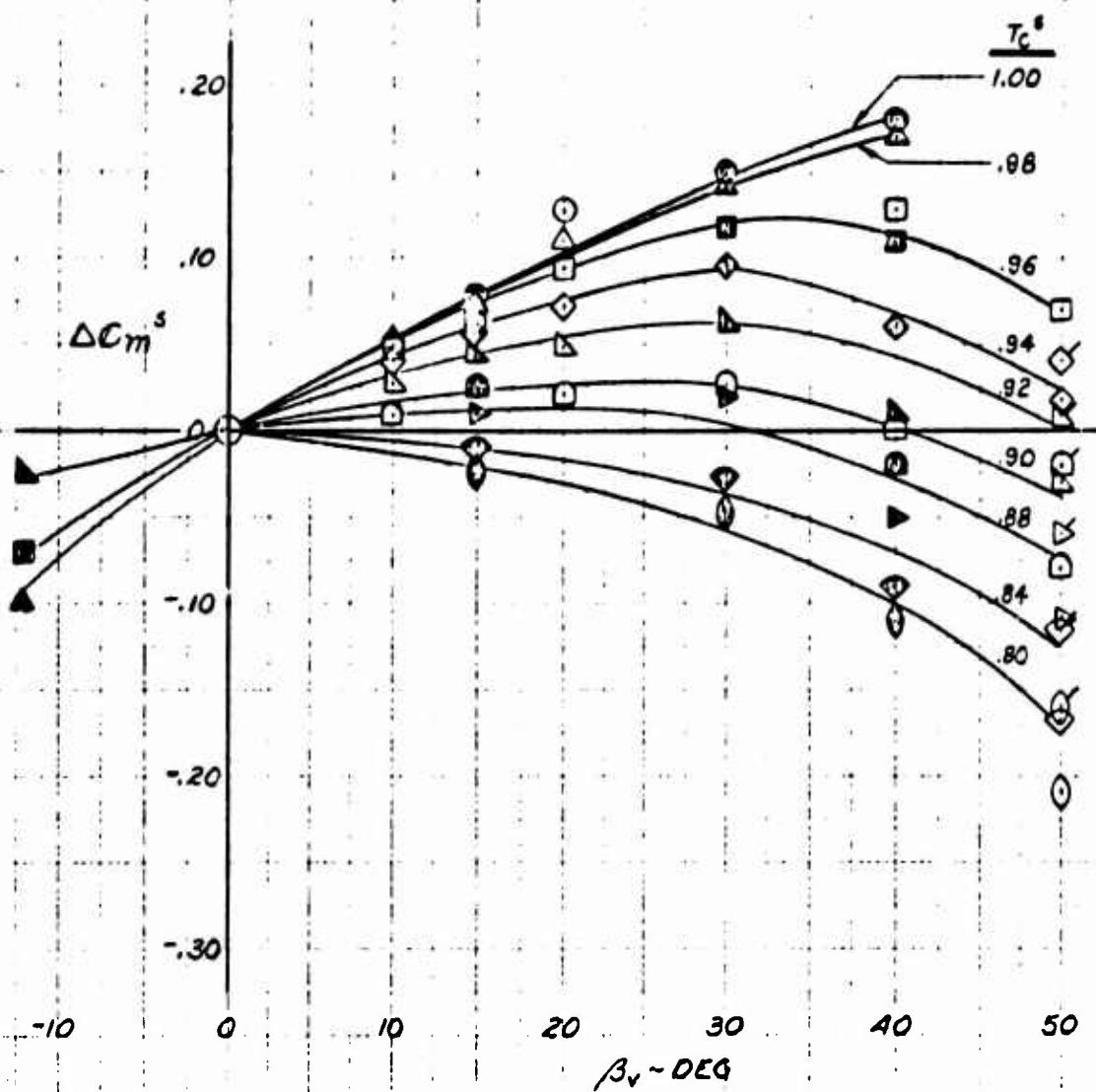
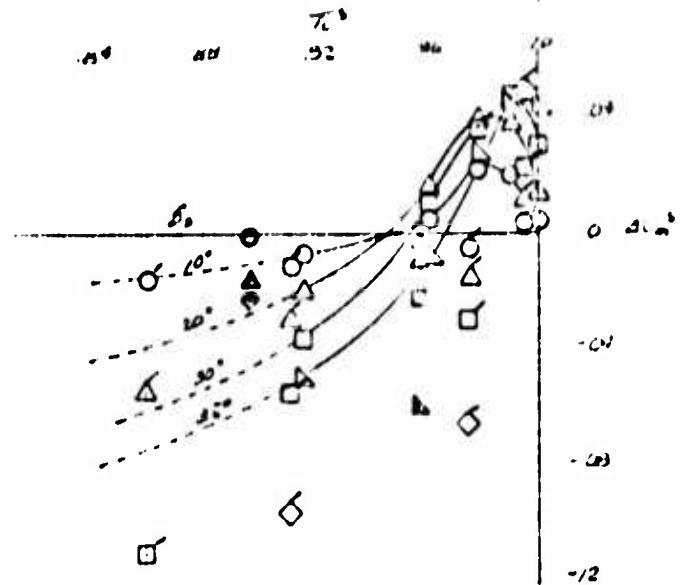


Figure 6.8

XV-5A
 COMPARISON OF EXIT LOUVER
 STAGGER EFFECTIVENESS DATA



$\alpha = 0^\circ$ $\delta_s = 45^\circ$ CB ST 246
 WL 112

SYMBOLS	SOURCE
OPEN	AMES TEST 173
SHADED	1/6 SCALE MODEL
FLATTED	AMES TEST 158 (REF. 12)

δ_s - URA
 ○ 10
 ◇ 15
 △ 20
 □ 30
 ▤ 35
 ◇ 40

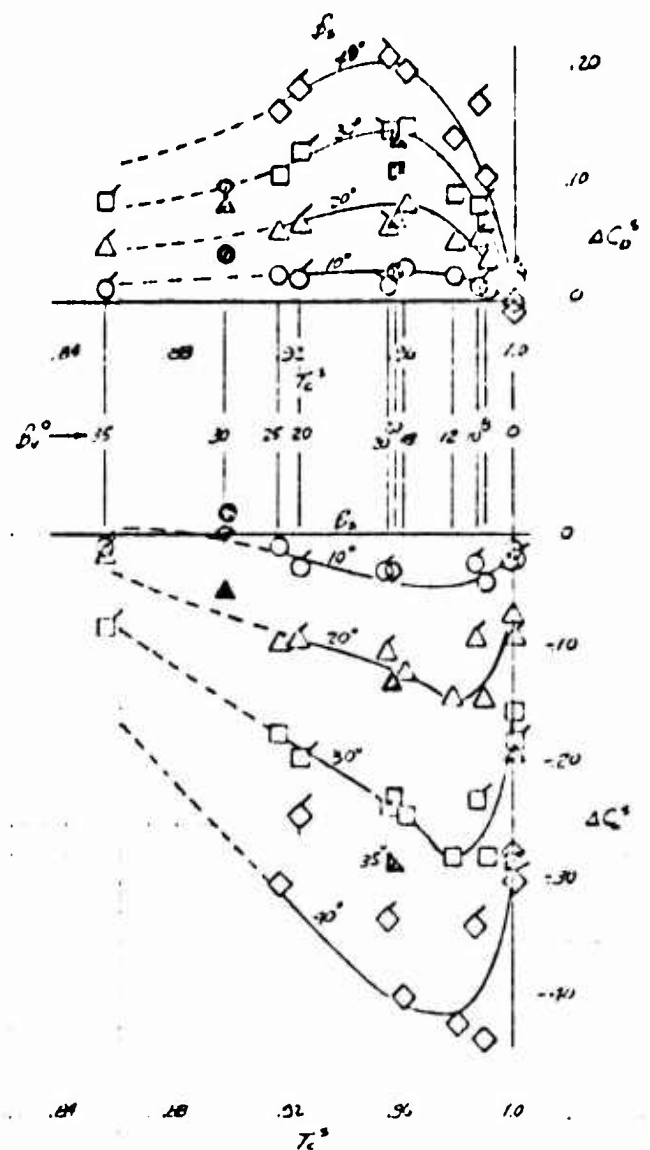


Figure 6.9

XV-5A

EFFECT OF NOSE FAN ON LONGITUDINAL STATIC STABILITY

SYM	SOURCE	CONFIGURATION
□	1/6 SCALE MODEL	$\alpha_i = 0^\circ, \alpha_s = 0^\circ, \delta_{NF} = 48^\circ$
◇	1/6 SCALE MODEL	$\alpha_i = 0^\circ, \alpha_s = 0^\circ, \delta_{NF} = 60^\circ$
○	AMES FULL SCALE	$\alpha_i = 0^\circ, \alpha_s = 0^\circ, \delta_{NF} = \text{VARIABLE}$
△	AMES FULL SCALE	$\alpha_i = \text{VARIABLE}, \alpha_s = \text{VARIABLE}$
◐	AMES FULL SCALE	NOSE FAN ONLY, $\delta_{NF} = 55^\circ$, TAIL-OFF

TAIL-ON

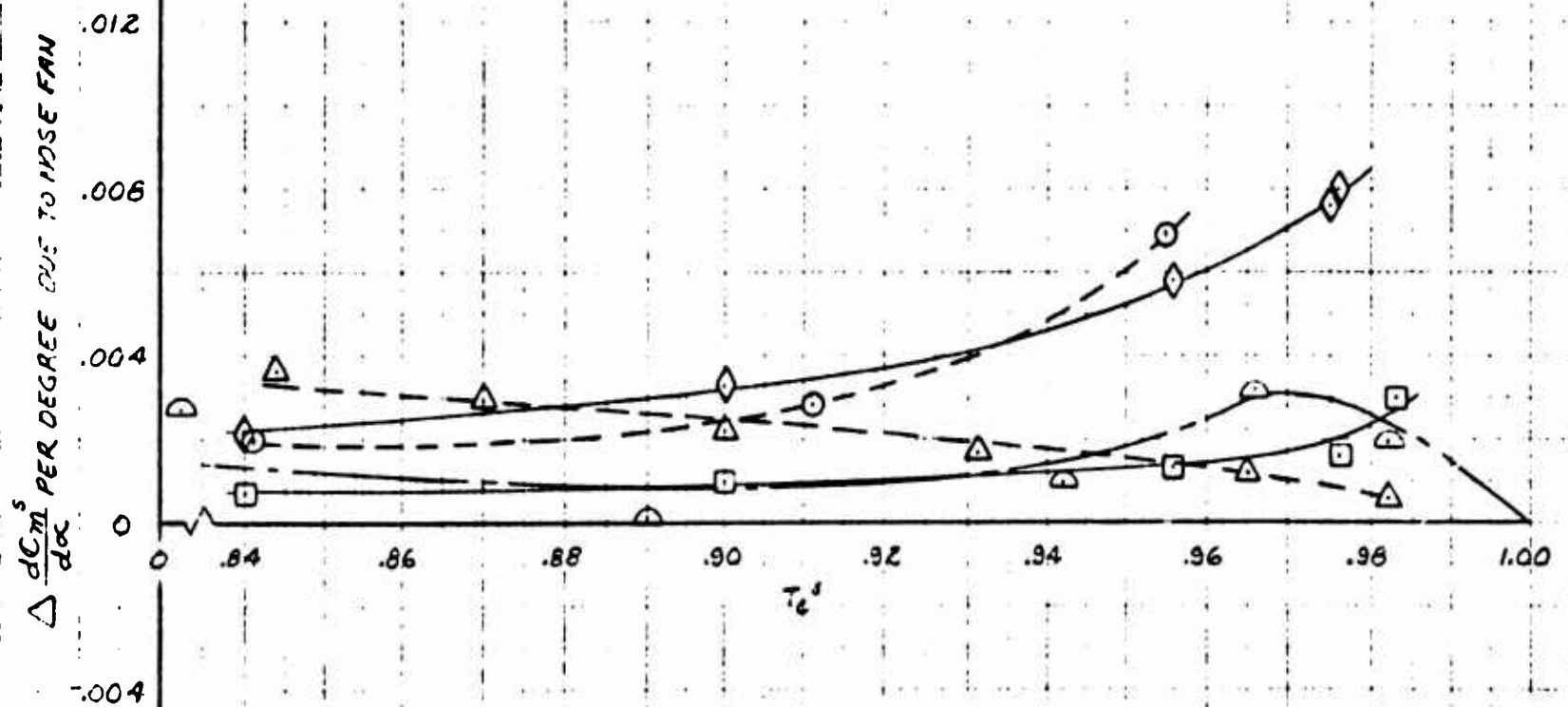


Figure 6.10

XV-5A
INCREMENTAL LIFT AND MOMENT COEFFICIENTS
DUE TO NOSE FAN OPERATION

$\alpha = 0^\circ, \delta_f = 15^\circ$

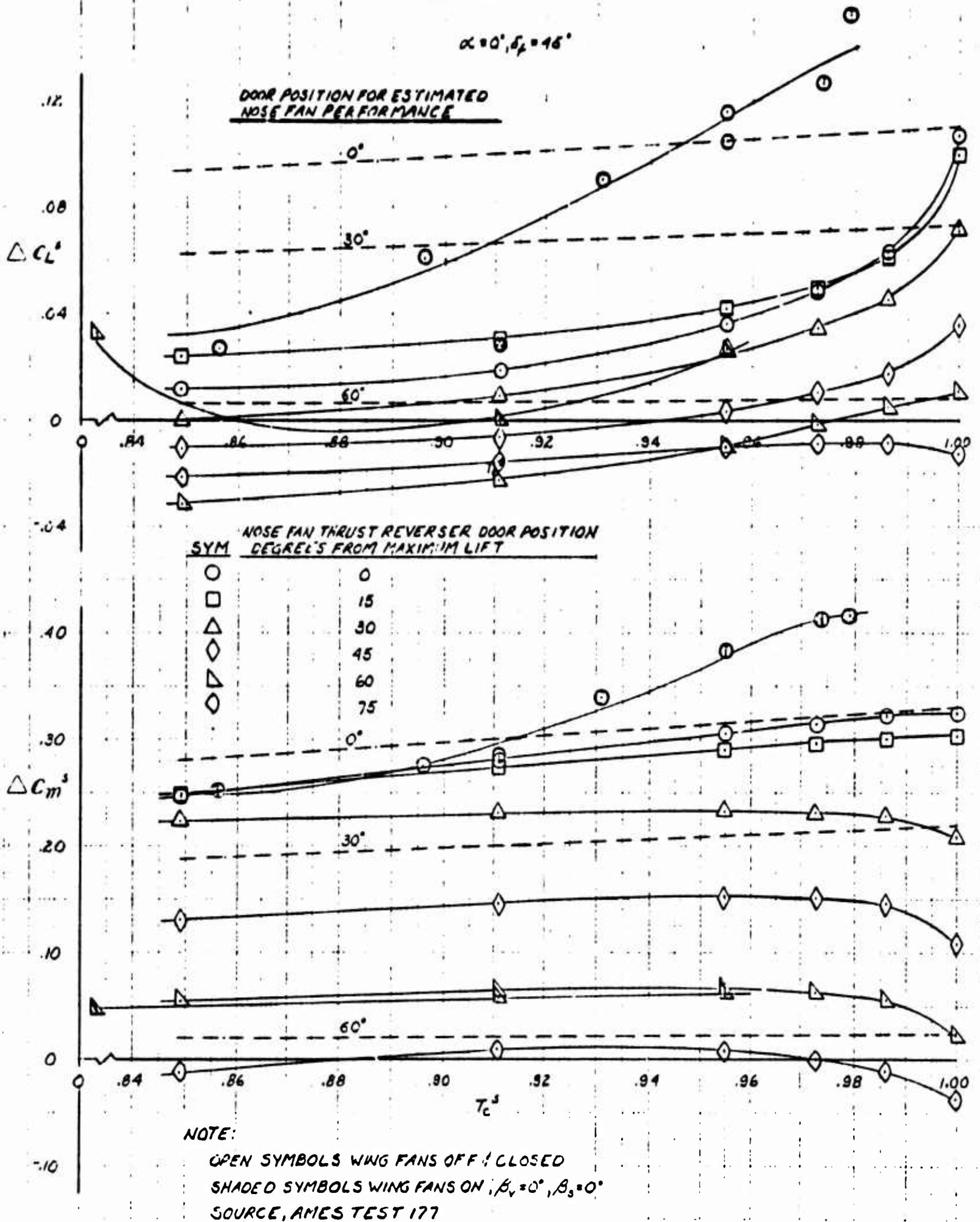


Figure 6.11

XV-5A

INCREMENTAL DRAG COEFFICIENT DUE TO NOSE FAN OPERATION

$$\alpha = 0^\circ, \delta_f = 45^\circ$$

SYM	NOSE FAN THRUST REVERSER DOCK POSITION DEGREES FROM MAXIMUM LIFT
○	0 & 15
△	30 & 75
◇	45
◡	60

NOTE:

OPEN SYMBOLS WING FANS OFF & CLOSED

SHADED SYMBOLS WING FANS ON, $\beta_1 = 0^\circ, \beta_2 = 0^\circ$

SOURCE, AMES TEST 177

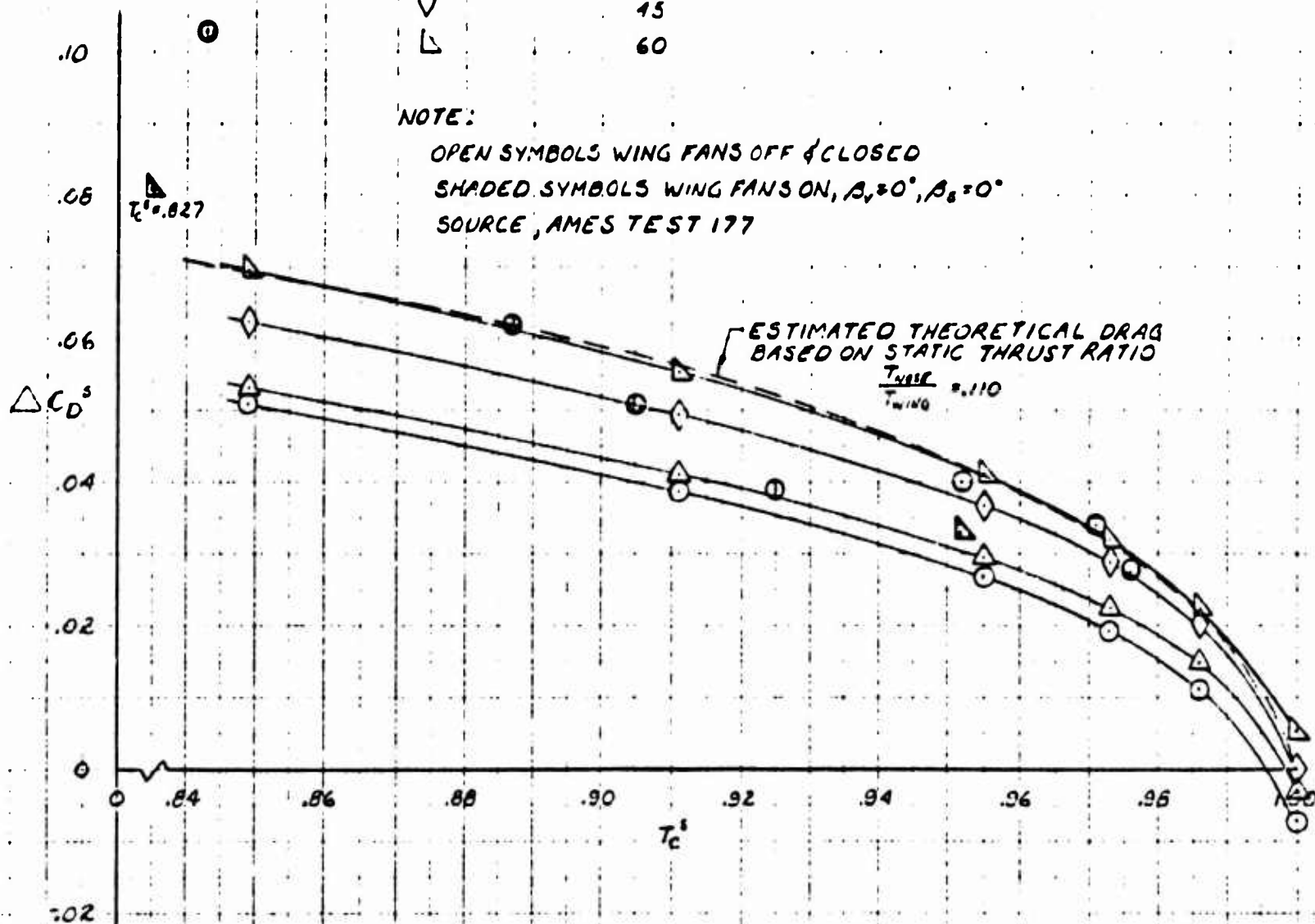


Figure 6.12

XV-5A

FAN SPEED VARIATION WITH FORWARD SPEED AND VECTOR ANGLE

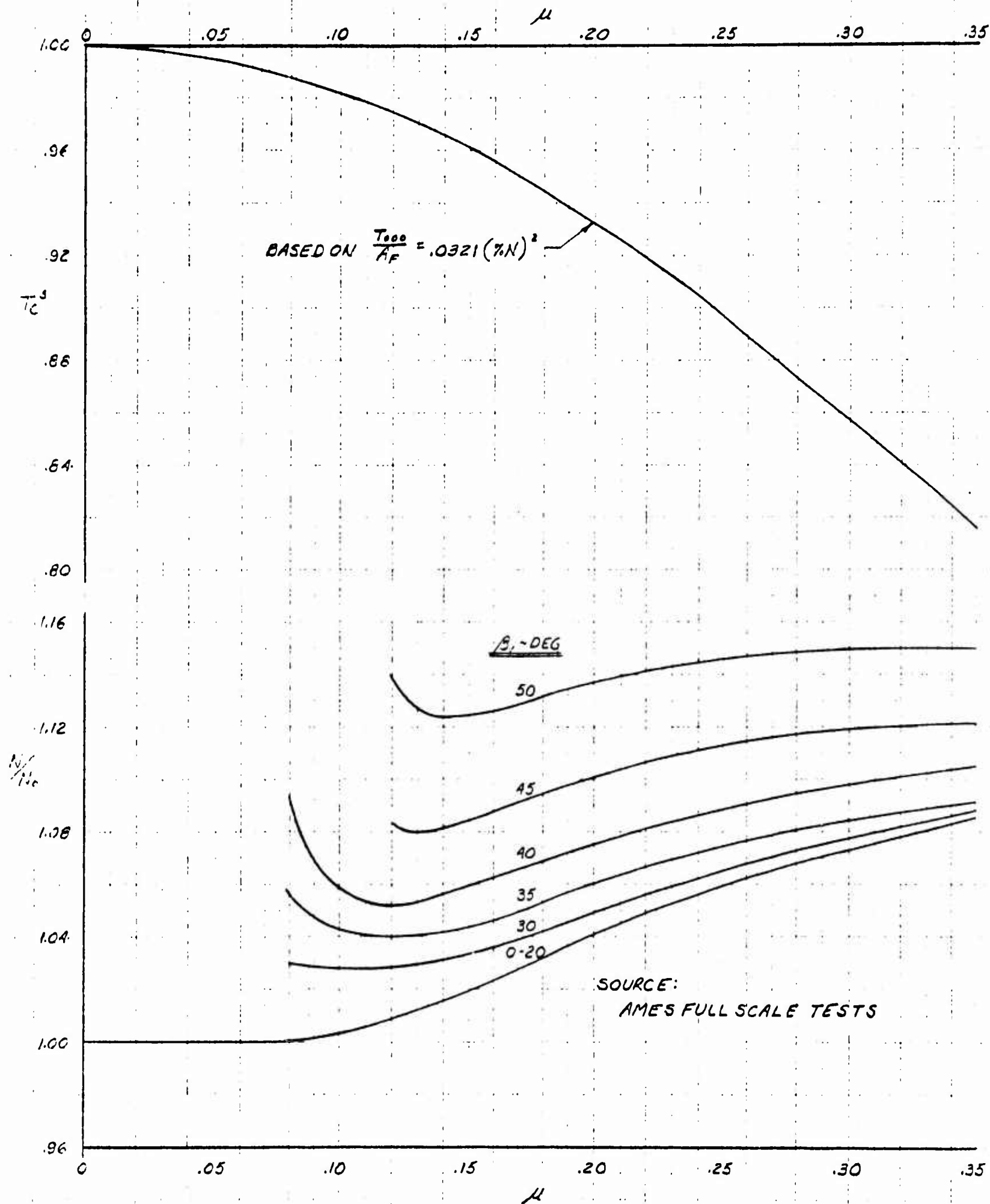


Figure 6.13

XV-5A

SIDE FORCE DERIVATIVE
WITH SIDESLIP IN FAN FLIGHT

STABILITY AXES

$\delta_f = 45^\circ$, TAIL-QN, NOSE FAN-OFF

SYM	α_f	β_f
○	0°	0°
□	50°	0° (FLAGGED SYMBOLS PLUS 15° DROOPEDAILERONS)
△		CLOSED (FAN INLETS CLOSED)

SOURCE:

$1/6$ SCALE MODEL DATA

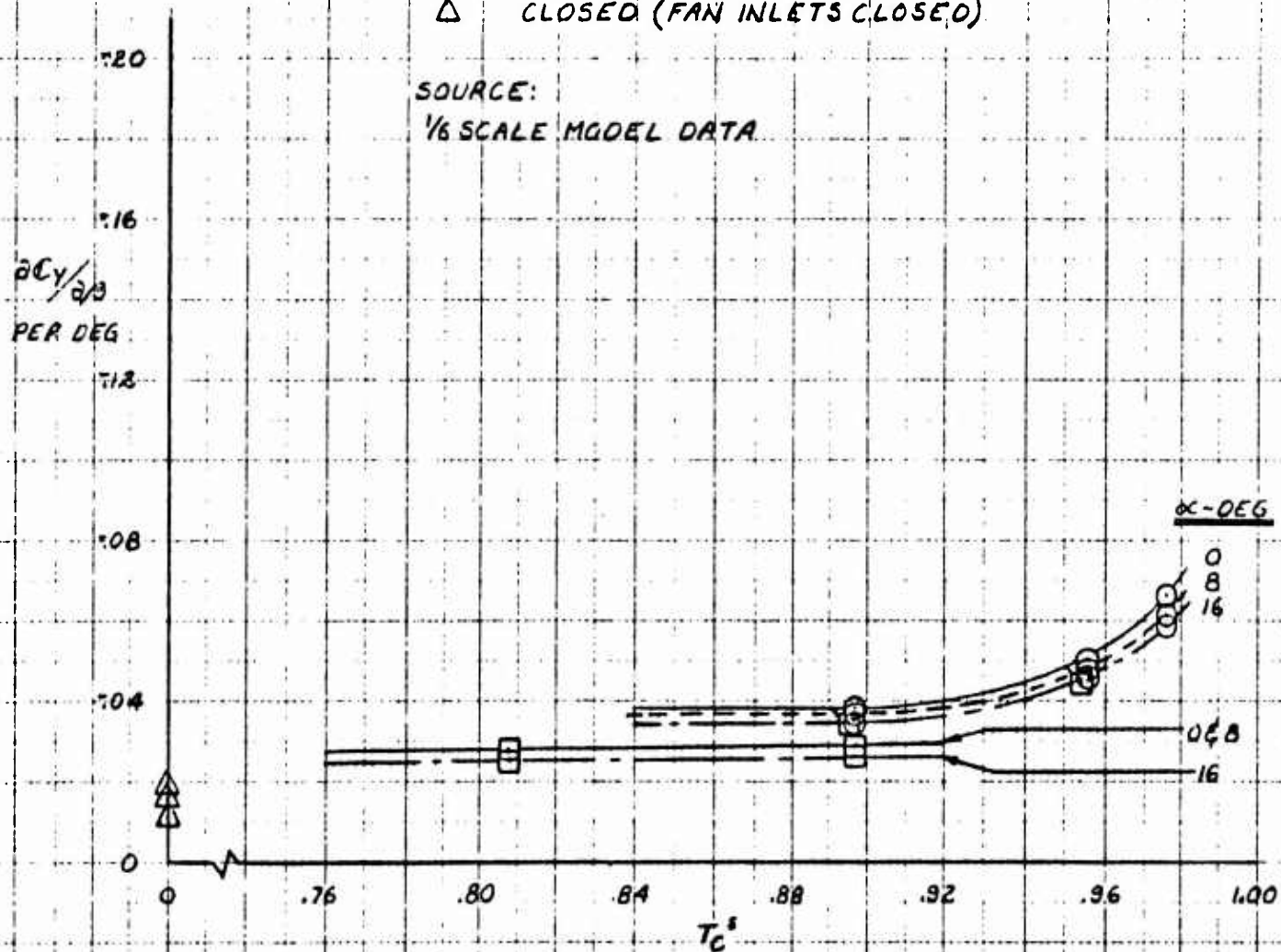


Figure 6.14

XV-5A

YAWING MOMENT DERIVATIVE WITH SIDESLIP IN FAN FLIGHT

STABILITY AXES, C.G. @ F.S. 246, W.L. 112

$\delta_f = 45^\circ$, TAIL-ON, NOSE FAN-OFF

SYM β_1 β_2

○ 0° 0°

□ 50° 0° (FLAGGED SYMBOLS PLUS 15° DROOPED AILERONS)

△ CLOSED (FAN INLETS CLOSED)

SOURCE:

$1/6$ SCALE MODEL DATA

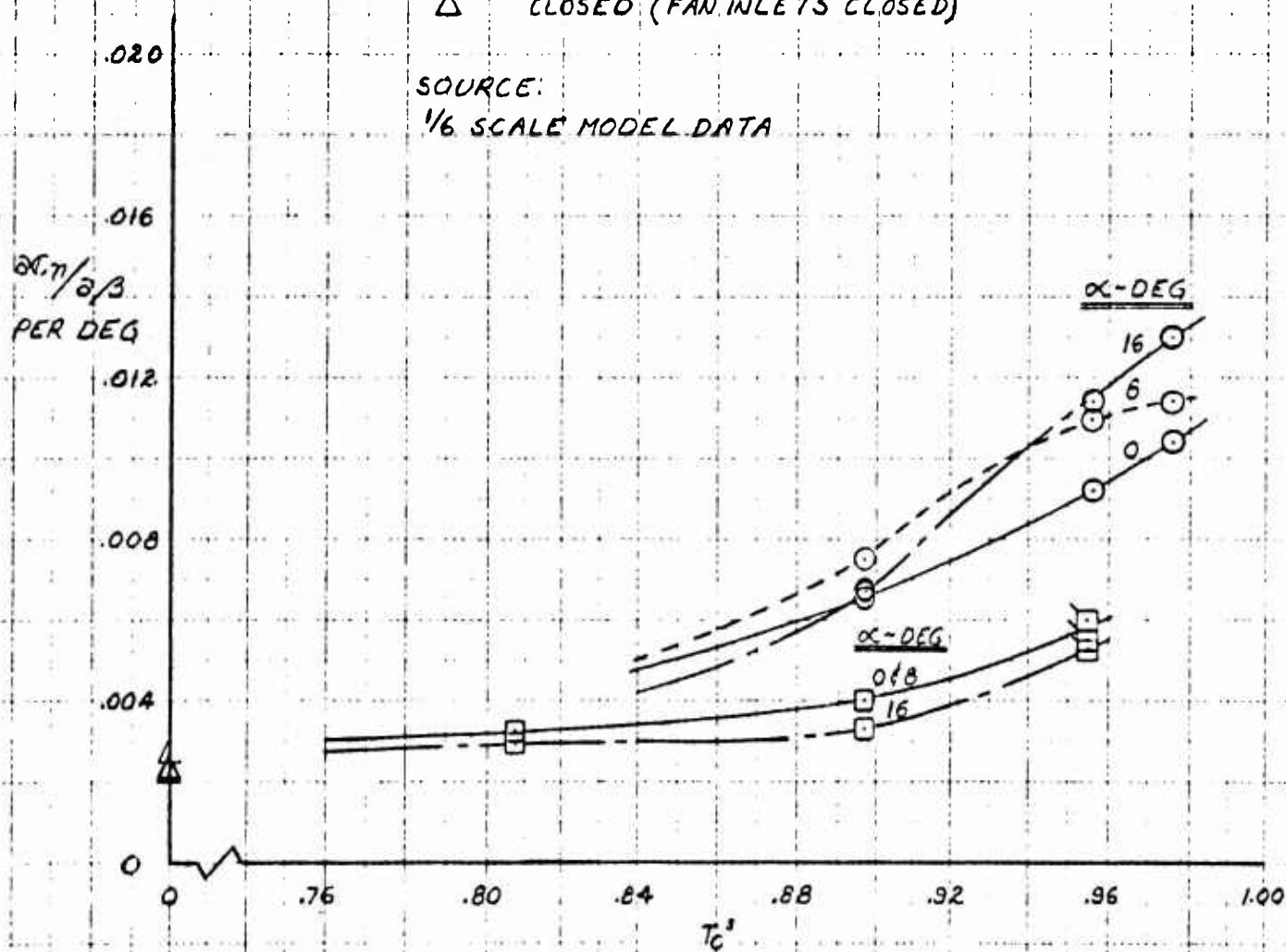


Figure 6.15

XV-5A
ROLLING MOMENT DERIVATIVE
WITH SIDESLIP IN FAN FLIGHT

STABILITY AXES, C.G. @ F.S. 246, W.L. 112
 $\delta_r = 45^\circ$, TAIL-ON, NOSE FAN-OFF

SYM	A_v	β_r
○	0°	0°
□	50°	0° (FLAGGED SYMBOLS PLUS 15° DROOPED AILERONS)
△		CLOSED (FAN INLETS CLOSED)

SOURCE:
1/6 SCALE MODEL DATA

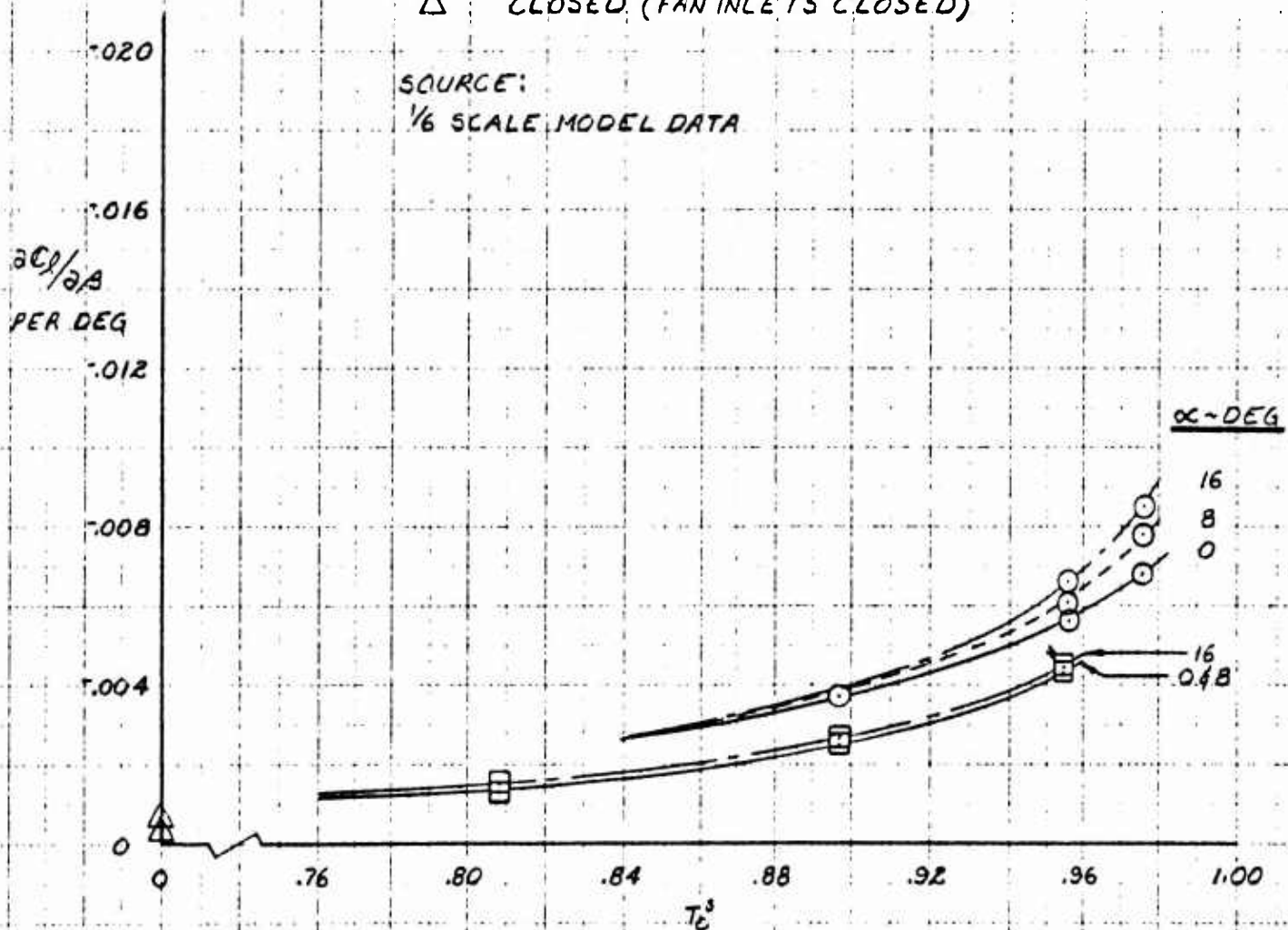


Figure 6.16

XV-5A

INCREMENTAL EFFECT OF NOSE FAN ON SIDE
FORCE DERIVATIVE WITH SIDESLIP

STABILITY AXES:

$\delta_f = 45^\circ$, TAIL-ON, $\beta_v = 0^\circ$ & 50° , $\beta_s = 0^\circ$

SOURCE:

1/6 SCALE MODEL DATA

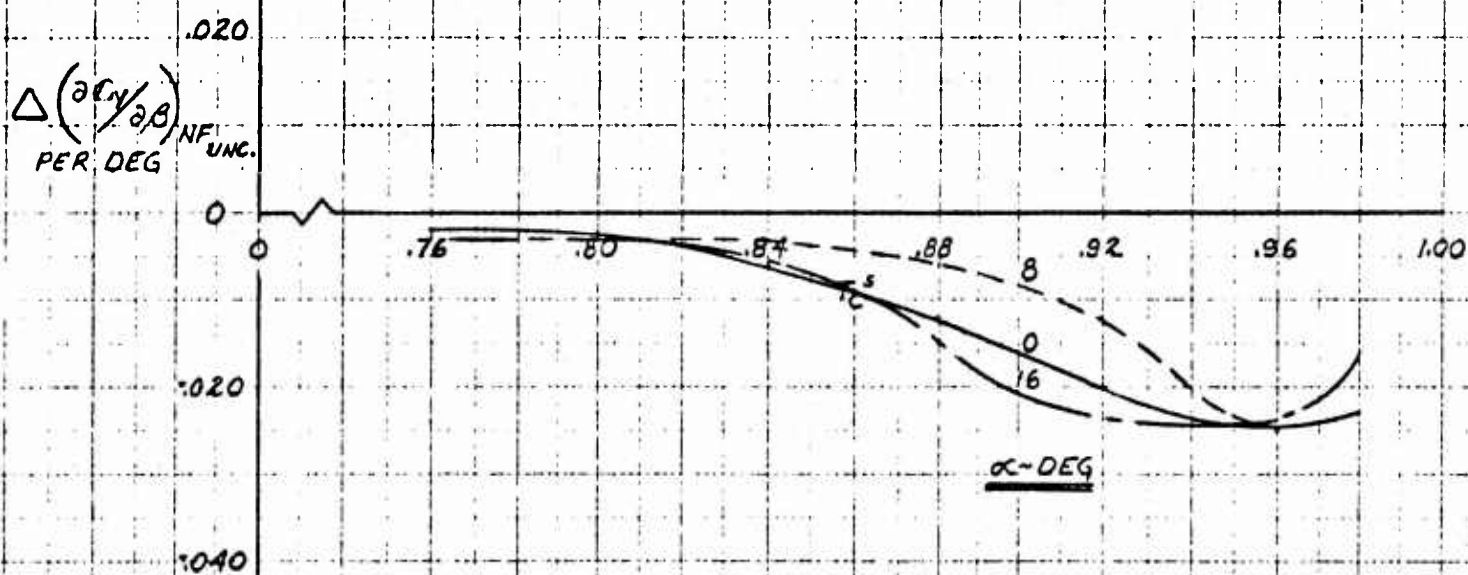


Figure 6.17

XV-5A

INCREMENTAL EFFECT OF NOSE FAN ON SIDE FORCE DERIVATIVE WITH SIDESLIP

STABILITY AXES, C.G. @ F.S. 246, W.L. 112
 $\delta_f = 45^\circ$, TAIL-ON, $\beta_v = 0^\circ \text{ to } 50^\circ$, $\beta_s = 0^\circ$

SOURCE:
 $\frac{1}{8}$ SCALE MODEL DATA

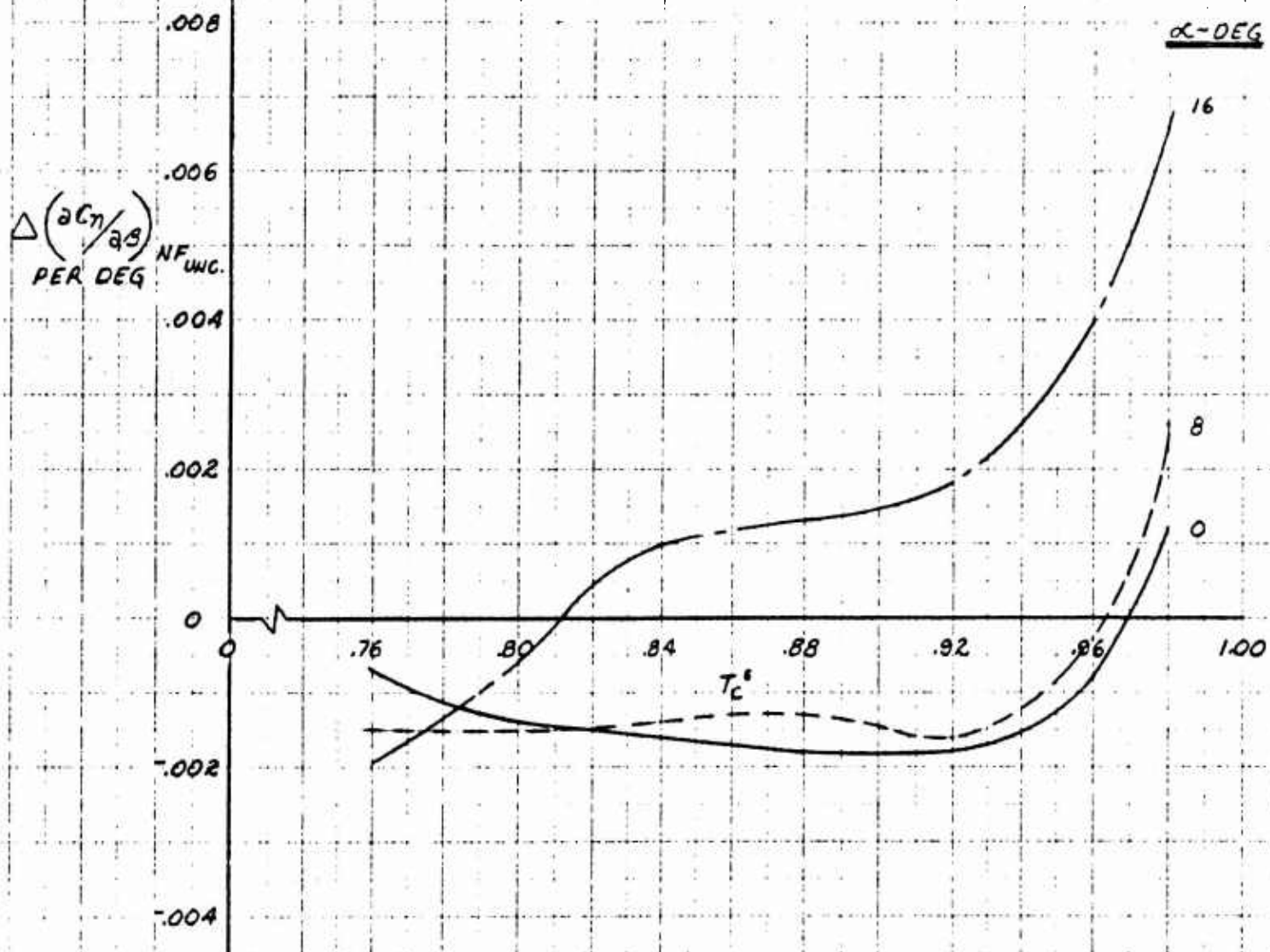


Figure 6.18

XY-5A

INCREMENTAL EFFECT OF NOSE FAN ON ROLLING
MOMENT DERIVATIVE WITH SIDESLIP

STABILITY AXES, C.G. @ F.S. 246, W.L. 112
 $\delta_f = 45^\circ$, TAIL-ON, $\beta_v = 0^\circ \text{ \& } 50^\circ$, $\beta_s = 0^\circ$

SOURCE:
1/6 SCALE MODEL DATA

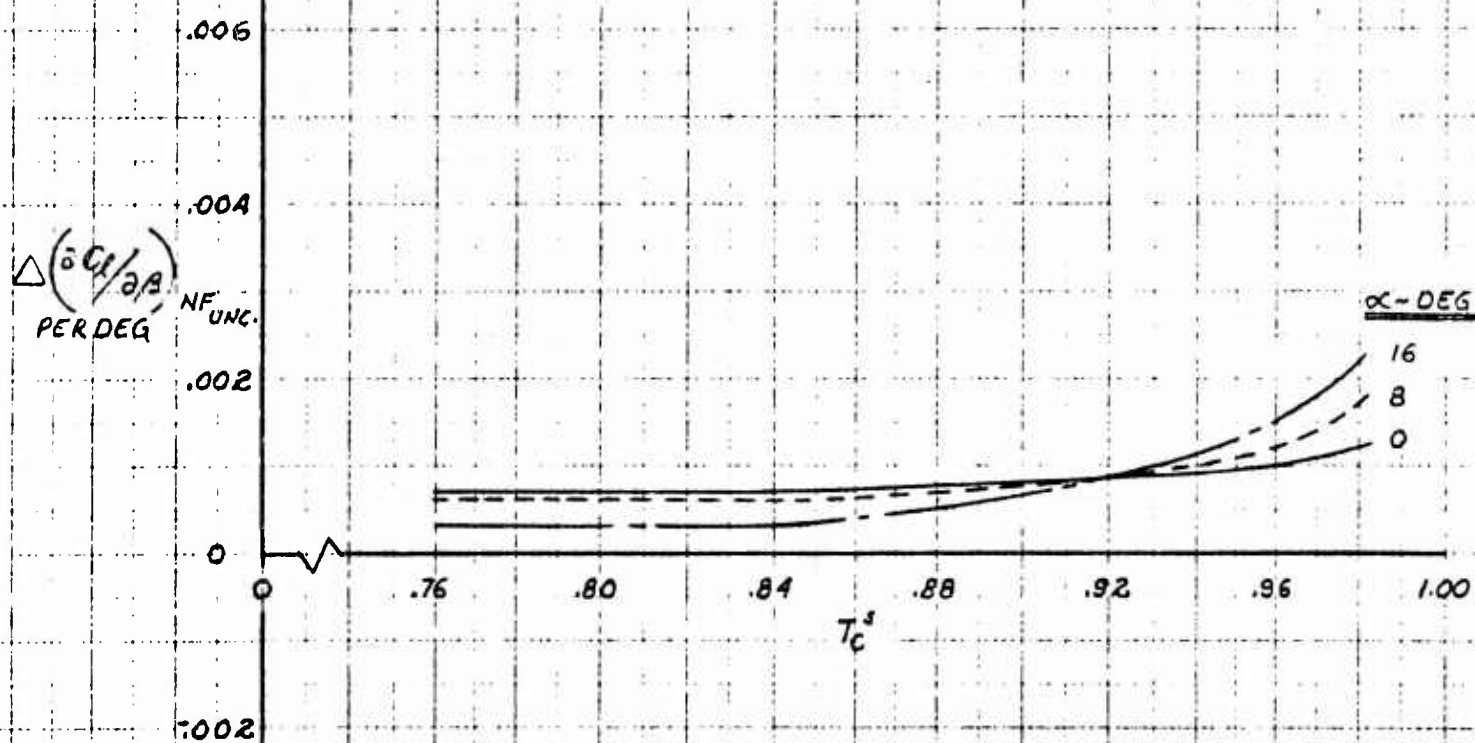


Figure 6.19

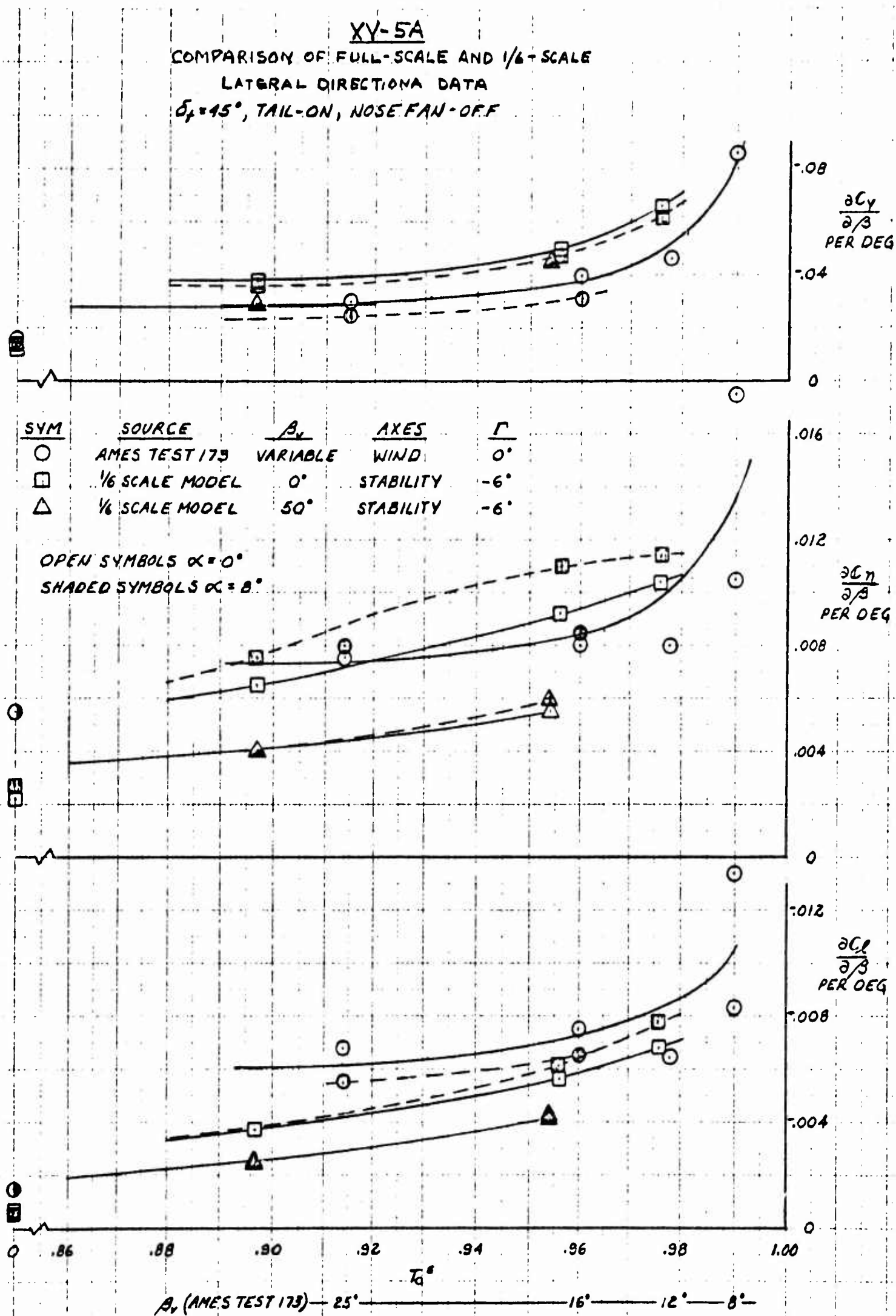
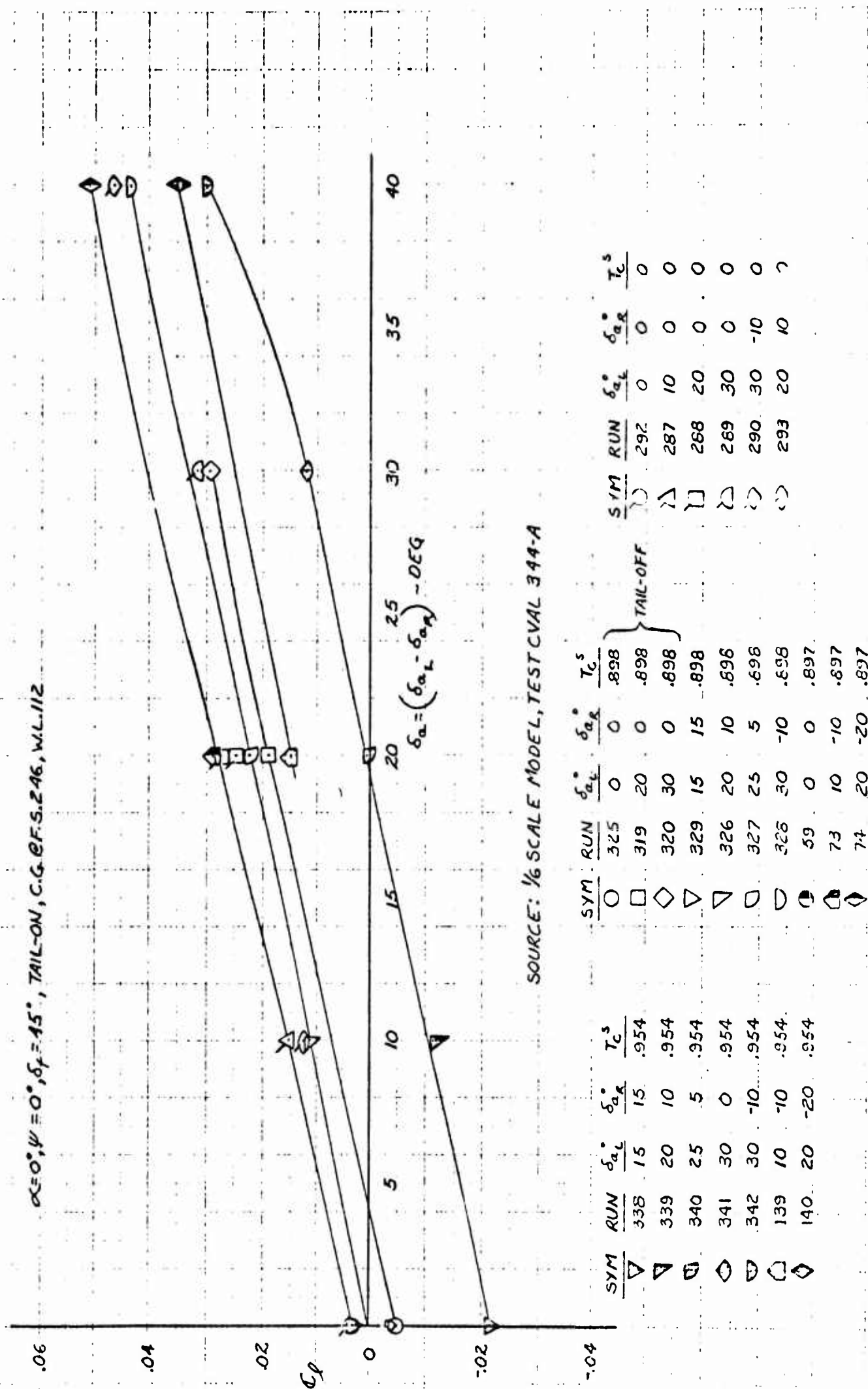


Figure 6.20

VARIATION OF ROLLING-MOMENT COEFFICIENT WITH DIFFERENTIAL AILERON

1- POSITIVE AILERON DEFLECTION IS TRAILING.
EDGE DOWN.



200

XV-5A

ESTIMATED YAWING-MOMENT COEFFICIENT
DUE TO DIFFERENTIAL AILERON DEFLECTION SCHEDULE

NOTE:

- 1- POSITIVE AILERON DEFLECTION IS TRAILING EDGE DOWN
- 2- DATA VALID FOR DIFFERENTIAL AILERON DEFLECTION SCHEDULE FOR 15° AILERON DROOP
- 3- STABILITY AXES

$$\delta_F = 45^\circ + \delta_A = 15^\circ, \text{ TAIL-ON, C.G. @ F.S. 240, N.L. 112}$$

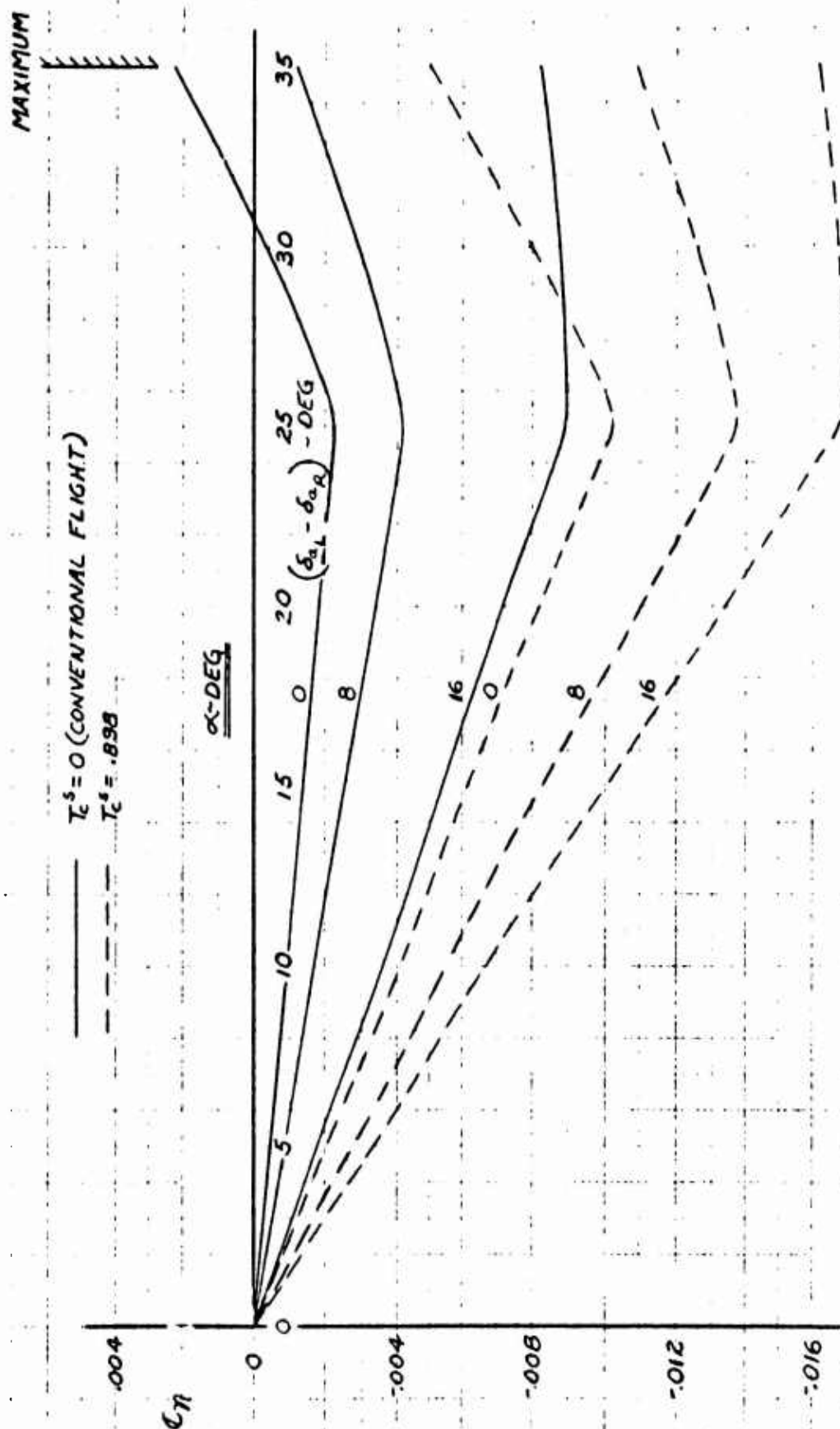


Figure 6.22

6.3 PHYSICAL CHARACTERISTICS

6.3.1 Wing Geometry

Dimensions based on a vertical projection onto a horizontal plane.

Gross area	260.321 sq ft
Aspect ratio	3.419
Taper ratio	
Inboard panel	.752
Outboard panel	.394
Span	29.833 ft
Chord length	
Root (BL 0.00)	145.000 in.
At break of quarter chord line (BL 100.75)	109.005 in.
Tip (BL 179.00)	43.000 in.
MAC	112.919
Airfoil section	
BL 170.05	NACA 0012-64
	a = 0.8 (modified), C _{li} = 0.2
See tabulated ordinates for other sections, Table 6.3.7	
Dihedral	
Inboard panel	0.000 deg
Outboard panel (from BL 107.000)	4.000 deg
Sweep	
Leading edge - inboard panel	19.660 deg
Leading edge - outboard panel	36.881 deg
Quarter chord line - inboard panel	15.000 deg
Quarter chord line - outboard panel	28.343 deg

Trailing edge - inboard panel	0.000 deg
Trailing edge - outboard panel	-5.399 deg
Geometric twist, see page 216.	
Fuselage Station of root chord leading edge (BL 0.00)	180.050
Fuselage Station of .25 MAC	239.380
BL of semi-span MAC	75.353
6.3.2 <u>Aileron Geometry</u>	
Gross area (aft of hinge line, per side)	10.057 sq ft
Aspect ratio	4.041
Taper ratio	.836
Span (per side, perpendicular to BL 0.00)	6.375 ft
Span-wise location	.573 to 1.000 b/2
Chord length (aft of hinge line, parallel to BL 0.00)	
BL 102.50	20.622 in.
BL 179.00	17.239 in.
MAC	18.981 in.
Fuselage Station of hinge line	
BL 103.61	304.370
BL 168-43	301.060
Fuselage Station of .25 MAC	307.249
BL of panel MAC	139.610
Deflection limits (from neutral position)	
as ailerons only	+15 deg
	-19
as flaps with +15.0 deg droop (differentially coupled)	+27 deg
	- 8

Type of balance - Internally sealed
pressure balance.

Control - 8.00 to 1.00 hydraulic power
boost

Aileron balance tab

(Serves as trim tab on left aileron)

Area (aft of hinge line, per side)	1.375 sq ft
Aspect ratio	8.026
Taper ratio	.927
Span (per side, perpendicular to BL 0.00)	3.322 ft
Span-wise location	.573 to .795 b/2
Chord length (aft of hinge line, parallel to BL 0.00)	
BL 102.50 (25% of local aileron chord)	5.156 in.
BL 142.36 (25% of local aileron chord)	4.777 in.
MAC	4.969 in.
Fuselage Station of hinge line	
BL 102.50	319.894
BL 142.36	316.506
Fuselage Station of .25 MAC	319.470
BL of panel MAC	122.176
Deflection limits (tab gear ratio .5 to 1.0 per deg. of aileron deflection from neutral)	
Right side	+13.5 to -9.5 deg
Left side (includes ± 3.0 deg. for trim)	+16.5 to -12.5 deg

Type of balance - Radius nose,
unsealed

6.3.3 Flap Geometry

Area (per side)	12.684 sq ft
Aspect ratio	3.246
Taper ratio	1.000
Span (per side, perpendicular to BL 0.00)	6.417 ft
Span-wise location	.138 to .568 b/2
Chord length	
BL 24.75	23.721 in.
BL 101.75	23.721 in.
MAC	23.721 in.
Fuselage Station of hinge line	308.150
WL of hinge line	92.580
Fuselage Station of .25 MAC	307.259
BL of panel MAC	63.250
Deflection limits	0.0 to +45.0 deg
Type of flap - single slotted with a NACA 634-021 modified airfoil section (see tabulated data for ordinates, Table 6.3.8)	

6.3.4 Fan Geometry

Rotor area (per wing fan, including hub)	21.305 sq ft
Rotor diameter	5.208 ft
Fuselage Station of fan center line	256.000
BL of fan center line	61.000
Vane deflection limits	
Simple vector	-7.5 to +50.0 deg
Simple stagger	13.0 to 37.0 deg

6.3.5 Horizontal Tail Geometry

Dimensions based on a vertical projection onto a horizontal plane.

Gross area	52.864 sq ft
Aspect ratio	3.288
Taper ratio	.466
Span	13.183 ft
Chord length	
Root (BL 0.00)	65.640 in.
Tip (BL 79.10)	30.600 in.
MAC	50.245 in.
Airfoil section	NACA 64A012
Dihedral	0.000 deg
Sweep	
Leading edge	19.519 deg
Quarter chord line	13.697 deg
Trailing edge	-5.058 deg
Incidence limits at root chord relative to fuselage reference plane (WL 100.00)	+20.0 to -5.0 deg
Fuselage Station root chord leading edge (WL 206.00)	468.560
Fuselage Station of .25 MAC (WL 206.00)	493.439
BL of panel MAC	34.749
Fuselage Station of horizontal tail pivot point (WL 201.25)	496.700
Tail length coefficient - Distance between wing .25 MAC and horizontal tail .25 MAC parallel to fuselage reference plane (WL 100.00) divided by the wing MAC	2.250

Elevator

Area (aft of hinge line, per side)	5.985 sq ft
Aspect ratio	5.001
Taper ratio	.638
Span (per side, perpendicular to BL 0.00)	5.471 ft
Span-wise location	.054 to .884 b/2
Chord length (aft of hinge line, parallel to BL 0.00)	
BL 4.26	16.033 in.
BL 69.91	10.224 in.
MAC	13.343 in.
Fuselage Station of elevator hinge line (WL 206.00)	517.790
Fuselage Station of .25 MAC (WL 206.00)	521.126
BL of panel MAC	34.664
Deflection limits	±25.0 deg
Type of balance - Internally sealed pressure balance	

6.3.6 Vertical Tail Geometry

Dimensions based on a horizontal projection onto a vertical plane.

Gross area (excluding dorsal)	50.995 sq ft
Aspect ratio	1.178
Taper ratio	.520
Span	7.750 ft
Chord length (parallel to WL 100.00)	
Root (WL 113.00)	103.920 in.
Tip (WL 206.00)	54.000 in.
MAC	81.590 in.

Airfoil section

WL 113.00 NACA 64A (012) - 016.5

WL 206.00 NACA 64A (012) - 013

Sweep

Leading edge 35.435 deg

Quarter chord line 30.000 deg

Trailing edge 9.918 deg

Fuselage Station of root chord leading
edge (WL 113.00) 408.450

Fuselage Station of .25 MAC 458.451

WL of MAC 154.600

Tail length coefficient - Distance
between wing .25 MAC and vertical
tail .25 MAC parallel to fuselage
reference plane (WL 100.00) divided
by the wing MAC 1.940

Rudder

Area (aft of hinge line) 6.395 sq ft

Aspect ratio 4.228

Taper ratio .674

Span (parallel with hinge line) 5.200 ft

Chord (aft of hinge line, perpendicular
with hinge line)

Root (18% of local vertical tail
chord) 17.634 in.

Tip (18% of local vertical tail
chord) 11.882 in.

MAC 14.945 in.

Sweep of rudder hinge line 15.184 deg

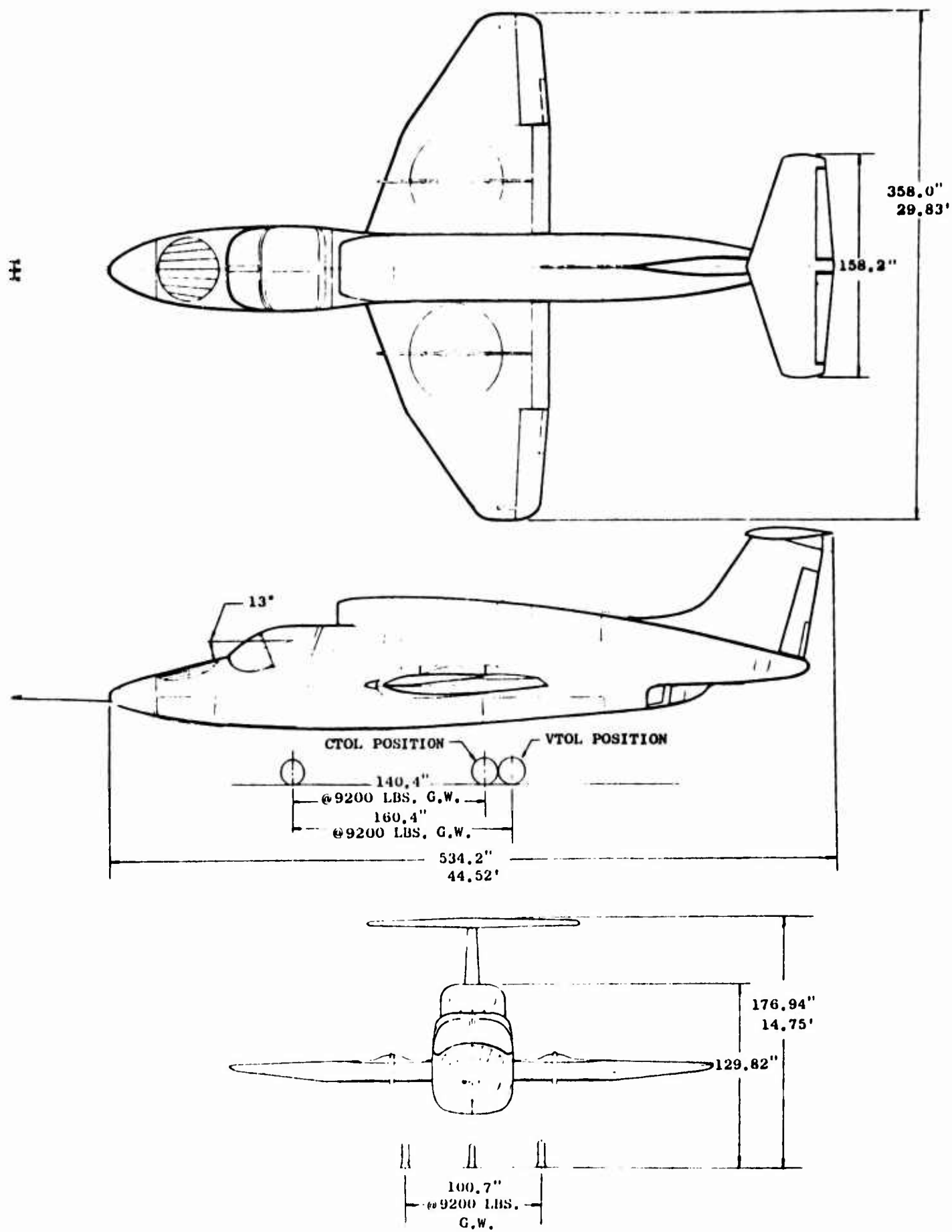
Fuselage Station of root chord at
hinge line 496.132

WL of root chord at hinge line 122.072

Fuselage Station of tip chord at hinge line	512.475
WL of tip chord at hinge line	182.293
Fuselage Station of .25 MAC	507.378
WL of .25 MAC	149.248
Deflection limits	±25.0 deg
Type of balance - Internally sealed pressure balance	

Rudder trim tab

Area (aft of hinge line)	.714 sq ft
Aspect ratio	6.057
Taper ratio	.870
Span (parallel to rudder hinge line)	2.080 ft
Chord (aft of hinge line, perpendicular to rudder hinge line)	
Root (25% of local rudder chord)	4.408 in.
Tip (25% of local rudder chord)	3.833 in.
MAC	4.128 in.
Sweep of rudder trim tab hinge line	11.451 deg
Fuselage Station of root chord at hinge line	508.896
WL of root chord at hinge line	118.608
Fuselage Station of tip chord at hinge line	513.768
WL of tip chord at hinge line	143.147
Fuselage Station of .25 MAC	512.271
WL of .25 MAC	130.322
Deflection limits	±10.0 deg
Type of balance - Radius nose, unsealed	



3 View - XV-5A

6.3.7 Wing Airfoil Ordinates

(Station and Ordinates Given in Percent of Local Chord)

BL - 25.000 ⁽¹⁾			BL - 40.000 ⁽¹⁾		
Station	Ordinate, Upper Surface	Ordinate, Lower Surface	Station	Ordinate, Upper Surface ⁽²⁾	Ordinate, Lower Surface
0.961	1.132	-0.977	0.961	1.285	-1.086
3.806	2.109	-1.712	3.806	2.356	-2.047
8.426	3.113	-2.396	8.426	3.350	-2.677
14.645	4.068	-2.962	14.645	4.284	-3.236
22.222	4.971	-3.642	22.222	5.171	-3.828
30.866	5.695	-3.851	30.866	5.944	-4.246
40.246	6.203	-4.079	40.246	6.418	-4.409
50.000	6.395	-4.197	50.000	6.530	-4.498
59.754	6.136	-4.189	59.754	6.204	-4.422
69.134	5.438	-3.844	69.134	5.462	-3.993
77.778	4.446	-3.153	77.778	4.437	-3.225
85.355	3.136	-2.183	85.355	3.106	-2.218
91.574	1.837	-1.286	91.574	1.820	-1.292
96.194	0.845	-0.588	96.194	0.818	-0.584
99.039	0.206	-0.154	99.039	0.198	-0.145

BL - 51.364 ⁽¹⁾			BL - 59.100 ⁽¹⁾		
Station	Ordinate, Upper Surface ⁽²⁾	Ordinate, Lower Surface	Station	Ordinate Upper Surface ⁽²⁾	Ordinate, Lower Surface
0.961	1.313	-1.152	0.961	1.323	-1.170
3.806	2.518	-2.289	3.806	2.579	-2.386
8.426	3.600	-2.992	8.426	3.780	-3.280
14.645	4.566	-3.624	14.645	4.786	-3.995
22.222	5.455	-4.266	22.222	5.626	-4.552
30.866	6.158	-4.563	30.866	6.296	-4.786
40.246	6.561	-4.686	40.246	6.667	-4.883
50.000	6.629	-4.737	50.000	6.883	-4.907
59.754	6.245	-4.603	59.754	6.279	-4.730
69.134	5.479	-4.105	69.134	5.492	-4.189
77.778	4.421	-3.284	77.778	4.420	-3.325
85.355	3.079	-2.250	85.355	3.067	-2.276
91.574	1.800	-1.310	91.574	1.795	-1.320
96.194	.805	-0.584	96.194	0.807	-0.589
99.039	.192	-0.142	99.039	0.196	-0.145

Notes: (1) Leading edge radius 1.25 in.

(2) Excluding door fairing.

(Station and Ordinates Given in Percent of Local Chord)

BL = 75.000 ⁽¹⁾			BL = 85.000 ⁽¹⁾		
Station	Ordinate, Upper Surface ⁽²⁾	Ordinate, Lower Surface	Station	Ordinate, Upper Surface ⁽²⁾	Ordinate, Lower Surface
0.961	1.238	-1.150	0.961	1.352	-1.264
3.806	2.656	-2.588	3.806	2.835	-2.787
8.426	4.199	-3.976	8.426	4.379	-4.296
14.645	5.262	-4.796	14.645	5.539	-5.264
22.222	6.006	-5.135	22.222	6.228	-5.487
30.866	6.573	-5.262	30.866	6.738	-5.556
40.246	6.860	-5.312	40.246	6.996	-5.583
50.000	6.810	-5.278	50.000	6.865	-5.504
59.754	6.336	-4.999	59.754	6.350	-5.173
69.134	5.515	-4.365	69.134	5.513	-4.479
77.778	4.390	-3.414	77.778	4.361	-3.463
85.355	3.042	-2.331	85.355	2.992	-2.355
91.574	1.776	-1.350	91.574	1.762	-1.369
96.194	0.798	-0.609	96.194	0.802	-0.628
99.039	0.203	-0.152	99.039	0.200	-0.157

BL = 90.000 ⁽¹⁾			BL = 100.75 ⁽¹⁾		
Station	Ordinate, Upper Surface ⁽²⁾	Ordinate, Lower Surface	Station	Ordinate, Upper Surface	Ordinate, Lower Surface
0.961	1.374	-1.294	0.961	1.410	-1.363
3.806	2.916	-2.850	3.806	3.052	-2.847
8.426	4.467	-4.388	8.426	4.693	-4.267
14.645	5.660	-5.487	14.645	6.029	-5.436
22.222	6.329	-5.682	22.222	6.706	-6.108
30.866	6.817	-5.735	30.866	7.105	-6.141
40.246	7.034	-5.739	40.246	7.254	-6.104
50.000	6.896	-5.638	50.000	7.050	-5.927
59.754	6.364	-5.265	59.754	6.465	-5.436
69.134	5.513	-4.538	69.134	5.575	-4.629
77.778	4.343	-3.501	77.778	4.360	-3.543
85.355	2.978	-2.375	85.355	2.977	-2.393
91.574	1.746	-1.400	91.574	1.744	-1.400
96.194	0.797	-0.638	96.194	0.793	-0.640
99.039	0.196	-0.163	99.039	0.204	-0.166

- Notes: (1) Leading edge radius = 1.25 in.
(2) Excluding door fairing.

(Station and Ordinates Given in Percent of Local Chord)

BL = 105.000⁽³⁾

Station	Ordinate, Upper Surface	Ordinate, Lower Surface
0.961	1.409	-1.409
3.806	3.065	-2.866
8.426	4.737	-4.208
14.645	6.031	-5.274
22.222	6.803	-6.150
30.866	7.150	-6.465
40.246	7.236	-6.436
50.000	6.969	-6.217
59.754	6.379	-5.646
69.134	5.503	-4.741
77.778	4.341	-3.551
85.355	2.970	-2.399
91.574	1.742	-1.413
96.194	0.828	-0.676
99.039	0.247	-0.209

BL = 110.000⁽³⁾

Station	Ordinate, Upper Surface	Ordinate, Lower Surface
0.961	1.451	-1.402
3.806	3.121	-2.824
8.426	4.780	-4.118
14.645	6.143	-5.205
22.222	6.914	-6.015
30.866	7.215	-6.489
40.246	7.235	-6.568
50.000	6.963	-6.301
59.754	6.385	-5.634
69.134	5.521	-4.671
77.778	4.365	-3.506
85.355	2.992	-2.370
91.574	1.768	-1.402
96.194	0.829	-0.661
99.039	.256	-0.217

BL = 112.154⁽³⁾

Station	Ordinate, Upper Surface	Ordinate, Lower Surface
0.961	1.471	-1.391
3.806	3.174	-2.797
8.426	4.821	-4.088
14.645	6.157	-5.163
22.222	6.921	-5.962
30.866	7.212	-6.439
40.246	7.222	-6.529
50.000	6.946	-6.253
59.754	6.378	-5.620
69.134	5.515	-4.651
77.778	4.354	-3.485
85.355	2.988	-2.360
91.574	1.768	-1.396
96.194	0.798	-0.637
99.039	0.251	-0.221

BL = 140.000⁽³⁾

Station	Ordinate, Upper Surface	Ordinate, Lower Surface
0.961	1.558	-1.387
3.806	3.202	-2.741
8.426	4.734	-3.885
14.645	5.983	-4.826
22.222	6.778	-5.490
30.866	7.166	-5.884
40.246	7.252	-5.957
50.000	7.015	-5.700
59.754	6.463	-5.115
69.134	5.602	-4.247
77.778	4.444	-3.208
85.355	3.103	-2.222
91.574	1.867	-1.341
96.194	0.894	-0.670
99.039	0.276	-0.223

Note: (3) Ordinates outboard of BL 100.75 are with respect to the dihedral plane.

(Station and Ordinates Given in Percent of Local Chord)

$$BL = 170.000^{(3)}$$

Station	Ordinate, Upper Surface	Ordinate, Lower Surface
0.961	1.780	-1.385
3.806	3.324	-2.572
8.426	4.590	-3.403
14.645	5.646	-4.028
22.222	6.667	-4.423
30.866	7.043	-4.669
40.246	7.300	-4.708
50.000	7.142	-4.471
59.754	6.647	-3.996
69.134	5.769	-3.339
77.778	4.610	-2.568
85.355	3.324	-1.860
91.574	2.077	-1.159
96.194	1.049	-0.586
99.039	0.376	-0.218

Note: (3) Ordinates outboard of BL 100.75 are with respect to the dihedral plane.

6.3.8 Wing Flap Airfoil Ordinates

(Station and Ordinates Given in Percent of Local Wing Flap Chord)

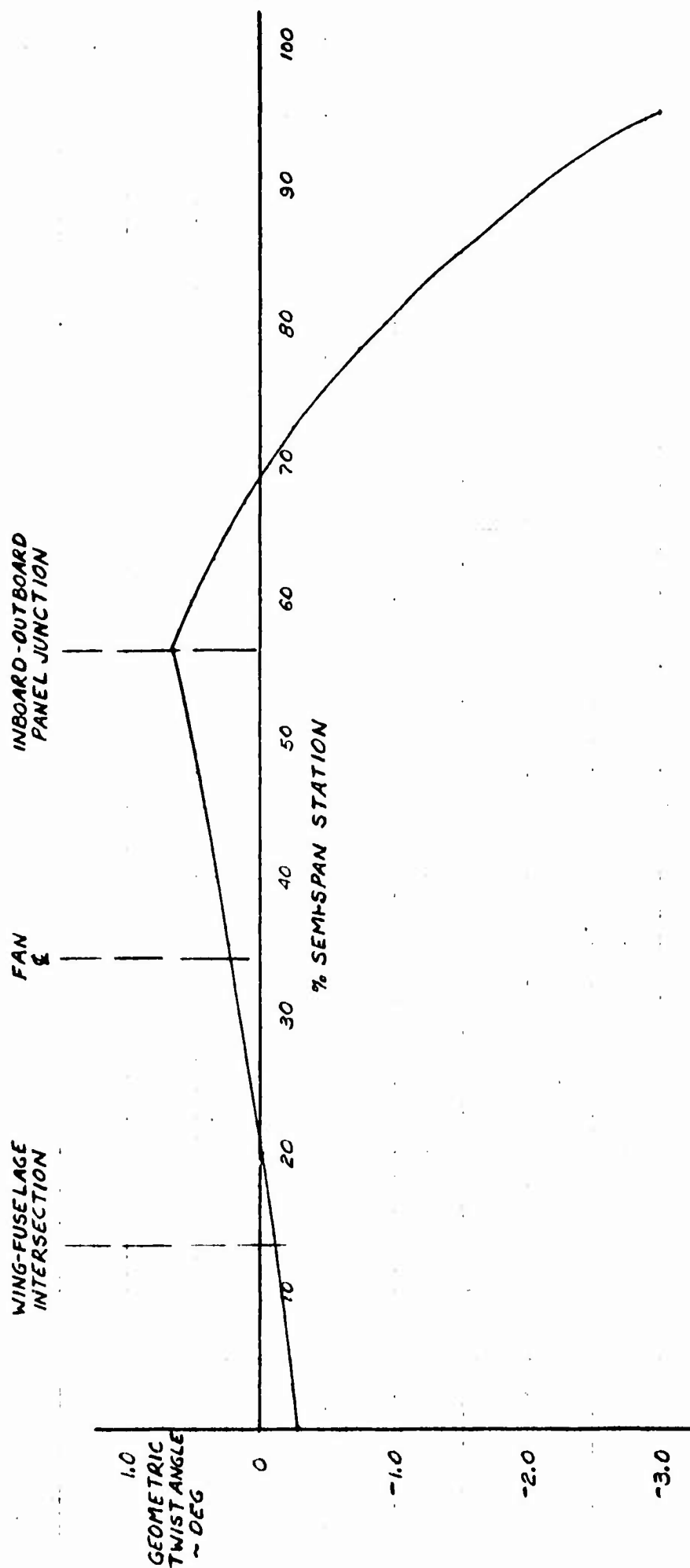
Station	Ordinate, Upper Surface	Ordinate, Lower Surface
0.000	0.000	0.000
0.500	1.799	-1.422
0.750	2.384	-1.799
1.250	3.305	-2.217
2.500	5.146	-2.594
5.000	8.033	-2.594
7.500	10.292	-2.552
10.000	12.050	-2.510
15.000	14.686	-2.426
20.000	16.569	-2.343
25.000	17.991	-2.217
30.000	18.744	-2.133
35.000	18.912	-2.050
40.000	18.702	-1.924
45.000	17.949	-1.799
50.000	16.820	-1.673
55.000	15.481	-1.506
60.000	13.807	-1.338
65.000	12.092	-1.171
70.000	10.376	-1.004
75.000	8.661	-0.836
80.000	6.945	-0.666
85.000	5.230	-0.502
90.000	3.514	-0.334
95.000	1.757	-0.167
100.000	0.000	0.000

- Notes:
- (1) Wing flap is a constant airfoil section from BL 24.00 to BL 101.75.
 - (2) Stations and ordinates are with respect to wing flap plane.
 - (3) Leading edge radius = 0.63 inches.

XV-5A
WING GEOMETRIC TWIST

NOTE

1- TWIST ANGLE MEASURED WITH RESPECT
TO FUSELAGE REFERENCE PLANE, WL 100.00



11-20-62

1.4.1